

# **Magnetic and Optical studies of Wide Band-gap Oxide Semiconductors**

*A thesis submitted for the award of the degree of*

**Doctor of Philosophy**

in

**Physics**

By

**Shyamsundar Ghosh**

Department of Physics

University of Calcutta,

Kolkata, India

May 2013

*Dedicated to my parents...*

## ACKNOWLEDGEMENTS

It is my extreme pleasure to grab the opportunity to acknowledge those peoples who helped and supported me in many ways during my entire Ph.D. student life. Almost four and half years back, I have joined myself as a Junior research fellow (JPF) under the supervision of Prof. Kalyan Mandal and now completed my Ph.D. thesis with his supreme care. Hence first of all, I would like to convey my sincere thanks to my Ph.D. supervisor for giving me a chance to work in his research group. His valuable words always inspired me in the field of science and also motivated me to my research. His academic discussions, suggestions helped me to improve my knowledge as well research skill. I am extremely grateful and also indebted to my supervisors, as this thesis could not have completed without his constant encouragement, help, support and active guidance.

I am also grateful to Dr. Gobinda Gopal Khan (Gogo Da), Research Associate (currently, DST-Inspire faculty at Calcutta University) and also the senior most member of our research group. His active collaboration helped me a lot to solve various research problems to complete my thesis. His constant encouragement to accept the challenges of performing research in various fields of nanoscience has broadened my experimental skill in this area also.

I wish to express my sincere gratitude to Dr. P. M. G. Nambissan, Professor at SINP, Kolkata for his active collaboration, fruitful discussions which were essential to complete a few parts of my thesis.

I would also like to convey my sincere thanks to Prof. Shikha Varma, Institute of Physics, Bhubaneswar, Orissa, India for providing me the facility of XPS measurements of some of my samples.

I am also thankful to Dr. Dipankar Das, UGC-DAE Consortium for Scientific Research, Kolkata for providing the SQUID measurement facility.

I am also grateful to Dr. Ranjan Chaudhury, (Acting registrar), SNBNCBS, Kolkata for his valuable discussions and suggestions which helped me to consolidate my theoretical knowledge on my research problem.

Besides, I would like to consider myself a bit of lucky for having blessed with some wonderful friends and labmates like Dr. Madhuri Mandal, Dr. Bipul Das, Debabrata Pal, Arka Chaudhary, Debasish Sarkar, Rajasree Das, Ashutosh Singh, Arup Ghosh, Rupali Rakshit and Monalisha Pal. It is my pleasure to express heartfelt gratitude to all of them for their supreme company, support and help in various aspects during the course of my Ph.D. work.

I am extremely thankful to Council of Scientific and Industrial Research (CSIR), Government of India, for providing me a research fellowship (both JRF and SRF) to complete my Ph.D. thesis.

I sincerely acknowledge the support of the Director of our Institute, Dr. Arup Kr. Roychaudhuri, the other faculty members, staffs and technical assistants, S. N. Bose National Centre for Basic sciences, Department of Condensed Matter Physics and Material Sciences, Kolkata during entire course of my research work.

Finally, I love to express to my gratitude to my family. It is all for their constant support, encouragement, especially my father, grand mother (Thakuma) and sisters; Pinka (Sumita) and Munmun (Manu). It was very tough for me when my mother (Maa) had expired in 2006, just after my graduation, but they continuously encouraged me to fulfill my aim and to step forward. I am also very happy to avail the wonderful company of Subir (Rintu) Da, my elder sister's husband during this journey. My little sweet nephew, Ankan (Gutu) has also added a new colour to my life and enriched me with many beautiful moments.

.....  
**(Shyamsundar Ghosh)**

## LIST OF PUBLICATIONS

1. **S. Ghosh** and K. Mandal, "Study of  $Zn_{1-x}Co_xO$  ( $0.02 \leq x \leq 0.08$ ) dilute magnetic semiconductor prepared by mechanochemical synthesis route," *Journal of Magnetism and Magnetic Materials* **322**, 1979-1984, (2010).
2. **S. Ghosh**, D. De Munshi and K. Mandal, "Paramagnetism in single-phase  $Sn_{1-x}Co_xO_2$  dilute magnetic semiconductors," *Journal of Applied Physics* **107**, 123919, (2010).
3. **S. Ghosh**, M. Mandal and K. Mandal, "Effects of Fe doping and Fe-N-codoping on magnetic properties of  $SnO_2$  prepared by chemical coprecipitation," *Journal of Magnetism and Magnetic Materials*, **323**, 1083-1087, (2011).
4. **S. Ghosh**, G. G. Khan, Bipul Das and K. Mandal, "Vacancy-induced intrinsic  $d^0$  ferromagnetism and photoluminescence in potassium doped ZnO nanowires" *Journal of Applied Physics* **109**, 23927, (2011).
5. G. G. Khan, **S. Ghosh** and K. Mandal, "Origin of room temperature  $d^0$  ferromagnetism and characteristic photoluminescence in pristine  $SnO_2$  nanowires: a correlation" *Journal of Solid State Chemistry* **186**, 278, (2012).
6. **S. Ghosh**, G. G. Khan, and K. Mandal, "Defect-Driven Magnetism in Luminescent n/p-Type Pristine and Gd-Substituted  $SnO_2$  Nanocrystalline Thin Films", *ACS Applied Materials and Interfaces* **4**, 2048, (2012).
7. **S. Ghosh**, G. G. Khan, S. Varma and K. Mandal, "Influence of Li-N and Li-F co-doping on defect-induced intrinsic ferromagnetic and photoluminescence properties of arrays of ZnO nanowires" *Journal of Applied Physics* **112**, 043910 (2012).
8. **S. Ghosh**, G. G. Khan and K. Mandal, " $d^0$  Ferromagnetism in Oxide Nanowires: Role of Intrinsic Defects" *European Physical Journal Web of Conferences* **40**, 03001 (2013).

9. **S. Ghosh**, G. G. Khan, Shikha Varma and K. Mandal , “Effect of film-thickness and oxygen partial pressure on zinc vacancy-induced room-temperature ferromagnetism in Na-doped ZnO thin films”, ACS Applied Materials and Interfaces **5**, 2455 (2013).
10. **S. Ghosh**, G. G. Khan, A. Ghosh, S. Varma and K. Mandal, “High temperature ferromagnetism induced by the alkali-substitutional defects in pulse laser deposited luminescent ZnO thin films”, 2012 (**Communicated**).
11. **S. Ghosh**, G. G. Khan, K. Mandal and P.M.G. Nambissan, “Positron annihilation spectroscopy studies of vacancy-type defects and room-temperature ferromagnetism in chemically synthesized Li-substituted ZnO nanoparticles”, 2012 (**Communicated**).

# Contents

<b>1</b>	<b>Introduction</b>	<b>1</b>
	1.1 Spin-based electronics or spintronics .....	1
	1.1.1 Spin injection, transport and detection .....	3
	1.1.2 Magnetic Semiconductors .....	4
	1.1.2.1 Concentred Magnetic Semiconductors .....	5
	1.1.2.2 Dilute Magnetic Semiconductors .....	5
	1.1.2.3 Earlier works on Magnetic semiconductors .....	6
	1.2 Wide band-gap oxide semiconductors .....	8
	1.2.1 Crystal structure and lattice parameters.....	9
	1.2.1.1 ZnO .....	9
	1.2.1.2 SnO <sub>2</sub> .....	9
	1.2.1.3 TiO <sub>2</sub> .....	10
	1.2.2 Transition metal-doped oxide semiconductors: A debate on presence or absence of intrinsic ferromagnetism .....	11
	1.3 Theoretical models for ferromagnetism in TM-doped oxides .....	12
	1.3.1 Zener's model for ferromagnetism .....	12
	1.3.2 Bound magnetic polaron model .....	13
	1.3.3 Double exchange mechanism .....	15
	1.4 <i>d</i> <sup>0</sup> ferromagnetism in oxide semiconductor .....	15
	1.4.1 Magnetic and nonmagnetic defects in oxides .....	15
	1.4.2 Defects and material dimensionality .....	17
	1.4.3 Alternative way to prepare high- <i>T</i> <sub>c</sub> ferromagnetic oxide semiconductors .....	18
	1.5 Motivation of our work .....	19
	1.6 Thesis organization .....	20
	References .....	21
<b>2</b>	<b>Experimental Techniques for Sample Preparation and Characterization</b>	<b>24</b>
	2.1 Preface .....	24

2.2 Synthesis techniques .....	25
2.2.1 Mechano-Synthesis (MS) techniques .....	25
2.2.2 Solvothermal Synthesis (SS) .....	28
2.2.2.1 Stainless steel Autoclave.....	28
2.2.2.2 Crystal growth mechanism.....	29
2.2.3 Chemical Co-precipitation technique.....	30
2.2.4 Template-assisted wet chemical synthesis of 1D NWs.....	31
2.2.4.1 Preparation of AAO template.....	31
2.2.4.2 Fabrication of oxide NWs within AAO template.....	33
2.2.5 Thin film Deposition Techniques.....	34
2.2.5.1 Sputtering Process.....	34
2.2.5.2 Pulsed laser deposition (PLD).....	37
2.3 Characterization and measurement techniques.....	38
2.3.1 X-ray diffraction.....	38
2.3.2 Electron-Matter Interaction (Electron Microscopy).....	40
2.3.2.1 Scanning Electron Microscopy and EDX spectroscopy.....	41
2.3.2.2 Transmission Electron Microscopy.....	43
2.3.3 X-ray Photoelectron Spectroscopy.....	45
2.3.4 Photoluminescence Spectroscopy.....	46
2.3.5 Electron Paramagnetic Resonance Spectroscopy.....	48
2.3.6 Vibrating Sample Magnetometer.....	49
2.3.7 SQUID Magnetometer.....	50
2.3.8 Atomic and Magnetic Force Microscopy.....	53
References.....	54
<b>3 Transition Metal-doped Wide-Band Oxide Semiconductors</b>	<b>56</b>
3.1 Preface.....	56
3.2 Co-doped ZnO bulk structures.....	57
3.2.1 Synthesis of $Zn_{1-x}Co_xO$ ( $x \leq 0.08$ ) bulk powders.....	57
3.2.2 Crystal Structural and morphology.....	58
3.2.3 UV-visible absorption spectroscopy studies.....	61
3.2.4 Magnetic properties of Co-doped ZnO.....	62
3.3 Co-doped SnO <sub>2</sub> bulk and nanostructures: Effects of	

particle size and annealing.....	67
3.3.1 Synthesis of Co-doped SnO <sub>2</sub> nanorods.....	67
3.3.2 Synthesis of Co-doped SnO <sub>2</sub> bulk-structures.....	68
3.3.3 Results and discussion.....	68
3.3.3.1 Morphology and crystal structure.....	68
3.3.3.2 UV-visible absorption spectroscopy.....	71
3.3.3.3 Size dependent magnetic properties of Co-doped SnO <sub>2</sub> .....	72
3.3.3.4 Temperature dependent magnetic behavior.....	74
3.4 Cr and V-doped TiO <sub>2</sub> bulk structures.....	76
3.5 Fe and Fe-N co-doped SnO <sub>2</sub> bulk structures: Effect of excess free carriers.....	77
3.5.1 Synthesis and characterization.....	78
3.5.2 Experimental result and discussions.....	78
3.5.2.1 Effect of dopants on structural properties.....	78
3.5.2.2 SEM images and EDAX spectra.....	80
3.5.2.3 UV-visible absorption spectra.....	81
3.5.2.4 Field dependent magnetization measurements.....	82
3.5.2.5 ZFC and FC measurements for O <sub>2</sub> annealed Sn <sub>1-x</sub> Fe <sub>x</sub> O <sub>2</sub> .....	84
3.5.2.6 ZFC and FC measurements for N <sub>2</sub> annealed Sn <sub>1-x</sub> Fe <sub>x</sub> O <sub>2</sub> .....	85
3.6 Conclusion.....	86
References.....	87

<b>4</b>	<b>Pristine and Rare Earth Element (Gd)-Doped SnO<sub>2</sub> Thin Films prepared by RF Sputtering</b>	<b>90</b>
4.1	Preface.....	90
4.2	Synthesis of Pure and Gd-doped SnO <sub>2</sub> thin films.....	91
4.3	Results and discussions.....	92
4.3.1	Crystal structure.....	92
4.3.2	Surface morphology.....	94
4.3.3	Magnetic properties.....	95
4.3.3.1	M-H behaviour of pure and Gd-doped SnO <sub>2</sub> films.....	95
4.3.3.2	AFM and MFM micrographs of SnO <sub>2</sub> films.....	98
4.3.3.3	Thermal dependent magnetic behaviour.....	99
4.3.4	Photoluminescence properties.....	100

4.3.5 Electrical properties.....	103
4.4 Conclusion.....	105
References.....	105
<b>5 Defect-induced <math>d^0</math> Ferromagnetism and Photoluminescence of Template embedded 1D Oxide Nanowires</b>	
5.1. Preface.....	108
5.2 Arrays of pristine SnO <sub>2</sub> nanowires.....	109
5.2.1 Fabrication of SnO <sub>2</sub> nanowires.....	109
5.2.2 Results and discussion.....	111
5.2.2.1 Morphology and crystallography.....	111
5.2.2.2 Photoluminescence study.....	112
5.2.2.3 Electron paramagnetic resonance spectroscopy.....	113
5.2.2.4 Magnetic properties of SnO <sub>2</sub> NWs.....	114
5.3 Nonmagnetic Potassium (K)-doped ZnO NWs.....	116
5.3.1 Fabrication of K-doped ZnO NWs.....	116
5.3.2 Morphology and crystal structure.....	117
5.3.3 Photoluminescence properties .....	119
5.3.4 Magnetic properties of K-doped ZnO NWs.....	121
5.4 Nitrogen (N)/Fluorine (F) and Lithium (Li) codoped ZnO NWs: Evidence of hole-mediated $d^0$ ferromagnetism.....	126
5.4.1 Fabrication of Li-N/F codoped ZnO NWs.....	126
5.4.2 Crystal structure and morphology.....	127
5.4.3 X-ray photoelectron spectroscopy.....	130
5.4.4 Defect analysis using photoluminescence spectroscopy.....	132
5.4.5 Magnetic properties of Li-N/F codoped ZnO NWs.....	135
5.5 Conclusions.....	139
References.....	140
<b>6. Defect-driven Magnetic, Luminescence and Electrical properties of Alkali-Metal doped ZnO Thin Films prepared by Pulsed Laser Deposition</b>	<b>144</b>

6.1. Preface.....	145
6.2 Alkali-doped ZnO thin films: A comparative study on effects of Li, Na and K substitutional defects.....	145
6.2.1 Fabrication of Li, Na and K-doped ZnO thin films.....	145
6.2.2 Characterization of alkali-doped ZnO thin films.....	145
6.2.3 Results and discussions.....	146
6.2.3.1 X-ray diffraction and crystal structure.....	146
6.2.3.2 Magnetic properties.....	147
6.2.3.3 Magnetic force microscopy studies.....	149
6.2.3.4 X-ray photoelectron spectroscopy studies.....	150
6.2.3.5 Photoluminescence spectroscopy studies.....	151
6.2.3.6 Electrical behaviour.....	154
6.3 Luminescent <i>p</i> -type Na-doped ZnO thin films: Influence of film-thickness and oxygen Pressure.....	157
6.3.1 Fabrication of <i>p</i> -type Na-doped ZnO thin films.....	157
6.3.2 Results and discussions.....	157
6.3.2.1 Structural and electrical properties.....	157
6.3.2.2 Thickness dependent magnetic behavior.....	159
6.3.2.3 Magnetic properties of Na-doped ZnO thin film: Influence of oxygen pressure.....	161
6.3.2.4 X-ray photoelectron spectroscopy studies.....	162
6.3.2.5. RT photoluminescence properties.....	163
6.4 Conclusion.....	168
References.....	168

<b>7. Positron Annihilation Spectroscopy study of Li-doped ZnO Nanoparticles</b>	<b>71</b>
7.1 Preface.....	171
7.2 Introduction to positron annihilation spectroscopy.....	172
7.3 Two-state trapping model.....	174
7.4 Positron lifetime spectroscopy.....	176
7.5 Doppler broadening spectroscopy.....	178
7.6 Experimental procedure of positron lifetime spectroscopy.....	179

7.7 Experimental procedure of Doppler broadening spectroscopy.....	180
7.8 Positron Annihilation study of Li-doped ZnO nanoparticles.....	181
7.8.1 Preparation of Li-doped ZnO nanoparticles.....	181
7.8.2. Results and discussion.....	182
7.8.2.1. Particle size and lattice effects.....	182
7.8.2.2. High-temperature ferromagnetism.....	185
7.8.2.3. Photoluminescence spectroscopy study.....	187
7.8.2.4 Positron annihilation spectroscopy studies.....	189
7.8.3. Conclusions.....	197
References.....	198
<b>8. Conclusion and Scope for Future Study</b>	<b>200</b>

*This page is intentionally left blank*

# Chapter 1

## Introduction

### 1.1 Spin-based electronics or spintronics

An electron has two degree of freedom; charge ( $q_e = 1.6 \times 10^{-19}$  C) and magnetic spin ( $s = \frac{1}{2}$ ). The charge degree of freedom of the electron defines the electrical transport properties of the respective material and used to develop conventional electronic devices. However in modern spintronics, also called spin based electronics, not only electronic charge but the magnetic spins also are exploited to define the transport properties [1]. Thus in case of conventional electronics, the electrons constituting the current may not have a definite spin orientation while in spintronics, all the electrons carries current have a reference spin direction and makes the current spin polarised. The most dramatic effects are found to seen for highly spin polarised current and therefore, there are continuing efforts to find 100% spin-polarized conducting materials. However, to find out appropriate materials with 100% spin polarization is not easy and therefore, the aim is to achieve maximum degree of spin polarization.

The spin polarization (P) can be defined as,

$$P = \frac{n_{\uparrow} - n_{\downarrow}}{n_{\uparrow} + n_{\downarrow}} \times 100\% ,$$

where  $n_{\uparrow}$  is the number of electron having spin up and  $n_{\downarrow}$  is the number of electron having spin down, and total number of electrons,  $n = n_{\uparrow} + n_{\downarrow}$ .

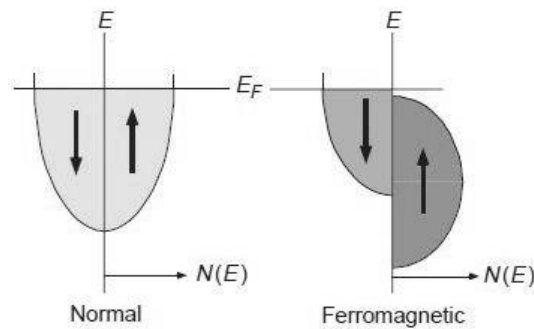


**Fig. 1.1:** A schematic diagram of the density of electronic states that are available to electrons in a normal metal and in a ferromagnetic metal whose majority spin states are completely filled. Where  $E$  is the electron energy,  $E_F$  is the Fermi level, and  $N(E)$  is density of states [Ref. 1].

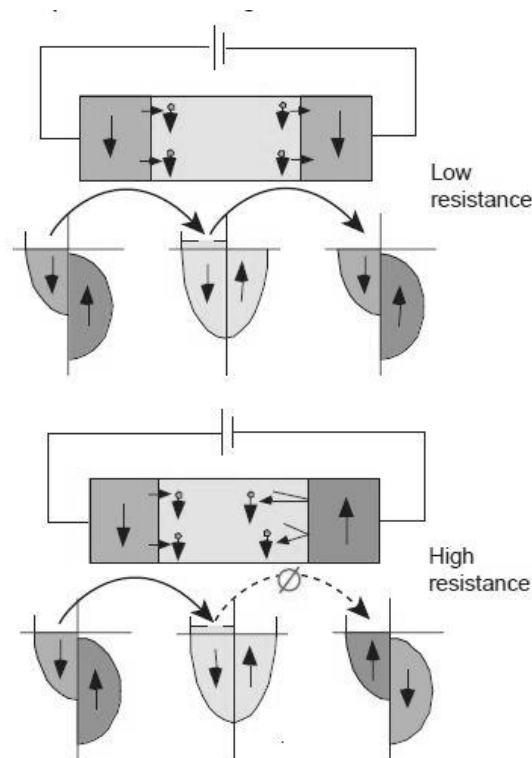


**Fig. 1.2:** A Schematic diagram of spin-polarized transport from a ferromagnetic metal, through a normal metal, and into a second ferromagnetic metal for aligned and antialigned magnetic moments.  $\Phi$  is disallowed channel [Ref. 1].

Ferromagnetic metals such as Fe, Co and Ni and their alloys are partially polarized materials and are found to have spin polarization  $P$  of 40% to 50% [2]. Figure 1.1 shows a schematic representation of the density of electronic states that are available to electrons in a normal metal and in a ferromagnetic metal whose majority spin states are completely filled. The discovery of giant magnetoresistance (GMR) effect [3] is the first visualization of spin-dependent transport in case of multilayered systems and now a day, it is being widely used in magnetic information storage application. GMR is a quantum mechanical effect observed in layered magnetic thin-film structures that are composed of alternating layers of ferromagnetic and nonmagnetic layers. When the magnetic moments of the ferromagnetic layers are parallel, the spin-dependent scattering of the carriers is minimized, and the material has its lowest resistance (see Fig. 1.2). When the ferromagnetic layers are antialigned, the spin-dependent scattering of the carriers is maximized, and the material has its highest resistance (Fig. 1.2). Thus, depending on the direction of magnetization of a material relative to the spin polarization of the current, a material can function as either a conductor or an insulator for electrons of a specific spin polarization. An analogy can be made with polarized light passing through an analyzer. However, in the optical case, crossing the polarization axis at  $90^\circ$  prevents the transmission of the light, whereas for spin-polarized electrons, the magnetization must be rotated  $180^\circ$  to stop electrical conduction. The directions of the magnetic moments are manipulated by external magnetic fields that are applied to the materials. These materials can now be fabricated to produce significant changes in resistance in response to relatively small magnetic fields and to operate at room temperature.

### 1.1.1 Spin injection, transport and detection

Spin-based electronics or spintronics is based on three primary functionalities. They are as follows; (i) spin injection from a ferromagnetic metal or semiconductor to a nonmagnetic metal or semiconductor (ii) spin transport through the nonmagnetic layer and finally (iii) spin detection in another ferromagnetic metal or semiconductor. Successful application of the wide range of possible spin-dependent phenomena in semiconductor systems requires effective and efficient techniques for the electrical injection of strongly spin-polarized currents (spin currents), as well as

electrical detection of such spin currents. Ferromagnetic metals such as Co, Fe, Ni can be used as a source of spin polarized carriers which can be injected into a semiconductor or a superconductor, or a normal metal or can be used to tunnel through an insulating barrier. The nature of the specific spin-polarized carriers and the electronic energy states associated with each material must be identified in each case. As semiconducting materials is most appropriate candidate to develop electronic devices, the effective and successful injection of spin polarized carriers into a non-magnetic semiconductor is in prime interest.

However, the injection of spin polarized carriers across the interface of a ferromagnetic (FM) metal (Co, Fe, Ni) to nonmagnetic (NM) semiconducting layer is not found to be very effective due to mismatch of electrical resistance of the two layers [4]. The effectiveness of the spin injection depends on the ratio of the (spin dependent) conductivities of the FM and NM layers,  $\sigma_F$  and  $\sigma_N$ , respectively. When  $\sigma_F \leq \sigma_N$  as in the case of a typical metal, then efficient and substantial spin injection can occur, but when the NM layer is a semiconductor,  $\sigma_F \geq \sigma_N$  and the spin-injection efficiency will be very low. Therefore, for successful spin injection into semiconducting layer, one need to reduce the conductivity of ferromagnetic layer such as the condition  $\sigma_F \leq \sigma_N$  can be satisfied. Although there are a number of materials that apparently have such half-metal ferromagnet [5, 6] which can solve this problem but these are challenging materials to work. Another way to solve this problem if we can fabricate ferromagnetic semiconductor (FMS) with sufficient spin polarization [7-10] then, it can be effective to inject spin polarized carriers from ferromagnetic semiconductor (FMS) to another nonmagnetic semiconductor (NMS) according to condition  $\sigma_F \leq \sigma_N$ . After words the efforts have been started to search for the appropriate ferromagnetic semiconductor (FMS) which can be used as spintronic materials for spin injection. However, it is essential that the FMS should have high Curie temperature ( $T_C$ ) i.e. above the room temperature ( $\geq 300K$ ) so that device using this FMS can operate at our living atmosphere.

## 1.1.2 Magnetic semiconductors

During last two decades, the scientists have been searching for new materials, called magnetic semiconductors (MS) in which both electronic charge and spin

degree of freedom coexists, to develop modern spin-based electronic devices. For that MS should exhibit both semiconducting as well as ferromagnetic properties well above the room-temperature (RT). Initially, people were started to focus on the existing natural semiconductors which are also ferromagnetic, called concentrated magnetic semiconductors (CMS) which were found to have very low Curie temperature ( $T_C$ ), well below the RT. In order to obtain the RT ferromagnetism, scientists were then tried to make nonmagnetic semiconductor magnetic by means of little amount of magnetic atom doping which is known as dilute magnetic semiconductor (DMS).

### 1.1.2.1 Concentred magnetic semiconductors

There exist some of the semiconducting materials which are intrinsically ferromagnetic, called concentrated magnetic semiconductor (CMS) in which all the constituent cations have individual atomic magnetic moment. For example,  $\text{EuX}$  ( $X = \text{O, S, Se, Te}$ ),  $\text{Fe}_3\text{O}_4$  ( $T_C = 400 \text{ K}$ ),  $\text{CrBr}_3$  ( $T_C = 37 \text{ K}$ ),  $\text{CdCr}_2\text{S}_4$  ( $T_C = 84.5 \text{ K}$ ),  $\text{BiMnO}_3$  ( $T_C = 105 \text{ K}$ ),  $\text{EuO}$  ( $T_C = 79 \text{ K}$ ) etc. However, most of the CMS are found to ferromagnetic at well below the room temperature (RT) which imposes restriction for practical application in spintronic devices. In addition, doping them with other elements cannot cause significant changes in those intrinsic physicochemical characteristics of CMS that differ from the properties of the known semiconductors. At the same time, distinctions between the crystal lattices of CMS and the known semiconductors impose severe restrictions on the possibility for CMS to be used in semiconductor devices.

### 1.1.2.2 Dilute magnetic semiconductors

Dilute magnetic semiconductor (DMS) is a new class of magnetic semiconductor in which few percentage of host cations are randomly replaced by magnetic ions such as transitional metal (TM) and rare earth (RE) ions. The host semiconductor is generally found to have a nonmagnetic (diamagnetic) lattice and the ferromagnetic properties are extrinsically incorporated by means of dilute doping of TM ions (Mn, for example). Figure 2.3 illustrates a schematic difference between a CMS, DMS and nonmagnetic semiconductor. This method of preparing a nonmagnetic semiconductor ferromagnetic has been attracted huge interest to the

scientist during last two decades. Such enormous interest to DMS is not due to only for possibility of their exciting practical application but also for the underlying physics behind the phenomena. In fact, the origin of ferromagnetism in such DMS is still not quite clear at all (controversial) and scientists are still looking for the appropriate explanation to all observed phenomena.

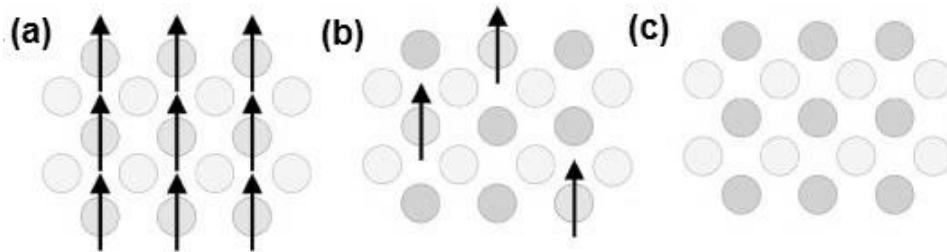


**Fig. 1.3:** (a) A concentrated magnetic semiconductor, in which all the semiconducting cations have intrinsic magnetic moment (b) a diluted magnetic semiconductor in which some of the diamagnetic host cations are randomly replaced by magnetic (TM) cations and (c) a nonmagnetic semiconductor, which contains no magnetic ions.

### 1.1.2.3 Earlier works on magnetic semiconductors

Extensive research works on magnetic semiconductors (especially CMS) were done in the late 1960s to early 1970s. The exchange interactions between the electrons in the semiconducting band and the localized electrons at the magnetic ions lead to a number of peculiar and interesting properties, such as a red shift of band gap when ferromagnetism sets in. However, it was found that the crystal growth of such materials was very difficult because of very different crystal structure compared to other semiconductors like Si and GaAs and which impose severe restrictions on the possibility for CMS to be used in semiconductor devices. Besides this, obtained values of  $T_C$  of such ferromagnetic semiconductors are well below the room temperature (RT) which again not appropriate for spintronic devices.

Therefore, keeping an aim for fabrication of high temperature (above RT) magnetic semiconductors, people were attracted towards DMS from 1990 onwards. At initial stage, the work were mainly on focused on Mn-doped Group II-VI compound semiconductors (for example; CdSe, CdTe, ZnSe, ZnTe) [11-15] and then it was gradually shifted to Group III-V (GaAs, GaP, GaN, GaSb, InAs, InP, InSb) [16-19], Group IV-IVc compounds (PbS, PbSe, PbTe) [20-23] and even elemental

semiconductors (Si, Ge) [24-28]. Ferromagnetism was reported to appear in such many systems but like CMS, here also Curie temperature ( $T_C$ ) lies well below the room temperature which has limited technological interest [16]. In II-VI semiconductors divalent ( $2^+$ ) magnetic ions (Mn, for example) can easily occupy the group-II cation sites of the host lattices, resulting in antiferromagnetic (AFM) or spin glass ordering at higher concentrations [11]. Evidence of ferromagnetism (FM) was observed in highly  $p$ -type doped ZnTe films with  $T_C \sim 30$  K [12]. In case of III-V DMS's, the highest reported  $T_C$  is 110 K for 5.3% Mn doped GaAs [16, 17]. Therefore, the search for high  $T_C$  ferromagnetic semiconductors was still on.

The major breakthrough in the field of DMS was appeared in the year of 2000, when the groups of T. Deitl et. al. [17] successfully explained the ferromagnetic ordering in Mn-doped GaAs. They showed that substitution of  $Mn^{2+}$  at trivalent Ga site can introduce holes within the host lattice and the ferromagnetic interaction between the localised Mn ions was mediated through these holes; giving rise to long range ferromagnetism. Besides this, they also estimated the values of probable  $T_C$  for a variety of TM-doped semiconductors and predicted that TM-doped wide band-gap oxide semiconductors (for example, ZnO,  $TiO_2$ ,  $SnO_2$ ,  $In_2O_3$ ,  $HfO_2$ , etc.) can be the promising candidate to exhibit required high  $T_C$  ferromagnetism. Their calculations also have shown that ferromagnetism (FM) is stable in a DMS which is based on a wide bandgap semiconductor. In addition to that, *ab initio* calculations based on local density approximation (LDA) was also performed for TM-doped ZnO-based semiconductors that showed it is very possible to stabilize FM in such oxides [29]. These theoretical studies were the first step to oxide-diluted magnetic semiconductors (O-DMS) and several groups started to work in this field. The experimental observation of RT FM in Co: $TiO_2$  thin-films [30] has obviously encouraged experimental studies and intensive experimental work has begun in the condensed matter community on O-DMS. However, before we go to the literature on O-DMS, we should introduce what are wide band gap oxides semiconductors and their novel properties which make them even more promising for multifunctional applications.

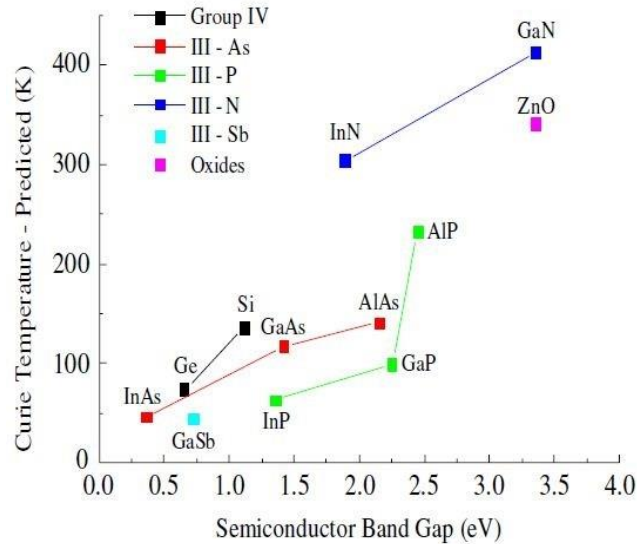


**Fig. 1.4:** Computed values of Curie temperature for various p-type semiconductors doped with 5 at.% Mn (after [17]).

## 1.2 Wide band-gap oxide semiconductors

Unlike the non-oxide semiconductors, oxide semiconductors are generally known to have wide energy band-gap which is greater than 3.0 eV. Having blessed with such large semiconducting band-gap, they are optically transparent in the visible region and suitable for short wavelength light applications. The most common examples of such oxide semiconductors are ZnO, TiO<sub>2</sub>, SnO<sub>2</sub>, In<sub>2</sub>O<sub>3</sub> or ITO (Sn-doped In<sub>2</sub>O<sub>3</sub>) etc. Using them as host to prepare DMS has the following advantages; (1) wide bandgap suited for applications with short wavelength light, (2) transparency and dyeability with pigments, (3) high *n*-type carrier concentration, (4) capability to be grown at low temperature even on plastic substrate, (5) ecological safety and durability, (6) low cost, etc. In addition, large electronegativity of oxygen is expected to produce strong *p-d* exchange coupling between band carriers and localized spins [31]. They are also the prime candidates for various multifunctional applications such as in transparent electronics, UV light emission, gas sensing, varistors and surface acoustic wave devices and after adding the spin functionality, they can be used to produce magnetic FETs [32] or low threshold spin-lasers [33]. As this thesis are mainly focused on ZnO, SnO<sub>2</sub> and a little bit on TiO<sub>2</sub> based MS, for the reader it is essential to have some knowledge about their crystal structures.

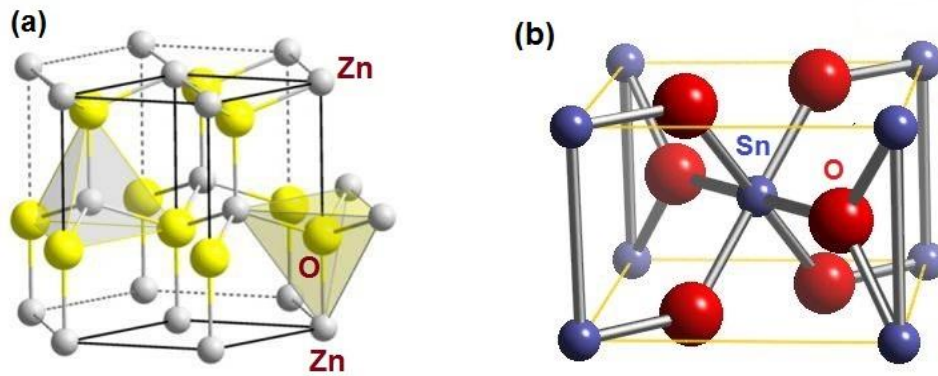
## 1.2.1 Crystal structure and lattice parameters

### 1.2.1.1 ZnO

Zinc oxide (ZnO) is a direct, wide band-gap ( $E_g \sim 3.37$  eV at 300K in bulk [34]) oxide semiconductor belonging to parent II-VI compounds. In common, ZnO has a hexagonal wurtzite crystal structure (shown in Fig. 1.5 (a)) where each anion is surrounded by four cations at the corners of a tetrahedron, and vice versa. This tetrahedral coordination is typical of  $sp^3$  covalent bonding, but ZnO also have a substantial ionic character. The ionicity of ZnO resides at the borderline between covalent and ionic semiconductor. Except the hexagonal wurtzite structure, ZnO can also crystalize in zinc blende and rocksalt type also. At ambient conditions, the thermodynamically stable phase is wurtzite. The zinc-blende ZnO structure can be stabilized only by growth on cubic substrates and the rocksalt (NaCl type) structure may be obtained at relatively high pressures. The wurtzite structure has a hexagonal unit cell with two lattice parameters,  $a = 3.25$  Å and  $c = 5.12$  Å, in the ratio of  $c/a = \sqrt{8/3} = 1.633$  [35] and belongs to the space group of  $C_{4v}^6$  or  $P6_3mc$ . Due to presence of oxygen vacancy or Zn interstitial defects, pure ZnO generally exhibits n-type conductivity and can be made also p-type introducing various acceptor dopants such N, P or Li, Na, K or co-doping elements [36].

### 1.2.1.2 SnO<sub>2</sub>

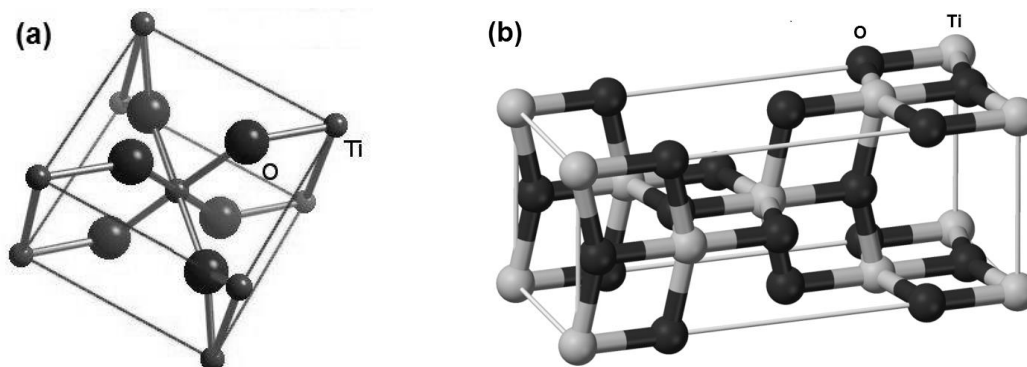
Like ZnO, tin (IV) or stannic oxide (SnO<sub>2</sub>) is another very important wide band transparent oxide semiconductor and presents special properties, such as transparency, remarkable chemical and thermal stabilities, with direct application for photodetectors, catalysts for oxidation and hydrogenations, solar cells, semiconducting gas sensors, liquid crystal displays and protective coatings. In the bulk, SnO<sub>2</sub> has a direct optical energy band gap of the order of 3.67 eV at 300 K [37]. As a mineral, stannic oxide is also called Cassiterite which has a rutile crystal structure. The rutile structure has a tetragonal unit cell, as shown in Fig. 1.5 (b), with a space-group symmetry of  $P4_2/mnm$ . The lattice constants are  $a = b = 4.7374$  Å and  $c = 3.1864$  Å [38]. In the bulk all Sn atoms are six-fold coordinated to three-fold coordinated oxygen atoms.



**Fig. 1.5:** (a) Hexagonal wurtzite ZnO crystal structure where each anion is surrounded by four cations at the corners of a tetrahedron, and vice versa and (b) Tetragonal rutile SnO<sub>2</sub> crystal structure

### 1.2.1.3 TiO<sub>2</sub>

Titanium dioxide (TiO<sub>2</sub>) is also belongs to the groups of wide-band oxide semiconductors and wide used as photocatalyst under UV-light. It crystallizes in several forms, such as rutile, anatase and brookite (see the diagrams of the most stable phases in Fig. 1.6). Rutile structure has a tetragonal unit cell ( $a = 4.59 \text{ \AA}$  and  $c = 2.96 \text{ \AA}$ ) with a bandgap of 3 eV while the anatase phase also crystallizes in a tetragonal structure ( $a = 3.78 \text{ \AA}$  and  $c = 9.52 \text{ \AA}$ ) with a bandgap of 3.2 eV [39]. The brookite has orthorhombic structure with lattice parameters  $a = 5.4558 \text{ \AA}$ ,  $b = 9.1819 \text{ \AA}$  and  $c = 5.1429 \text{ \AA}$  and is rare compared to anatase and rutile. Brookite has a larger cell volume than either anatase or rutile, with 8 TiO<sub>2</sub> groups per unit cell, compared with 4 for anatase and 2 for rutile.



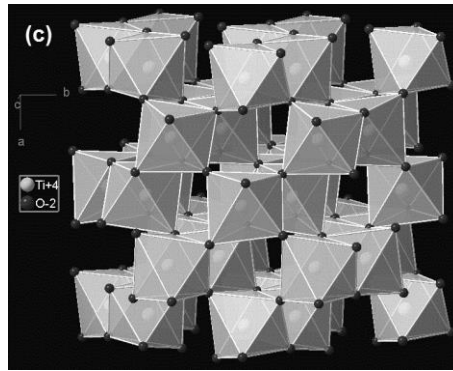


**Fig. 1.6:** Crystal structures of TiO<sub>2</sub> (a) rutile (b) anatase and (c) brookite phase.

## 1.2.2 Transition metal-doped oxide semiconductors: A debate on presence or absence of intrinsic ferromagnetism

Since the year 2000, after the theoretical prediction by Deitl *et al.* [17] about the possibility of achieving high- $T_C$  ferromagnetism in wide band oxides, many efforts have been made to prepare oxide-based DMS by doping various TM or RE ions. The first principle calculations by Sato and Katayama-Yoshida [40] showed the ferromagnetic ordering in various TM (V, Cr, Fe, Co and Ni)-doped ZnO matrix is stable. After that several experimental reports appeared about the magnetic properties of ZnO doped with Ni [41, 42], V [43], Mn [42, 44-49], Cr [42, 49], Fe [49, 50] and also Co [42, 49, 51-58]. Although, the existences of room-temperature ferromagnetism (RTFM) were reported, still the origin of FM in such oxides is still a debate, both the theoretical as well as the experimental point of view [59-63]. In fact, different controversial magnetic properties such as paramagnetism, ferromagnetism, antiferromagnetism, superparamagnetism and also spin glass behavior have been observed [64]. Magnetic properties of TM-doped oxides are found to largely depend on the sample preparation condition and thus the reproducibility becomes very difficult. There are reports which were initially reported to exhibit RTFM but later, only paramagnetic contributions of substituted TM ion have been detected by x-ray magnetic circular dichroism (XMCD) study [65-66]. This is indicating that the TM  $3d$  electrons may not be responsible for the origin of ferromagnetism in such oxides. In most of the cases, small amount of TM impurity secondary phases or defects might be accounted for the origin of observed ferromagnetism [67]. Straumal *et al.* [68] suggested that grain boundaries and related vacancies are the intrinsic origin for RTFM in Mn doped ZnO whereas Liu *et al.* [69] reported that ferromagnetism in V:

ZnO powder is highly correlated with the structural defects rather V ions. Therefore, in order to overcome the existing controversial on oxide DMS, a systematic study accompanied by careful identification of the phases and microstructures present is of high need.

## 1.3 Theoretical models for ferromagnetism in TM-doped oxides

Although RTFM was observed experimentally, the fundamental description about the origin of ferromagnetism in semiconductors remains incomplete. There exists several proposed theoretical models to explain how ferromagnetism can appear; such as Zener's model for ferromagnetism, bound magnetic polaron model, double exchange mechanism and virtual transitions etc.

### 1.3.1 Zener's model for ferromagnetism

Dietl *et al.* [17] was successful to explain the occurrence of FM in III-V and II-VI compound semiconductors using Zener's model for ferromagnetism, driven by exchange interaction between carriers and localized spins. The theory assumes ferromagnetic correlations mediated by holes from shallow acceptors in a matrix of localized spins in a magnetically doped semiconductor.  $Mn^{2+}$  ions substituted on the group II or III site provide the local spin and also provide holes in the case of III-V semiconductors. High concentrations of holes are believed to mediate the ferromagnetic interactions among  $Mn^{2+}$  ions. Direct exchange among Mn is anti-ferromagnetic as observed in fully compensated (Ga, Mn)As that is donor doped. In the case of electron-doped or heavily Mn-doped materials, no ferromagnetism is detected. Theoretical results suggest that carrier-mediated ferromagnetism in n-type material is relegated to low temperatures, if it occurs at all, while it is predicted at higher temperatures for p-type materials [17].

The strength of such carrier-mediated ferromagnetism in semiconductors depends on the magnetic ion concentration as well as on the carrier type and carrier density. As these systems can be envisioned as approaching a metal-insulator transition when carrier density is increased and ferromagnetism is observed, it is useful to consider the effect of localization on the onset of ferromagnetism. As carrier

density is increased, the progression from localized states to itinerant electrons is gradual. On the metallic side of the transition, some electrons populate extended states while others reside at singly occupied impurity states. On crossing the metal-insulator boundary, the extended states become localized, although the localization radius gradually decreases from infinity. For interactions on a length scale smaller than the localization length, the electron wave function remains extended. In theory, holes in extended or weakly localized states could mediate the long-range interactions between localized spins. This suggests that for materials that are marginally semiconducting, such as in heavily doped semiconducting oxides, carrier-mediated ferromagnetic interactions may be possible. The model by Dietl *et al* predicts that the transition temperature will scale with a reduction in the atomic mass of the constituent elements due to an increase in p-d hybridization and a reduction in spin-orbit coupling. Most importantly, the theory predicts a  $T_c$  greater than 300 K for the p-type GaN and ZnO, with  $T_c$  dependent on the concentration of magnetic ions and holes.

In absence of ferromagnetic clusters, precipitation or secondary phases, the other basic models for explaining ferromagnetism in TM-doped oxides are the bound magnetic polaron, double exchange and virtual transition. Most of the theories describing ferromagnetism in DMS assume that the TM ions, ( $Mn^{2+}$ ,  $Co^{2+}$ ) are randomly substituted on the cation sites where they act as acceptors. However, for ZnO which belongs to II-VI compounds, the realization of hole mediated FM in Mn-doped ZnO is not possible because both Zn and Mn ions are in  $2+$  oxidation state. However, in case of Mn or Co-doped  $SnO_2$  it might be again possible. As the pure oxides like ZnO,  $SnO_2$  is generally an n-type due to oxygen vacancy defects, the compensation will occur and the carrier density can be significantly less than the dopant density. Under these conditions, the exchange interaction between nearest-neighbour transition metal ions is mediated by the carriers and gives rise to ferromagnetism. However, if there exists any ferromagnetic impurity phases and/or TM clustering then the mechanism for ferromagnetism is need not necessarily be carrier mediated.

### 1.3.2 Bound magnetic polaron model

The bound magnetic polaron (BMP) Model is quite successful to explain the ferromagnetic exchange coupling between the TM local moments in n-type oxide

DMS [70-71]. During fabrication, oxides generally contain significant amount of oxygen vacancy defects which introduce electrons with the system. An electron associated with a particular defect (oxygen vacancy here) will be confined in a hydrogenic orbital of radius  $r_h = \epsilon(m/m^*)a_0$ , where  $\epsilon$  is the high-frequency dielectric constant,  $m$  is the electron mass,  $m^*$  is the effective mass of the donor electrons and  $a_0$  is the Bohr radius (53 pm). Now the hydrogenic donor electrons tend to form bound magnetic polarons (BMP) by coupling with the  $3d$  moments of the TM ions within their orbits [70, 72]. The extent of these polarons increases as the temperature is lowered and the transition temperature occurs essentially when the polaron size is the same as that of the sample. The overlap of the individual polarons produces long-range interactions, as shown schematically in Fig 1.7, and energetically it is favorable for the spin polarization to develop. This model is inherently attractive for low carrier density systems such as many of the electronic oxides.

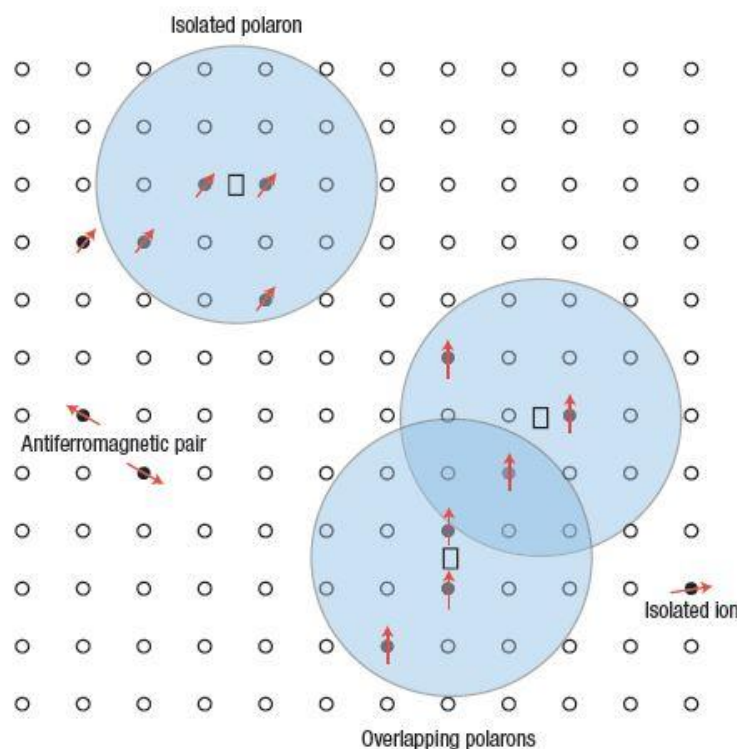


**Fig. 1.7:** Representation of magnetic polarons. A donor electron in its hydrogenic orbit couples with its spin antiparallel to impurities with a  $3d$  shell that is half-full or more than half-full. The figure is drawn for  $x = 0.1$ ,  $\gamma = 12$ . Cation sites are represented by small circles. Oxygen is not shown; the unoccupied oxygen sites are represented by squares [Ref. 70].

### 1.3.3 Double exchange mechanism

The double exchange mechanism is based on the multivalence of doped TM ions. For example, for Mn, the hopping between the  $Mn^{3+}$  and  $Mn^{4+}$  levels is operative in the manganite materials, stabilizing the ferromagnetic state. Sato and Katayama-Yoshida [40] have suggested that the n-type doping in ZnO can increase the Curie temperature of Fe-, Co- and Ni-doped samples. In most II-VI compounds they looked at, the spin-glass state was stabilized with the transition metal in the  $d^5$  configuration. The ferromagnetism arises from a competition between the double-exchange interaction and the anti-ferromagnetic super-exchange interaction in these materials. Litvinov and Dugaev [73] also suggested that virtual excitations from the magnetic impurity levels to the valence band or the ligand orbitals could produce the requisite p-d exchange needed for ferromagnetism in the absence of a large density of free carriers.

## 1.4 $d^0$ ferromagnetism in oxide semiconductors

The unusual form of ferromagnetism which do not require the presence of magnetic  $d$ -block ions such as  $Mn^{2+}$ ,  $Co^{2+}$ ,  $Gd^{3+}$  etc. or  $f$ -block ions  $Gd^{3+}$ ,  $Eu^{2+}$  etc. is called " $d^0$  ferromagnetism". The term " $d^0$ " ferromagnetism was coined to describe this general phenomenon. There are suggestions that defects such as cation or anion vacancies, grain boundaries, interfaces can play a crucial role in inducing magnetism in these oxide materials in which  $d$ - or  $f$ -shells of anions/cations are either empty or completely filled. Such kind of " $d^0$  ferromagnetism" was observed experimentally, for the first time, in case of  $HfO_2$  thin film by M. Venkatesan *et al.* [74] which opened up fresh challenge for the theory of magnetism and also the possibility of designing completely new class of spintronic oxide-based materials.

### 1.4.1 Magnetic and nonmagnetic defects in oxides

During the growth of oxide materials, many structural defects such as cation vacancy, oxygen vacancy, interstitials, antisite defects, grain boundaries, interfacial defects can stabilize within the materials. These type defects are already known to control various intrinsic or extrinsic properties such as optical, luminescence properties, electrical conductivity etc. in oxides. A. Janotti and Chris G.

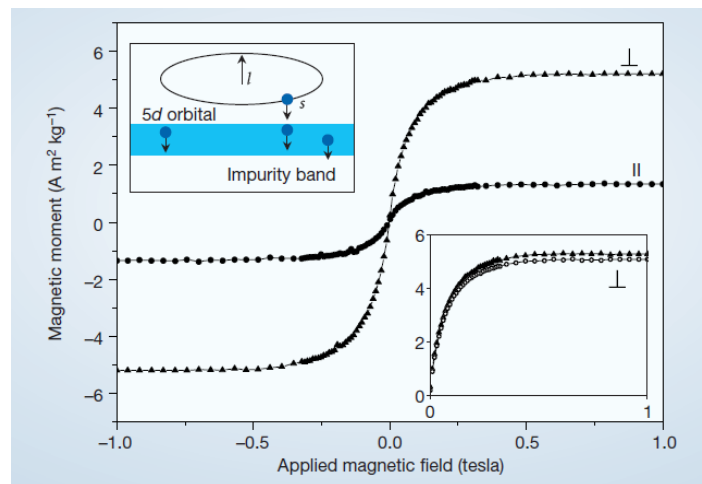


**Fig. 1.8** Magnetization curves for a HfO<sub>2</sub> thin film with the field parallel or perpendicular to the plane of an R-cut sapphire substrate. These room temperature data are corrected for background diamagnetism of the substrate. Insets: top left, proposed coupling scheme for orbital, spin and impurity-band magnetism in hafnium dioxide (blue circles represent electrons, arrows show direction of their spin moment, the orbital and spin moments  $l$  and  $s$  of an electron in a  $5d$  state couple antiparallel to form a  $j=3/2$  state); bottom right, magnetization curves at different temperatures (triangles, 5 K; circles, 400 K) [Ref. 74].

Van de Walle [74, 75] recently reported a comprehensive first-principles investigation of native point defects in ZnO based on density functional theory and estimated various defect behaviours such as defect formation energy, migration, energy levels within band gap etc.. However, investigation of local magnetic properties of these defects becomes essential after the observation of quite unexpected ferromagnetism in HfO<sub>2</sub> [76] which do not contain any magnetic ions. Among the various defects, mainly cation vacancy (e. g. Zn vacancy in ZnO [77-79], Sn vacancy in SnO<sub>2</sub> [80], Hf (Zr) vacancy in HfO<sub>2</sub> (ZrO<sub>2</sub>) [81, 82], Ca vacancy in CaO [83] etc.) can induce an almost localized magnetic moment which originates from the 2p orbital electrons of nearest oxygen atoms neighboring the vacancy site. On the other hand, oxygen vacancy within oxide materials can capture one or two electrons and can be stabilized in three different ionized state such as doubly ionized oxygen vacancy (V<sub>O</sub><sup>++</sup>), singly ionized oxygen vacancy (V<sub>O</sub><sup>+</sup>) and neutral oxygen vacancy (V<sub>O</sub><sup>0</sup>). However, theoretical investigation have shown that among these, only singly ionized oxygen vacancy (V<sub>O</sub><sup>+</sup>) i.e. F<sup>+</sup> centre have a local magnetic moment  $\sim 1\mu_B$  [84, 85] which originates due to trapping of one electron. Other point defects such as cation or oxygen interstitials, antisites are all non-magnetic. Besides the intrinsic

defects, the various substitutional defects arising due to nonmagnetic doping of C, N at oxygen site are also found to induce magnetic moment in oxides [86, 87]. In addition, G. Bouzerar and T. Ziman proposed a model [82] for vacancy-induced ferromagnetism in oxides and have shown that cationic substitution of group-IA elements such as Li, Na, K, Cs etc. in II-VI and IV-VI oxides can stabilize significant ferromagnetic ordering. Thus defect-induced ferromagnetism in oxide semiconductors can be stabilized with proper control and tuning of various magnetic defects within the materials.

## 1.4.2 Defects and material dimensionality

During the growth of a crystal, the formation of defects within the crystal depends on the dimension of the sample materials. In other words, the concentration of defects in bulk materials should be considerably low compared to the low dimensional structures such as nanostructures or thin films. For nanostructured materials particularly, one dimensional (1D) oxide nanowires or nanorods, the defect concentration can be very high due to their large surface to volume ratio. Significant amount of defects can also stabilize within the two dimensional (2D) oxide thin film structures grown by conventional deposition techniques such as sputtering, molecular beam epitaxy or pulsed laser deposition methods. Therefore, probability of defect formation is inversely proportional to the material dimensionality i.e. as one reduces the dimension of the materials, the formation of defects will be more. At equilibrium condition, the concentration ( $N_d$ ) of particular type of defects, for example cation or anion vacancy, can be given by the Boltzmann factor as,

$$N_v = N \exp(-E_v / K_B T)$$

where,  $N$  is the total number of atoms in the crystal,  $E_v$  is the vacancy formation energy,  $K_B$  is Boltzmann constant and  $T$  is the equilibrium temperature. The above equation suggests the two facts; firstly, the defects or vacancies having low formation energy should grow in more and secondly, the concentration of defects will increase with the rise of temperature of the crystal. Wang et al. [77] have estimated the formation energy of Zn vacancy ( $V_{Zn}$ ) and oxygen vacancy ( $V_O$ ) in case of ZnO thin film (2D) and nanowires (1D). They have found that formation energy of  $V_{Zn}$  ( $\sim 5.3$  eV) is quite high as compared to  $V_O$  ( $\sim 3.2$  eV) which suggests that the

formation of  $V_O$  is much easier than formation of  $V_{Zn}$  in ZnO. Besides that, they also discovered that in case of ZnO nanowires, the vacancy formation energies (both for  $V_O$  and  $V_{Zn}$ ) are low compared to the ZnO thin film which indicates it is quite easy to form significant amount of vacancies in nanowires than the thin film. In order to stabilize magnetic interaction between such vacancy-type defects ( $V_O$  and  $V_{Zn}$ ), the defect concentration in the material should be large enough so that the defects come close to one another and interact. As the nanostructure or thin films samples contain significant amount of defects, people are interested to study the existence  $d^0$  ferromagnetism mainly in such low dimensional (1D/2D) oxide semiconductors. For bulk (oxide) sample, it is quite difficult to achieve enough defect concentration (threshold concentration), required to stabilize long range ferromagnetic interaction between the magnetic defects.

### 1.4.3 Alternative way to prepare high- $T_c$ ferromagnetic oxide semiconductors

In recent times, the study defect-induced  $d^0$  ferromagnetism in wide-band oxide semiconductors has been attracted great attention as an alternative of TM-based oxide-DMS for spintronic devices. The observation of unexpected RT FM in pure  $HfO_2$  thin film [76] has opened up a new challenge to explain the origin of magnetic moment without the presence of any d or f-orbital electrons. After that the experimental evidence of RTFM were also observed in case of different oxide thin films and nanostructures such as ZnO,  $SnO_2$ ,  $TiO_2$ ,  $In_2O_3$  etc. in their purest phase or even using dopant elements which are completely nonmagnetic [85, 88, 89]. The theoretical calculations performed in case of different oxides such as  $HfO_2$  [81, 82], CaO [83],  $SnO_2$  [80] and ZnO [77-79] revealed that cation vacancies can induce magnetic moment which is found to be localized at vacancy site and the ferromagnetic ordering between these cation vacancies is energetically favorable when vacancy concentration reaches above a threshold concentration. Sundaresan *et al.* [85] have reported that FM is a universal property of oxide nanostructures where they have attributed oxygen vacancy ( $V_O$ ) defects for the origin of observed FM. However, density functional theory (DFT)-based first principle investigation have shown that neutral  $V_O$  is non-magnetic whereas Zn and Sn vacancy in ZnO and  $SnO_2$  matrix respectively can have magnetic moment originating from the unpaired 2p

orbital of O atom in the vicinity of cation vacancy site [77, 80]. Therefore, the proper realization of defects and defect-dynamics within the oxides can provide exciting opportunities to achieve the desired goal of high- $T_C$  ferromagnetic oxide semiconducting materials.

## 1.5 Motivation of our work

Since from the last decade, the search for high- $T_C$  ferromagnetic oxide-DMS has been continued even up to still now, for the development of new class of semiconducting electronics or spin-based electronics. In this regard, the controversial magnetic properties of TM-based oxide DMS is imposing a serious restriction for finding application in technology. In fact, the presence or absence of intrinsic ferromagnetism in TM-doped wide band oxides is a debatable issue which should be overcome through a series of systematic and careful study. In fact, several important factors such as sample's phase identification, dimensional and morphological effects, sample preparation conditions and defects must be incorporated. Our motivation is to investigate the origin of magnetism in TM or RE-doped wide band transparent oxide semiconductors correlating with their optical and electrical properties and also considering different sample length scale such as bulk (3D), thin film (2D) as well as nanostructures (1D) prepared under various experimental conditions.

The study of defect-induced  $d^0$  ferromagnetism in pure and non-magnetic doped oxides can serve as alternative of TM-based oxide DMSs. The realization of such completely new class of ferromagnetic oxides can be possible though proper understanding the role of defects and their modification depending on experimental condition and dopant used. Although some experimental evidence about RTFM was observed and it has been suggested that structural defects are responsible for ferromagnetism, but which type of defects that is not properly known. Some people have reported oxygen vacancy related magnetic origin while another group suggesting cation vacancy as origin of RTFM in oxides nanostructures or thin films. The reproducibility also becomes a serious issue as the accurate control of defects is quite difficult even if the samples are prepared under similar experimental condition. Therefore, one has to think some external parameters, may be non-magnetic doping, oxygen pressure, carrier concentration etc. to stabilize and also tune certain kind of defect, so that the observed ferromagnetic behavior can be

reproduce to a high degree. Therefore, the motivation behind this work as follows; (i) to investigate what kinds of defects are responsible for RTFM in oxides, (ii) to find the ways how to control the defects within oxides, (iii) how to stabilize, enhance and also tune the ferromagnetic signature in such oxides, (iv) to understand the defect formation and defect modification responsible for RTFM in oxides using positron annihilation spectroscopy (PAS).

## 1.6 Thesis organization

The thesis begins with a brief introduction (present chapter) describing the significance of the present work, introduction to spin-based electronics, dilute magnetic semiconductor as spintronic materials, necessary literatures on earlier work done, defect-induced  $d^0$  ferromagnetism and possibility of having new class of high- $T_C$  ferromagnetic oxide semiconductors.

In **Chapter 2** we have discussed about various techniques for sample preparation, characterization and measurements.

**Chapter 3** focuses on synthesis and study of  $3d$ -transition metal-doped ZnO, SnO<sub>2</sub> and TiO<sub>2</sub>. It discusses the detailed description of magnetic behavior of Bulk oxide-DMS in single phase form. In addition, a comparison between the bulk and nano-phase magnetic properties of Co-doped SnO<sub>2</sub> is highlighted.

In **Chapter 4**, the role of  $4f$ -rare earth ions (magnetic ions) in inducing magnetism in gadolinium (Gd)-doped SnO<sub>2</sub> thin films deposited by RF-Magnetron sputtering are discussed. Besides that, the origin of room-temperature ferromagnetism (RTFM) in pure SnO<sub>2</sub> thin films is investigated and in this regards, photoluminescence and electrical properties are presented.

**Chapter 5** explores the evidence of defect-induced high- $T_C$   $d^0$  ferromagnetism in one dimensional (1D) ZnO and SnO<sub>2</sub> nanowires fabricated within the nanopores of AAO template by wet-chemical route. Here, we have identified which type of defects are responsible to stabilize RTFM in such oxides and presented methods to stabilize,

enhance and tune such ferromagnetic signature in ZnO nanowires using various nonmagnetic dopants such as K, Li, N etc.

In **Chapter 6**, we have discussed the defect-driven magnetic, luminescence and electrical properties of group-1A alkali-Metal (Li, Na, K)-doped ZnO thin films prepared by pulsed laser deposition (PLD) techniques. The effects of film-thickness and oxygen pressure (during deposition) on ferromagnetic behavior are also presented.

**Chapter 7** discusses about positron annihilation spectroscopy (PAS) studies on evolution of vacancy-type defects and RT ferromagnetism in chemically synthesized Li-doped ZnO nanoparticles.

In **Chapter 8**, we have presented the conclusions and the scope for future works

## References

- [1] Gary A. Prinz, et al. *Science* **282**, 1660 (1998)
- [2] R. J. Soulen Jr. et al., *Science* **282**, 85 (1998).
- [3] M. Baibich et al., *Phys. Rev. Lett.* **61**, 2472 (1988).
- [4] S. Hershfield, H. L. Zhao, *Phys. Rev. B* **56**, 3296 (1997).
- [5] R. A. de Grot et al., *Phys. Rev. Lett.* **50**, 2024 (1983).
- [6] K. P. Kamper et al., *Phys. Rev. Lett.* **59**, 2788 (1988).
- [7] M. Johnson, *Phys. Rev B* **58**, 9635 (1998).
- [8] P. R. Hammar, B. R. Bennett, M. J. Yang, M. Johnson, *Phys. Rev. Lett.* **83**, 203 (1999).
- [9] P. R. Hammar, M. Johnson, *Phys. Rev. B* **61**, 7207 (2000).
- [10] M. Johnson, *Physica E* **10**, 472 (2001).
- [11] J. K. Furdyna, *J. Appl. Phys.* **64**, R29 (1988).
- [12] D. Ferrand et al., *Phys. Rev. B* **63**, 085201 (2001).
- [13] W. Mac, Nguyen The Khoi, A. Twardowski et al., *Phys. Rev. Lett.* **71**, 2327 (1993).
- [14] W. Mac, Nguyen The Khoi et al., in *Proc Intl. Conf.on Phys. Semicond. (Vancouver 1994)*; ed. D. J. Lockwood, 2573 (World Scientific, 1995).
- [15] Lijuan Zhao, Bei Zhang, and Qi Pang et al., *Appl. Phys. Lett.* **89**, 092111 (2006).
- [16] H. Ohno, *Science* **281**, 951 (1998).
- [17] T. Dietl, H. Ohno, F. Matsukura, J. Cibert, and D. Ferrand, *Science* **287**, 1019 (2000).

- [18] H. Ohno, J. Magn. Mater. **200** 110 (1999).
- [19] H. Ohno, J. Vac. Sci. Technol. B **18** 2039 (2000).
- [20] T. Story, in Proc. Intl. Workshop on Doped Magnetic Semiconductors (Linz 1994),
- [21] T. Story, P. J. T. Eggenkamp, C. H. W. Swuste et al., Phys. Rev. B **45**, 1660 (1992);
- [22] T. Story, P. J. T. Eggenkamp, C. H. W. Swuste, et al., Phys. Rev. B **47**, 227 (1993).
- [23] W. J. M. de Jonge, T. Story, H. J. M. Swagten, et al., Europhys. Lett. **17**, 631 (1992).
- [24] Hwa-Mok Kim et al., Chem. Mater. **15**, 3964 (2003).
- [25] F. M. Zhang et al., Appl. Phys. Lett. **85**, 786-788 (2004).
- [26] M. Bolduc et al., Phys. Rev. B **71**, 033302 (2005).
- [27] S. Cho, S. Choi, S. C. Hong et al., Phys. Rev. B **66**, 033303 (2002).
- [28] A. P. Li, J. Shen, J. R. Thompson et al., Appl. Phys. Lett. **86**, 152507 (2005).
- [29] K. Sato and H. Katayama-Yoshida Japan. J. Appl. Phys. **39** L555 (2000)
- [30] Y. Matsumoto, M. Murakami, T. Shono et al., Science **291** 854 (2001).
- [31] T. Mizokawa, T. Nambu, A. Fujimori, et al., Phys. Rev. B **65**, 085209 (2002).
- [32] R. N. Gurzhi, A. N. Kalinenko, A. I. Kopeliovich, et al., Appl. Phys. Lett. **83** 4577 (2003).
- [33] J. Rudolph, D. Hagele, H. M. Gibbs et al., Appl. Phys. Lett. **82** 4516 (2003).
- [34] M. Bouloudenine, N. Viart, S. Colis et al., Appl. Phys. Lett. **87**, 052501 (2005).
- [35] Wyckoff R W G 1986 *Crystal Structures* 2nd edn (New York: Wiley)
- [36] Joseph M, Tabata H and Kawai T *Japan. J. Appl. Phys.* **38** L1205 (1999).
- [37] J. Kang, S. Tsunekawa, and A. Kasuya, Appl. Surf. Sci. **174**, 306 (2001).
- [38] A.A. Bolzan, C. Fong et al., Acta Crystallogr. Sect. B—Struct. Sci. **53** 373 (1997).
- [39] H. Tang, H. Berger, P. E. Schmid and F. Levy, *Solid State Commun.* **92** 267 (1994).
- [40] Sato K and Katayama-Yoshida H *Japan. J. Appl. Phys.* **39** L555 (2000).
- [41] Wakano T, Fujimura N, Morinaga Y et al., *Physica E* **10** 260 (2001).
- [42] Ueda K, Tabata H and Kawai T *Appl. Phys. Lett.* **79** 988 (2001).
- [43] Saeki H, Tabata H and Kawai T 2001 *Solid State Commun.* **120** 439 (2001).
- [44] Fukumura T, Jin Z, Ohtomo A and Koinuma H *Appl. Phys. Lett.* **75** 3366 (1999)
- [45] Cheng X M and Chien C L *J. Appl. Phys.* **93** 7876 (2003).
- [46] Kim D S, Kim H M, Yuldashev S U, Lee S J et al., *J. Korean Phys. Soc.* **42** S333 (2003).
- [47] Tiwari A, Jin C, Kvit A, Kumar D et al., *Solid State Commun.* **121** 371 (2002).
- [48] Jung S W, An S J, Yi G C, Jung C U et al., *Appl. Phys. Lett.* **80** 4561 (2002)
- [49] Jin Z et al., *Appl. Phys. Lett.* **78** 3824 (2001)
- [50] Han S J, Song J W, Yang C H, Park S H, et al., *Appl. Phys. Lett.* **81** 4212 (2002).
- [51] Prellier W, Fouchet A, Mercey B et al., *Appl. Phys. Lett.* **82** 3490 (2003).
- [52] Rode K, Anane A, Mattana R, Contour J P et al., *J. Appl. Phys.* **93**, 7676 (2003)
- [53] Kim J H, Kim H, Kim D, Ihm Y E and Choo W K 2003 *Physica B* **327** 304
- [54] Kim J H, Choo W K, Kim H, Kim D and Ihm Y E 2003 *J. Korean Phys. Soc.* **42** S258
- [55] Yoo Y-Z, Fukumura T, Jin Z, Hasegawa K, et al., *J. Appl. Phys.* **90** 4246 (2001).

- [56] Lim S W, Hwang S K and Myoung J M 2003 *Solid State Commun.* **125** 231
- [57] Kim J H, Kim H, Kim D, Ihm Y E and Choo W K 2002 *J. Appl. Phys.* **92** 6066
- [58] Lee H J, Jeong S Y, Cho C R and Park C H 2002 *Appl. Phys. Lett.* **81** 4020
- [59] R. Seshadri, *Curr. Opin. Solid State Mater. Sci.* **9**, 1 (2005).
- [60] A. S. Risbud, N. A. Spaldin, Z. Q. Chen et al., *Phys. Rev. B* **68**, 205202 (2003).
- [61] S. W. Yoon, S.-B. Cho, S. C. We et al., *J. Appl. Phys.* **93**, 7879 (2003).
- [62] J. H. Kim, H. Kim, D. Kim, S. G. Yoon et al., *Solid State Commun.* **131**, 677 (2004).
- [63] P. Sati, R. Hayn, R. Kuzian, S. Régnier et al., *Phys. Rev. Lett.* **96**, 017203 (2006).
- [64] C. Liu, F. Yun, and H. Morkoç, *J. Mater. Sci.: Mater. Electron.* **16**, 555 (2005).
- [65] A. Barla, G. Schmerber, E. Beaupaire, et al., *Phys. Rev. B* **76**, 125201 (2007).
- [66] M. Gacic, G. Jakob, C. Herbort, H. Adrian et al., *Phys. Rev. B* **75**, 205206 (2007).
- [67] T. C. Kaspar, S. M. Heald, C. M. Wang, et al., *Phys. Rev. Lett.* **95**, 217203 (2005).
- [68] B. B. Straumal, A. A. Mazilkin, S. G. Protasova et al., *Phys. Rev. B* **79**, 205206 (2009).
- [69] S. H. Liu, H. S. Hsu, C. R. Lin et al., *Appl. Phys. Lett.* **90**, 222505 (2007).
- [70] J. M. D. Coey, M. Venkatesan and C. B. Fitzgerald, *Nature materials* **4**, 173 (2005)
- [71] Dietl T, Matsukura F and Ohno H 2002 *Phys. Rev. B* **66** 033203
- [72] Dietl, T. & Spalek, J. *J. Phys. Rev. B* **28**, 1548–1563 (1983)
- [73] V. I. Litvinov and V. K. Dugaev *Phys. Rev. Lett.* **86** 5593 (2001).
- [74] A. Janotti and C. G. Van de Walle, *Phys. Rev. B* **76**, 165202 (2007).
- [75] A. Janotti and C. G. Van de Walle, *Rep. Prog. Phys.* **72**, 126501 (2009).
- [76] M. Venkatesan, C. B. Fitzgerald, and J. M. D. Coey, *Nature (London)* **430**, 630 (2004).
- [77] Q. Wang, Q. Sun, G. Chen, Y. Kawazoe, and P. Jena, *Phys Rev. B* **77**, 205411 (2008).
- [78] J. A. Chan, Stephan Lany, and Alex Zunger, *Phys. Rev. Lett.* **103**, 016404 (2009)
- [79] H. Peng, H. J. Xiang, S.-H. Wei, S.-S. Li et al., *Phys. Rev. Lett.* **102**, 017201 (2009).
- [80] G. Rahman, V. M. Garcia-Suarez, and S. C. Hong, *Phys. Rev. B* **78**, 184404 (2008).
- [81] C. D. Pemmaraju and S. Sanvito, *Phys. Rev. Lett.* **94**, 217205 (2005).
- [82] G. Bouzerar and T. Ziman, *Phys. Rev. Lett.* **96**, 207602 (2006).
- [83] I. S. Elfimov, S. Yunoki, and G. A. Sawatzky, *Phys. Rev. Lett.* **89**, 216403 (2002).
- [84] J.M.D. Coey, M. Venkatesan, C.B. Fitzgerald, *Nature Mater.* **4** (2005) 173.
- [85] A. Sundaresan, R. Bhargavi, N. Rangarajan et al., *Phys. Rev. B* **74**, 161306(R) (2006).
- [86] B. Gu, N. Bulut, T. Ziman and S. Maekawa, *Phys. Rev. B* **79**, 024407 (2009).
- [87] C. F. Yu, T. J. Lin, S. J. Sun and H. Chou, *J. Phys. D: Appl. Phys.* **40** 6497 (2007).
- [88] (7) Hong, N. H.; Sakai, J.; Poirot, N.; Brizé, V. *Phys. Rev. B* **2006**, **73**, 132404.
- [89] (11) Gao, F; Hua, J; Wang, J; Yang, C.; Qin, H. *Chemical Physics Letters* **2010**, **57** 488.

# Chapter 2

## Experimental Techniques for Sample Preparation and Characterization

### 2.1 Preface

In this chapter, we will describe various techniques for sample preparation and their characterization. Bulk samples such as  $Zn_{1-x}Co_xO$ ,  $Sn_{1-x}Co_xO_2$  and  $Sn_{1-x}Fe_xO_2$  are prepared by solid state reaction using Fritsch make (Germany) Pulverisette-7 ball mill machine. Nanorods of pure  $SnO_2$  and  $Sn_{1-x}Co_xO_2$  are prepared by solvothermal techniques. Template assisted wet-chemical route is used to fabricate the nanowires of pure  $SnO_2$  and non-magnetic doped ZnO. Thin films of Gd-doped  $SnO_2$  and alkali-metal doped ZnO thin films are prepared using radio-frequency (RF) magnetron sputtering and pulsed laser deposition (PLD) unit. The pristine and doped oxide samples are characterized by scanning electron microscopy (SEM), field emission scanning electron microscopy (FESEM), transmission electron microscopy (TEM), x-ray diffraction (XRD). Chemical composition of the materials are analysed by energy dispersive electron diffraction (EDX) and x-ray photoelectron spectroscopy (XPS). Optical properties are measured by ultraviolet-visible (UV)

absorption spectroscopy and photoluminescence (PL) spectroscopy. Magnetic properties are measured using vibrating sample magnetometer (VSM) and superconducting quantum interference devices (SQUID) and magnetic force microscope (MFM) attached with atomic force microscopy (AFM) unit. Resistivity of the thin films is measured by four probe method and carrier concentration is estimated from hall measurement.

## 2.2 Synthesis techniques

### 2.2.1 Mechano-synthesis techniques

Mechano-synthesis (MS) or mechanical milling (also called ball milling) is a power metallurgical process [1]. It has gained a lot of attention as a non-equilibrium process resulting in a solid state alloying beyond the equilibrium solubility limit and the formation of amorphous and nanostructured materials for a broad range of alloys, inter-metallics, ceramics and composites. Mechano-synthesis is basically performed on the principle of solid state reaction method [2] in which all the reactant materials are in solid phase in the form of powder, granules. The reactants are grinded with continuous mechanical thrusting which leads to reduction of particle size to a fraction of micrometer or nanosize regime so that small particles can react with one another at the atomic or molecular level. The grinding of starting materials can be performed within the hard metal tungsten carbide bowls of Fritsch planetary micro mill "PULVERISETTE 7" using tungsten carbide balls. The typical weight ratio of sample and balls depends on the type of materials to be grinded. However, for milling of oxide materials such as ZnO, CoO, SnO<sub>2</sub>, TiO<sub>2</sub> etc. the ratio is usually taken as 1:10. Mechano-synthesis is known to create inhomogeneous, non-equilibrium phase during alloying. However, high-temperature annealing (500°C - 800°C depending on the materials) after milling process can reduce or even exclude such unwanted phases.

#### 2.2.1.1 The Planetary Micro Mill "PULVERISETTE 7 premium line:

Fritsch PULVERISETTE 7 premium line is universally applicable for quick dry or wet grinding of inorganic and organic samples for analysis, quality control and materials testing. In synthesis, the Planetary Micro Mill can be used for mixing

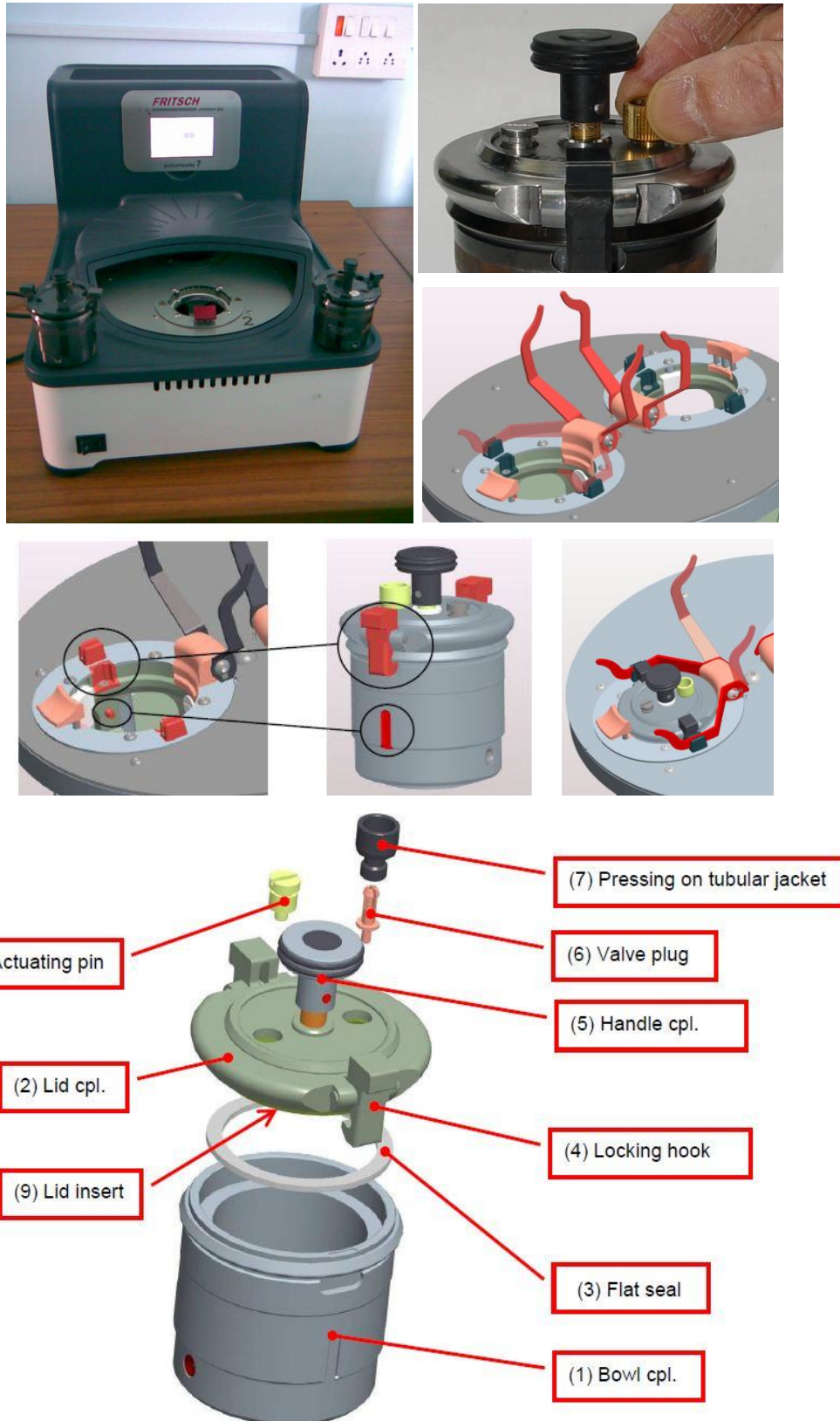


**Fig. 2.1:** Picture of Fritsch Planetary Micro Mill "PULVERISETTE 7 premium line with various internal sections.

and homogenization of dry samples, emulsions and pastes. It contains two bowls and balls with various diameter made with hardmetal tungsten carbide. The machine is driven by a maintenance-free electric motor that is operated with a frequency converter. Fig. 2.1 shows the picture of the PULVERISETTE 7 ball mill unit.

The grinding material is pounded and ground by grinding balls in a grinding bowl. Centrifugal forces from the rotation of the grinding bowl around its own axis and the rotating supporting disc act on the grinding bowl filling consisting of the grinding material and grinding balls (Fig. 2.2). The grinding bowl and supporting disc rotate in opposite directions so that the centrifugal forces alternately act in the same and opposite directions. This results in the grinding balls running along the inner wall of the grinding bowl as a frictional effect and the balls impacting against the opposite wall of the grinding bowl as an impact effect.

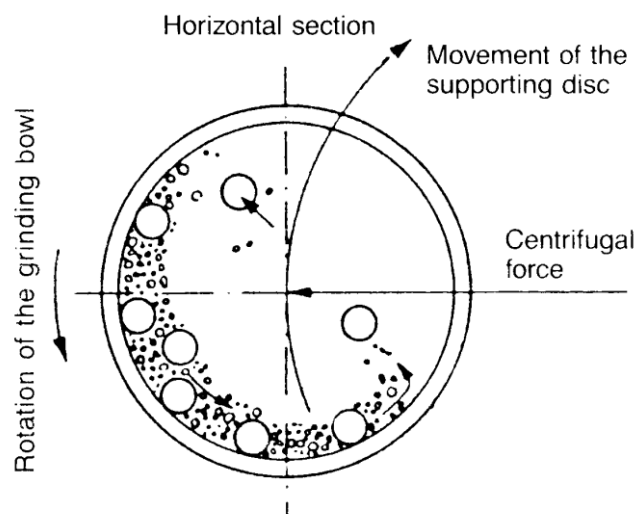


**Fig. 2.2:** Schematic diagram of milling of materials within the bowls

Here, we have synthesized Co-doped ZnO and SnO<sub>2</sub> powder samples by mechano-synthesis technique using PULVERISETTE 7 premium line. Mixture of high purity ZnO or SnO<sub>2</sub> and CoO powders are used as starting materials which was grinded within the bowls at different milling time (maximum up to 12 hours) [3]. In Fig. 2.3 we show the estimated crystallite size of the Co-doped ZnO after different

milling time and it was found that the crystallite size decreases gradually with increase of milling time [3].

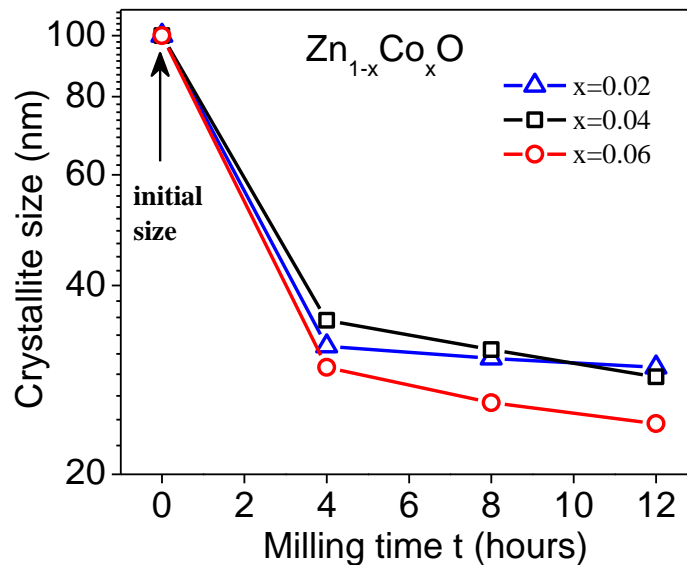


Fig. 2.3: Change in crystallite size of Co-doped ZnO with milling time

## 2.2.2 Solvothermal Synthesis

Solvothermal synthesis (SS) is a variety of hydrothermal process for synthesis of nanomaterials [4]. It is basically a chemical synthesis performed under controlled temperature and vapor pressure. The reactants in solution phase (water or alcoholic solution) are putted in a stainless steel autoclave inside which the crystal growth takes place. The autoclave is generally heated inside a furnace and a gradient of temperature is maintained at the opposite ends of the growth chamber so that the hotter end dissolves the nutrient and the cooler end causes seeds to take additional growth [4].

### 2.2.2.1 Stainless steel autoclave

Stainless steel autoclave is the main equipment for the crystallization process. It is usually thick-walled steel cylinder with a hermetic seal which must withstand high temperatures and pressures for prolonged periods of time. Furthermore, the autoclave material must be inert with respect to the solvent. The closure is the most important element of the autoclave. In most cases steel-corroding solutions are used

in hydrothermal experiments. To prevent corrosion of the internal cavity of the autoclave, protective inserts are generally used. These may have the same shape of the autoclave and fit in the internal cavity (contact-type insert) or be a "floating" type insert which occupies only part of the autoclave interior. Inserts may be made of carbon-free iron, copper, silver, gold, platinum, titanium, glass or quartz, Teflon, depending on the temperature and solution used.

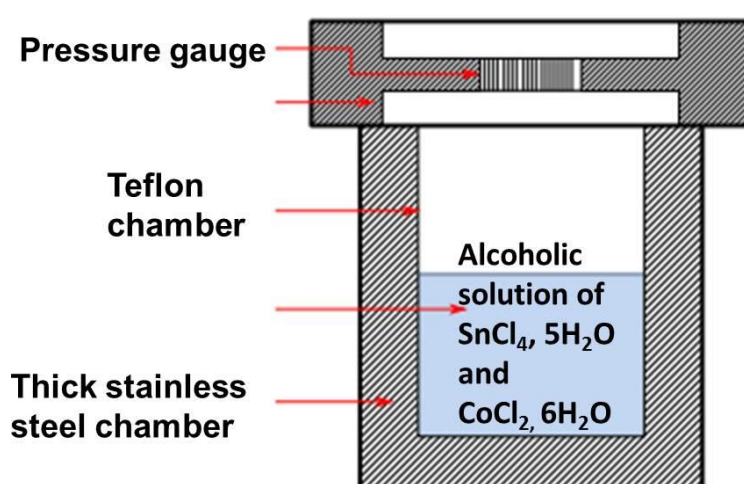


Fig. 2.4: Schematic representation of stainless steel autoclave for solvothermal synthesis

## 2.2.2.2 Crystal growth mechanism

### Temperature-difference method

This method is very frequently used in solvothermal synthesis and crystal growing. The super-saturation is achieved by reducing the temperature in the crystal growth zone. The nutrient is placed in the lower part of the autoclave filled with a specific amount of solvent. The autoclave is heated in order to create two temperature zones. The nutrient dissolves in the hotter zone and the saturated aqueous solution in the lower part is transported to the upper part by convective motion of the solution. The cooler and denser solution in the upper part of the autoclave descends while the counterflow of solution ascends. The solution becomes supersaturated in the upper part as the result of the reduction in temperature and crystallization takes place [4].

Using solvothermal methods, we have synthesized pure and Co-doped  $\text{SnO}_2$  nanorods [5]. A precursor solution of Stannic chloride ( $\text{SnCl}_4 \cdot 5\text{H}_2\text{O}$ ), Cobalt chloride ( $\text{CoCl}_2$ ) and Sodium hydroxide ( $\text{NaOH}$ ) in ethyl alcohol was transferred into a Teflon lined stainless steel Autoclave and kept in a Furness at temperature  $200^\circ\text{C}$  for 10 hrs. A reddish-brown precipitate is washed repeatedly by water and ethanol, and then dried in air at  $80^\circ\text{C}$  for 24 hours to obtain the required rod-shaped samples, as shown in Fig. 2.5 [5].

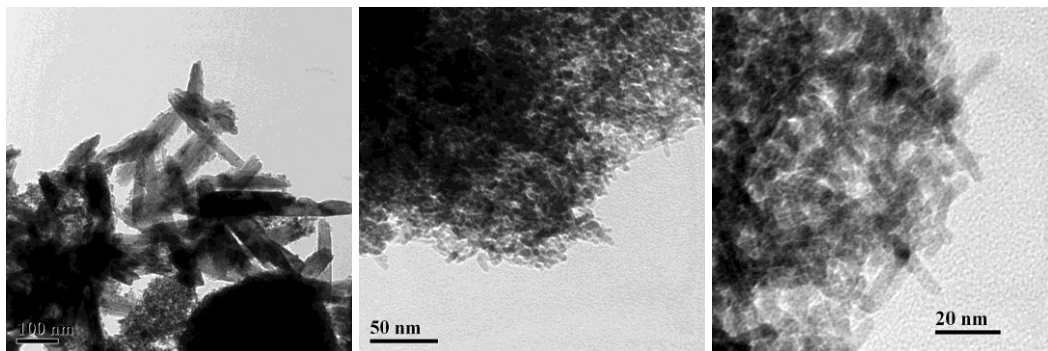


**Fig. 2.5:** TEM image of (a) pure  $\text{SnO}_2$  and (b) & (c) C-doped  $\text{SnO}_2$  nanorods prepared by solvothermal synthesis [5].

### 2.2.3 Chemical Co-precipitation technique

In industry and research laboratory, the chemical co-precipitation method is widely used to synthesize micro and nano-particle of various oxide composites [6]. Using this method high quality ceramic powder of higher compositional homogeneity, better stoichiometry, fine particle size and unagglomerated particles required for practical applications can be synthesized. At the first stage of chemical co-precipitation starting salts are dissolved in aqueous medium. The solution is then mixed with a solution of dissolved precipitating agent such as ammonium hydroxide or sodium hydroxide or oxalic acid. The final crystalline oxide is obtained by firing the precipitates at a higher temperature. Precipitation temperature can be in the range of  $0^\circ\text{C}$  to  $80^\circ\text{C}$ . A significant role is played by colloidal chemistry in the precipitation of powder from solution. The main controlling factor in this method that causes individual particles to bond to form larger agglomerates is interparticle force [7]. The agglomeration rate is largely dependent on the rate of particle collisions per unit time caused by Brownian motion, thermal convection and shear

forces (caused by stirring). In our laboratory, we have synthesized pure and transition metal Fe-doped  $\text{SnO}_2$  crystals using chemical co-precipitation techniques [8].

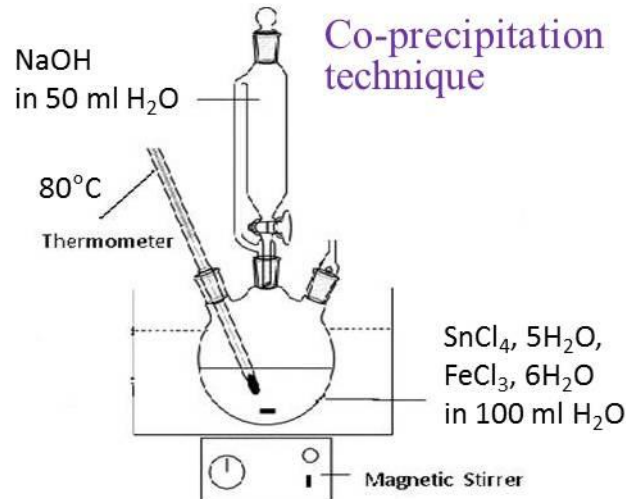


Fig. 2.6: Chemical co-precipitation technique for synthesis of Fe-doped  $\text{SnO}_2$  [8]

## 2.2.4 Template-assisted wet chemical synthesis of 1D NWs

Template-assisted methods are known to be very exciting techniques to synthesize metal and semiconductor nanowires (NWs). There are several physics and chemical methods in which template are used to grow nanowires. Among them, electrodeposition method is best known to grow well-vertical metal, metal oxides or semiconductor NWs within the porous templates such as polycarbonate membranes, anodic aluminum oxide (AAO). However, here we have used wet chemical template assisted route to synthesize  $\text{ZnO}$  and  $\text{SnO}_2$  NWs using porous AAO as template. Before the fabrication of oxide nanowires, first we have prepared nanoporous AAO template by the controlled two-step anodization of high purity (99.99%) aluminum foils [9] in our laboratory.

### 2.2.4.1 Preparation of AAO template

AAO Templates have been fabricated by the controlled two-step anodization of high purity (99.99%) aluminium foils [9, 10]. The aluminium foils, which were annealed at  $400^\circ\text{C}$  for 4 h for the necessary grain enlargement, were electropolished

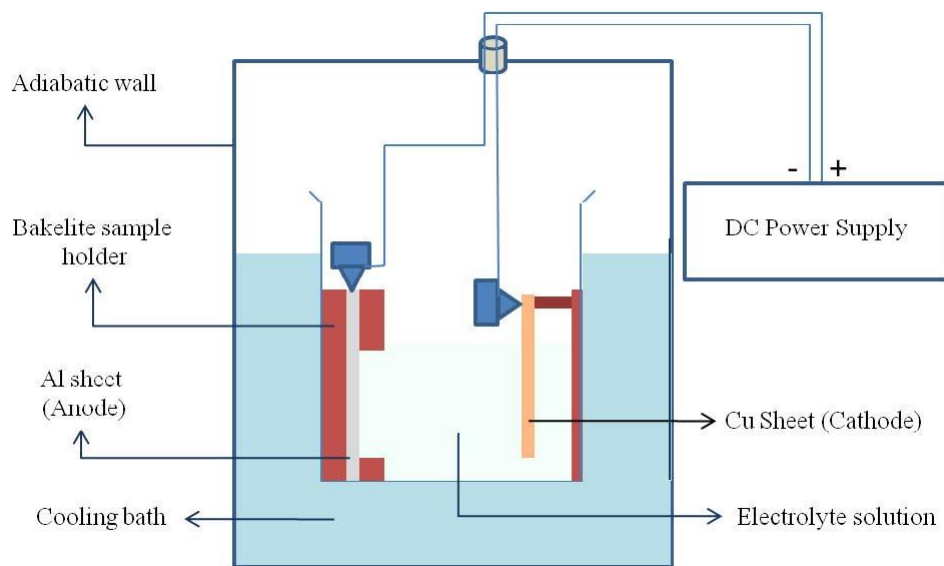


**Fig. 2.7:** Schematic of electrochemical anodization bath set-up.

at 40 V for 20 s using the universal acidic electrolyte solution. The electropolished samples were degreased in acetone and kept in an ultrasonic vibration bath for cleaning. The two-step electrochemical anodization of the electropolished aluminium foils were carried out separately in 3 wt% oxalic, sulfuric and phosphoric acid electrolyte solutions, where the aluminium foil was used as the anode and a copper plate was used as the cathode in the electrochemical oxidation bath. The whole anodization process has been carried out inside a cooling system maintained at 10°C. The anodization bath set-up is shown in Fig. 2.7.

AAO templates were prepared in oxalic acid solution by using the D.C. bias in between 45-50 V maintaining a current density of 200 A/m<sup>2</sup>. For the templates synthesized in phosphoric and sulfuric acid the anodization voltages were kept in between 40-45 and 25-30 V, respectively to maintain a constant current density of 200 A/m<sup>2</sup>. The first-step anodization was carried out for 30 min at 10°C for all the cases. The alumina layer grown on the aluminium foil surface after the first-stage of anodization was removed by chemical etching using a mixture of 60 wt% phosphoric, 28 wt% H<sub>2</sub>SO<sub>4</sub> and 12 wt % HNO<sub>3</sub> acid solution and the foils were re-anodized for the second time keeping all the anodization parameters same as that in the first-stage to obtain more uniform porous structure.

The AAO template grown on the aluminium foil substrate has been extracted by a simple electrical method. In this method, after the growth of the AAO template by electrochemical anodization using the aluminium foil as the anode, a reverse bias was introduced between the electrodes for 5 min, where the AAO template on the aluminium substrate was used the cathode and the copper plate as anode. This reverse bias makes the AAO template/aluminium metal contact weak and in the later stage the AAO template was separated carefully from the aluminium foil substrate.

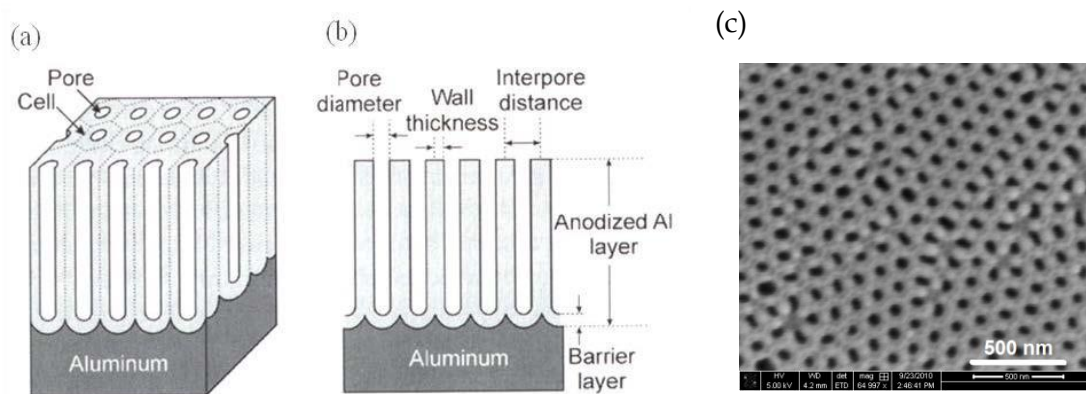


**Fig. 2.8:** (a) Schematic diagram of idealized structure of porous alumina template obtained from anodization of thin aluminum sheet and (b) a cross sectional view of the anodized layer (The figure is taken from Ref. 11). (c) FESEM image of porous AAO template obtained after two step atomization (top view).

#### 2.2.4.2 Fabrication of oxide NWs within AAO template

After fabricating the AAO template, arrays of ZnO NWs were grown by dipping the template into a saturated 0.1 M solution of zinc acetate [ $\text{Zn}(\text{CH}_3\text{COOH})_2 \cdot 2\text{H}_2\text{O}$ ] prepared in ethanol followed by drying and annealing of the template. The doping of K, Li, N, F in ZnO NWs are performed by adding potassium acetate ( $\text{CH}_3\text{COOK}$ ), lithium acetate ( $\text{CH}_3\text{COOLi}$ ), ammonium acetate ( $\text{CH}_3\text{COONH}_4$ ) and ammonium fluoride ( $\text{NH}_4\text{F}$ ) salt in the precursor solution of  $\text{Zn}(\text{CH}_3\text{COOH})_2 \cdot 2\text{H}_2\text{O}$  solution in appropriate ratios [12, 13]. Then AAO templates were immersed in these mixed solution and left for five days so that the solution can reach inside the nanopores. Surface of the templates were washed very carefully in order to remove the mixed acetate solution from surface. All the templates dipped in the zinc acetate and the mixed acetate solution were dried in room temperature and

annealed in air at 450°C for 2 h. During annealing the arrays of ZnO NWs and doped ZnO NWs were grown within the pores of AAO through the decomposition of the acetate salts. Similarly, pristine SnO<sub>2</sub> nanowires are grown by using a solution of 1.2 M urea in a saturated 0.2 M solution of SnCl<sub>4</sub>·5H<sub>2</sub>O in ethanol [14].

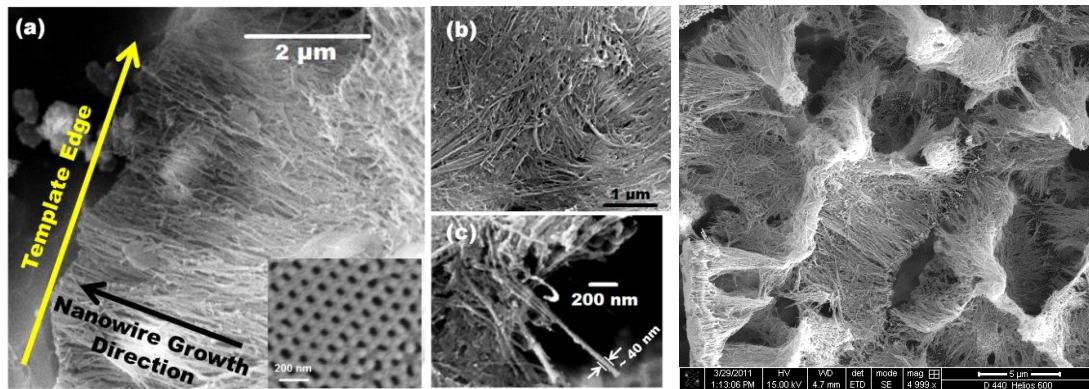


**Fig. 2.9:** FESEM images of 10% Li-doped ZnO NWs with (a) partially released (b) fully released from the AAO template, and (c) show an isolated single nanowire showing average diameter  $\sim 40$  nm. Inset of (a) show the FESEM image of AAO template with average pore diameter  $\sim 50$  nm [13]. (d) FESEM image of pure SnO<sub>2</sub> nanowires [14].

## 2.2.5 Thin film deposition techniques

There are several chemical and physical methods for deposition of two dimensional (2D) thin films of oxide semiconductors. These are chemical vapor deposition, sputtering, thermal evaporation, pulsed laser deposition, sol-gel methods, spin coating techniques etc. However, here we have used radio-frequency (RF) magnetron sputtering and pulsed laser deposition (PLD) to fabricate pure and doped SnO<sub>2</sub> and ZnO thin films. Therefore, here we have discussed the above two methods for thin film deposition.

### 2.2.5.1 Sputtering process

Sputtering and sputter deposition are widely used techniques for the erosion of surfaces and the deposition of films. Sputter deposition is a physical vapor deposition process for depositing thin films of metals or oxides. Sputtering means ejecting material from a target and depositing it on a substrate. The target is the bulk source material with specific chemical composition which will be deposited on the

substation. Substrates are placed in a vacuum chamber and are pumped down to a prescribed process pressure. Prior to the sputtering coating process, a vacuum of  $\sim 10^{-5}$  mbar was achieved. Once the appropriate pressure has been reached, a controlled flow of an inert gas such as argon is introduced. Sputtering starts when a potential difference is applied between the target and substrate holder causing a plasma or glow discharge. The negative terminal is connected to the target material. Positively charged gas ions generated in the plasma region are attracted to the negatively biased target plate at a very high speed. This collision creates a momentum transfer and can eject atomic size particles from the target.

If the energy transferred to a lattice site is greater than the binding energy, primary recoil atoms can be created which can collide with other atoms and distribute their energy via collision cascades. A surface atom becomes sputtered if the energy transferred to it normal to the surface is larger than about three times the surface binding energy (approximately equal to the heat of sublimation). These particles are deposited as a thin film on the surface of the substrates. A Schematic diagram of the mechanism of sputtering process is shown in Fig. 2.10.

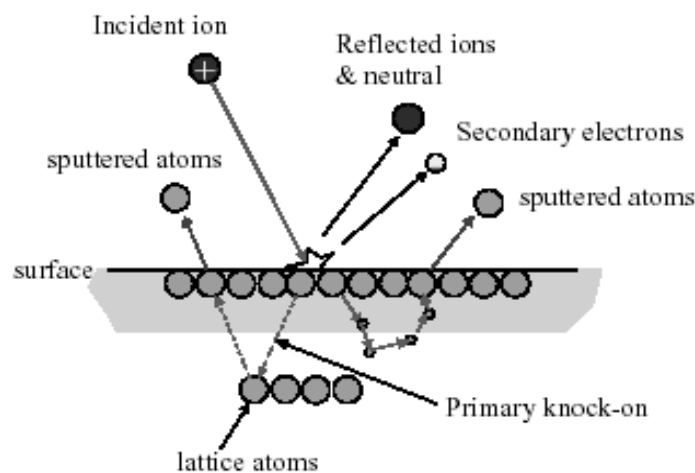


**Fig. 2.10.** Schematic diagram of the mechanism of sputtering process

For efficient momentum transfer, the atomic weight of the sputtering gas should be close to the atomic weight of the target. Hence, for sputtering of light elements, neon is preferable while for heavy elements krypton or xenon is used. Reactive gases can also be used to sputter compounds. The compound can be

formed on the target surface, in-flight or on the substrate, depending on the process parameters.

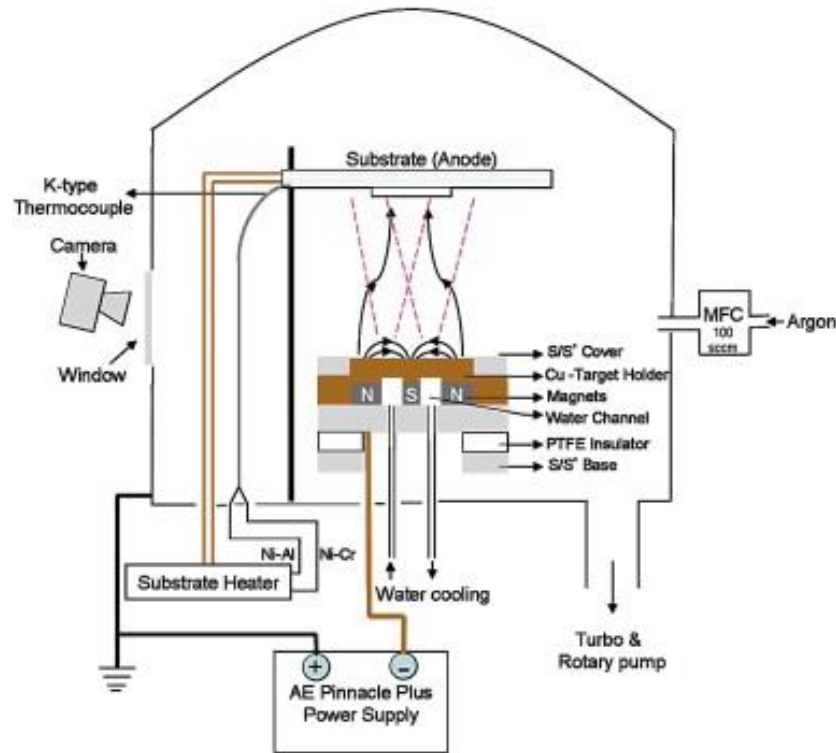


**Fig.2.11:** A Schematic diagram for RF magnetron sputtering unit.

Magnetron sputtering can be done either in DC or RF (radio frequency) modes. DC sputtering is done with conducting materials. If the target is a non conducting material, the positive charge will build up on the material and it will stop sputtering. In such a situation, RF sputtering is employed [15]. In magnetron sputtering which has almost no restrictions on target materials, magnets are used to increase the length of the electron path, thereby increase the probability of electrons striking the Argon atoms, and hence increase the ionization efficiency significantly. A schematic diagram for RF magnetron sputtering deposition technique is shown in Fig. 2.11. We have deposited pure and Gd-doped  $\text{SnO}_2$  thin films on on Si (100) substrate using RF magnetron sputtering [16]. For the preparation of the target, high purity  $\text{SnO}_2$  (99.99%) and  $\text{Gd}_2\text{O}_3$  (99.99%) with appropriate ratio are mechanically milled using Fritsch Pulverisette-7 mill. The mixture is sintered at  $800^\circ\text{C}$  for 12 hrs and a pallet of one inch diameter is prepared out of it. The pallet is sintered again at high temperature ( $1000^\circ\text{C}$ ) for 4 hrs. Afterwards, it is used as target material for the deposition of  $\text{SnO}_2$  and  $\text{Sn}_{1-x}\text{Gd}_x\text{O}_2$  ( $x = 0.02$  and  $0.05$ ) thin films [16].

### 2.2.5.2 Pulsed laser deposition (PLD)

The technique of PLD has been used to deposit high quality films of materials for more than a decade [17]. The technique uses high power laser pulses (typically  $\sim 10^8 \text{ Wcm}^{-2}$ ) to melt, evaporate and ionize material from the surface of a target. This "ablation" event produces a transient, highly luminous plasma plume that expands rapidly away from the target surface. The ablated material is collected on an appropriately placed substrate upon which it condenses and the thin film grows. Applications of the technique range from the production of superconducting and insulating circuit components to improved wear and biocompatibility for medical applications.

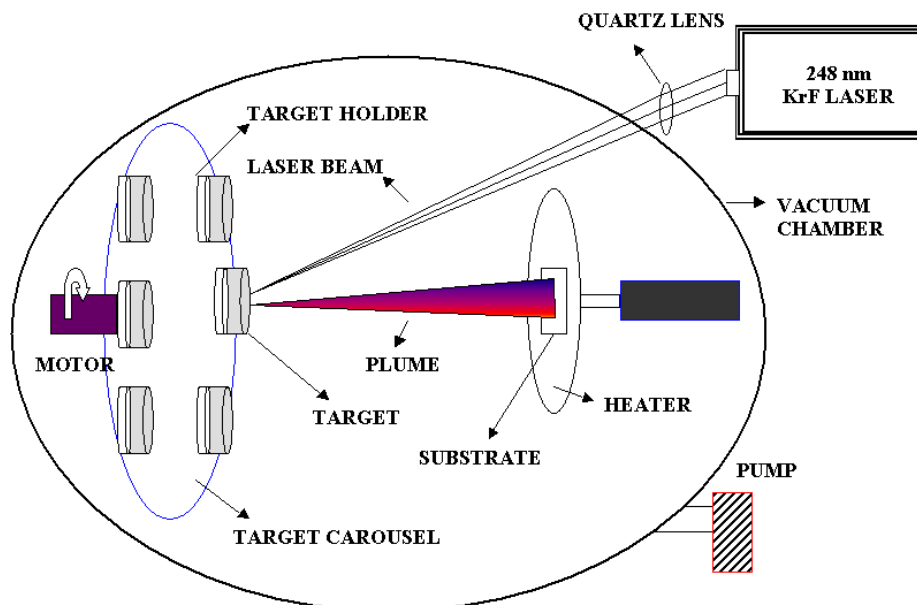


Fig. 2.12. Schematic diagram of PLD

In principle PLD is an extremely simple technique, which uses pulses of laser energy to remove material from the surface of a target, as shown schematically in Fig. 2.12. The vaporized material, containing neutrals, ions, electrons etc., is known as a laser-produced plasma plume and expands rapidly away from the target surface (velocities typically  $\sim 10^6 \text{ cms}^{-1}$  in vacuum). Film growth occurs on a substrate upon which some of the plume material re-condenses. In practice, however, the situation is not so simple, with a large number of variables affecting the properties of the film, such as laser fluence, background gas pressure and substrate temperature. These variables allow the film properties to be manipulated somewhat, to suit individual applications. However, optimization can require a considerable amount of time and

effort. Indeed, much of the early research into PLD concentrated on the empirical optimization of deposition conditions for individual materials and applications, without attempting to understand the processes occurring as the material is transported from target to substrate.

The technique of PLD was found to have significant benefits over other film deposition methods, including: (i) The capability for stoichiometric transfer of material from target to substrate, i.e. the exact chemical composition of a complex material such as YBCO, can be reproduced in the deposited film. (ii) Relatively high deposition rates, typically  $\sim 100 \text{ s \AA/min}$ , can be achieved at moderate laser fluences, with film thickness controlled in real time by simply turning the laser on and off. (iii) The fact that a laser is used as an external energy source results in an extremely clean process without filaments. Thus deposition can occur in both inert and reactive background gases. (iv) The use of a carousel, housing a number of target materials, enables multilayer films to be deposited without the need to break vacuum when changing between materials.

We have deposited pristine and doped ZnO thin films by pulse laser deposition (PLD) technique on c-axis-sapphire ( $\text{Al}_2\text{O}_3$ ) substrate using a KrF excimer laser of laser power density of  $2.14 \text{ J/cm}^2$  and pulse repetition rate of 5 Hz. The targets were prepared from the mixture of high purity (99.99%) ZnO and Li-acetate, Na-acetate and K-acetate powders for the deposition of pure ZnO and 6 at.% Li, Na and K-doped ZnO thin films respectively. The base pressure and oxygen pressure ( $\text{PO}_2$ ) of the deposition chamber was maintained at  $5 \times 10^{-5}$  and  $1 \times 10^{-2}$  torr respectively, keeping substrate temperature fixed at  $500^\circ \text{ C}$ . All the films are intentionally prepared under high oxygen pressure ( $10^{-2}$  torr) to reduce the formation of oxygen vacancy within the films. Each film was deposited with a total of 12,000 laser shot [discussed in detailed in Chapter 6].

## 2.3 Characterization and measurement techniques

### 2.3.1 X-ray diffraction

X-ray diffraction technique has been widely used (i) to identify the various phases within materials, (ii) to determine crystal structural and (iii) to estimate crystallite size and lattice parameter of unit cell of the materials.

The basic principle lies on the mechanism of electron (x-ray) diffraction within the crystalline lattice. Since all the atoms in a crystalline solid are regularly arranged with interatomic spacing of the order of few angstrom, the crystal can behave as a three-dimensional grating for x-rays. When monochromatic an x-ray beam passes through such crystalline solid, the x-ray electron gets diffracted as the wavelength of x-ray is comparable to interatomic spacing with the solids. In 1912, W.H Bragg and W. L. Bragg put forward a model which generates the condition for diffraction considering the reflection of x-rays beam from atomic planes as shown in Fig. 2.13. It was discovered that the constructive diffraction pattern will occur in accordance with Bragg's law condition

$$\text{Path difference } ABC = 2d \sin \theta = n\lambda \text{ for } n = 1, 2, 3, \dots;$$

Where,  $n$  denotes an integer value,  $d$  is the interatomic spacing,  $\lambda$  is the wavelength of monochromatic x-ray beam of incident on the set of parallel planes at a glancing angle  $\theta$ , as shown in Fig. 2.13.

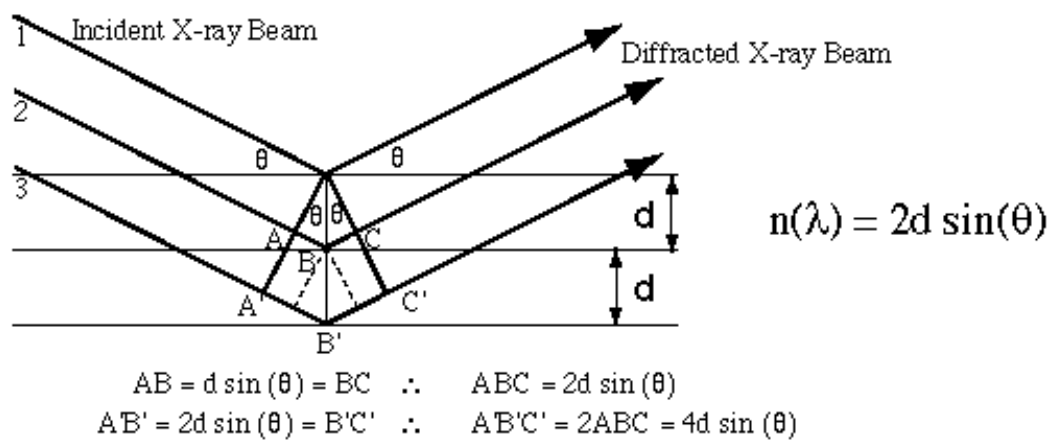


**Fig. 2.13:** Bragg's reflection of x-rays from the atomic planes.

In our laboratory, we have used X-ray diffractometer (X'Pert Pro, Panalytical) using copper Cu-K $\alpha$  radiation having wavelength  $\lambda = 1.5418 \text{ \AA}$  for sample characterization. It uses a ceramic tube consists of a tungsten filament (electron source) and metallic anode of Cu kept under high vacuum. The maximum power of the x-ray generator is 3 kW. For the detection of diffracted beams, it consists of a gas proportional detector (PW3011/20) which has a typical energy resolution (for Cu K $\alpha$

radiation) of 20%. (The energy resolution of a detector is a measure of its ability to resolve two X - ray photons of different energy). The resolution of this instrument in terms of scanning angle is  $0.001^\circ$ . For characterization of thin films samples we have used grazing angle XRD (GIXRD) mode in which the monochromatic x-ray beam is made to incident at an angle  $\sim 1^\circ$  with the film surface in order to avoid thick substrate contribution.

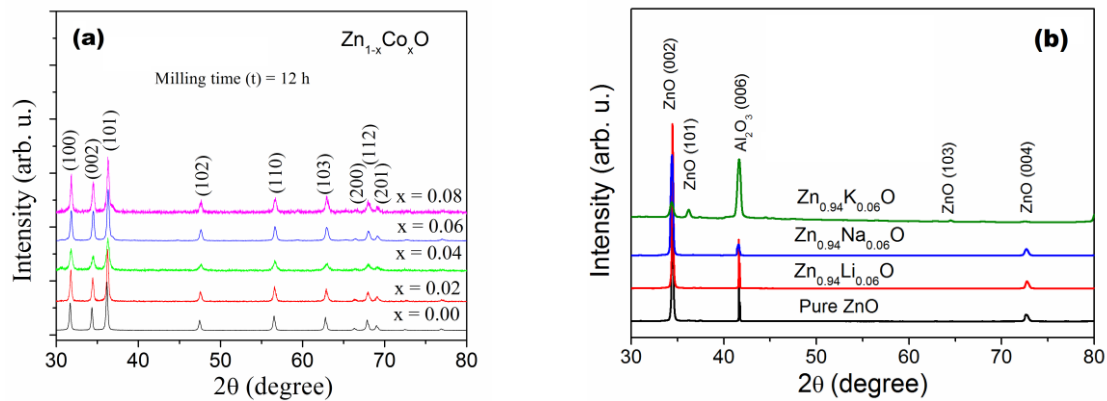


**Fig. 2.14:** XRD pattern of Co-doped ZnO bulk powders (b) alkali-metal doped ZnO thin films obtained using GIXRD mode.

### 2.3.2 Electron-Matter interaction (Electron microscopy)

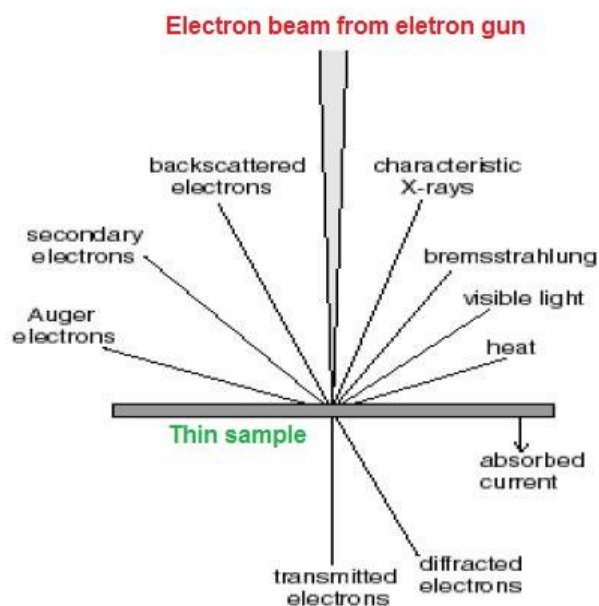


**Fig. 2.15:** Interaction of electron with thin sample specimen matter

The principle of electron microscopy [18, 19] stands on the mechanism of electron interaction with matter or sample specimen. Electron can interact various way with mater (Fig. 2.15). If a beam of electron is incident on mater it can undergo two types of scattering, elastic and inelastic. In elastic scattering only the trajectory changes and the kinetic energy and velocity remain constant. In the case of inelastic scattering, some incident electrons will actually collide with and displace electrons from their orbits (shells) around nuclei of atoms comprising the sample. This interaction places the atom in an excited (unstable) state. The inelastic interactions noted on the top side of the diagram are utilized when examining thick or bulk specimens in Scanning Electron Microscopy (SEM) while on the bottom side are those examined in thin or foil specimens in Transmission Electron Microscopy (TEM).

### 2.3.2.1 Scanning electron microscopy and EDX spectroscopy

SEM is one of the most widely used electron microscopy techniques for imaging the surface morphology of thick-sample. Fig. 2.16(a) shows a schematic diagram of SEM. A beam of electrons is focused on to sample after passing through several lens systems. The electron beam passes through scan coils and objective lens deflects horizontally and vertically so that the beam scans the surface of the sample. As the electrons penetrate the surface, a number of interactions occur that can result in the emission of electrons or photons from or through the surface. A reasonable fraction of the electrons emitted can be collected by appropriate detectors, and the output can be used to modulate the brightness of a cathode ray tube (CRT) whose x- and y- inputs are driven in synchronism with the x-y voltages rastering the electron beam. In this way an image is produced on the CRT; every point that the beam strikes on the sample is mapped directly onto a corresponding point on the screen [2]. SEM (Quanta 200 ESEM, FEI) works on a voltage between 30 to 200kV with spatial resolution of 3 nm at 30kV and its beam diameter that scans the specimen is 5nm-2 $\mu$ m. The principle images produced in SEM are of three types: secondary electron images, backscattered electron images and elemental X-ray maps.

When the electron bombards with the atoms, it can ejects the core electrons of the individual atoms leads to the generation of characteristic x-ray for each composite elements of the samples. EDX spectroscopy techniques attached with SEM set up collects that characteristic x-ray which are analyzed to get the

information about the chemical composition and atomic percentages of individual elements. In our laboratory, SEM (Quanta 200 ESEM, FEI) is employed to characterize oxides semiconductors in form of bulk, nanowires as well as thin films. Fig. 2.16 show SEM images of (b) 5% Gd-doped  $\text{SnO}_2$  thin film [16] and (c) 2% Co-doped  $\text{SnO}_2$  bulk samples. The Fig.2.16 (d) shows the EDX spectrum of 5%Gd-doped  $\text{SnO}_2$  thin films [16].

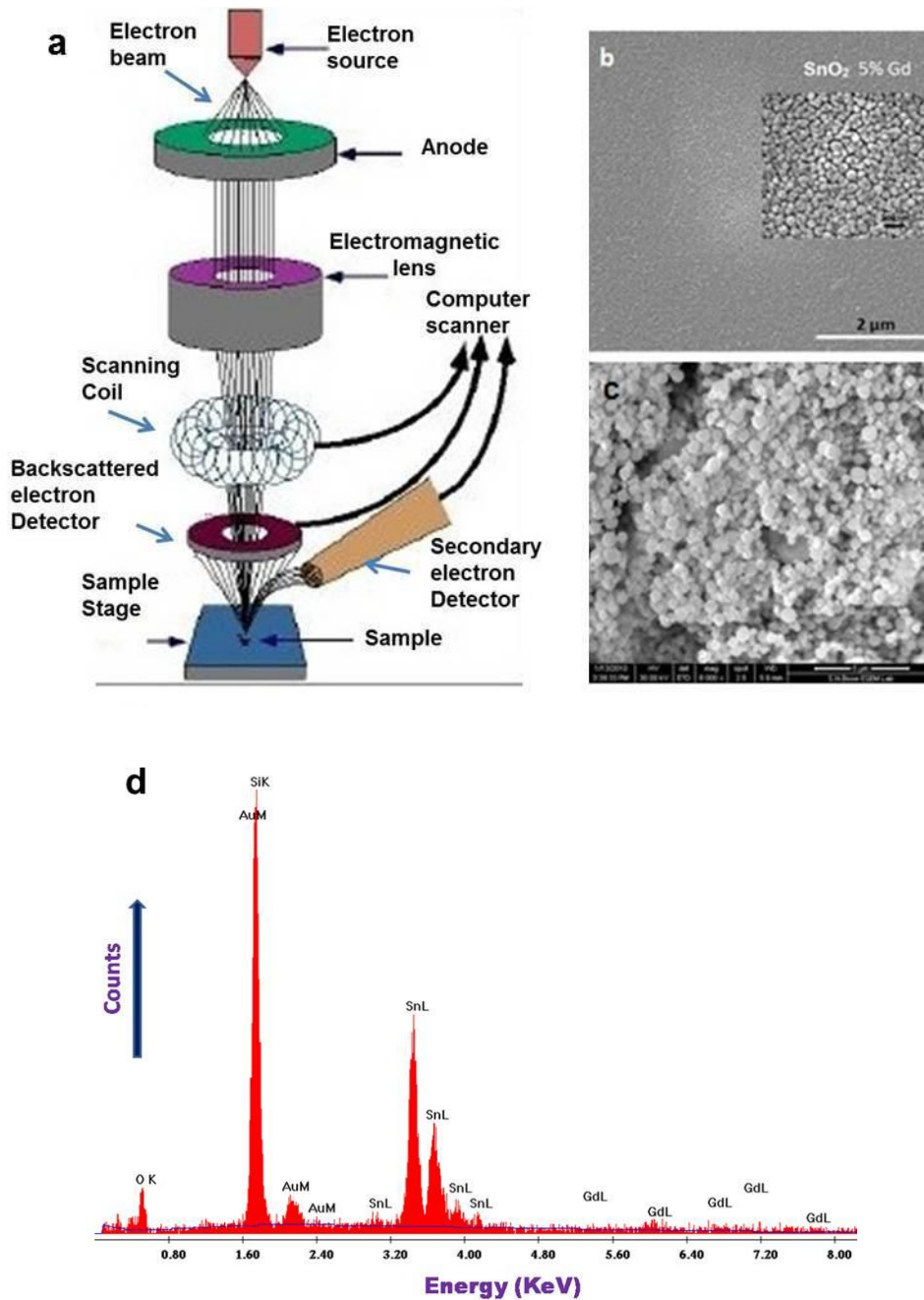


**Fig. 2.16:** (a) Schematic diagram of SEM components; SEM image of (b) Gd-doped  $\text{SnO}_2$  thin film and (c) Co-doped  $\text{SnO}_2$ .

### 2.3.2.2 Transmission electron microscopy

Transmission Electron Microscopy (TEM) imaging exploits the electrons that are transmitted through ultrathin specimen [19]. Nanopowder samples are initially dissolved in aqueous or alcoholic solution and ultrasonicated 20-30 minutes so that the particle gets dispersed very well inside the solution. After that a drop of solution is made to fall on the copper grid which was dried under infra-red (IR) lamp. Samples are mounted on the sample holder of TEM unit. Images were obtained by TEM, FEI TECHANI G2 SERIES having LaB<sub>6</sub> electron gun for operation between 20-200kV. A beam of electrons (typical wavelength less than 1Å) are emitted by the source and focused on the samples after passing two condenser lenses which also control the brightness of the beam (Fig. 2.17(a)). The electrons that are elastically scattered consists the transmitted beams, which pass through the objective lens. The objective lens forms the image display and the following apertures, the objective and selected area aperture are used to choose of the elastically scattered electrons that will form the image of the microscope. Finally, the beam goes to the magnifying system that is consisted of three lenses, the first and second intermediate lenses which control the magnification of the image and the projector lens. The formed image is shown either on a fluorescent screen or in monitor or both and is printed on a photographic film. The spatial resolution i.e. the minimum spatial separation that can be resolved by TEM (FEI TECHANI G2 SERIES) is 0.2 nm. Fig.2.17 show TEM image of (b) pure SnO<sub>2</sub>; (c) and (d) for 2% Co-doped SnO<sub>2</sub> nanorods prepared by solvothermal synthesis [5].

### High resolution TEM and SAED

High resolution TEM (HRTEM) is an imaging mode of TEM which provides the opportunity to imaging the crystal in an atomic scale and used to study the crystallographic orientation of atomic planes and also to estimate the inter-planar spacing. HRTEM is also very useful to detect various crystalline defects within the materials. In Fig. 2.17 (e) we show the HRTEM image of pure SnO<sub>2</sub> nanorods. It indicates the growth of SnO<sub>2</sub> nanorods along (110) direction.

Selected area electron diffraction (SAED) is a crystallographic experimental technique that can also be performed inside a transmission electron microscope (TEM). In this method, a selected area aperture which is a thin strip of metal located

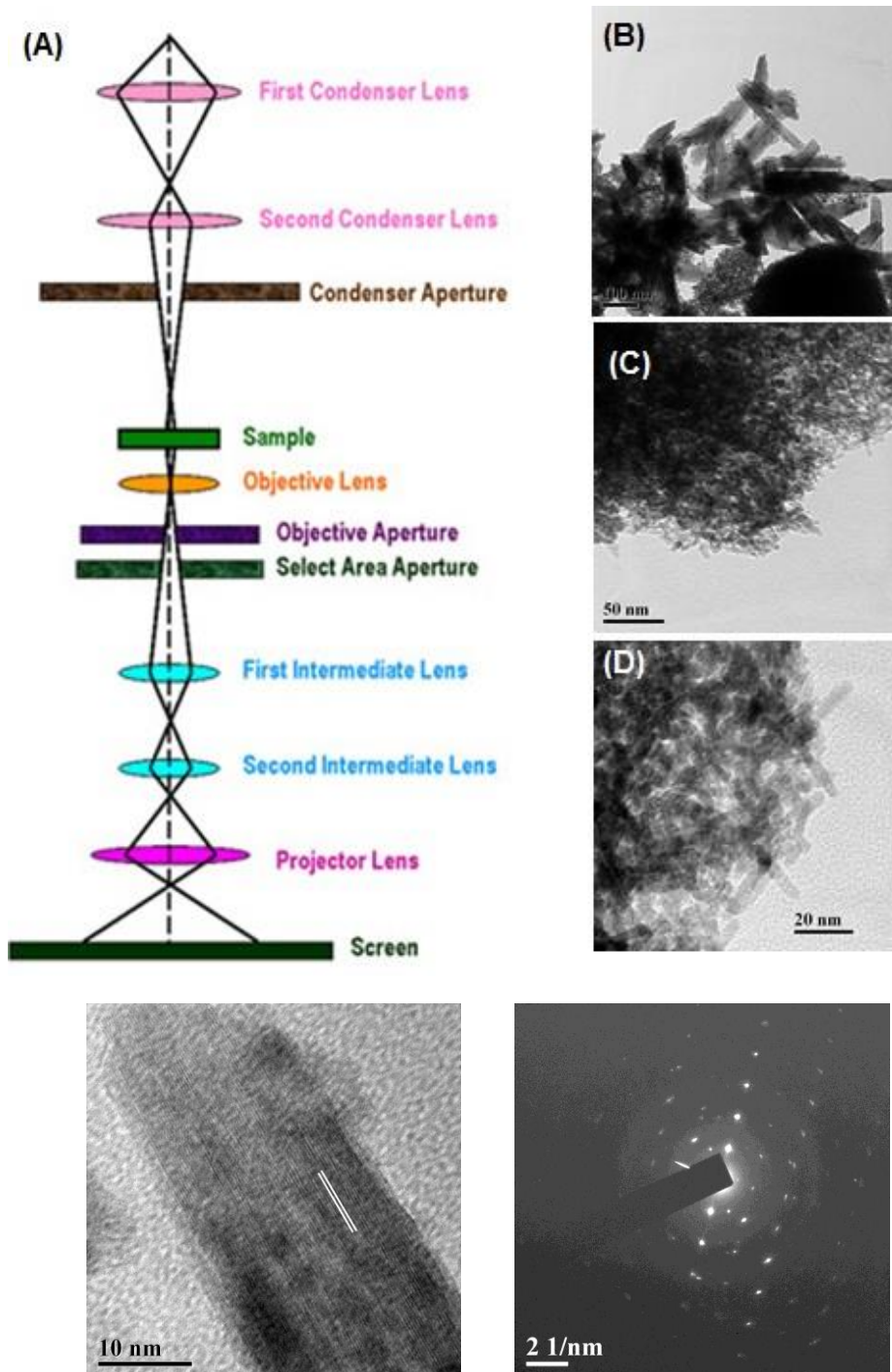


**Fig.2.17:** Schematic diagram of TEM; TEM image of (a) pure SnO<sub>2</sub>; (b) and (c) for 2% Co-doped SnO<sub>2</sub> nanorods; (e) HRTEM image of SnO<sub>2</sub> nanorods presenting the lattice fringes along (110) direction and (f) SAED pattern of SnO<sub>2</sub> nanorods.

below the sample holder on the TEM column can be inserted into the beam path. The aperture contains several different sized holes, and can be moved by the user. The effect is to block all of the electron beam except for the small fraction passing

through one of the holes; by moving the aperture hole to the section of the sample the user wishes to examine, this particular area is selected by the aperture, and only this section will contribute to the SADP on the screen. For polycrystalline material, the diffraction pattern are found to formed in the form of concentric circular rings which signifies individual atomic planes in different direction. On the other hand, a diffraction pattern with regular periodic bring spots appears for a single crystalline sample. Figure 2.17 (f) shows the SAED pattern of SnO<sub>2</sub> nanorods. The presence of both regular periodic bright spot and concentric circular rings represents that sample are polycrystalline in nature.

### 2.3.3 X-ray photoelectron spectroscopy

X-ray photoelectron spectroscopy (XPS) is generally employed to investigate the surface chemistry of electrically conducting and non-conducting materials. It is often used to determine the ionic valence state and chemical composition of the materials. It is extremely surface sensitive and provides information from the top 10nm of the sample.

#### Working principle

Photoelectron spectroscopy is based upon a single photon in/electron out process. The surface of the sample is irradiated with X-rays (commonly Al K $\alpha$  or Mg K $\alpha$ ) in vacuum. The photon energy ( $h\nu$ ) of Al K $\alpha$  and Mg K $\alpha$  radiation are 1486.6 and 1253.6 eV respectively. When an x-ray photon hits and transfers this energy to a core-level electron, it is emitted from its initial state with a kinetic energy dependent on the incident X-ray and binding energy of the atomic orbital from which it originated (Fig. 2.18(a)). The energy and intensity of the emitted photoelectrons are analysed to identify and determine the concentrations of the elements present. These photoelectrons originate from a depth of <10 nm therefore the information obtained is from within this depth.

If incident photon has energy  $h\nu$  which is transferred to an electron in the core shell, then the kinetic energy ( $KE$ ) of the ejected electron can be given by

$$KE = \frac{1}{2}mv^2 = h\nu - (BE + \Phi_{spec.}) \quad \text{where, BE = binding energy specific atomic}$$

core orbital such as 1s, 2s, 2p etc..  $\Phi_{spec.}$  is the work function of spectrometer.

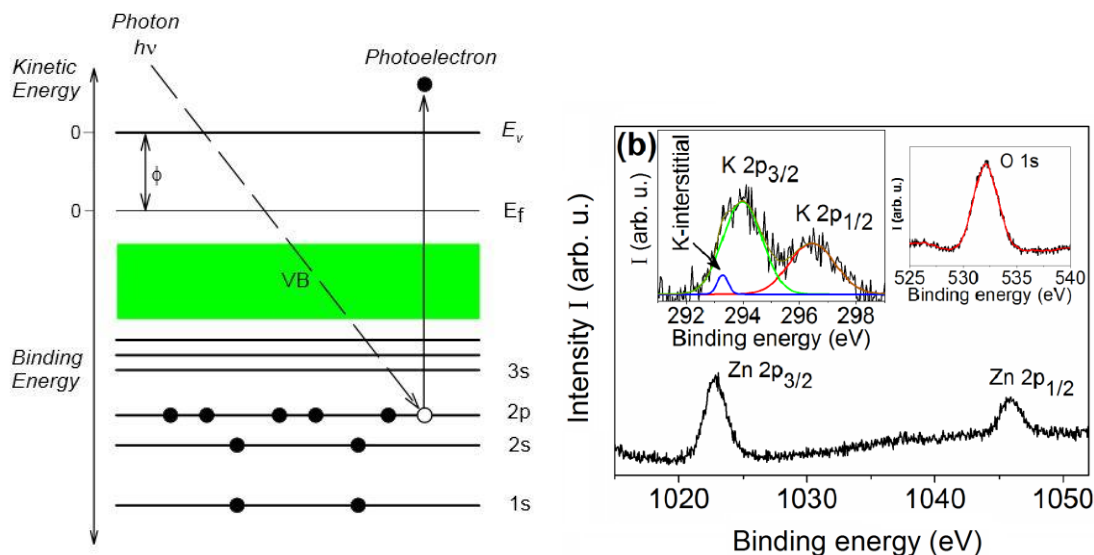


**Fig. 2.18:** (a) Schematic representation of XPS demonstrating the ejection of a core electron due to x-ray photon excitation. (b) Experimentally measured XPS spectra of Zn 2p, O 1s and K 2p core level in K-doped ZnO nanowires.

As for each and every element, there will be a characteristic binding energy associated with each core atomic orbital i.e. each element will give rise to a characteristic set of peaks in the photoelectron spectrum at kinetic energies determined by the photon energy and the respective binding energies. We have performed XPS measurements using Mg K $\alpha$  source (1253.6 eV) in VG system having energy resolution 0.9 eV FWHM on Au 4f<sub>7/2</sub> with pass energy of 20eV. Initially, the sample is scanned by the incident x-ray photon energy which falls gradually from 1253.6 eV to 0 eV and it gives the information about the presence of various constituent elements within the sample. After that the individual elemental high resolution spectrum was collected one by one. In Fig. 2.18 (b) we show high resolution XPS spectra of Zn 2p, O 1s and K 2p core level within K-doped ZnO nanowires. The spectra explores that elements like Zn, O and K are in +2, -2 and +1 valence state respectively and the K<sup>1+</sup> ions are substituting at Zn site replacing Zn<sup>2+</sup> ions within the ZnO lattice [20].

### 2.3.4 Photoluminescence spectroscopy

Photoluminescence (PL) spectroscopy is an important tool to identify various energy levels within the energy gap of semiconducting materials. A monochromatic

light from Xe lamp are used to excite the electrons in valence band. If the incident photon energy ( $E = hc/\lambda$ ) is greater than the band gap energy, then it can be absorbed by the valence band electrons which goes up to the conduction band crossing the forbidden energy gap (Fig. 2.19(a)). During the photoexcitation, the electrons generally have excess energy which loses during coming to rest at the lowest energy in the conduction band. At this point the electron eventually falls back down to the valence band or nearby acceptor states arises due to different defect levels. Similarly, electrons can also fall from the various donor impurity states near to the conduction band. As they (electrons) fall down, the energy associated is emitted as luminescent photons which are emitted from the material. The process of photon excitation followed by photon emission is called photoluminescence.

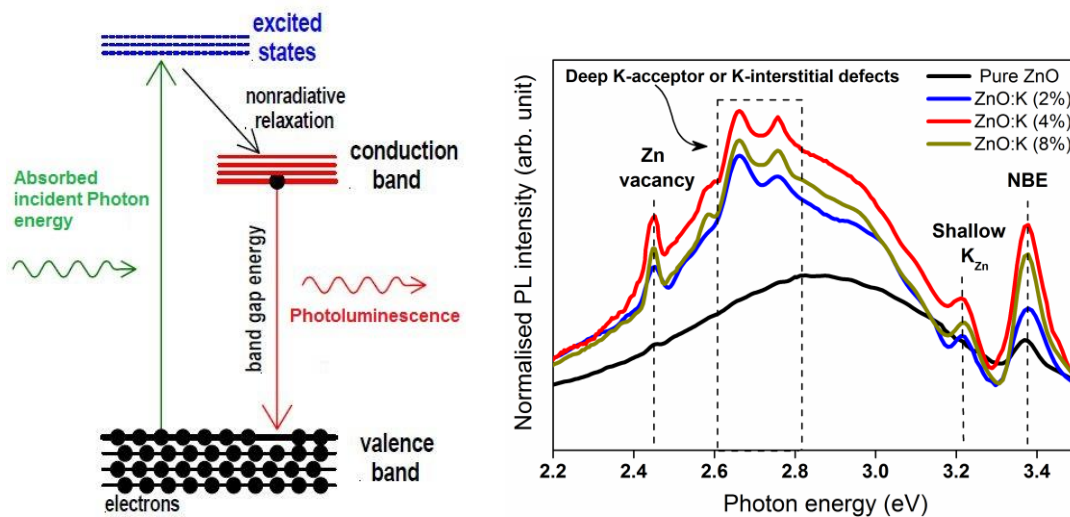


**Fig. 2.19:** (a) Schematic diagram of photoluminescence process (b) Experimentally measured PL spectra of pure ZnO and K-doped ZnO nanowires using spectrofluorometer (Horiba Jobin Yvon, Fluorolog-3).

We have conducted PL measurement for different oxide nanostructure and thin film samples using a spectrofluorometer (Horiba Jobin Yvon, Fluorolog-3) having Xe lamp source. During the fabrication of wide band gap ( $\geq 3$  eV) oxide nanostructures or thin films various structural defects such as ion vacancy, interstitials, antisites, various dopant substitutional defects can grow within the lattice and their (defects) respective energy level lies within the energy band gap of the host materials. Acceptor impurity or defect states lie near to valence band maxima while the donor defects reside below the conduction band minima.

Thereby these defect (acceptor or donor or both) levels also get involved and the associated electronic transitions can generate the characteristic luminescence in the visible region of the electromagnetic radiation energy spectrum. Therefore, investigating such characteristic luminescence, it is possible to identify the presence of various defects with the materials. In Fig. 2.19 (b) we show PL spectra of pure and potassium (K)-doped ZnO nanowires fabricated within anodic aluminum oxide (AAO) template. The evidence of K-substitutional, K-interstitial and Zn vacancy defects are observed within the ZnO host nanowires [21] (discussed in details in Chapter 5, section 5.3.3).

### 2.3.5 Electron paramagnetic resonance spectroscopy

Electron paramagnetic resonance (EPR) spectroscopy is often employed in material research to investigate the presence of any unpaired spin species such as paramagnetic radicals, vacancies etc. In case of oxide materials, EPR spectroscopy is widely used to identify the presence of oxygen vacancies ( $V_O$ ). Depending on the charge, there exist three types of  $V_O$  such as doubly ionized ( $V_O^{++}$ ), singly ionized ( $V_O^+$ ) and neutral ( $V_O^0$ ). Among them only singly ionized ( $V_O^+$ ) is EPR active while the other two are EPR silent.

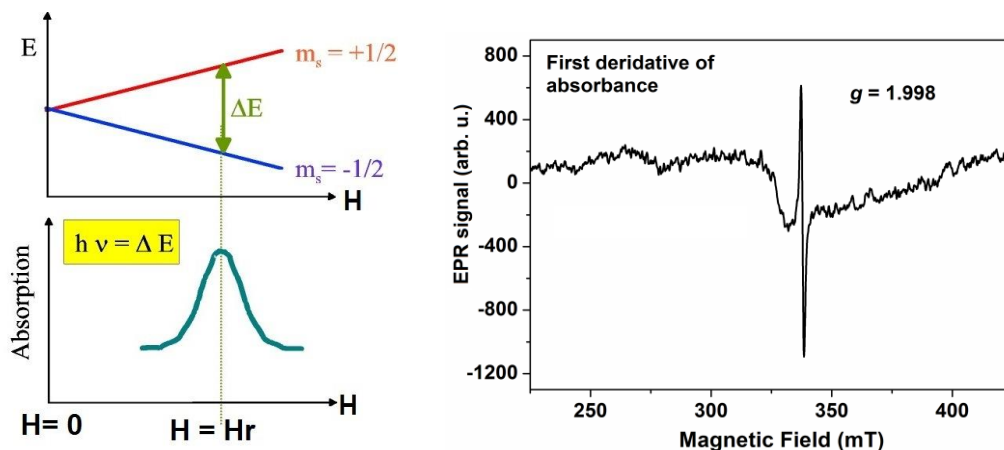


**Fig. 2.20:** (a) Schematic diagram of EPR principle. (b) Measured EPR spectrum for pure  $\text{SnO}_2$  nanowires revealing the presence of singly ionized oxygen vacancy.

The basic principle of EPR spectroscopy is quite analogous to those of nuclear magnetic resonance (NMR), but it is electron spins that are excited instead of the

spins of atomic nuclei. An electron with spin  $S = \frac{1}{2}$  has its two possible magnetic spin quantum number  $m_s = \frac{1}{2}$  and  $m_s = -\frac{1}{2}$ . In presence of an external magnetic field (H) the electron magnetic moment ( $\mu_B$ ) aligns itself either parallel ( $m_s = -\frac{1}{2}$ ) or antiparallel ( $m_s = \frac{1}{2}$ ) to the direction of external magnetic field and individual alignment having a specific energy  $E = g\mu_B m_s H$  due to Zeeman effect. Where, g is Lande g factor,  $\mu_B$  is Borh magnetron.

In laboratory, EPR spectroscopy is performed using microwaves with frequency 9-10 GHz and the corresponding magnetic field strength is about 3500 G. Absorbed spectrum is collected by scanning the magnetic field strength keeping frequency at a fixed value. An unpaired electron can move between the two energy levels by either absorbing or emitting a photon of energy  $h\nu$  such that at resonance condition  $h\nu = \Delta E = g\mu_B H_r$ , which is the fundamental equation of EPR spectroscopy.  $H_r$  is resonant magnetic field strength. In Fig. 2.20 we show (a) schematic diagram of EPR phenomena and (b) the experimentally measured EPR spectrum for pure SnO<sub>2</sub> nanowires and the obtained g factor  $\sim 1.998$  indicates the signal is arising due to the presence of singly ionized oxygen vacancy (discussed in details in chapter 5, section 5.2.2.3).

### 2.3.6 Vibrating sample magnetometer

Vibrating sample magnetometer (VSM) is used to measure the magnetic properties of the sample. The basic principle of VSM lies on Faraday's Law of Induction,  $\nabla \times \vec{E} = \frac{\partial \vec{B}}{\partial t}$  which tells us that a changing magnetic field (B) will produce an electric field (E). This electric field can be measured and can give us information about the changing magnetic field. Thus, the sample is placed in a constant magnetic field and oscillated with a fixed frequency near a set of detection (pickup) coils. If the sample is magnetic, the constant magnetic field induces a magnetic dipole moment in the sample. This magnetic dipole moment creates a magnetic field around the sample. As the sample is oscillated, this magnetic flux changes as a function of time and the voltage induced (proportional to the rate of change of flux) in the pickup

coils is synchronously detected. The voltage will also be proportional to the magnetic moment of the sample. In Fig.2.21 we show (a) schematic of VSM and (b) detailed configuration near the pick-up coils. The system detection capability can be maximized by optimizing the geometry of the pickup coils and by having oscillation amplitude that is relatively large (1 – 3 mm peak). The time dependent voltage induced in the pickup coils is given by

$$V_{\text{induced}} = (d\phi/dt) = (d\phi/dz)(dz/dt)$$

where,  $\phi$  represents the magnetic flux, the axis of oscillation of the sample is conventionally chosen to be the  $z$  - axis, and  $z$ , therefore, represents the position of the sample along this axis and  $t$  is the time. If the sample is made to oscillate sinusoidally, then the induced voltage in the pickup coils will have the form  $V_{\text{induced}} = c m A \omega \sin \omega t$ , where,  $c$  is a coupling constant,  $m$  is the DC magnetic moment of the sample,  $A$  is the amplitude of oscillation, and  $\omega = 2\pi f$ , where  $f$  is the frequency of oscillation of the sample. The detection of the magnetic moment of the sample, thus, amounts to measuring the coefficient of sinusoidal voltage response induced in the detection coil. In our laboratory, we have used a VSM, Lakeshore, model 7144 (with maximum field strength 1.6 T and minimum achievable temperature of 80K) to measure the magnetic properties of the samples.

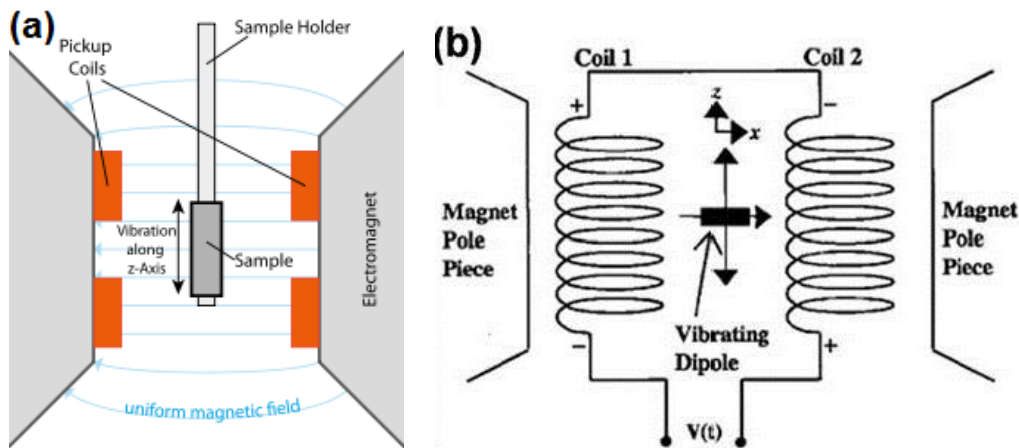


Fig. 2.21: Schematic diagram of (a) VSM and (b) details near the pickup coils.

### 2.3.7 SQUID magnetometer

Superconducting Quantum Interference Devices (SQUID) is another-type of magnetometer which has much higher sensitivity ( $\sim 10^{-8}$  emu) compared to the VSM

( $\sim 10^{-6}$  emu). Thus SQUID magnetometer provides the opportunity to measure the sample having very low magnetic moment with high degree of accuracy. The basic principle of a SQUID is based on the quantum interference of wave functions that describe the state of the superconducting charge carriers (the Cooper pairs). A SQUID is based on an interferometer loop in which two weak links (Josephson contacts) are established. A weak link is established by interrupting a superconductor by a very thin insulating barrier. The function of the SQUID is to link the quantum mechanical phase difference of the Cooper pairs wave functions over a weak link with the magnetic flux penetrating the interferometer loop [23-24].

There are two types of SQUID operation such as direct current (DC) which uses two parallel Josephson junction and the another is the radio frequency (RF) SQUID which have only one Josephson junction. The components of a SQUID magnetometer typically consist of the following: a detection coil which senses changes in the external magnetic field and transforms them into an electrical current, an input coil (i.e. the SQUID element with one or two Josephson junction) which transforms the resulting current into a magnetic flux in the SQUID sensor, electronics which transform the applied flux into a room temperature voltage output and acquisition hardware and software for acquiring, storing and analyzing data. Both the SQUID amplifier and detection coils are superconducting devices.

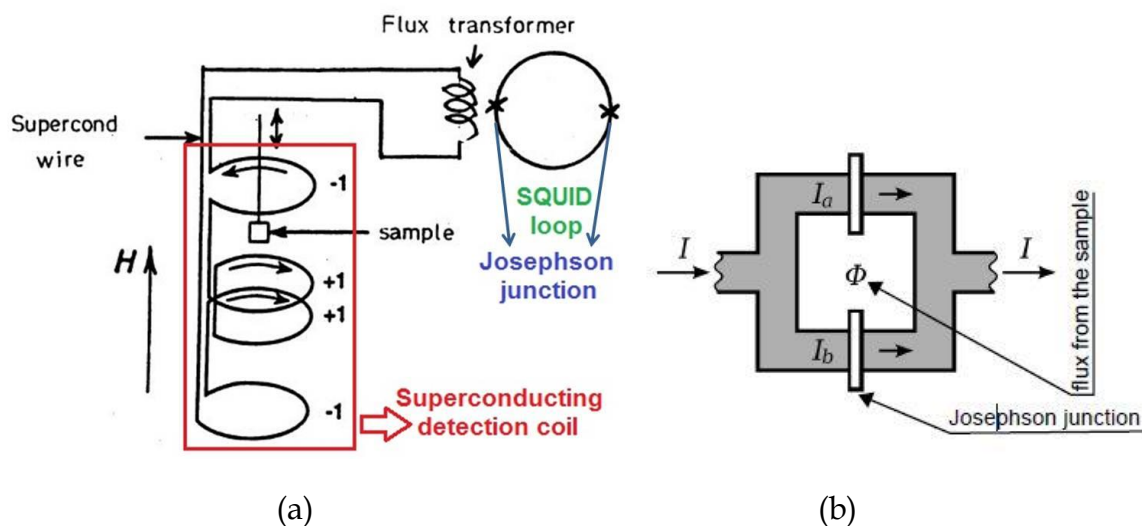
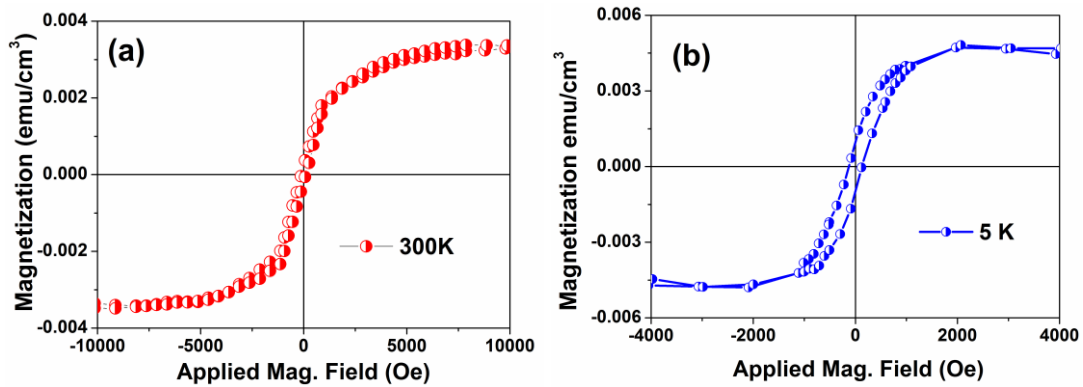


Fig. 2.22: Schematic diagram of SQUID magnetometer.

## Superconducting detection Coil and SQUID loop:

These are the two principle parts for the function of SQUID magnetometer. The detection coil consists of a superconducting wire in a set of three coils configured as a second order gradiometer (as shown in Fig. 2.22(a)). The coil sits outside the sample space within the liquid helium bath. The upper coil is a single turn wound clockwise, the centre coil comprises two turns wound counter-clockwise and the bottom coil is a single turn wound clockwise. The coils are positioned at the centre of the superconducting magnet outside the sample chamber such that the magnetic field from the sample couples inductively to the coils as the sample is moved through them.



**Fig. 2.23:** Field dependent Magnetization (M-H) plot for pure SnO<sub>2</sub> thin films on Si (001) substrate measured using SQUID at (a) 300 K and (b) 5 K.

The SQUID loop is superconducting loop with two Josephson junction (Fig. 2.22(b)) and can be used to convert the sample magnetic flux to equivalent voltage which is detected computer system through a lock in-amplifier. The Josephson junction [23] is a junction between two superconductors which are weakly coupled separated (in the case of low-  $T_c$  Tunnel junction) by thin insulating barrier. Under this condition, cooper pairs of electrons can pass from one superconductor to the other even with no applied voltage. It operates under the principle of flux quantization within the superconducting loop. Magnetic flux passing through a superconducting current circuit is quantized  $\phi_0 = \frac{h}{2e} \approx 2.067 \times 10^{-15} Tm^2$  and the current passing through the Josephson junction will be a function of the flux due to

sample's moment and is given by  $J_{total} = J_0 \cos\left(\frac{2\pi e}{h} \phi\right)$ . Since the junction has a resistance, the voltage drop across the junction is measured using appropriate electronics devices.

## 2.8. Atomic and Magnetic force microscopy

Atomic force microscopy (AFM) is a high resolution imaging techniques in which the forces due to individual atom are exploited. The AFM consists of a silicon or silicon nitride cantilever with a sharp tip which are used to scan the specimen surface. The tip radius of curvature is generally of the order of nanometers. When the tip is brought into proximity of a sample surface, forces between the tip and the sample lead to a deflection of the cantilever according to Hooke's law [24]. Depending on the situation, forces that are measured in AFM include mechanical contact force, van der Waals forces, capillary forces, chemical bonding, electrostatic forces, magnetic force, Casimir forces, solvation forces, etc. The AFM can be operated in a number of modes, depending on the application. In general, possible imaging modes are divided into static (also called *contact*) modes and a variety of dynamic (non-contact or "tapping") modes where the cantilever is vibrated.

Unlike AFM in which the atomic or electrostatic forces are measured, the magnetic force microscopy (MFM) technique uses the magnetic force of sample to generate the images of magnetic domains within the specimen (Fig. 2.24 (a)). The MFM is another mode of AFM in which the sharp tip of the cantilever is magnetized and it scans over the magnetic sample [25]. The tip-sample magnetic interactions are used to reconstruct the magnetic structure of the sample surface. Many kinds of magnetic interactions are measured by MFM, including magnetic dipole-dipole interaction. MFM scanning often uses non-contact AFM (NC-AFM) mode. During MFM measurements, the magnetic force between the sample and the tip can be expressed as [2]

$$\vec{F} = \mu_0 (\vec{m} \cdot \nabla) \vec{H}$$

where  $\vec{m}$  is the magnetic moment of the tip (approximated as a point dipole),  $\vec{H}$  is the magnetic stray field from the sample surface, and  $\mu_0$  is the magnetic permeability of free space.

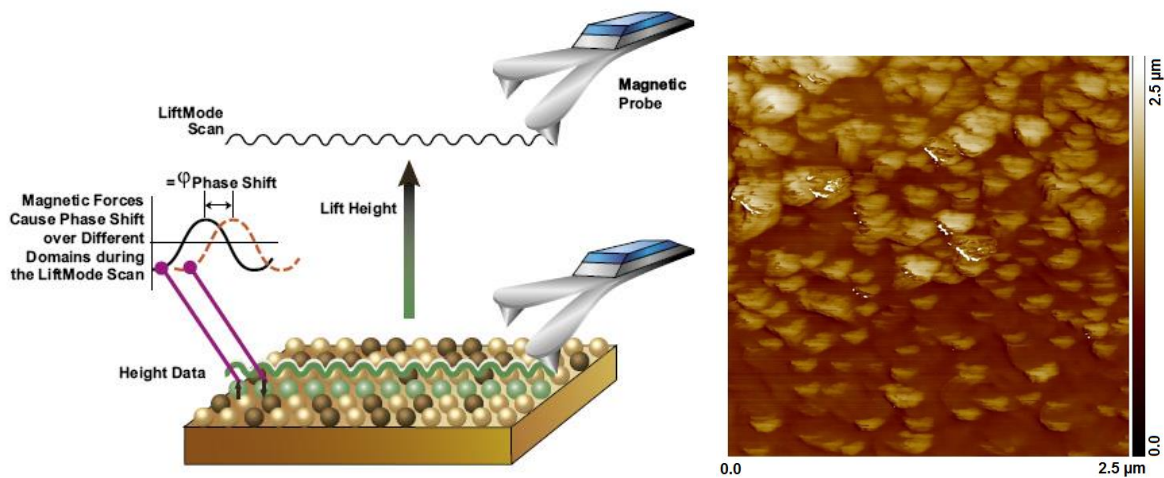


**Fig. 2.24:** (a) Magnetic Force Microscopy using silicon probe (magnetically coated with Ni) scanning. (b) MFM image for Li-doped ZnO thin film sample.

In our laboratory, we have obtained AFM and MFM images of the samples using the AFM, veeco-3100 set up. The imaging is performed keeping the probe (tip) at a lift height of  $\sim 300$  nm over a scan size of  $2.5 \times 2.5$   $\mu\text{m}$  on the surface. Typical resolution of 30 nm can be achieved [26], although resolutions as low as 10 to 20 nm are attainable. In Fig. 2.24 (b) we show a typical MFM image of Li-doped ZnO film revealing the magnetic domains over the film surface. The bright and dark contrasts of the domains correspond to high concentrations of positive and negative poles, respectively. The presence of prominent and quite regularly distributed magnetic domains indicates the strong ferromagnetic signature in the Li-doped ZnO film (discussed in details in Chapter 6, section 6.2.2).

## References

- [1] M. I. Florez-Zamora et al., *Rev. Adv. Mater. Sci.* **18**, 301 (2008)
- [2] *Solid State Chemistry and its Applications*, Anthony R. West, Wiley and Sons, 2005
- [3] S. Ghosh and K. Mandal, *J. Magn. Magn. Mater.* **322**, 1979 (2010).
- [4] K. Byrappa and Masahiro Yoshimura, *Handbook of Hydrothermal Technology* (Norwich, New York: Noyes Publications, 2001
- [5] S. Ghosh, D. De Munshi, K. Mandal, *J. Appl. Phys* **107**, 123919 (2010).
- [6] Patnaik, P. *Dean's Analytical Chemistry Handbook*, 2nd ed. McGraw-Hill, 2004.
- [7] Harvey, D. *Modern Analytical Chemistry*. McGraw-Hill, 2000.
- [8] S. Ghosh, M. Mandal, K. Mandal, *J. Magn. Magn. Mater.* **323**, 1083 (2011).
- [9] H. Masuda and K. Fukuda, *Science* **268**, 1466 (1995).
- [10] J. Sarkar, G. G. Khan, and A. Basumallick, *Bull. Mater. Sci.* **30**, 271 (2007).
- [11] Eftekhari, A., *Nanostructured materials in electrochemistry*, Wiley-VCH publishers (2007).
- [12] Ghosh, S.; Khan, G. G.; Das, B.; Mandal, K. *J. Appl. Phys.* **2011**, 109 123927.
- [13] Ghosh, S.; Khan, G. G.; Varma, S.; Mandal, K. *J. Appl. Phys.* **2012**, 112, 043910.
- [14] Khan, G. G.; Ghosh, S.; Mandal, K. *J. Solid State Chem.* **2012**, 186, 278.
- [15] Ohring, Milton. *Materials Science of Thin Films*. Academic Press. p. 215.
- [16] S. Ghosh, G. G. Khan and K. Mandal, *ACS Appl. Mater. Interfaces*, **4**, 2048 (2012).
- [17] *Pulsed Laser Deposition of Thin Films*, edited by Douglas B. Chrisey and Graham K. Hubler, John Wiley & Sons, 1994.
- [18] Erni, Rolf; Rossell, MD; Kisielowski, C; Dahmen, U (2009). "Atomic-Resolution Imaging with a Sub-50-pm Electron Probe". *Physical Review Letters* **102** (9): 096101.
- [19] H Gunther Rudenberg and Paul G Rudenberg (2010). "Origin and Background of the Invention of the Electron Microscope: Commentary". *Advances in Imaging and Electron Physics* (Elsevier) **160**.
- [20] C. D. Wagner, W. M. Riggs, L. E. Davis, J. F. Moulder, G. E. Muilenberg, in *Handbook of X-ray Photoelectron Spectroscopy*, edited by G. E. Muilenburg (Perkin Elmer, Eden Prairie, 1979).
- [21] S. Ghosh, G. G. Khan and K. Mandal, *EPJ Web of Conferences* **40**, 03001 (2013).

- 
- [22] J. Clarke and A. I. Braginski (Eds.) (2004). *The SQUID handbook* **1**. Wiley-Vch.
- [23] R. C. Jaklevic, J. Lambe, A. H. Silver, and J. E. Mercereau (1964). "Quantum Interference Effects in Josephson Tunneling". *Phys. Rev. Letters* **12** (7): 159-160.
- [24] B. Cappella and G. Dietler, *Surface Science Reports* **34** (1999) 1-104.
- [25] U. Hartmann *Annu. Rev. Mater. Sci.* **29** (1999) 53-87
- [26] Leon Abelmann, Steffen Porthun et al., *J. Magn. Magn. Mater.* **190** (1998) 135-147

# Chapter 3

## Transition Metal-doped Wide-Band Oxide Semiconductors

### 3.1 Preface

In chapter 1, we have discussed the importance of wide band-gap oxide semiconductors as host to prepare dilute magnetic semiconductors (DMS) for spintronic and optospintronic applications [1-3]. The bulk magnetic properties of such wide-band oxides with high structural perfection are generally known to be diamagnetic. Therefore, question arises that how we can make such non-magnetic oxides ferromagnetic? Transition metal (TM) atoms ( $Z = 21-30$ ) are known to have localize atomic magnetic moment due to their unfilled 3d electrons. Among them, only the three TM elements Fe, Co and Ni exhibit ferromagnetism at room temperature (RT). Therefore, the idea of introducing magnetic moment in such non-magnetic oxides was to dope or substitute some of the host semiconducting cations randomly with TM ions and then investigate whether it is possible to stabilize RT ferromagnetic ordering between the substituted TM ions within the host oxide semiconductors.

In the present chapter, we have discussed the role of TM elements such as cobalt (Co), iron (Fe), chromium (Cr) vanadium (V) etc. in stabilizing magnetism in wide-band oxide semiconductors such as ZnO, SnO<sub>2</sub>, TiO<sub>2</sub> etc. Ultraviolet-visible (UV) absorption spectroscopy has been employed to confirm the substitution of TM ions in host cation site which is the most important criteria to prepare DMS. Otherwise the presence of different secondary phases or TM metal impurity phases will lead to exhibit some undesirable responses which simply make it difficult to find some technological applications. In order to understand the origin of magnetism properly, it is essential to study of bulk magnetic properties in TM-doped oxides first. Bulk materials prepared using simple techniques such as solid state reaction or chemical processes generally contains little amount of structural defects or disorder, compared to the corresponding low dimensional (1D/2D) structures such nanostructures or thin films. In this chapter, we will study TM Co-doped ZnO bulk powder samples prepared by mechanical milling and investigate the role of Co substitution [4]. Then we will present a comparative study of magnetic properties between bulk and nanostructured Co-doped SnO<sub>2</sub> prepared by mechano-synthesis and solvothermal synthesis [5]. Here we will discuss the effect of particle size reduction on the magnetic behavior of Co-doped SnO<sub>2</sub>. Then we will see that the dependence of magnetic interaction between the substituted TM ions on various annealing atmosphere such as oxygen (O), nitrogen (N) in Fe-doped SnO<sub>2</sub> bulk system [6].

## 3.2 Co-doped ZnO bulk structures

### 3.2.1 Synthesis of Zn<sub>1-x</sub>Co<sub>x</sub>O (x ≤ 0.08) bulk powders

All the Zn<sub>1-x</sub>Co<sub>x</sub>O (x ≤ 0.08) bulk powders samples are prepared by solid state reaction using Fritsch make (Germany) Pulverisette-7 ball mill machine discussed in Chapter 2. Commercial ZnO powder having hexagonal wurtzite crystal structure (with lattice parameter as a=b=3.258 Å & c = 5.216 Å) and CoO with 99.999% purity (purchased from Sigma-Aldrich) were used as the starting materials. A mixture of 5 gm of ZnO & CoO powders were taken in the vials with powder: ball ratio as 1:10 by weight and then rotated with frequency of 800 rpm. The mixtures were milled for different times such as 4, 8, and 12 hours. After that the compounds are sintered in air at 700°C for 6 hrs in order to avoid non-equilibrium phases. The Co concentration

in ZnO was varied from 2, 4, 6, & 8 at.%. For identification of crystal phases and morphology, the samples were characterized by X-ray powder diffraction (XRD, X'Pert Pro, Panalytical) using Cu  $K_{\alpha}$  radiation ( $\lambda=1.540598\text{\AA}$ ), and field emission scanning electron microscope (FESEM, FEI Helios Nanolab-600), Energy dispersive X-rays (EDX) spectroscopy attached with FESEM set up. The substitution of Co ions at Zn site is confirmed from the Ultra violet-Visible (UV) absorption spectroscopy measurements and magnetic properties are measured using Vibrating sample magnetometer (VSM, Lakeshore, model 7144) within the temperature range of 80 to 350 K.

### 3.2.2 Crystal structural and morphology

The X-ray diffraction patterns show that the undoped ZnO powders as well as all  $\text{Zn}_x\text{Co}_{1-x}\text{O}$  samples have hexagonal wurtzite structures as shown in Fig. 3.1. Most importantly it is noticeable that all the XRD peaks are identified to the ZnO and no other undesired peaks appear due to secondary phases or impurity phases within the detection limit of X-ray diffractometer. At the same time the XRD peaks for the doped samples show significant shift in the higher  $2\theta$  direction (shown in the inset of Fig. 3.11) with respect to the undoped ZnO peak position. This higher shift can be explained due to incorporation of smaller  $\text{Co}^{2+}$  ions ( $0.58\text{\AA}$ ) replacing the  $\text{Zn}^{2+}$  ( $0.6\text{\AA}$ ) in the hexagonal wurtzite structure [7, 8]. It reveals that although the  $\text{Co}^{2+}$  ions are substituting the  $\text{Zn}^{2+}$ , the symmetry of the crystal structure remains the unchanged.

The time evolution of XRD peaks of the  $\text{Zn}_{0.96}\text{Co}_{0.04}\text{O}$  sample starting from unmilled mixture have been shown in Fig. 3.2 (a). It is seen from the figure that initially at  $t=0$ , CoO (200) and CoO (220) peaks have appeared with ZnO peaks for unmilled ZnO and CoO mixtures and the intensities of CoO peaks are very weak which is expectable due to presence of small amount CoO. After 1 h milling time the broadening of CoO peaks have been observed due to decrease in crystalline size. The intensities of CoO peaks become very feeble after 4 h milling time. In case of 8 h and 12 h milling time, no CoO peaks are detected. So this gradual decrease of intensities of CoO peaks with the increase of milling time indicates that the  $\text{Co}^{2+}$  ions enters gradually inside the ZnO unit cell replacing the  $\text{Zn}^{2+}$  ions. Pure ZnO are also milled alone by the same process and the corresponding XRD patterns at different milling time are presented in Fig. 3.2 (b). As the milling time goes on increasing, the

crystallite sizes of ZnO decrease resulting the broadening of the ZnO peaks. No impurity peaks coming from the tungsten carbide (WC) bowl or any other sources are detected up to 12 h milling time.

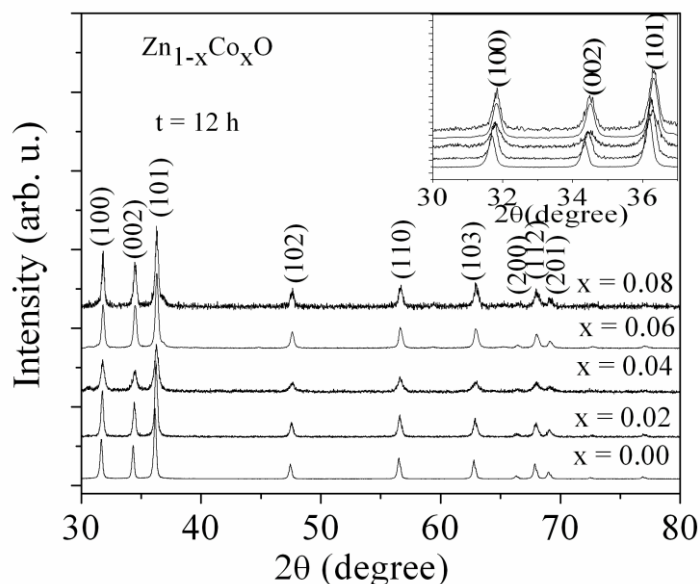


**Fig. 3.1:** X-ray Diffraction pattern of the  $\text{Zn}_{1-x}\text{Co}_x\text{O}$  samples. Inset shows the shift of XRD peaks towards higher  $2\theta$  due to Co-doping.

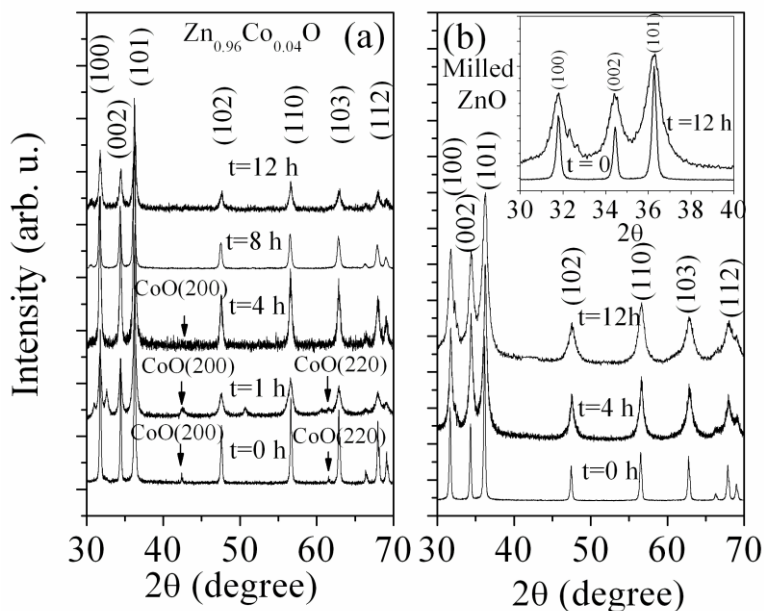


**Fig. 3.2:** Milling time evolution of XRD pattern of (a)  $\text{Zn}_{0.96}\text{Co}_{0.04}\text{O}$  sample and (b) undoped milled ZnO.

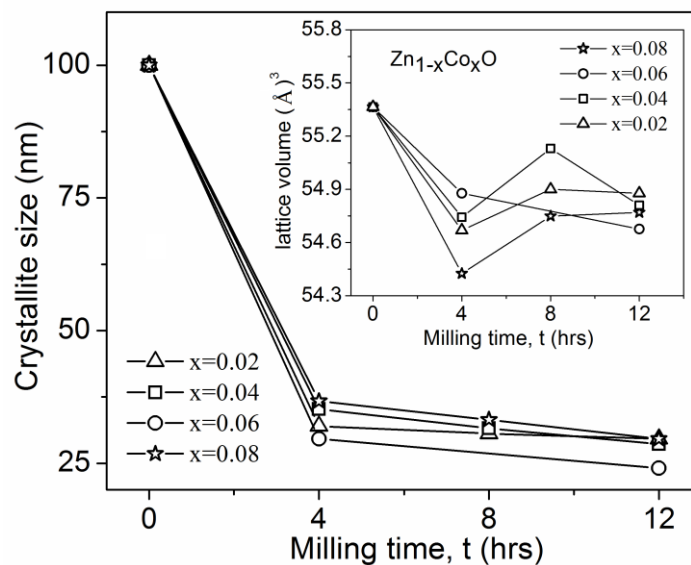


**Fig. 3.3:** Variation of crystallite size with milling time for doped samples. Inset: the change in unit cell volume of Co doped ZnO as a function of milling time.

The crystallite sizes ( $\tau$ ) are estimated using Scherrer formula, as discussed in Chapter 2, and its variation with milling time is shown in Fig. 3.3. The lattice parameters of the undoped and doped samples are estimated using the Bragg's law  $2d\sin\theta=n\lambda$ , where  $\theta$  is the peak position,  $\lambda$  is the wave length of X-rays and  $d$  is the interplaner spacing defined as  $1/d^2=4/3[(h^2+hk+k^2)/a^2] + l^2/c^2$  for hexagonal crystal structures, where  $(h,k,l)$  the miller indices of the crystallographic planes and  $a$  and  $c$  are the lattice parameters of the hexagonal structures. The variation of lattice volumes of the Co-doped samples with the milling times is shown in the inset of Fig. 3. Both the crystallite size as well as the unit cell volume reduces significantly within first 4 hours of milling. Further milling does not affect them too much. The Scanning Electron Micrographs in Fig. 3.4 show that our samples are mostly homogeneous throughout and no sign of Co accumulation.

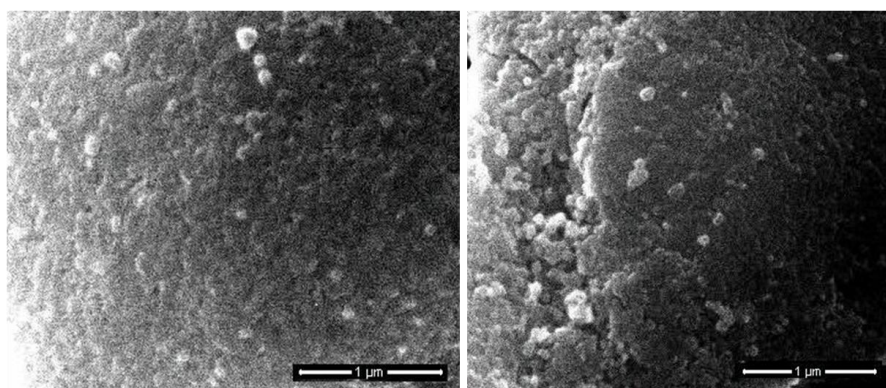


**Fig. 3.4:** SEM images of (a) 4 at.% and (b) 6 at.% Co-doped ZnO samples.

### 3.2.3 UV-visible absorption spectroscopy studies

It is very essential to confirm whether  $\text{Zn}^{2+}$  ions are replaced by  $\text{Co}^{2+}$  ions in our Co-doped samples and the change in band-gap is a signature for this substitution. The variation of band gap with Co substitution is studied at room temperature by conventional ultraviolet-visible (UV) spectrometer and Fig. 3.5 shows the collection of the UV-visible absorption spectra for ZnO doped with Co at different at. %. The Fig. 3.5 (a), (b) and (c) represent characteristic spectrum of 2%, 4% and 6% Co doped ZnO. In case of 2% Co doped sample, the peak at 375 nm corresponds to the Co doped ZnO energy band gap which is slightly less than the undoped ZnO band gap ( $E_g$ )  $\sim$  3.3 eV and is in agreement what reported in literature [9-11]. But for the 4% and 6% Co doped samples much larger shift of this peak has been observed compared to undoped ZnO which ensures significant number of  $\text{Co}^{2+}$  ions inside the ZnO lattice. Fig. 3.5 (d) shows the milling time evolution of absorption spectra of  $\text{Zn}_{0.96}\text{Co}_{0.04}\text{O}$ . On increasing milling time, the band gap ( $E_g$ ) also shifts to lower energy than that of pure ZnO (3.3 eV). In case of 12 hours milled  $\text{Zn}_{0.96}\text{Co}_{0.04}\text{O}$ , energy bad gap reduces to 3.2 eV. The redshift of the energy band gap ( $E_g$ ) on incorporating  $\text{Co}^{2+}$  in ZnO has been already observed [12] and explained as mainly due to sp-d exchange interactions between the band electrons and the localized d electrons of the  $\text{Co}^{2+}$  ions substituting  $\text{Zn}^{2+}$  ions [9, 12, 13]. The exchange interactions between s-d and p-d orbital give rise to a negative and a positive correction to the conduction-band and valence-band edges, respectively, resulting to a decrease in band gap [14].

The substitution of  $\text{Co}^{2+}$  in the tetrahedral sites of ZnO wurtzite structure replacing  $\text{Zn}^{2+}$  ions is confirmed by the appearance of three additional absorption peaks in the 550-700nm region for all doped samples. In  $\text{Zn}_{0.96}\text{Co}_{0.04}\text{O}$  sample these peaks are sharp enough to distinguish which are at 565 nm, 610 nm and 649nm, but broadening of these peaks are observed for higher Co concentration such as for 6 or 8 at.%. These absorption edges have been already explained as electronic transitions involving crystal-field-split of 3d levels in  $\text{Co}^{2+}$  ions substituting  $\text{Zn}^{2+}$  ions [15, 16]. These transitions are assigned due to  $\nu_3$  ( $\text{Co}^{2+}$ ):  $T_1(P) \leftarrow A_2(F)$  between the bands formed due to crystal field splitting [17]. These d-d transitions are possible in the  $\text{Co}^{2+}$  ion with  $3d^7$  high-spin configuration under tetrahedral crystal-field formed by neighboring  $\text{O}^{2-}$  ions. Since the spectral data show the characteristic transitions of the tetrahedrally coordinated  $\text{Co}^{2+}$  ions, it can be concluded that the  $\text{Co}^{2+}$  ions substituted the  $\text{Zn}^{2+}$  ions. This crystal-field splitting of 3d levels in  $\text{Co}^{2+}$  ions results

in the quenching of orbital angular momentum which has been discussed in course of explaining the magnetic properties in the next section.

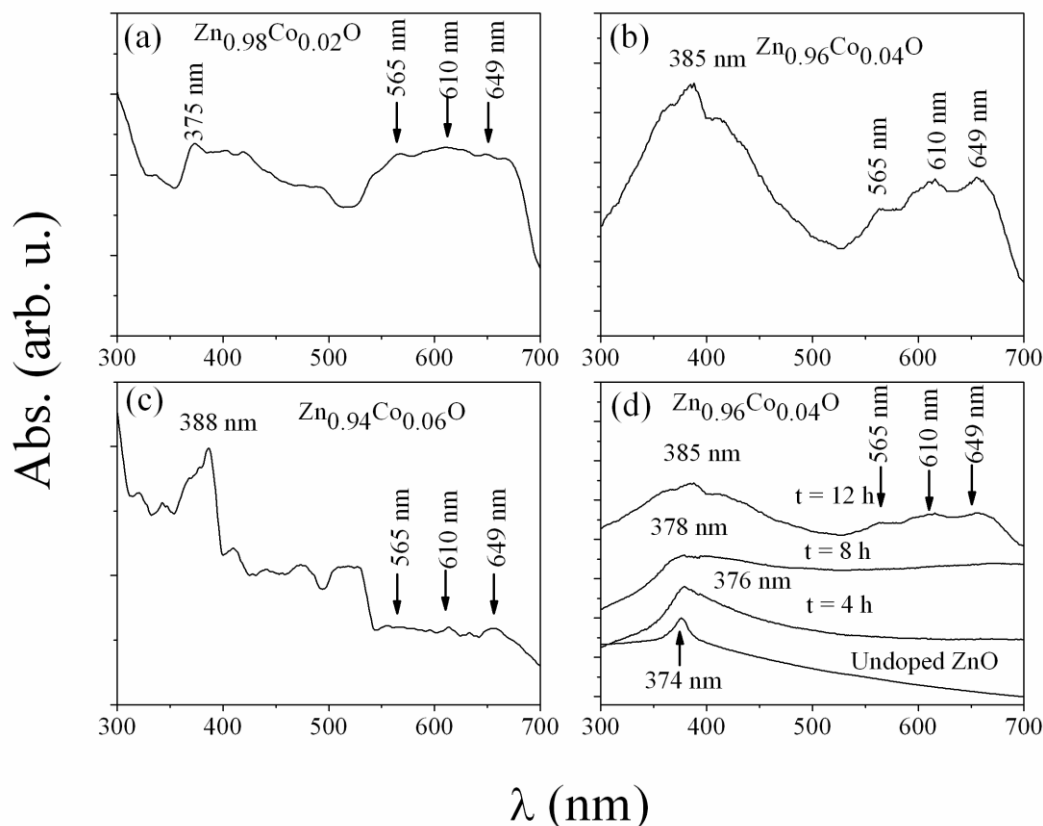


**Fig. 3.5:** UV-visible absorption spectroscopy of  $Zn_{1-x}Co_xO$  samples for (a)  $x = 0.02$ , (b)  $x = 0.04$  (c)  $x = 0.06$  and (d) evolution of spectra for  $Zn_{0.96}Co_{0.04}O$  samples with increase of milling time.

### 3.2.4 Magnetic properties of Co-doped ZnO

Magnetic measurements were performed by a Vibrating Sample Magnetometer (VSM) in the temperature range  $80K \leq T \leq 300K$ . At room temperature single-phase  $Zn_{1-x}Co_xO$  samples show the paramagnetic behavior with no indication of ferromagnetism as shown in Fig. 3.6 (a). The same behavior has also been observed for magnetization curve measured at 80 K and presented in Fig. 3.6 (b) indicating that no ferromagnetic transition is observed between room and low temperatures. As no other secondary phase is detected in the XRD pattern, the paramagnetism is the result of incorporation of  $Co^{2+}$  ions into the ZnO lattice. Although it is evident from the UV-visible absorption measurement that  $Co^{2+}$  ions

substitute for  $\text{Zn}^{2+}$  ions, ferromagnetism is not observed. This result is in good agreement with the results of M. Bouloudenine et al. [18] and Risbud et al. [19].

Figure 3.7 shows the magnetization curve for the initial CoO and  $\text{Zn}_{0.96}\text{Co}_{0.04}\text{O}$  at different milling time (t) and finally the undoped 12 h milled ZnO. It is noticeable that the nature of the magnetization curve for the 1 h and 4 h milled ZnO: Co (4%) is similar to that of the initial CoO with reduced magnetic moment due to the presence of small amount of CoO. It is expected because initially all  $\text{Co}^{2+}$  ions do not substitute for  $\text{Zn}^{2+}$  up to 4 h milling which is also evident from Fig. 3.2 (a). Now beyond 4 h milling time the replacement process of  $\text{Zn}^{2+}$  ions by  $\text{Co}^{2+}$  ions has started and the paramagnetic nature has begun to develop which are observable for 8 h and 12 h milled samples. We have also milled ZnO alone for 12 h through the same process and the magnetization curve show the diamagnetic nature like ZnO before milled. It states that no change of magnetic nature is observed due to structural change of ZnO during milling. Therefore this gradual development of paramagnetism with milling time shows that Co-doped ZnO with sufficient milling time is paramagnetic which originate due to the interaction between  $\text{Co}^{2+}$  ions replacing the  $\text{Zn}^{2+}$  ions. However, when the magnetization of the doped samples are plotted in unit of Bohr magneton per  $\text{Co}^{2+}$  ion, as shown in the inset of Fig. 3.6 (a), it is observed that the magnetization per  $\text{Co}^{2+}$  ion decreases with the increase of Co concentration. Therefore the effective magnetic moment ( $\mu_{\text{eff}}$ ) of  $\text{Co}^{2+}$  ion plotted in the inset of Fig. 3.6 (b) shows a rapid decrease with increasing Co concentration. This decrease in effective moment of  $\text{Co}^{2+}$  ion can be understood by considering the symmetry of the Co site inside the ZnO host lattice. The magnetic moment of the  $\text{Co}^{2+}$  can vary depending on the ion environment. The degree of symmetry of Co site determines the electronic levels splitting and the orbital contribution to the cation magnetic moment [20, 21], while the spin remains about constant with  $S=3/2$ . An increase in Co concentration can yield to lattice distortion decreasing the site symmetry and modifying the orbital magnetic moment. Actually, the Co site symmetry determines the shape of the bands in the optical absorption spectra, in agreement with the optical spectra presented in Fig. 3.5 where the spectral shape changes with the Co concentration.

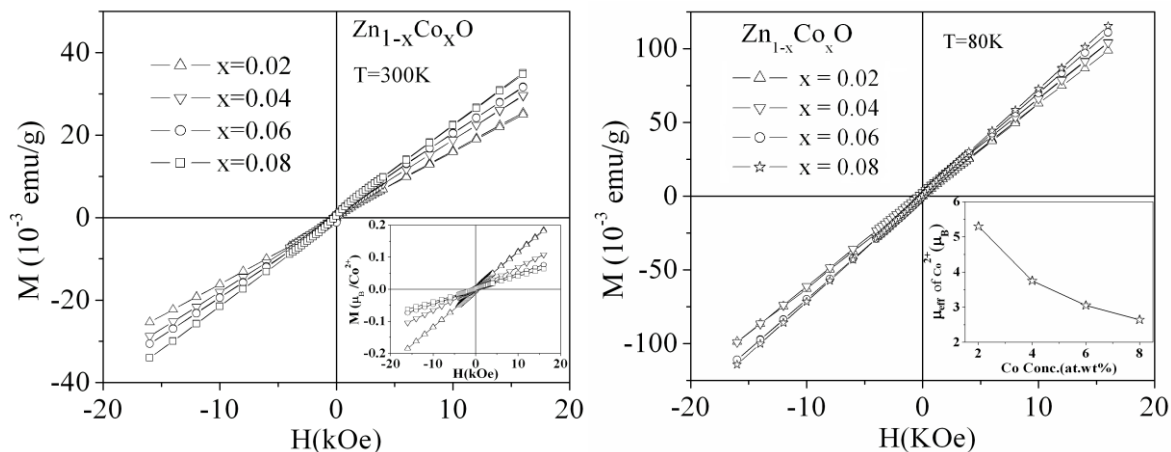


**Fig. 3.6:** Variation of magnetization ( $M$ ) as a function of magnetic field ( $H$ ) of  $Zn_{1-x}Co_xO$  at (a) 300K, Inset: the magnetization per  $Co^{2+}$  ion for doped samples (b) 80K, Inset: the change in effective magnetic moment of  $Co^{2+}$  ion with Co concentration in at. %.

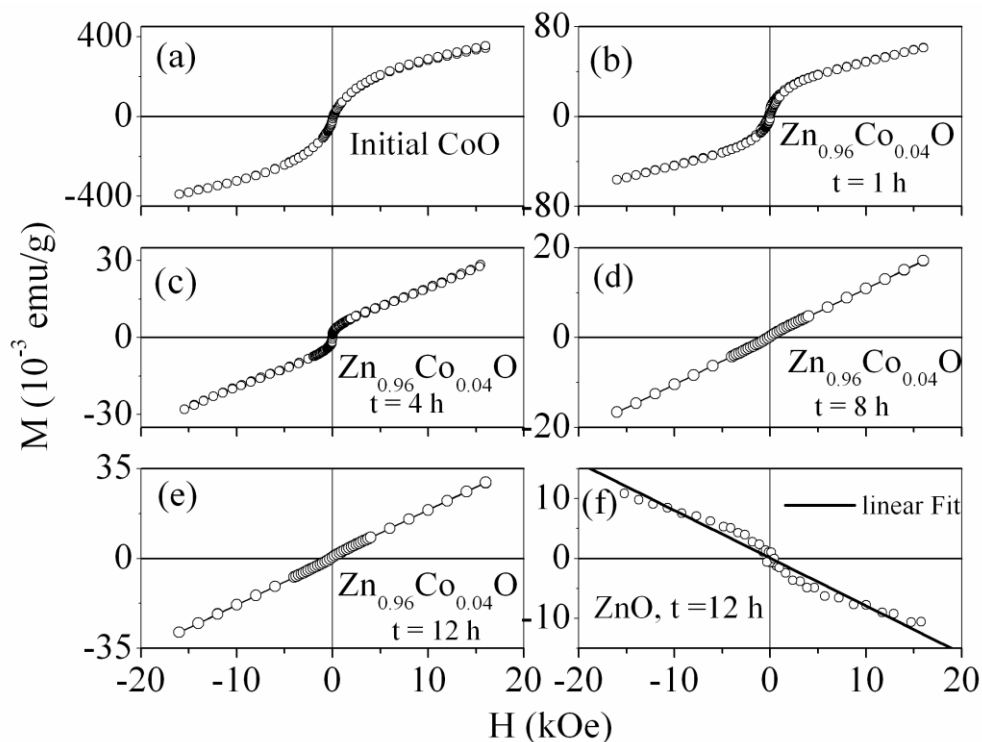


**Fig. 3.7:** Magnetization ( $M$ ) as a function of magnetic field ( $H$ ) (a) for initial CoO, for  $Zn_{0.96}Co_{0.04}O$  at milling time (b)  $t = 1h$  (c)  $t = 4h$ , (d)  $t = 8h$ , (e)  $t = 12h$  and (f) for milled ZnO after  $t = 12h$ .

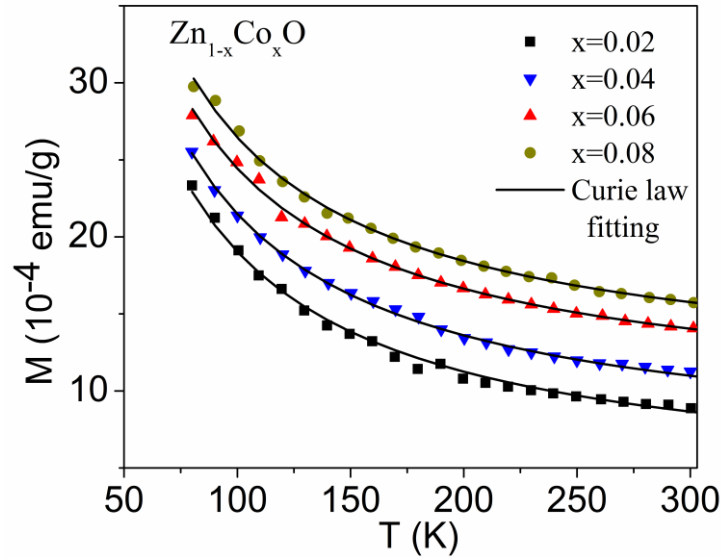


**Fig. 3.8:** Temperature dependence of magnetization ( $M$ ) for  $Zn_{1-x}Co_xO$  at  $H = 1kOe$ . Bold solid lines are the Curie's law fitting to the experimental data.

The temperature ( $T$ ) dependence of magnetic moment ( $M$ ) with a constant magnetic field of 1 kOe within  $80K \leq T \leq 350K$  is shown in Fig. 3.8. It is observed that the thermal dependence magnetization fits excellently with Curie's law for paramagnetism for all doped samples. The temperature dependence of volume susceptibility ( $\chi_v$ ) for  $Zn_{0.96}Co_{0.04}O$  within the temperature range  $80K \leq T \leq 300K$  is plotted in Fig. 3.9. The inset of Fig. 3.9 shows the plot of inverse susceptibility ( $1/\chi_v$ ) versus temperature ( $T$ ) which can be well fitted to a straight line which confirms paramagnetic behavior.

In a magnetic field an atom with angular momentum quantum number  $J$  has  $2J+1$  equal spaced energy levels and the paramagnetic susceptibility can be defined using Curie law as

$$\chi = N (p_{eff})^2 \mu_B^2 / 3k_B T = C/T \quad (3.1)$$

where  $C = N (p_{eff})^2 \mu_B^2 / 3k_B$  is the Curie constant,  $N$  is the number of interacting  $Co^{2+}$  ions with total angular momentum  $J$ ,  $p_{eff} = g[J(J+1)]^{1/2}$  is the effective number of Bohr magneton,  $g$  is the spectroscopic splitting factor ( $g=2.0023$  for free electrons),  $\mu_B$  is magnitude of the Bohr magnetron,  $k_B$  is the Boltzmann constant and  $T$  is the temperature in Kelvin scale. The Curie constant ( $C$ ), estimated from the inverse of the slope of the straight line is about  $0.07 \text{ erg.K/Oe}$ . Using this value of experimental Curie constant ( $C$ ) we have estimated the value of effective number of Bohr

magneton ( $p_{\text{eff}}$ ) which is  $3.75 \pm 0.1$ . It is interesting that our estimated value of  $p_{\text{eff}}$  agree well with magneton number  $p = 2[S(S+1)]^{1/2}$  which is 3.87 for  $\text{Co}^{2+}$  ions, where  $S=3/2$ , is the ground state spin for  $\text{Co}^{2+}$ . This agreement leads to the phenomenon of quenching of orbital angular momentum which is possible due to crystal-field splitting of 3d levels in the  $\text{Co}^{2+}$  ion with  $3d^7$  high-spin configurations under tetrahedral crystal-field formed by neighboring  $\text{O}^{2-}$ . The d-d transitions between the crystal-field splitted levels are already observed in optical spectroscopy (Fig. 3.5) with the appearance of three additional absorption peaks in 550-700 nm regions. It reveals that our estimation based on the simple theoretical quantum mechanical paramagnetic model between the spins of the  $\text{Co}^{2+}$  ions are successful in explaining the observed crystal-field splitting in  $\text{Co}^{2+}$  ions.

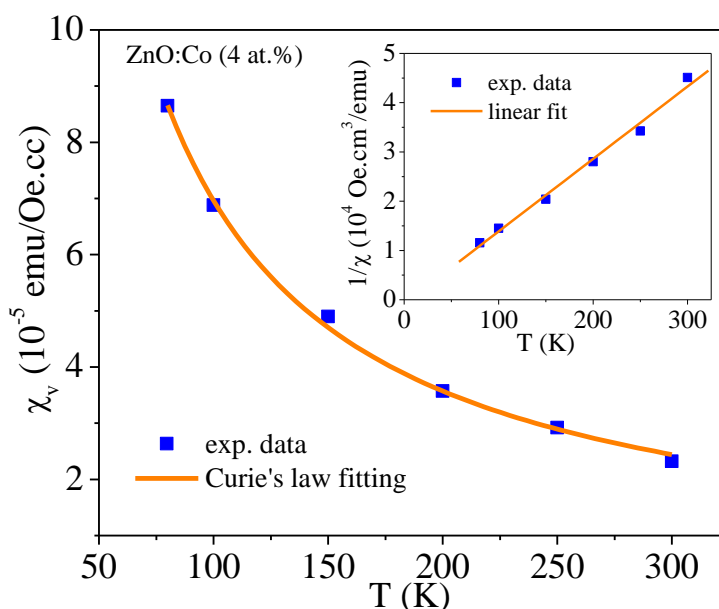


**Fig. 3.9:** Plot of magnetic volume susceptibility ( $\chi_v$ ) with temperature  $T$ , solid line represents the Curie's law fitting. Inset: Linear fitting of  $1/\chi_v$  versus  $T$  to experimental data.

Ferromagnetism in dilute magnetic semiconductors is considered to originate from the exchange interaction between free delocalized carriers (holes or electrons from the valence band) and the localized d spins of the TM ions. Therefore, the presence of free carriers becomes necessary for the ferromagnetic mediation of localized moments of  $\text{Co}^{2+}$  ions substituted in Zn site. Free carriers may be induced from other metallic secondary phases, oxygen vacancies, from defects [22] or from Co ions in another oxidation state like  $\text{Co}^{3+}$ . Here, as the valence state of both substituted Co and Zn cations are identical (+2). Therefore, the doping of Co could

not introduce any free carriers (electron/hole) in ZnO. Therefore, the absence of significant impurities or defects such as oxygen vacancies might be a possible reason for the absence of free carriers and consequently the ferromagnetism in bulk Co-doped ZnO.

### 3.3 Co-doped SnO<sub>2</sub> bulk and nanostructures: Effects of particle size and annealing

In this section, we will discuss a comparative study regarding the magnetic behavior of Co-doped SnO<sub>2</sub> in bulk and nanostructures. The effect of particle size and annealing on the magnetic behaviors of Co-doped SnO<sub>2</sub> nanorods (NRs) prepared by solvothermal synthesis (discussed in Chapter 2) will also be discussed. The bulk Sn<sub>1-x</sub>Co<sub>x</sub>O<sub>2</sub> samples are prepared by mechanical milling with 12 hrs milling time. Tin-dioxide (SnO<sub>2</sub>) also belongs to an important n-type wide band (E<sub>g</sub>~ 3.63 eV) oxide semiconductor which also presents special properties, such as optical transparency, remarkable chemical and thermal stabilities.

#### 3.3.1 Synthesis of Co-doped SnO<sub>2</sub> nanorods

As rod-shaped magnetic semiconductors are more desirable structure for applications in spintronics, we attempted to prepare rod-shaped Sn<sub>1-x</sub>Co<sub>x</sub>O<sub>2</sub> (x = 0.02 and 0.04) nanostructures by solvothermal synthesis (SS). For synthesis we have prepared two precursors (i) 0.05 M SnCl<sub>4</sub>, 5H<sub>2</sub>O and 0.0005 M CoCl<sub>2</sub>, 6H<sub>2</sub>O in 30 ml ethanol and (ii) 0.2 M NaOH in 30 ml ethanol. After 15 minutes of stirring each precursor separately, the precursor (i) is poured slowly in precursor (ii). This mixture is stirred again for 30 minutes. It is transferred to an 80 ml teflon-lined stainless steel autoclave. Then the autoclave is heated at 200°C for 10 hours. A reddish-brown precipitate is washed repeatedly by water and ethanol, and then dried in air at 80°C for 24 hours to obtain the required rod-shaped samples. In order to make bulk samples, these nanorods were sintered at high temperatures 800° C.

### 3.3.2 Synthesis of Co-doped SnO<sub>2</sub> bulk-structures

Bulk Sn<sub>1-x</sub>Co<sub>x</sub>O<sub>2</sub> samples are prepared by mechano-synthesis (MS) technique using Fritsch make (Germany) Pulverisette-7 (discussed in Chapter 2). Commercial high purity (99.999%) SnO<sub>2</sub> powder having tetragonal crystal structure (with lattice parameter as  $a = b = 4.74 \text{ \AA}$  &  $c = 3.19 \text{ \AA}$ ) and CoO were used as starting materials. A mixture of 5 gm of SnO<sub>2</sub> & CoO powders were taken in the vials with rotational frequency of 800 rpm. The mixtures were milled for 12 hours with powder: ball ratio as 1:10 by weight. After that the compounds are sintered in air at 700°C for 1hrs to obtain the single-phase samples. Three Sn<sub>1-x</sub>Co<sub>x</sub>O<sub>2</sub> samples are prepared with different Co concentration such as  $x = 0.02, 0.05$  and  $0.08$ .

### 3.3.3 Results and discussion

#### 3.3.3.1 Morphology and crystal structure

The X-ray diffraction patterns of Sn<sub>1-x</sub>Co<sub>x</sub>O<sub>2</sub> ( $x = 0, 0.02$  and  $0.04$ ) nanorods prepared by solvothermal synthesis (SS) are shown in Fig. 3.10. All XRD peaks correspond to tetragonal (rutile cassiterite) SnO<sub>2</sub>, indicating no other impurity phases like metallic Co, CoO or Co<sub>3</sub>O<sub>4</sub> present in our samples. The XRD peaks of as prepared samples also show the large full width at half maximum (FWHM) which indicates the formation of nanostructures. But the samples sintered at 800° C have relatively small FWHM and consequently larger particle size close to bulk state. Bulk Sn<sub>1-x</sub>Co<sub>x</sub>O<sub>2</sub> ( $x = 0.02, 0.05$  and  $0.08$ ) samples by mechanosynthesis (MS) route and the corresponding XRD pattern are presented in Fig. 3.11(a). The lattice parameters of the undoped and Co doped SnO<sub>2</sub> are estimated from the XRD peak positions using the Bragg's law  $2d\sin\theta = n\lambda$ , where  $\theta$  is the peak position,  $\lambda$  is the wave length of X-rays and  $d$  is the interplanar spacing defined as  $1/d^2 = (h^2+k^2)/a^2 + l^2/c^2$  for tetragonal crystal structures, where (h, k, l) the miller indices of the crystallographic planes,  $a$  and  $c$  are the lattice parameters of the tetragonal structures. The variation of lattice volumes of the Co-doped samples is shown in the inset of Fig. 3.11(b). It is important to observe that the lattice volume decreases considerably for doped samples prepared by both processes. This contraction in lattice volume with the increase in Co concentration can be understood by the incorporation of smaller Co<sup>2+</sup> ions ( $0.6 \text{ \AA}$ ) replacing larger Sn<sup>4+</sup> ions ( $0.69 \text{ \AA}$ ) in tetragonal host semiconducting SnO<sub>2</sub> lattice structure in agreement with what reported for Co doped with other

semiconducting oxides [23, 24]. The crystallite sizes ( $t$ ) are also estimated for all the samples using the Debye-Sherrer formula and presented in Table.1. It is noticeable that the crystallite sizes are increased significantly after sintering the as-prepared nanostructures prepared by SS which indicates a transformation from nano-state to corresponding bulk state.

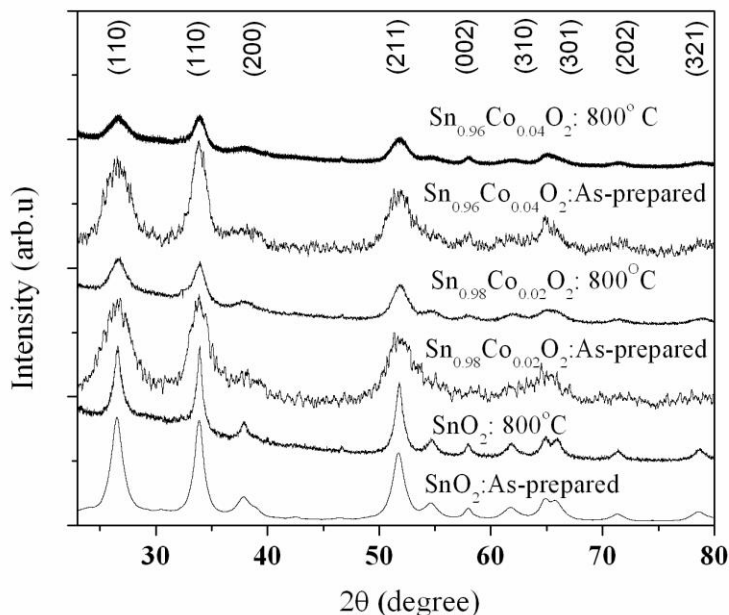


**Fig. 3.10:** X-ray diffraction pattern of as-prepared and sintered (800° C)  $\text{SnO}_2$  and  $\text{Sn}_{1-x}\text{Co}_x\text{O}_2$  obtained by solvothermal synthesis.

**TABLE I.** Some typical estimated values of lattice parameters ( $\text{\AA}$ ), lattice volumes ( $\text{\AA}^3$ ), and crystallite sizes (nm) for undoped  $\text{SnO}_2$  and  $\text{Sn}_{1-x}\text{Co}_x\text{O}_2$  samples prepared by SS and MS.

Synthesis process	Samples	Lattice parameters			Crystallite sizes (nm)	
		a=b ( $\text{\AA}$ )	c ( $\text{\AA}$ )	Lattice volume V ( $\text{\AA}^3$ )	As-prepared	Sintered
SS	$\text{SnO}_2$	$4.74 \pm 0.005$	$3.19 \pm 0.005$	71.7	$11.0 \pm 0.5$	$59.0 \pm 0.5$
	$\text{Sn}_{0.98}\text{Co}_{0.02}\text{O}_2$	$4.73 \pm 0.005$	$3.18 \pm 0.005$	71.2	$4.5 \pm 0.5$	$20.0 \pm 0.5$
	$\text{Sn}_{0.96}\text{Co}_{0.04}\text{O}_2$	$4.72 \pm 0.005$	$3.18 \pm 0.005$	70.8	$5.0 \pm 0.5$	$22.0 \pm 0.5$
MS	$\text{SnO}_2$	$4.74 \pm 0.005$	$3.19 \pm 0.005$	71.7	$91.0 \pm 0.5$	
	$\text{Sn}_{0.98}\text{Co}_{0.02}\text{O}_2$	$4.73 \pm 0.005$	$3.18 \pm 0.005$	70.2	$39.0 \pm 0.5$	
	$\text{Sn}_{0.95}\text{Co}_{0.05}\text{O}_2$	$4.72 \pm 0.005$	$3.18 \pm 0.005$	70.8	$33.0 \pm 0.5$	
	$\text{Sn}_{0.92}\text{Co}_{0.08}\text{O}_2$	$4.72 \pm 0.005$	$3.18 \pm 0.005$	70.8	$46.0 \pm 0.5$	

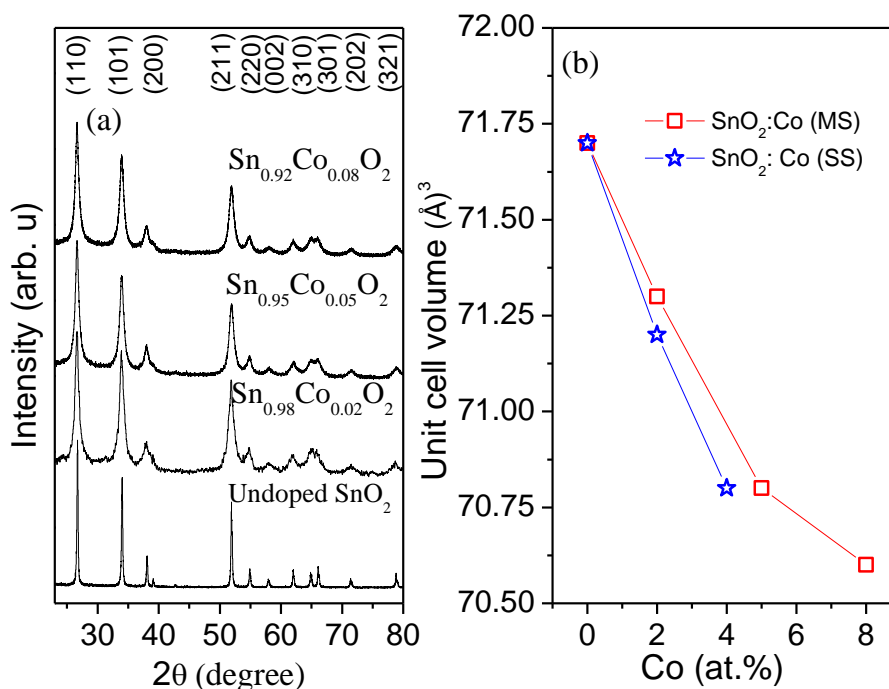


**Fig 3.11:** (a) X-ray diffraction pattern of bulk  $\text{SnO}_2$  and  $\text{Sn}_{1-x}\text{Co}_x\text{O}_2$  prepared by MS route and (b) variation of unit cell volume ( $\text{\AA}^3$ ) for  $\text{Sn}_{1-x}\text{Co}_x\text{O}_2$  obtained by both solvothermal (SS) and mechano-synthesis (MS) route with Co concentration.

Transmission electron microscopy (TEM) image, shown in Fig. 3.12 indicates the rod-like morphology of nanosized (a) pure and (d)  $\text{Sn}_{0.98}\text{Co}_{0.02}\text{O}_2$  nanorods. The dimension of  $\text{SnO}_2$  nanorods is found to reduce significantly after Co-doping. High-resolution TEM (HRTEM) and selected area diffraction pattern (SAED) of pure  $\text{SnO}_2$  shown in (b) and (c) indicates the single crystalline growth of pure  $\text{SnO}_2$  nanorods. However,  $\text{Sn}_{0.98}\text{Co}_{0.02}\text{O}_2$  nanorods are found to be polycrystalline in nature.

The scanning electron microscopy (SEM) images, shown in Fig 3.12 (f)-(g) shows the morphology of pure and  $\text{Sn}_{0.98}\text{Co}_{0.02}\text{O}_2$  after annealing in  $\text{O}_2$  at  $800^\circ\text{C}$ . It can be seen that the as-prepared  $\text{SnO}_2$  nanorods are converted to the corresponding bulk state with irregular morphologies after sintering at  $800^\circ\text{C}$  where as the as-prepared  $\text{Sn}_{0.98}\text{Co}_{0.02}\text{O}_2$  nanorods forms near spherical particle of micrometer size. Similar results are also obtained for as-prepared  $\text{Sn}_{0.96}\text{Co}_{0.04}\text{O}_2$  nanorods. The SEM image of bulk  $\text{Sn}_{0.98}\text{Co}_{0.02}\text{O}_2$  prepared by mechanical milling process is shown in Fig. 3.12 (i) which indicates the samples are mostly homogeneous and no sign of Co accumulation.

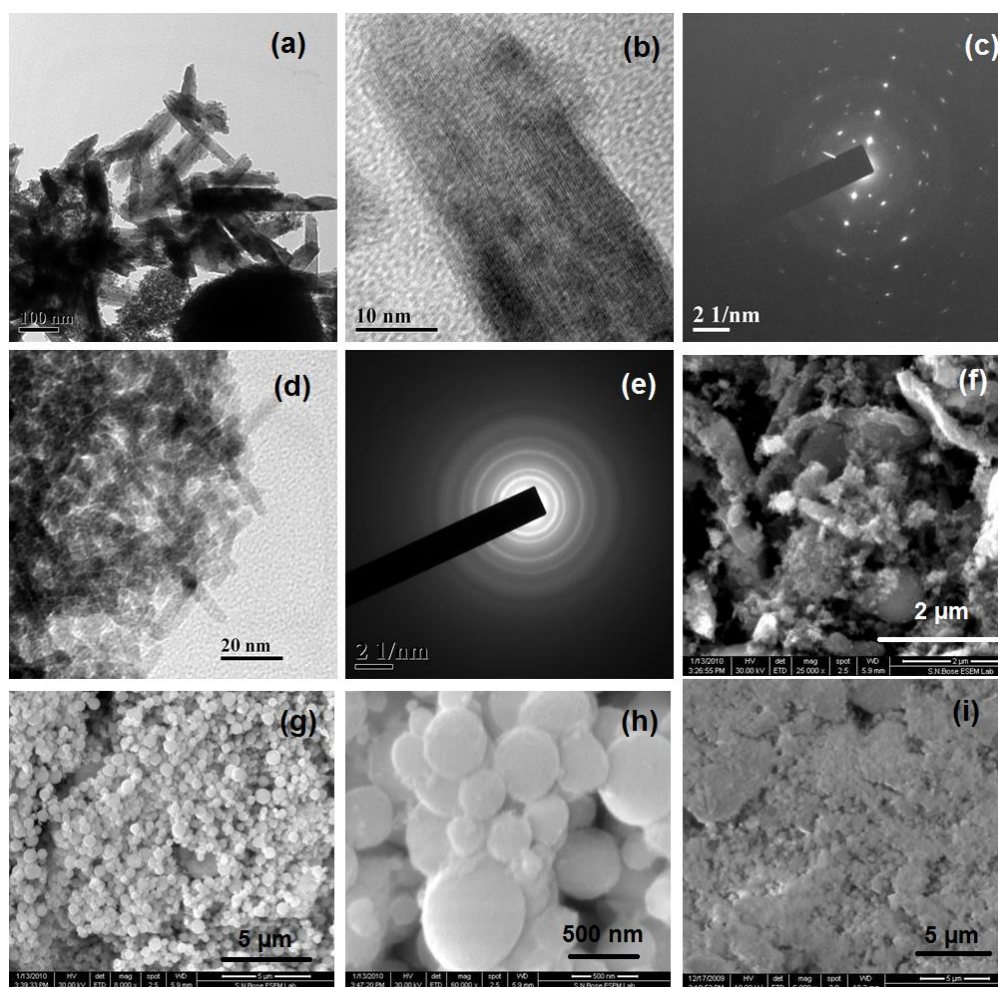


**Fig. 3.12:** (a) TEM (b) HRTEM image and (c) SAED pattern of undoped  $\text{SnO}_2$ , (d) TEM and (e) SAED pattern of  $\text{Sn}_{0.98}\text{Co}_{0.02}\text{O}_2$  nanorods, SEM images of (f) pure and (g)  $\text{Sn}_{0.98}\text{Co}_{0.02}\text{O}_2$  after annealing ( $800^\circ\text{C}$ ), (h) high magnification image of (g) and (i) SEM image of bulk  $\text{Sn}_{0.98}\text{Co}_{0.02}\text{O}_2$  prepared by mechanical milling process.

### 3.3.3.2 UV-visible absorption spectroscopy of Co-doped $\text{SnO}_2$ bulk and nanorods

It is very essential to confirm whether  $\text{Sn}^{4+}$  ions are replaced by  $\text{Co}^{2+}$  ions in our Co-doped samples and the change in semiconductor energy band-gap is a signature for this substitution. The variation of band gap with Co substitution is studied at room temperature by conventional ultraviolet-visible (UV) spectrometer and the absorption spectra of the doped samples are shown in Fig. 3.13. The value of energy band gap is estimated according to the formula  $\alpha h\nu = \text{const} (h\nu - E_g)^{1/2}$ , where  $h$  is Planck's constant and  $\nu$  is the frequency of the incident photon. The estimated values of band gap ( $E_g$ ), obtained by extrapolating the Tauc plot  $(\alpha h\nu)^2$  versus  $h\nu$  curves, and are provided in the inset of Fig. 3.13. The estimated energy band gap for

undoped  $\text{SnO}_2$  is  $E_g \sim 3.85$  eV and is in agreement with that reported in literature [25]. But in case of Co doped samples this energy band gap ( $E_g$ ) decreases which signifies the influence of incorporated Co on the electronics states, as reported earlier [26]. The amount of decrease in band gap is also depends on the Co concentration. This observed redshift in energy band gap can be explained on the basis of the sp-d exchange interactions between the band electrons and the localized d electrons of the  $\text{Co}^{2+}$  ions substituting  $\text{Sn}^{4+}$  ions [27, 28]. The s-d exchange interactions give rise to a negative correction to conduction-band edge whereas the p-d exchange interaction lead to a positive correction to the valence band edges, resulting a decrease in band gap [29].

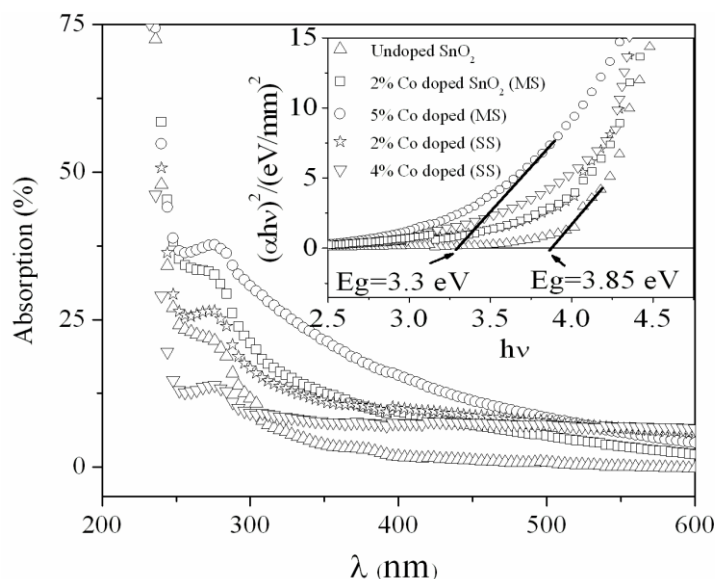


**Fig. 3.13:** Relative absorption (%) versus wave length of incident photons for  $\text{Sn}_{1-x}\text{Co}_x\text{O}_2$  samples. Inset: Tauc plot of  $(\alpha h\nu)^2$  as a function of photon energy ( $h\nu$ ).

### 3.3.3.3 Size dependent magnetic properties of Co-doped $\text{SnO}_2$

The magnetic properties are measured using a vibrating sample magnetometer (VSM) in the temperature range  $80 \leq T \leq 350$  K. Fig. 3.14 shows room temperature magnetization curves for (a) as-prepared and sintered  $\text{Sn}_{0.98}\text{Co}_{0.02}\text{O}_2$  (b) as-prepared and sintered  $\text{Sn}_{0.96}\text{Co}_{0.04}\text{O}_2$  (c) as-prepared  $\text{SnO}_2$  and (d) sintered  $\text{SnO}_2$  prepared by solvothermal synthesis. It is seen that the  $M$  (H) curves of as-prepared Co doped  $\text{SnO}_2$  nanorods show ferromagnetic behaviour with hysteresis loop having coercivity ( $H_c$ )  $\sim 140$  Oe; saturation magnetization ( $M_s$ )  $\sim 12 \times 10^{-3}$  emu/g for Co concentration  $x = 0.02$  and  $H_c \sim 100$  Oe;  $M_s \sim 40 \times 10^{-3}$  emu/g for  $x = 0.04$ . At the same

time even the as-prepared  $\text{SnO}_2$  nanorods are also showing a ferromagnetic behaviour with low magnetic moment  $\sim 6 \times 10^{-3}$  emu/g which is in agreement of the results reported by A. Sundaresan *et. al.*[30]. On the other hand ferromagnetism is suppressed in  $\text{SnO}_2$  with  $\sim 500$  nm particle size due to sintering at  $800^\circ\text{C}$  for 1h and they exhibits a linear  $M(H)$  curve, a diamagnetic, in Fig. 4.5 (d), behavior as normally expected in case of  $\text{SnO}_2$ . Therefore, ferromagnetism is observed in  $\text{SnO}_2$  nanostructure whereas the corresponding bulk samples are diamagnetic. Similarly the ferromagnetism of  $\text{Sn}_{1-x}\text{Co}_x\text{O}_2$  nanostructures also vanishes in bulk samples obtained by sintering at same temperature ( $800^\circ\text{C}$ ) and show a linear paramagnetic behaviour. To check this paramagnetic behaviour of the bulk state we have also prepared bulk  $\text{Sn}_{1-x}\text{Co}_x\text{O}_2$  ( $x = 0.02, 0.05$  and  $0.08$ ) by mechanosynthesis route and the magnetization  $M(H)$  curve for all the bulk  $\text{Sn}_{1-x}\text{Co}_x\text{O}_2$  samples with different Co concentration are shown in Fig. 3.15 at  $T = 300$  K and  $80$  K. The magnetization ( $M$ ) depends linearly on magnetic field ( $H$ ) at room temperature as well as low temperature for  $x = 0.02$  and  $x = 0.05$  which indicates the paramagnetic behaviour. The Room temperature  $M(H)$  curve for  $x = 0.08$  shows linear field dependence in the higher field region whereas an 'S' shaped  $M(H)$  curve (Inset of Fig. 3.15 (a)) is observed in the low field region. Careful observation shows that there is no such significant coercivity present. It is also interesting that this effect is absent when we

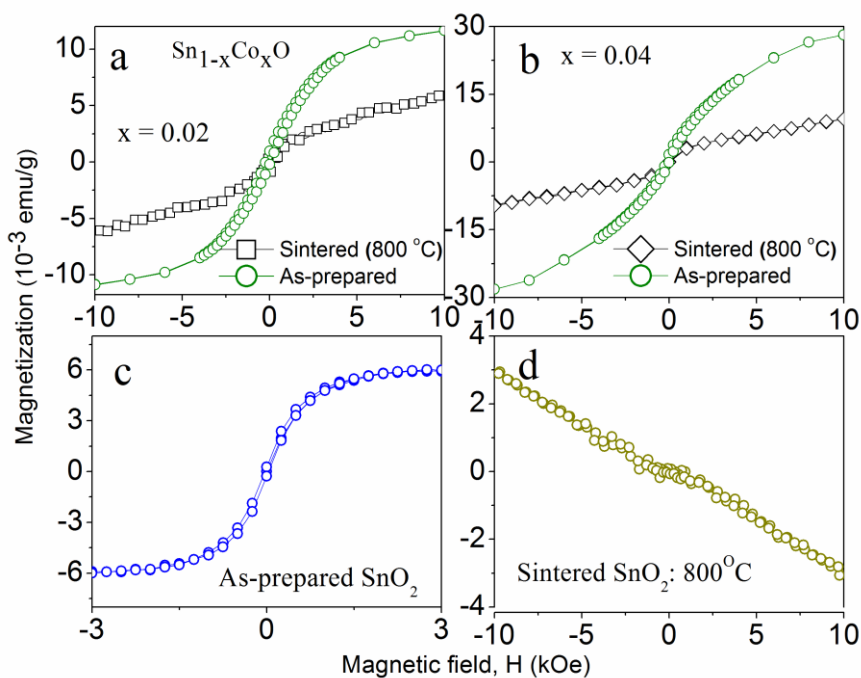


**Fig. 3.14:** Magnetization curves for (a) as-prepared and sintered  $\text{Sn}_{0.98}\text{Co}_{0.02}\text{O}_2$  (b) as-prepared and sintered  $\text{Sn}_{0.96}\text{Co}_{0.04}\text{O}_2$  (c) as-prepared  $\text{SnO}_2$  and (d) sintered  $\text{SnO}_2$  prepared by Solvothermal synthesis.

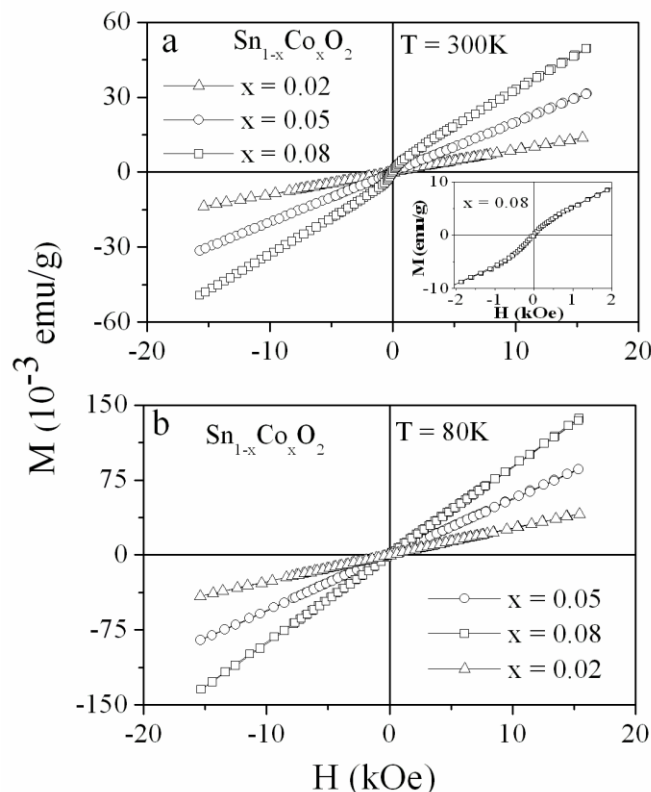


**Fig. 3.15:** Magnetization  $M(H)$  curves for  $\text{Sn}_{1-x}\text{Co}_x\text{O}_2$  prepared by MS at (a) 300 K, Inset:  $M(H)$  loop for  $x = 0.08$  in low field region and (b) 80 K.

measured  $M(H)$  curve at low temperature (80 K) which shows perfectly linear behavior. One possible reason might be presence of some non-equilibrium states in room temperature due to higher Co concentration and one might need relatively higher sintering temperature ( $>700^\circ\text{C}$ ) to obtain the required equilibrium state. The magnetic moments of the Co doped samples increases quite linearly with increasing Co concentration which demonstrates linear insertion of Co ions replacing the  $\text{Sn}^{4+}$  ions. As no other secondary or impurity phases are detected in XRD pattern (Fig. 3.11 (a)) within the detection limit of the x-ray diffractometer, paramagnetism is the results of insertion of Co ions replacing the  $\text{Sn}^{4+}$  ions.

### 3.3.3.4 Temperature dependent magnetic behavior

The thermal dependence of magnetization at constant magnetic field  $H = 1$  kOe is measured for all Co doped samples prepared under different conditions. The  $M(T)$  curves for bulk  $\text{Sn}_{1-x}\text{Co}_x\text{O}_2$  samples prepared by mechano-synthesis and bulk samples obtained by high temperature sintering prepared by solvothermal route are shown in Fig. 3.16 (a) and (c) respectively. It is seen that they can be fitted well

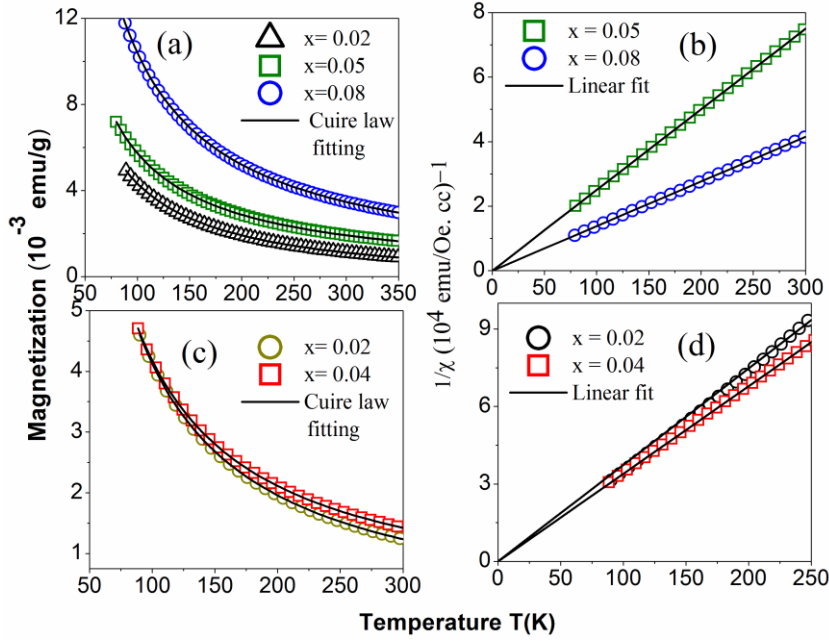


**Fig. 3.16:** Thermal dependence of  $M(T)$  and inverse susceptibility ( $1/\chi$ ) versus temperature in (a) and (b) respectively for  $\text{Sn}_{1-x}\text{Co}_x\text{O}_2$  prepared by MS and (c) and (d) respectively for bulk samples obtained by sintering ( $800^\circ\text{C}$ ) prepared by SS.

according to the magnetization for paramagnetic materials (Curie's law) for low field and high temperature limit, defined as  $M = Ng^2\mu_B^2 H J(J+1)/3k_B T = C H / T$ , where  $C = Ng^2\mu_B^2 J(J+1)/3k_B$ , the Curie constant,  $N$  is the number of interacting  $\text{Co}^{2+}$  ions with total angular momentum  $J$ ,  $g$  is the spectroscopic splitting factor ( $g = 2.0023$  for free electrons),  $\mu_B$  is the magnitude of Bohr magneton,  $k_B$  is the Boltzmann constant and  $T$ , the temperature in Kelvin. The magnetic susceptibilities of these samples are estimated and the temperature variation of inverse susceptibility ( $1/\chi$ ) is plotted in Fig. 3.16 (b) and (d). The linear fitting of the inverse susceptibility passing through the origin versus temperature plots confirms the paramagnetic interaction between the Co ions. These results are in agreement with the results reported for Co doped ZnO [4, 31]. The effective magnetic moment of  $\text{Co}^{2+}$  ions inside the  $\text{Sn}_{1-x}\text{Co}_x\text{O}_2$  are also estimated using  $\mu_{\text{eff}}^2 = 3k_B T \chi / N$ , where  $\chi$  is magnetic susceptibility at temperature  $T$ . For  $\text{Sn}_{0.95}\text{Co}_{0.05}\text{O}_2$ , putting  $N = 2.04 \times 10^{20}$ ,  $k_B = 1.38 \times 10^{-16} \text{erg K}^{-1}$ ,  $\chi = 1.96 \times 10^{-6} \text{ emu cc}^{-1} \text{ Oe}^{-1}$  at  $T = 300 \text{ K}$  we have obtained effective magnetic moment  $\mu_{\text{eff}} = 3.72 \mu_B / \text{Co}^{2+}$  ion which is much less than that of full magnetic moment of  $\text{Co}^{2+}$  ( $6.63 \mu_B$ ) with  $L = 3$  and  $S = 3/2$ . In fact, it is close to the theoretical value  $3.87 \mu_B / \text{Co}^{2+}$  ion if only the spin contribution of  $\text{Co}^{2+}$  ( $J = S = 3/2$ ) is considered. This leads to the phenomenon of quenching of orbital angular momentum. Similar observations are also observed for 2% and 8% Co doped  $\text{SnO}_2$ . This quenching of

orbital angular momentum might be possible due to crystal field splitting of 3d levels of  $\text{Co}^{2+}$  ions with 3d<sup>7</sup> high-spin configuration under the crystal field formed by neighbouring  $\text{O}^{2-}$  ions which is also observed for Co doped ZnO [4, 32].

Therefore, the ferromagnetism in these Co doped  $\text{SnO}_2$  dilute magnetic semiconductor oxides is associated with only the nanostructure of these materials whereas the corresponding bulk state are paramagnetic which is intrinsic. Even the much expected diamagnetic material  $\text{SnO}_2$  show ferromagnetism in its nano-phase. The origin of ferromagnetism in these nanostructures seems to be similar to that in thin films of  $\text{TiO}_2$ ,  $\text{HfO}_2$  and  $\text{In}_2\text{O}_3$  where the oxygen deficiency results from thin film growth conditions [33, 34]. Ferromagnetic signature may also come from different sources such as ferromagnetic impurity, vacancies, interstitials and other defects and/or disorders at surfaces, interfaces, grain boundaries or inside of samples. As no impurity peaks are detected in XRD pattern, any impurity or secondary phase is not responsible for observed ferromagnetism in  $\text{SnO}_2$  and  $\text{Sn}_{1-x}\text{Co}_x\text{O}_2$  nanorods prepared by solvothermal synthesis. Additionally this ferromagnetism is suppressed when the particular nanostructure is being converted to micrometer-sized particle by sintering at 800° C. This observation helps to understand that the origin of ferromagnetism exists in the formation of nanostructure and it is possible that the unpaired electron spins responsible for ferromagnetism in the nanorods have their origin in the oxygen vacancies, especially on the surface of the nanorods. Although the nature of exchange interaction is not clear at present, one may expect that electron trapped in oxygen vacancies are polarized to give room-temperature ferromagnetism [35].

### 3.4 Cr and V-doped $\text{TiO}_2$ bulk structures

Chromium (Cr) and vanadium (V)-doped  $\text{TiO}_2$  bulk powder samples are also prepared by mechano-synthesis route and magnetic properties are studied. Similar to Co-doped ZnO and  $\text{SnO}_2$  bulk structures, no evidence of ferromagnetism are observed in  $\text{Ti}_{0.95}\text{Cr}_{0.05}\text{O}_2$  and  $\text{Ti}_{0.95}\text{V}_{0.05}\text{O}_2$  at room-temperature as well as low temperatures. A linear M-H behavior again indicates the stabilization of paramagnetism both in  $\text{Ti}_{0.95}\text{Cr}_{0.05}\text{O}_2$  and  $\text{Ti}_{0.95}\text{V}_{0.05}\text{O}_2$ . Although the substitution of  $\text{Cr}^{3+}$  and  $\text{V}^{5+}$  ions replacing  $\text{Ti}^{4+}$  cations introduces excess hole and electrons within the doped  $\text{TiO}_2$  system, still ferromagnetic exchange interaction is not to be mediated between the substituted TM ions.

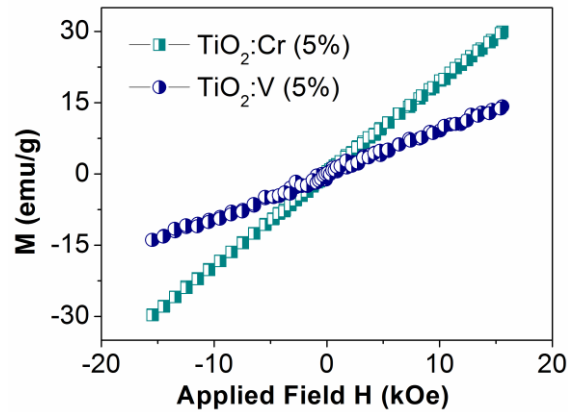


Fig. 3.17: Room-temperature M-H behavior for bulk  $\text{Ti}_{0.95}\text{Cr}_{0.05}\text{O}_2$  and  $\text{Ti}_{0.95}\text{V}_{0.05}\text{O}_2$

### 3.5 Fe and Fe-N co-doped $\text{SnO}_2$ bulk structures: Effect of excess free carriers

In last section, it is found that the doping TM (Co, Cr or V) alone could not able to stabilize ferromagnetism (FM) in TM oxides. The ab initio calculations by Sato and Katayam-Yoshida [36] have shown stabilization of ferromagnetic (FM) states in  $\text{Zn}_{1-x}\text{Mn}_x\text{O}$  by introducing holes. Recently, Peng et al. [37] pointed out that a threshold hole concentration is necessary to induce room temperature ferromagnetism (RTFM) and hole doping at anion site is more effective for localizing the hole and enhancement of hole-induced ferromagnetism in carbon (C)-doped ZnO. Due to the compensation effect and limited solubility of TM in n-type oxide semiconducting host, it is found to be difficult to achieve sufficient hole concentration.

Here, the effect of Fe-doping (alone) and Fe-N co-doping on the magnetic properties of  $\text{SnO}_2$  hosts are investigated in details [6]. Group V elements such as N, P, are known as acceptor type dopants in oxides like  $\text{SnO}_2$  [38]. Pure  $\text{SnO}_2$  is generally found to be n-type [38]. When Fe ions are substituting at Sn sites, holes will be generated but this minority carrier holes easily recombine with the majority carriers (electron), present in n-type host. Therefore, the co-doping of N at oxygen (O) site along with Fe at Sn site may be effective to stabilize significant hole concentration which may affect the magnetic behavior of the doped system.

### 3.5.1 Synthesis and characterization

All  $\text{Sn}_{1-x}\text{Fe}_x\text{O}_2$  ( $x = 0.05$  and  $0.10$ ) samples were prepared by chemical co-precipitation method. For synthesis of 5 at.% Fe doped  $\text{SnO}_2$ , we have used two precursors as (i) 0.012 M  $\text{SnCl}_4$ ,  $5\text{H}_2\text{O}$  and 0.0006 M  $\text{FeCl}_3$ ,  $6\text{H}_2\text{O}$  in 100 ml water (Precursor A) and (ii) 0.05 M  $\text{NaOH}$  in 50 ml water (Precursor B). Precursor A was then heated at  $100^\circ\text{C}$  under constant stirring and precursor B was added slowly drop by drop in boiled Precursor B using sophisticated pressure equalizer. Then the resultant solution was heated constantly for 1h at  $100^\circ\text{C}$  until a yellowish precipitate was formed which was washed repeatedly with water and ethanol and dried at  $80^\circ\text{C}$  for 24 h. The as-prepared samples were annealed at  $900^\circ\text{C}$  in a tube furnace under a continuous flow of  $\text{O}_2$  and  $\text{N}_2$  for 5h to obtain Fe-doped and Fe-N-codoped  $\text{SnO}_2$  samples respectively. The structural properties were analyzed by x-ray diffraction (XRD) using  $\text{Cu K}_\alpha$  radiation ( $\lambda = 1.540598\text{\AA}$ ), Scanning electron microscopy (SEM), Energy dispersive X-ray (EDX) spectroscopy and UV-Visible spectroscopy was used for the study optical properties. Vibrating sample magnetometer (VSM) (Lake Shore Cryotronics) and Superconducting quantum interference device (SQUID) were used for magnetic measurements within  $5\text{K} \leq T \leq 300\text{K}$ .

### 3.5.2 Experimental result and discussions

#### 3.5.2.1 Effect of dopants on structural properties

The XRD pattern of undoped and Fe-doped  $\text{SnO}_2$  samples annealed in  $\text{O}_2$  and  $\text{N}_2$  are shown in Fig. 3.18. All XRD peaks of the undoped and doped  $\text{SnO}_2$  corresponds to the tetragonal (rutile cassiterite) crystal structure. No other secondary phase or impurity peaks like metallic Fe, FeO or  $\text{Fe}_2\text{O}_3$ , iron nitride or nitrate were detected in our samples within the detection limit of X-ray diffractometer. High temperature ( $900^\circ\text{C}$ ) annealing in presence of  $\text{O}_2$  decreases the possibility of non-equilibrium structural defects or oxygen vacancy whereas N ions were doped at anion oxygen site through partial replacement of  $\text{O}^{2-}$  ions during annealing in  $\text{N}_2$  atmosphere at the same temperature. It is noticeable that the XRD peaks of all doped samples annealed at  $\text{O}_2$  and  $\text{N}_2$  atmosphere are shifted towards the lower  $2\theta$  direction (Inset of Fig. 3.18). The lattice parameters were estimated from XRD peak positions and the variation of lattice parameters with Fe concentration are shown in Fig. 3.19 (a)-(c). It is observed that the lattice parameters in both direction (a-axis and

c-axis) increases with Fe content for all doped samples annealed at O<sub>2</sub> and N<sub>2</sub> atmosphere which indicates insertion of Fe ions in SnO<sub>2</sub> lattice.

There are two major Fe ions such as Fe<sup>2+</sup> (0.77 Å) and Fe<sup>3+</sup> (0.63 Å). Fe<sup>2+</sup> ions have larger ionic radius than Sn<sup>4+</sup> (0.69 Å) ions while Fe<sup>3+</sup> have smaller ionic radius. Therefore, the expansion of lattice parameters as well as lattice volumes with Fe concentration can be understood by the incorporation of Fe<sup>2+</sup> ions replacing Sn<sup>4+</sup> (0.69 Å) ions in tetragonal host lattice. However, a contraction in lattice volume was observed in Fe doped SnO<sub>2</sub> prepared by J. F. Liu et al. [39] and was explained by the incorporation of smaller Fe<sup>3+</sup> ions replacing larger Sn<sup>4+</sup> ions. Crystallite sizes were also estimated from XRD pattern using the Scherrer formula,  $t = K\lambda/\beta\cos\theta$ , where  $t$  is the crystallite size,  $K$  is the shape factor,  $\lambda$  is the wavelength of incident X-ray radiation,  $\theta$  is the Bragg angle and  $\beta$  is the full width at half maxima (FWHM) in radian of the peak with given (h, k, l) value. The variations of crystallite sizes ( $t$ ) with

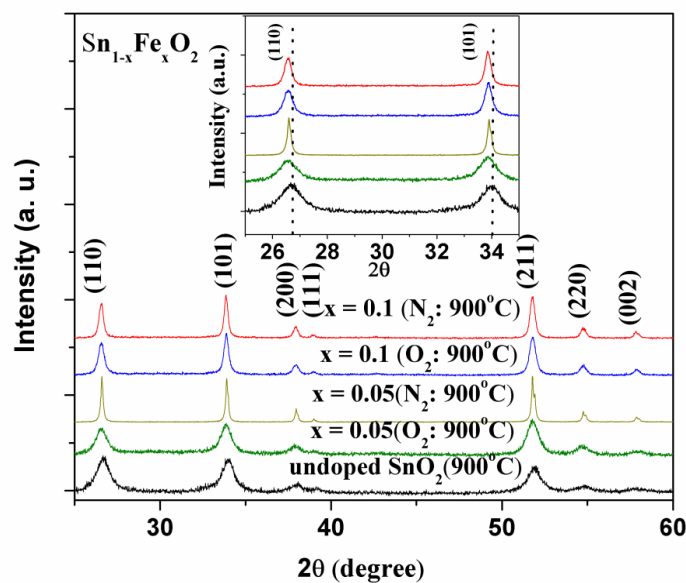


**Fig. 3.18:** XRD spectra of Sn<sub>1-x</sub>Fe<sub>x</sub>O<sub>2</sub> samples annealed (900°C) in O<sub>2</sub> and N<sub>2</sub> atmosphere. Inset: Observed shift of (110) and (101) peak position towards the lower 2θ direction for Fe doped SnO<sub>2</sub> samples.

the Fe-concentration for all samples are plotted in Fig. 3.19 (d). It is observed that Sn<sub>1-x</sub>Fe<sub>x</sub>O<sub>2</sub> samples annealed in N<sub>2</sub> atmosphere show larger crystallite sizes compared to that annealed at O<sub>2</sub> atmosphere. High temperature annealing in N<sub>2</sub>, resulting incorporation of N ions with partial replacement of O<sup>2-</sup> ions, might favour larger particle size for the preparation of equilibrium solid solution.

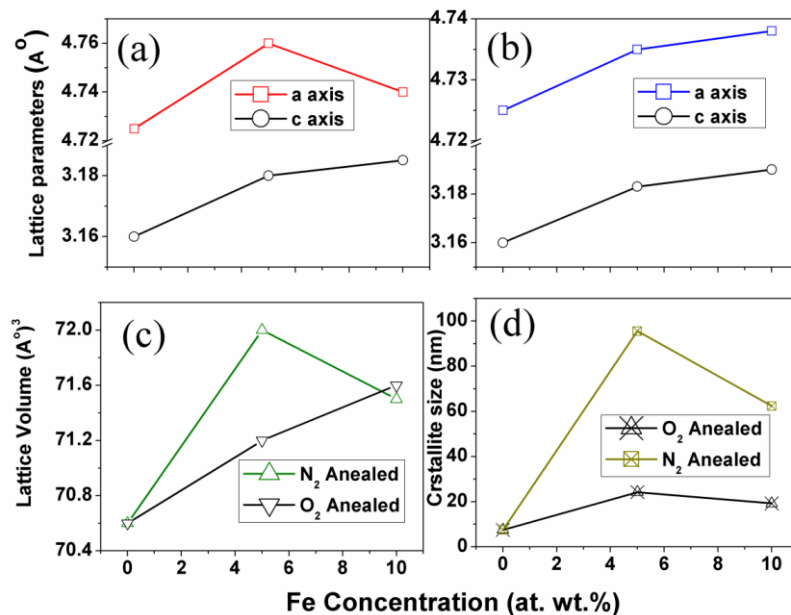


**Fig. 3.19:** Variation of lattice parameters with Fe concentration (at. wt.%) for all Fe doped SnO<sub>2</sub> samples annealed in (a) O<sub>2</sub> atmosphere (b) N<sub>2</sub> atmosphere. The variation of (c) lattice volume and (d) crystallite size are also shown.

### 3.5.2.2 SEM images and EDAX spectra

SEM images of Fe-N-codoped SnO<sub>2</sub> samples are shown in insets of Fig. 3.20 and the corresponding spot EDX pattern of N-doped Sn<sub>0.9</sub>Fe<sub>0.1</sub>O<sub>2</sub> is plotted in Fig. 3.20. Homogeneity of Fe ions in the samples was confirmed through EDAX mapping experiment which indicated uniform distribution of Fe ions and no possible accumulation of Fe ions in the samples. The peaks corresponding to Fe K and N K in EDX pattern showed the presence of Fe and N in Sn<sub>0.9</sub>Fe<sub>0.1</sub>O<sub>2</sub>. Similar results were also obtained for Sn<sub>0.95</sub>Fe<sub>0.05</sub>O<sub>2</sub>. The Fe concentration obtained from EDX analysis were 4.78 and 9.82, less than the nominal percentages 5 and 10 at. wt.% respectively whereas N concentration were of the order of 4.22 and 5.31 at. wt.% respectively. The peaks corresponding to Au M come from Au coating that was deposited over the surface of the samples before performing SEM and EDX analysis to prevent the insulating samples from the electron charging effect.

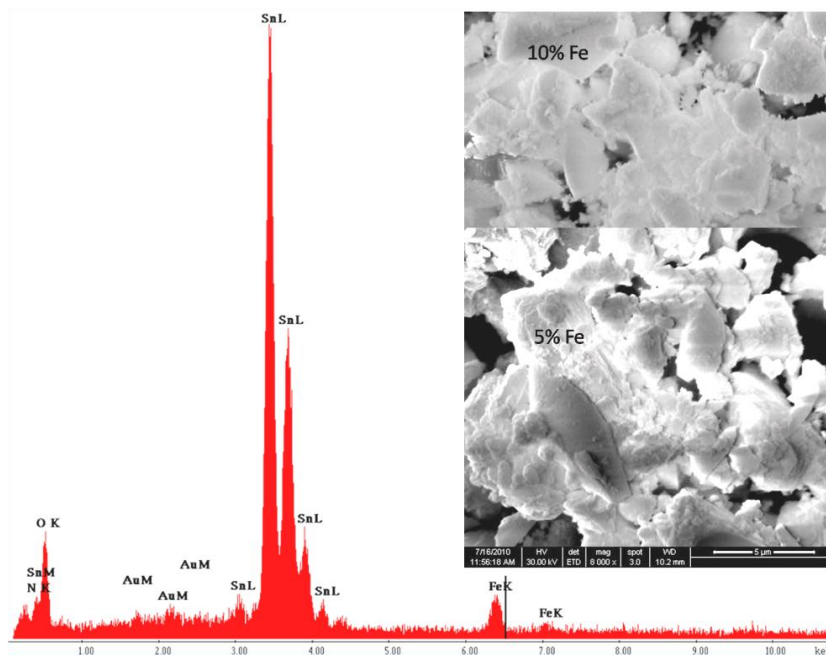


**Fig. 3.20:** EDX spectra of N<sub>2</sub> annealed Sn<sub>0.9</sub>Fe<sub>0.1</sub>O<sub>2</sub> samples. Inset: SEM images of Fe doped SnO<sub>2</sub> samples.

### 3.5.2.3 UV-visible absorption spectra

The effect of Fe incorporation replacing Sn<sup>4+</sup> ions in semiconducting SnO<sub>2</sub> host lattice can be observed from the change in energy band gap ( $E_g$ ) of SnO<sub>2</sub> as studied by UV-visible absorption spectra for undoped and Fe-N-codoped SnO<sub>2</sub> samples and they are shown in Fig. 3.21. The value of energy band gap was estimated according to the formula  $\alpha_d(h\nu) = \text{const.} (h\nu - E_g)^{1/2}$ , where  $h$  is the Plank constant,  $\nu$  is the frequency of incident photon and the absorption coefficient  $\alpha_d = \text{absorption}/d$ , where  $d$  is the thickness of the sample. The inset (i) of Fig. 3.21 shows the plot of  $\alpha_d^2(h\nu)$  versus incident photon energy ( $h\nu$ ). The estimated values of band gap ( $E_g$ ) were obtained by extrapolation as shown by dotted lines in the same inset. For undoped SnO<sub>2</sub>, the estimated value of band gap ( $E_g$ ) is  $\sim 3.72$  eV which is in agreement with that reported in the literature [40]. The variation of  $E_g$  for Fe-N-codoped samples with Fe concentration is shown in the inset (ii) of Fig. 3.21. The decrease of energy band gap with Fe concentration signifies the influence of incorporated Fe ions on the electronic states, as reported earlier for other TM doped SnO<sub>2</sub> [5, 41]. This redshift of energy band gap can be explained on the basis of the  $sp-d$  exchange interaction between the band electrons and the localized  $d$  electrons of Fe<sup>2+</sup> ions replacing Sn<sup>4+</sup> ions in semiconducting host lattice [42-43]. The  $s-d$  exchange interactions give rise to negative corrections to conduction band edge

whereas the p-d exchange interaction lead to positive correction to the valance band edge which results in a decrease in band gap [44].

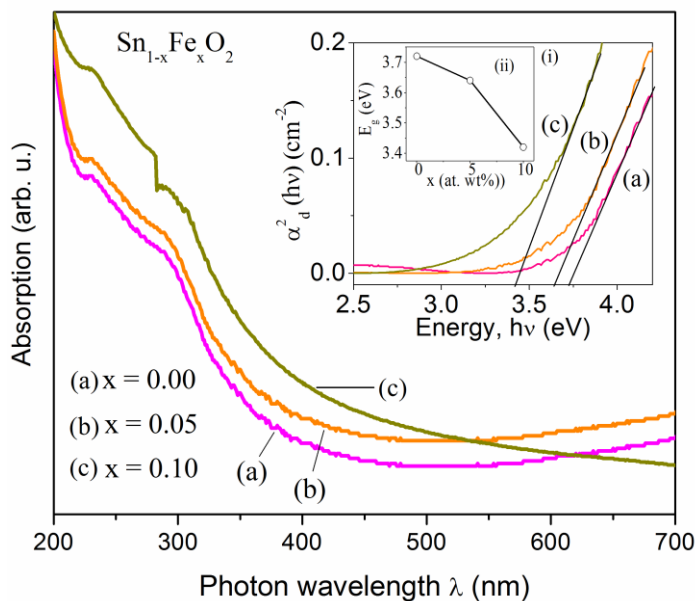


**Fig. 3.21:** UV-visible absorption spectra for all Fe doped  $\text{SnO}_2$  with N co-doping. Inset (i): plot of  $\alpha^2(h\nu)$  as a function of photon energy ( $h\nu$ ) and Inset (ii): change in energy band gap ( $E_g$ ) with Fe concentration ( $x$ ).

### 3.5.2.4 Field dependent magnetization, $M$ (H) measurements

Magnetic properties of all  $\text{Sn}_{1-x}\text{Fe}_x\text{O}_{2-\delta}\text{N}_\delta$  samples were measured using VSM and SQUID magnetometer above and below room temperature respectively. Fig. 3.22 (a) shows the field dependence of magnetization,  $M$  (H) curves at 300 K and 80 K (in inset) for  $\text{Sn}_{1-x}\text{Fe}_x\text{O}_2$  annealed in presence of  $\text{O}_2$ . The undoped  $\text{SnO}_2$  shows a linear  $M$  (H) with negative slope which represents the diamagnetic behaviour as normally expected in case of  $\text{SnO}_2$ . But in case of Fe doped  $\text{SnO}_2$  samples, the linear behavior of  $M$  (H) with positive slope signifies absence of any ferromagnetic interaction between  $\text{Fe}^{2+}$  ions and rather a paramagnetic like interaction is observed which is in agreement with the results obtained by Q. Xu et al. [45] and also with our previous work [4, 5]. It is noticeable from Fig. 4.12 (a) that magnetization ( $M$ ) is not proportional to Fe ions concentration changing from 5 to 10 at. wt.% which indicates the presence of antiferromagnetic interaction for higher Fe concentration. In fact, this antiferromagnetic exchange interaction is further confirmed through temperature dependent magnetization  $M$  (T) measurement, highlighted in the next section. Even at low temperature (80 K), paramagnetic interactions are much stronger and no ferromagnetic transition is observed in between  $80 \text{ K} \leq T \leq 300 \text{ K}$ .

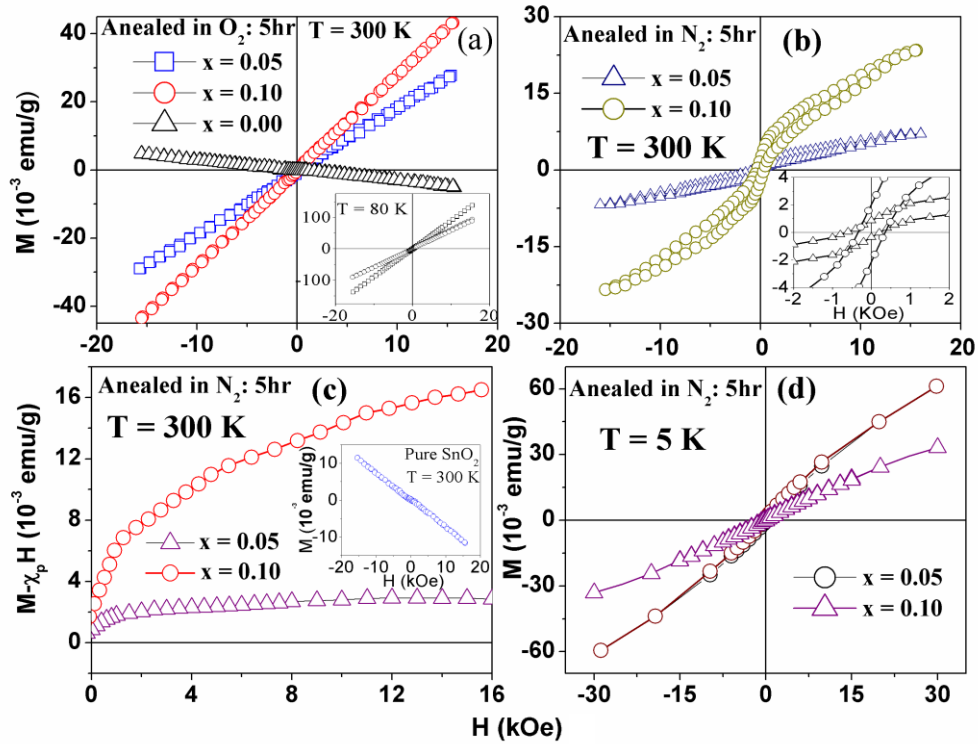


**Fig. 3.22:** Magnetization  $M(H)$  curve for  $\text{Sn}_{1-x}\text{Fe}_x\text{O}_2$  (a) annealed in  $\text{O}_2$  at 300 K (Inset: at 80 K), (b) annealed in  $\text{N}_2$  at 300 K (Inset:  $M(H)$  at low field region), (c) plot of  $(M - \chi_p H)$  versus  $H$  at 300 K (inset:  $M(H)$  for pure  $\text{SnO}_2$  annealed in  $\text{N}_2$ ) and (d)  $M(H)$  curve obtained at 5 K for Fe doped  $\text{SnO}_2$  samples annealed in  $\text{N}_2$ .

High temperature annealing at  $\text{O}_2$  atmosphere removes the possible oxygen vacancies or any structural defects which might have developed during synthesis process. But interestingly, in case of  $\text{Sn}_{1-x}\text{Fe}_x\text{O}_2$  samples annealed at  $\text{N}_2$  atmosphere clear hysteresis loops are observed at 300 K and 5 K as shown in Fig. 3.22 (b) and (d) respectively. The coercivity ( $H_c$ ) and retentivity ( $M_r$ ) are  $\sim 352$  Oe and  $2.1 \times 10^{-3}$  emu/g for  $x = 0.10$  respectively and  $\sim 420$  Oe and  $6.3 \times 10^{-4}$  emu/g respectively for  $x = 0.05$ . The magnetization curves in Fig. 3.22 (b) are not saturated properly and an upward linear slope at higher field is observed which indicates a dominant paramagnetic contribution at higher magnetic field. This paramagnetic susceptibility ( $\chi_p$ ) at higher field is also estimated from the temperature dependence of magnetization ( $M(T)$ ) curve. This high field paramagnetic moment ( $\chi_p H$ ) is subtracted from the magnetization  $M(H)$  and the plot of ferromagnetic moment ( $M - \chi_p H$ ) with  $H$  is shown in Fig. 3.22 (c). From this figure, it is observed that the  $(M - \chi_p H)$  curves almost saturates above 10 kOe with saturation magnetization  $M_s \sim 16 \times 10^{-3}$  emu/g and  $2.5 \times 10^{-3}$  emu/g for  $x = 0.10$  and 0.05 respectively. Although the ferromagnetic saturation magnetization ( $M_s$ ) increases with Fe concentration,

coercivity decreases. Similarly the  $M(H)$  curves at 5 K also show the hysteresis loops but with much higher saturation magnetization.

### 3.5.2.5 ZFC and FC measurements for $O_2$ annealed $Sn_{1-x}Fe_xO_2$

The temperature dependence magnetization  $M(T)$  for all  $Sn_{1-x}Fe_xO_2$  samples was also measured for detailed magnetic characterization. The field-cooled (FC) and zero field-cooled (ZFC) curves at  $H = 8$  kOe for  $Sn_{1-x}Fe_xO_2$  samples annealed in  $O_2$  atmosphere are shown in of Fig. 3.23. It is clear from these figures that the FC and ZFC curves are retracing the same path which indicates a paramagnetic behaviour. The FC curves are also fitted according to the modified Cuire-Weiss law  $\chi = M(T)/H = \chi_0 + C/(T+\theta)$ , where  $\chi_0 = 1.1 \times 10^{-6}$  represents weak non-paramagnetic susceptibility,  $C = N\mu^2/3k$  is the curie constant which represents the paramagnetic ion concentration ( $N$  = number of magnetic ions/g,  $\mu$  = magnetic moment of the ion and  $k$  = Boltzman constant),  $T$  is the temperature in K and  $\theta$  is the Curie-Weiss temperature which represents the magnetic exchange interactions between the spins. These fits yields  $\theta = 4.06$  and  $3.86$  K, and  $C = 2 \times 10^{-4}$  and  $0.2 \times 10^{-4}$  emu K/g Oe for  $x = 0.10$  and  $0.05$  respectively. The positive value of Curie-Weiss temperature ( $\theta$ ) signifies antiferromagnetic exchange interaction between the  $Fe^{2+}$  ions.  $Fe^{2+}-O^{2-}-Fe^{2+}$  superexchange interaction might be the possible origin of antiferromagnetism whereas the  $Fe^{2+}-Fe^{2+}$  direct interaction is paramagnetic.

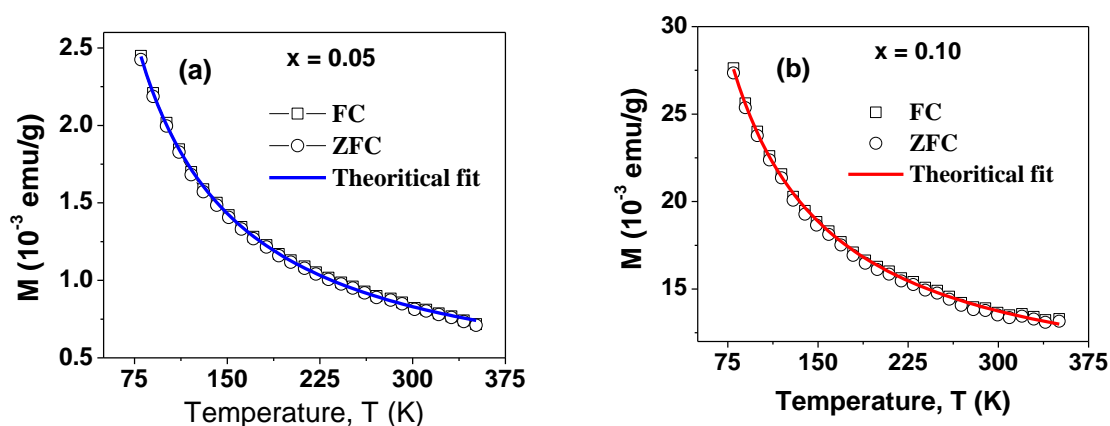


**Fig. 3.23:** ZFC and FC curves for  $Sn_{1-x}Fe_xO_2$  annealed in  $O_2$ . The solid lines are theoretical fitting according to modified Cuire-Weiss law.

### 3.5.2.6 ZFC and FC measurements for N<sub>2</sub> annealed Sn<sub>1-x</sub>Fe<sub>x</sub>O<sub>2</sub>

Fig. 3.24 show ZFC-FC curves at constant magnetic field  $H = 8$  kOe for Sn<sub>1-x</sub>Fe<sub>x</sub>O<sub>2</sub> samples annealed at N<sub>2</sub> atmosphere and the corresponding insets show the high temperature magnetization  $M$  ( $T$ ) curves. The difference between ZFC and FC magnetization indicate the hysteresis behavior. The theoretical fitting of FC magnetization according to modified Curie-Weiss law yields  $\theta = -14.6$  and  $-6.9$  K for  $x = 0.05$  and  $0.10$  respectively. These negative values of Curie-Weiss temperature ( $\theta$ ) also indicate ferromagnetic exchange interaction between the spins of Fe<sup>2+</sup> ions in Sn<sub>1-x</sub>Fe<sub>x</sub>O<sub>2- $\delta$</sub> N <sub>$\delta$</sub>  samples. The high temperature  $M$  ( $T$ ) curves of respective Sn<sub>1-x</sub>Fe<sub>x</sub>O<sub>2- $\delta$</sub> N <sub>$\delta$</sub>  samples are shown in the inset of Fig. 3.24. The estimated values of Curie temperature ( $T_c$ ) obtained from these high temperature measurement are  $\sim 431$  and  $464$  K for  $x = 0.05$  and  $0.10$  respectively. The Curie temperature ( $T_c$ ) is found to be increasing with Fe concentration in N doped Sn<sub>1-x</sub>Fe<sub>x</sub>O<sub>2</sub> samples. Another ferromagnetic transition temperature is also observed from the fitting of Curie-Weiss law to the FC experimental data for N doped Sn<sub>1-x</sub>Fe<sub>x</sub>O<sub>2</sub> samples and the possible reason might be the presence of weak ferromagnetic interaction between N defects below the transition temperatures ( $14.6$  and  $6.9$  K for  $x = 0.05$  and  $0.1$  respectively). It is possible because N defect at O site behaves as an acceptor which also has a magnetic moment of the order of  $\mu_B$ . Now depending on the degree of localization of the acceptor and the distance between two neighbouring N defects, a weak ferromagnetic interaction between them might be possible especially at very low temperature in our powder samples. This type of d<sup>0</sup> ferromagnetism was reported in N doped ZnO and MgO thin film at room temperature [46, 47].

As no other secondary or impurity phase is detected in XRD analysis and the presence of N in Fe doped SnO<sub>2</sub> is confirmed by EDX analysis, ferromagnetic interaction between Fe ions might be mediated through these holes due to N defect. SnO<sub>2</sub> is intrinsically an n-type semiconductor and although Fe doping in SnO<sub>2</sub> generates both magnetic moment as well as holes in this system, ferromagnetism is not observed. Due to the compensation effect and limited solubility limit of TM ions, the sufficient hole concentration needed to turn on the FM [37] is very difficult in case of these oxide semiconductor. Additional N doping at anion site replacing O<sup>2-</sup> ions might be very effective to achieve the required threshold hole concentration and stabilize hole-mediated ferromagnetism, as observed in our Fe-N-codoped SnO<sub>2</sub>. On the other hand, we have not observed any ferromagnetism in N-doped SnO<sub>2</sub> powder at room temperature (300 K) prepared under same condition (inset of Fig. 3.22 (c)).

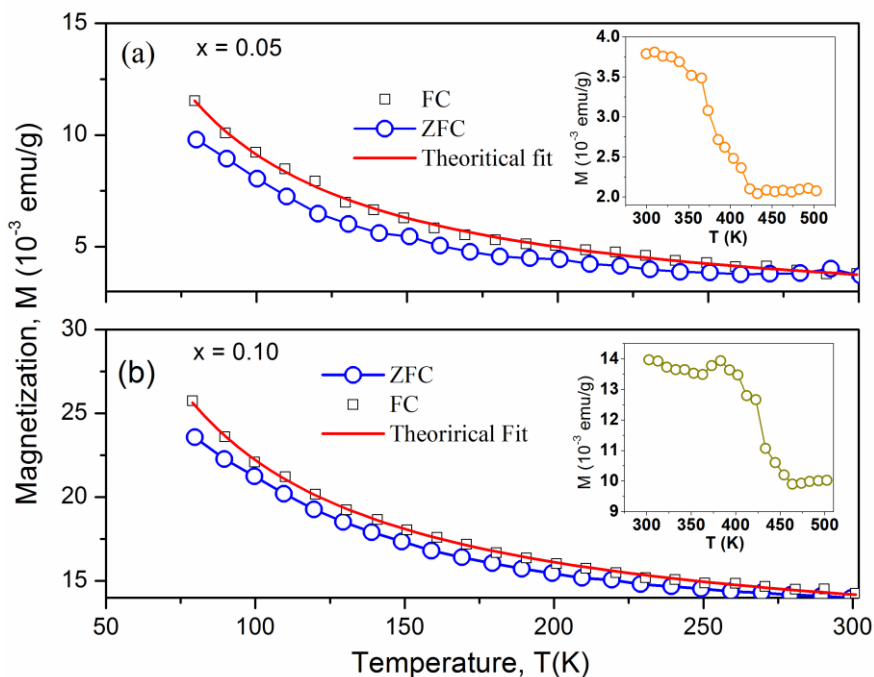


**Fig. 3.24:** ZFC and FC magnetization for  $\text{Sn}_{1-x}\text{Fe}_x\text{O}_2$  samples annealed in  $\text{N}_2$  for (a)  $x = 0.05$  and (b)  $x = 0.10$  and Bold lines represent the theoretical fitting of FC curve according to modified Curie-Weiss law. Insets represent high-temperature  $M(T)$  curve of  $\text{N}_2$  annealed  $\text{Sn}_{1-x}\text{Fe}_x\text{O}_2$  samples.

But at very low temperature, an evidence of ferromagnetic interaction between N defects is observed from Curie-Weiss fitting to the FC curves for N doped  $\text{Sn}_{1-x}\text{Fe}_x\text{O}_2$  samples. It is also noticeable from Fig. 3.22 (c) that magnetization ( $M-\chi_p H$ ) of Fe-N-codoped  $\text{SnO}_2$  samples increases significantly with Fe concentration. In samples with higher Fe concentration, the distance between two  $\text{Fe}^{2+}$  ions decreases and the same hole-concentration becomes more effective to establish ferromagnetic alignment between  $\text{Fe}^{2+}$  ions in our N doped samples.

### 3.6 Conclusion

Single-phase  $\text{Zn}_{1-x}\text{Co}_x\text{O}$  bulk,  $\text{Sn}_{1-x}\text{Co}_x\text{O}_2$  both bulk and nanorods with different Co concentration prepared by mechano-synthesis route and solvothermal route respectively. It is found that although the  $\text{Co}^{2+}$  ions are successfully substituted at host cation (Zn or Sn) site, no evidence of ferromagnetic exchange interaction is observed in both Co doped ZnO and  $\text{SnO}_2$  bulkstructures. The magnetization curve, thermal dependence of magnetization and magnetic susceptibility data confirmed the paramagnetic interaction between the Co ions in the bulk samples. On the other

hand, the  $\text{Sn}_{1-x}\text{Co}_x\text{O}_2$  nanorods are found to exhibit RT ferromagnetism which is found to decrease significantly due to annealing in  $\text{O}_2$ . RTFM is also observed even in case of pure  $\text{SnO}_2$  nanorods and vanishes when annealed in  $\text{O}_2$  at  $800^\circ\text{C}$ . Hence, we attribute structural defect like oxygen vacancy as the origin of FM in  $\text{Sn}_{1-x}\text{Co}_x\text{O}_2$  nanostructure. Similar to Co-doped  $\text{SnO}_2$ , no ferromagnetism is found to observe in  $\text{O}_2$  annealed bulk Fe-doped  $\text{SnO}_2$  prepared by chemical co-precipitation technique. On the other hand, high  $T_C$  ferromagnetism is found to appear in Fe-doped  $\text{SnO}_2$  bulk structures after annealing in  $\text{N}_2$  atmosphere. The magnetic hysteresis loops as well as ZFC-FC magnetization measurements confirmed the ferromagnetic exchange interaction in N doped  $\text{Sn}_{1-x}\text{Fe}_x\text{O}_2$  samples. As we have not observed any evidence of secondary phases in the samples, observed FM should be appeared intrinsically in the material. Additional N substitution at anion site might be very effective to achieve the required threshold hole concentration to mediate long-range ferromagnetic interaction between the  $\text{Fe}^{2+}$  ions. Hence, one possible way to stabilize RTFM in TM-doped oxides is to enhance the hole concentration with additional doping at oxygen site.

## References:

- [1] H. Ohno *Science* **281**, 951 (1998)
- [2] G.A. Prinz, *Science* **282**, 1660 (1998).
- [3] S. A. Wolf, D. D. Awschalom, R.A. Buhrman, J. M. Daughton, S. von Molnár, M.L. Roukes, A.Y. Chtchelkanova, D.M. Treger, *Science* **294**, 1488 (2001).
- [4] S. Ghosh and K. Mandal, *J. Magn. Magn. Mater.* **322**, 1979 (2010).
- [5] S. Ghosh, D. De Munshi, K. Mandal, *J. Appl. Phys* **107**, 123919 (2010).
- [6] S. Ghosh, M. Mandal, K. Mandal, *J. Magn. Magn. Mater.* **323**, 1083 (2011).
- [7] A. Fauchet, W. Prellier, P. Padhan, Ch. Simon, and B. Mercey, *J. Appl. Phys.* **95**, 7187 (2004).
- [8] H. Kimura, T. Fukumura, M. Kawasaki, K. Inaba, T. Hasegawa and H. Koinuma, *Appl. Phys. Lett.* **80**, 94 (2002).
- [9] M. Bouloudenine, N. Viart, S. Colis, A. Dinia, *Chem. Phys. Lett.* **397**, 73 (2004).
- [10] M. Bouloudenine, N. Viart, S. Colis, J. Kortus, A. Dinia, *Appl. Phys. Lett.* **87**, 052501 (2005).
- [11] J. H. Kim, H. Kim, D. Kim, Y.E. Ihm, W.K.Choo, *J. Appl. Phys* **92**, 6066 (2002).
- [12] J. Kim, Y.R. Park, *Appl. Phys. Lett.* **81**, 1420 (2002).

- [13] Y.D. Kim, S.L. Cooper, M.V. Klein, B.T. Jonker, *Phys. Rev. B* **49**, 1732 (1994).
- [14] Y.R. Lee, A.K. Ramdas, R.L. Agarwal, *Phys. Rev. B* **38**, 10600 (1988).
- [15] P. Koidl, *Phys. Rev. B* **15**, 2493 (1977).
- [16] S.W. Lim, D. K. Hwang, and J.M. Myoung, *Solid State Commun.* **125**, 231 (2003).
- [17] F. A. Cotton, D. M. L. Goodgame, M. Goodgame, *J. Am. Chem. Soc.* **83**, 4690 (1961).
- [18] M. Bouloudenine, N. Viart, S. Colis, A. Dinia, *Chem. Phys. Lett.* **397**, 73 (2004).
- [19] S. Risbud, N. A. Spaldin, Z. Q. Chen, S. Stemmer, R. Seshadri, *Phys. Rev. B* **68**, 205202 (2003).
- [20] N. Sakamoto, *J. Phys. Soc. Jpn* **17**, 99 (1962)
- [21] H. Kumagai, Y. Oka, S. Kawata, M. Ohba, K. Inoue, M. Kurmoo, H. Okawa, *Polyhedron* **22**, 1917 (2003).
- [22] N.H. Hong, J. Sakai, N.T. Huong, N. Poirot and A. Ruyter, *Phys. Rev. B* **72**, 045336 (2005).
- [23] H. Kimura, T. Fukumura, M. Kawasaki, K. Inaba, T. Hasegawa, H. Koinuma, *Appl. Phys. Lett.* **80**, 94 (2002).
- [24] A. Fauchet, W. Prellier, P. Padhan, Ch. Simon, B. Mercey, *J. Appl. Phys.* **95**, 7187 (2004)
- [25] J. Kang, S. Tsunekawa, A. Kasuya *Appl. Surf. Sci.* **174**, 306 (2001).
- [26] A. Bouaine, N. Brihi, G. Schmerber, C. Ulhaq-Bouillet, S. Colis and A. Dinia *J. Phys. Chem. C* **111**, 2924 (2007)
- [27] J. Kim, Y.R. Park, *Appl. Phys. Lett.* **81**, 1420 (2002).
- [28] Y.D. Kim, S.L. Cooper, M.V. Klein, B.T. Jonker, *Phys. Rev. B* **49**, 1732 (1994).
- [29] Y.R. Lee, A.K. Ramdas, R.L. Agarwal, *Phys. Rev. B* **38**, 10600 (1988)
- [30] A. Sundaresan, R. Bhargavi, N. Rangarajan, U. Siddesh and C. N. R. Rao *Phys. Rev. B* **74**, 161306(R) (2006)
- [31] A. Ney, K. Ollefs, S. Ye, T. Kammermeier, V. Ney, T. C. Kaspar, S. A. Chambers, F. Wilhelm and A. Rogalev 2008 *Phys. Rev. Lett.* **100**, 157201 (2008).
- [32] M. Bouloudenine, N. Viart, S. Colis and A. Dinia *Chem. Phys. Lett* **397**, 73 (2004)
- [33] M. Venkatesan, C. B. Fitzgerald, and J. M. D. Coey *Nature (London)* **430**, 630 (2004)
- [34] N. H. Hong, J. Sakai, N. Poirot, and V. Brizé, *Phys. Rev. B* **73**, 132404 (2006)
- [35] I. Vinokurov, Z. Zonn, and V. Ioffe, *Sov. Phys. Solid State* **9**, 2659 (1968)
- [36] K. Sato, H. Katayam-Yoshida, *Physica E* **10**, 251 (2001).
- [37] H. Peng, H. J. Xiang, S. H. Wei, S. S. Li, J. B. Xia and J. Li, *Phys. Rev. Lett.* **102**, 017201 (2009).
- [38] C. H. Park, S. B. Zhang, and Su-Huai Wei, *Phys. Rev. B* **66**, 073202 (2002).
- [39] J. F. Liu et al., *J. Magn. Magn. Mater.* **317**, (2007) 1.
- [40] J. Kang, S. Tsunekawa, A. Kasuya *Appl. Surf. Sci.* **174**, 306 (2001).
- [41] A. Bouaine, N. Brihi, G. Schmerber, C. Ulhaq-Bouillet, S. Colis, A. Dinia *J. Phys. Chem. C* **111**, 2924 (2007).
- [42] J. Kim, Y.R. Park, *Appl. Phys. Lett.* **81**, 1420 (2002).

- 
- [43] Y.D. Kim, S.L. Cooper, M.V. Klein, B.T. Jonker, *Phys. Rev. B* **49**, 1732 (1994).
- [44] Y.R. Lee, A.K. Ramdas, R.L. Agarwal, *Phys. Rev. B* **38**, 10600 (1988).
- [45] Q. Xu, S. Zhou, D. Marko, K. Potzger, J. Fassbender, M. Vinnichenko, M. Helm, H. Hochmuth, M. Lorenz, M. Grundmann, H. Schmidt, *J. Phys. D: Appl. Phys.* **42**, 085001 (2009).
- [46] C-F Yu, T-F Lin, S-J Sun, H. Chou, *J. Phys. D: Appl. Phys.* **40**, 6497 (2007).
- [47] B. Gu, N. Bulut, T. Ziman, S. Maekawa, *Phys. Rev. B* **79**, 024407 (2009).

# Chapter 4

## Pristine and Rare Earth Element (Gd)- Doped SnO<sub>2</sub> Thin Films prepared by RF-Sputtering

### 4.1 Preface

In chapter 3, we have discussed the role of TM ions (magnetic ion with 3d outer shell) such as Co, Fe, Cr, V etc. in inducing magnetism in bulk and nanostructured wide band oxide semiconductors [1-3]. Here in present chapter, effects of rare earth element Gd-doping on the intrinsic magnetic ordering, photoluminescence and electrical properties of the pristine SnO<sub>2</sub> nanocrystalline thin films fabricated by Rf-sputtering are investigated [4]. The basic difference between the TM and RE ions is that for earlier one, the ionic magnetic moment originates from localised 3d orbital electrons whereas for the later, the moment mainly comes from 4f electrons which are more localised than 3d electrons. Among the various RE ions, trivalent Gd ion have largest magnetic moment due to its half-fill 4f (4f<sup>7</sup>) orbital. It has no orbital momentum ( $L = 0$ ) and thus the spin angular momentum (S)

equals with total angular momentum, i.e.  $J=S = 7/2$  which give rise to  $^8S_{7/2}$  ground state according to Hund's rule [5]. Theoretically, the effective magnetic moment of the Gd<sup>3+</sup> is found to be  $g_{\mu_B} [J(J+1)]^{1/2} = 7.94 \mu_B$  which is quite large. Hence, if it is possible to stabilize ferromagnetism on SnO<sub>2</sub> with Gd-doping, one can expect that the composite system may exhibit quite large magnetization. Beside this high moment, the substitution of trivalent Gd ions at tetravalent Sn site can also introduce holes in the SnO<sub>2</sub> system which may also favour to sustain long-range ferromagnetic ordering. Hence, we have investigated the magnetic, electrical and photoluminescence properties in pristine and Gd-doped SnO<sub>2</sub> thin films prepared by radio-frequency (RF) magnetron sputtering [4].

## 4.2 Synthesis of pure and Gd-doped SnO<sub>2</sub> thin films

Pure and Gd-doped SnO<sub>2</sub> thin films have been deposited on Si (100) substrate by radio frequency (RF) magnetron sputtering technique (technique details is discussed in Chapter 2). For the preparation of the target, high purity SnO<sub>2</sub> (99.99%) and Gd<sub>2</sub>O<sub>3</sub> (99.99%) with appropriate ratio are mechanically milled using Fritsch Pulverisette-7 mill. The mixture is sintered at 800°C for 12 hrs and a pallet of one inch diameter is prepared out of it. The pallet is sintered again at high temperature (1000°C) for 4 hrs. Afterwards, it is used as target material for the deposition of SnO<sub>2</sub> and Sn<sub>1-x</sub>Gd<sub>x</sub>O<sub>2</sub> ( $x = 0.02$  and  $0.05$ ) thin films. The RF-sputtering is conducted with 50 W dc powers, where the ratio of Argon (Ar) and Oxygen (O<sub>2</sub>) is 10:1. The base pressure of the sputtering chamber is  $2.7 \times 10^{-2}$  mbar. The average deposition rate is  $\sim 4.5$  nm/min and the total deposition time is 45 min. Afterwards, the as-deposited pure and Gd-doped SnO<sub>2</sub> films are annealed at 700°C in oxygen atmosphere for 3 hrs to improve the crystalline quality of the films. All the annealed SnO<sub>2</sub> thin films are characterized by XRD for phase identification and thicknesses of the films are measured by ellipsometer. Scanning electron microscopy (SEM) is used to examine the surface morphology of the films. Magnetic measurements are performed by superconducting quantum interference devices (SQUID). Photoluminescence (PL) spectroscopic measurements are conducted to observe the defect-levels transitions between the optical band-gap of SnO<sub>2</sub> thin films. Hall measurement is carried out to investigate the types (n-type /p-type) of the semiconductors and to estimate the

carrier concentrations. The resistivity of films is measured with standard four-probe method with two current and voltage leads.

## 4.3 Results and discussions

### 4.3.1 Crystal structure

The crystallographic phase identification of the pure and Gd-doped SnO<sub>2</sub> thin films have been performed using XRD pattern, shown in Fig. 4.1. All the peaks with mentioned (*h k l*) values correspond to the tetragonal rutile structure of SnO<sub>2</sub> lattice. It is noticeable that all the films are in single phase without the presence of any impurity phase. The peak around 44.3° originates from the Si substrate on which the SnO<sub>2</sub> films are deposited. The variation of the lattice parameters and *d*-spacing (*d*<sub>110</sub> and *d*<sub>101</sub>) between parallel planes of SnO<sub>2</sub> unit cell, estimated using Bragg's diffraction law, are shown in Fig. 4.2. It is important to notice that the lattice parameters (*a* = *b* and *c*) as well as lattice volume (*V*) are found to increase with Gd-doping. This expansion of the lattice volume ensures the substitution of larger Gd<sup>3+</sup> ion (1.07 Å) replacing smaller Sn<sup>4+</sup> ion (0.69 Å) in SnO<sub>2</sub> matrix. This type of variation of the lattice parameters are also observed for other TM-doped SnO<sub>2</sub> thin films [1, 2, 6]. The values of lattice parameters and *d*-spacing for different crystallographic planes of the different films are also summarized in Table 1. It is found that the full width at half maximum (FWHM) of the (110) peak increases with Gd-doping, which signifies the decrease of average crystallite sizes (*t*) of the films. The values of average crystallite sizes of the thin films are estimated using Debye-Scherrer formula,  $t = 0.9 \lambda / \beta \cos \theta$ , where  $\lambda$  is the wave length of x-ray beam used (1.54 Å for Cu-K $\alpha$  radiation),  $\theta$  is peak position of given (*hkl*) and  $\beta$  is the corresponding FWHM in radian. The average '*t*' values of all thin films are found to be less than 10 nm which demonstrates nanocrystalline nature of the thin films (see Table 1). The thicknesses of the thin films measured by ellipsometer are found to be 228, 217, 210 and 205 nm for pure, 1%, 2% and 5% Gd-doped SnO<sub>2</sub>, respectively.

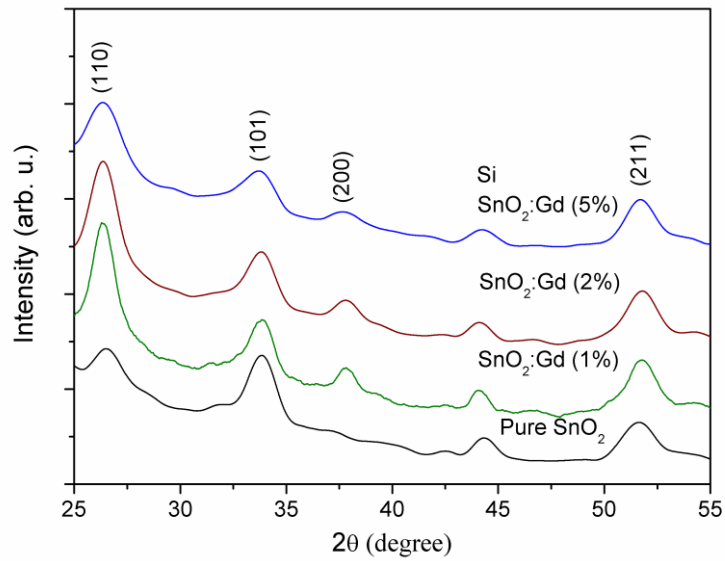


Fig. 4.1: X-ray diffraction patterns of pristine SnO<sub>2</sub> and Gd-doped SnO<sub>2</sub> thin films.

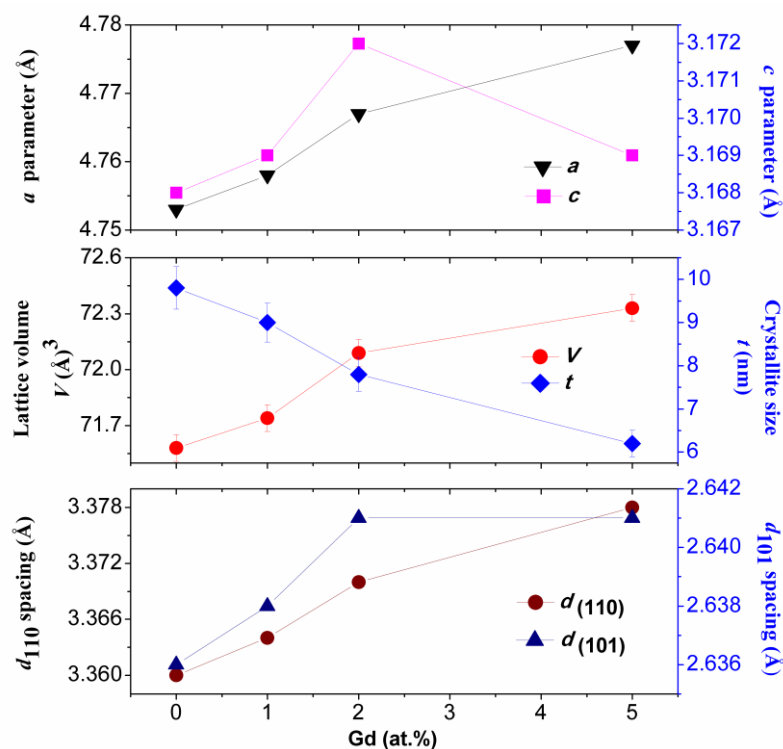


Fig. 4.2: Variation of lattice parameters (*a* and *c*), lattice volumes (*V*), crystallite sizes (*t*) and d-spacing of (110) and (101) crystal planes of SnO<sub>2</sub> lattice with Gd concentration (at. %).

Table 1. Typical Estimated Values of Lattice Parameters ( $a$  and  $c$ ), Lattice Volume ( $V$ ),  $d$ -Spacing of the (110) and (101) Planes, Full Width at Half Maximum (fwhm) of the (110) Plane, and Crystallite Size ( $t$ ) of As-Deposited Pristine and Gd-Doped SnO<sub>2</sub> Thin Films

thin film	Lattice Parameters			$d$ -Spacing (Å)		fwhm at (110) (°)	crystallite size, $t$ (nm)
	$a^a$ (Å)	$c$ (Å)	volume, $V$ (Å <sup>3</sup> )	$d_{110}$	$d_{101}$		
SnO <sub>2</sub>	4.753	3.168	71.56 ± 0.07	3.360	2.636	1.85 ± 0.02	9.8 ± 0.3
SnO <sub>2</sub> :Gd (1%)	4.758	3.169	71.74 ± 0.07	3.364	2.638	2.02 ± 0.02	9.0 ± 0.3
SnO <sub>2</sub> :Gd (2%)	4.767	3.172	72.08 ± 0.07	3.370	2.640	2.34 ± 0.02	7.8 ± 0.3
SnO <sub>2</sub> :Gd (5%)	4.777	3.169	72.31 ± 0.07	3.378	2.641	2.91 ± 0.02	6.3 ± 0.3

<sup>a</sup>Note that  $a = b$ .

### 4.3.2 Surface morphology

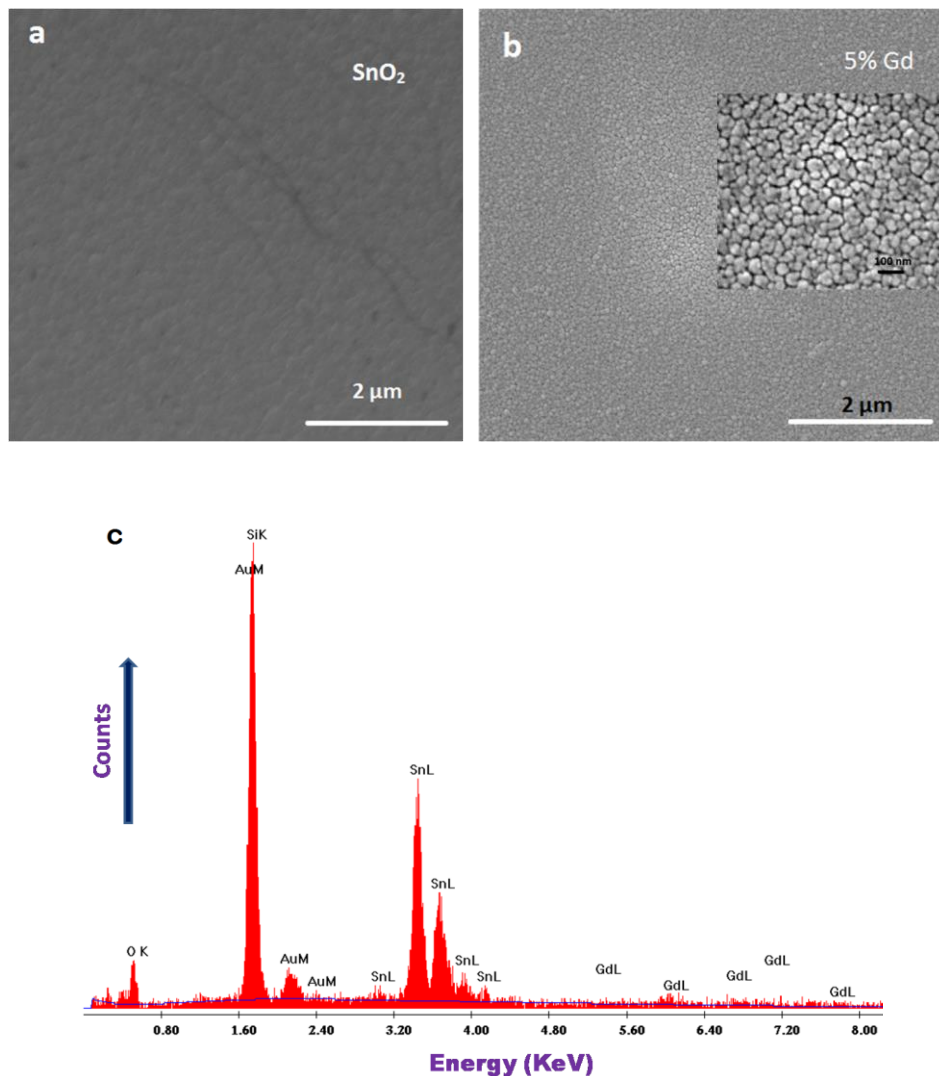


Fig. 4.3: SEM images of (a) pristine SnO<sub>2</sub> (b) 5% Gd-doped SnO<sub>2</sub> thin films. Inset: High magnification image of the corresponding thin film which shows the nanocrystalline nature of the film. (c) EDAX spectrum of the 5% Gd-doped SnO<sub>2</sub> thin film.

Figure 4.3 shows the low magnification SEM images of the pure and 5% Gd-doped SnO<sub>2</sub> thin films, where the inset of Fig. 4.3(b) shows the high magnification image of the corresponding thin film. The SEM images show that both the pure and Gd-doped SnO<sub>2</sub> films are homogenous throughout, demanding a uniform Gd-doping with no Gd-accumulation for Gd-doped film. From the SEM image of 5% Gd-doped SnO<sub>2</sub> thin film (inset of Fig 4.3(b)) it is also clear that the thin film is nanocrystalline with prominent grains having average grain size around 50 nm. The grains are also very much clear for Gd-doped SnO<sub>2</sub> thin films compared to that of pure SnO<sub>2</sub> thin films, which indicates a better crystallinity of the 5% Gd-doped SnO<sub>2</sub> film. This is probably because the doping of trivalent Gd ions, which favours to achieve better crystallinity in SnO<sub>2</sub> films. The energy dispersive x-ray (EDAX) spectrum of the 5% Gd-doped SnO<sub>2</sub> thin films is shown in Fig. 4.3(c). The Gd concentrations in the thin films quantified by EDAX spectroscopy are found to be 4.87, 1.91 and 0.82 at. wt.% for 5, 2 and 1 at. wt.% nominal Gd concentration. The Si K peak is originated from Si substrate on which SnO<sub>2</sub> films are deposited whereas; the Au K signal appears from the gold layer coated on the SnO<sub>2</sub> films required for the SEM investigation.

### 4.3.3 Magnetic properties

#### 4.3.3.1 M-H behaviour of pure and Gd-doped SnO<sub>2</sub> films

Figure 4.4 shows the M-H measurements of pure and Gd-doped SnO<sub>2</sub> thin films. Interestingly, the pure SnO<sub>2</sub> thin film exhibits a clear hysteresis loop, which indicates that the pristine SnO<sub>2</sub> thin films are ferromagnetic at room temperature as shown in Fig. 4.4(a) as well as at low temperature in inset (ii) of Fig. 4.4(a). Significant amount of coercivity ( $H_c$ ) ~110 and 125 Oe at 300 and 5 K, respectively, are found in case of pure SnO<sub>2</sub> film which assure the FM nature. The saturation magnetization ( $M_s$ ) and retentivity ( $M_r$ ) are found to be  $3.4 \times 10^{-3}$  and  $2.2 \times 10^{-4}$  emu/cm<sup>3</sup> at 300 K and  $4.6 \times 10^{-3}$  and  $9.8 \times 10^{-4}$  emu/cm<sup>3</sup> at 5 K, respectively. This type of ferromagnetic response in other pristine oxides is also reported earlier [7, 8]. On the other hand, it's quite interesting to observe that Gd-doped SnO<sub>2</sub> films show a linear M-H behaviour (Fig. 4.4(b) and (d)) which indicates a dominant paramagnetic ordering present in the Gd-doped films. In case of 1% Gd doped film as shown in

Fig. 4.4(b), a curvature is observed near the origin which indicates that a FM component is superimposed over a strong paramagnetic background. Therefore, we have subtracted the strong paramagnetic component ( $M_{\text{Para}}$ ) from the total moment ( $M_{\text{Total}}$ ) and plotted the residual component ( $M_{\text{Total}} - M_{\text{Para}}$ ) in Fig. 4.4c which shows the clear hysteresis type behaviour with coercivity  $H_C \sim 95$  Oe. Saturation moment ( $M_s$ ) is found to be  $1.05 \times 10^{-3}$  emu/cm<sup>3</sup> which is much smaller compared to that of pure SnO<sub>2</sub> film. Therefore, with 1 at.% Gd doping in SnO<sub>2</sub> film the FM is found to be suppressed subsequently and a large paramagnetic moment is established within the system. For 2% Gd-doped film, ferromagnetic component ( $M_{\text{Total}} - M_{\text{Para}}$ ) is found to be completely vanished while the paramagnetic component has enhanced significantly. Similarly, no FM is found for 5% Gd-doped

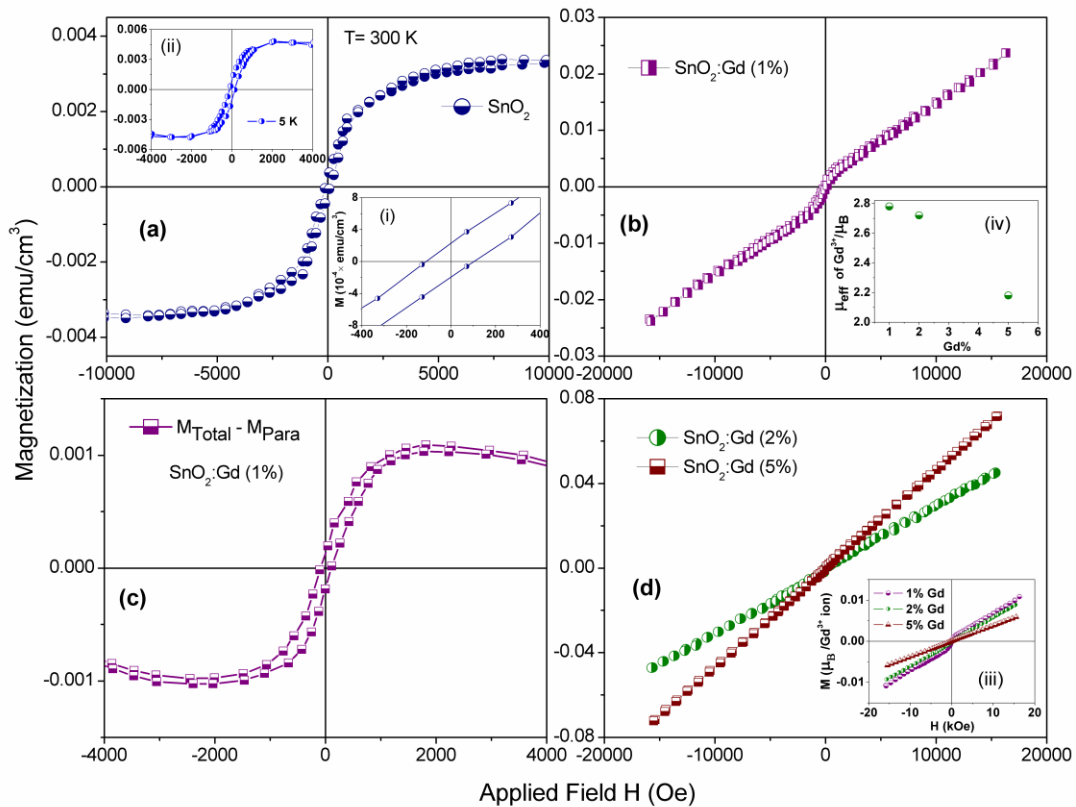


**Fig. 4.4:** Field-dependent magnetization, M-H loops of (a) the pristine SnO<sub>2</sub> thin film at 300 K, (b) 1% Gd-doped SnO<sub>2</sub>, (c) Ferromagnetic component ( $M_{\text{Total}} - M_{\text{Para}}$ ) of 1% Gd-doped film after subtracting the paramagnetic component and (d) 2 and 5% Gd-doped SnO<sub>2</sub> thin films. Inset: (i) magnetization of pure SnO<sub>2</sub> in low field area at 300K. Inset: (ii) M-H loop of pure SnO<sub>2</sub> at 5 K. Inset: (iii) Magnetization of Gd-doped films in the units of  $\mu_B$  per Gd<sup>3+</sup> ion and Inset: (iv) the effective magnetic moment ( $\mu_{\text{eff}}$ ) of the individual Gd ion in units of Borh

magneton ( $\mu_B$ ) versus Gd-concentration in the film. (All data presented after correcting the diamagnetic substrate contribution).

films also. Therefore, the FM in pure SnO<sub>2</sub> film tends to diminish gradually with the increase of Gd doping and then over a certain Gd concentration (lying somewhere in between 1-2 at.%) it is completely vanished. However, the earlier MFM studies also showed the indication of long-range FM ordering in the pure SnO<sub>2</sub> films whereas no such observation was found for 5% Gd-doped film. It is important to notice that although the associated magnetic moment is increased by one order of magnitude due to the insertion of Gd<sup>3+</sup> ions, which have localised *f*-shell paramagnetic moment, but there is no intrinsic FM ordering in the Gd-doped SnO<sub>2</sub> films. However, similar results were also obtained by Ney *et al.* [9], Xu *et al.* [10], and Barla *et al.* [11] in case of Co-doped ZnO thin films and also in our previous work on the Co-doped SnO<sub>2</sub> [1]. Recently loss of magnetization is also observed in CeO<sub>2</sub> thin films [12] with doping of TM ions. Herein, we estimated the magnetization per Gd<sup>3+</sup> ion and the effective magnetic moment ( $\mu_{\text{eff}}$ ) of the individual Gd ion in units of Bohr magneton ( $\mu_B$ ), shown in the inset (iii) and (iv) of Fig. 4.4 respectively. It is interesting to notice that the magnetization per Gd ion as well as the  $\mu_{\text{eff}}$  decreases with the increase of Gd-concentration which may be because of the enhancement of the anti-ferromagnetic superexchange interaction between Gd<sup>3+</sup> ions via oxygen ligands. With the increase of Gd concentration in the SnO<sub>2</sub> matrix, the average distance between the Gd<sup>3+</sup> ions should decrease leading to the enhancement of this type of antiferromagnetic superexchange interaction. The  $\mu_{\text{eff}}$  of Gd<sup>3+</sup> ion is found to be maximum (2.78  $\mu_B$ ) in 1% Gd-doped SnO<sub>2</sub> film which is much less than full moment of Gd<sup>3+</sup> (7.94  $\mu_B$ ) ion. Similar results are also observed in case of Co: ZnO [13], Co:SnO<sub>2</sub> [1] and Gd: ZnO [14] where the effective moment of respective TM or RE ion is found to decrease significantly. This can happen because the moment of magnetic ions depends on the ionic environment [15, 16] and ion symmetry within the host matrix. The increase of Gd concentration results in a lattice distortion which can change the Gd<sup>3+</sup> site symmetry as well as the effective magnetic moment of the Gd<sup>3+</sup> ion.

### 4.3.3.2 AFM and MFM micrographs of the SnO<sub>2</sub> films

Atomic force microscopy (AFM) image of the film surface are shown in Fig. 5.4 (a) and (c) for the pure and 5% Gd-doped SnO<sub>2</sub> films respectively, at a lift height of ~300 nm over a scan size of 2×2 μm<sup>2</sup>. The corresponding magnetic force microscopy (MFM) images are shown in Fig. 4.5 (b) and (c). It is evident from Fig. 4.5 that the MFM features of the films are different from the AFM topography of the films. It is found that the MFM amplitude image shows some coarse grain-like domain structures, where the bright and dark contrast of domains corresponds to high concentrations of positive and negative poles. The domain configurations are also different for the pure and 5% Gd-doped SnO<sub>2</sub> films. The grain-like domain structures is more prominent and vivid in case of the pure SnO<sub>2</sub> nanocrystalline thin films (Fig. 4.5(b)) compared to the 5% Gd-doped SnO<sub>2</sub> film (Fig. 4.5(d)). In case of 5% Gd-doped SnO<sub>2</sub> films the bright grain-like domains are less in number as well as they are random and far from each other. Therefore, the observed regular distribution of the bright and dark grain-like magnetic domains in the pure SnO<sub>2</sub> thin film is an indication of long-range magnetic ordering in it over the Gd-doped SnO<sub>2</sub> films [17-19].

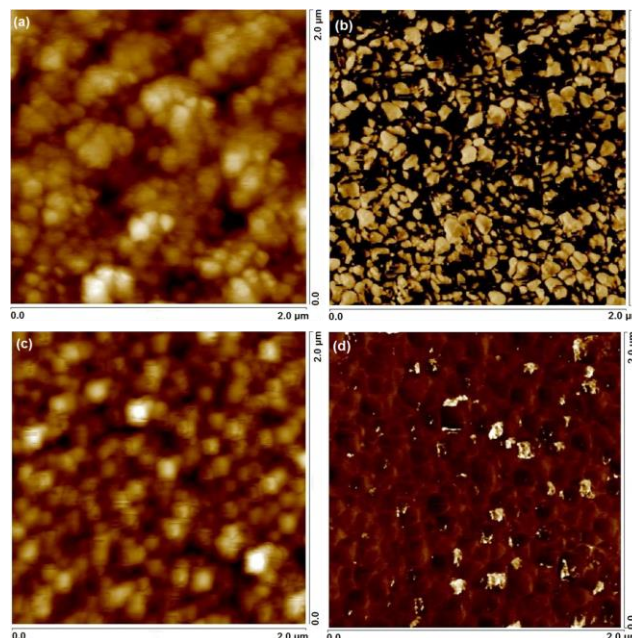


**Fig. 4.5:** The topographic atomic force microscopy (AFM) images (a) and (c) and the corresponding grain-like magnetic domain structures revealed by the magnetic force microscopy (MFM) imaging (b) and (d), for the pure and 5% Gd-doped SnO<sub>2</sub> films, respectively.

### 4.3.3.3 Thermal dependent magnetic behaviour

To understand the magnetic properties in further details, zero field cooled (ZFC) and field cooled (FC) measurements are also performed for Gd-doped SnO<sub>2</sub> films, shown in Fig. 4.6. In case of 2 and 5% Gd-doped SnO<sub>2</sub> films both ZFC and FC curves shown in Fig. 4.6 (b) and (c) respectively, traces the same path in the entire range of temperature which demonstrates the presence of a non-interacting paramagnetic moments in the system. But in case of 1% Gd-doped film FC curve showed a higher moment that ZFC which indicate the presence of FM phase. FC curves are also fitted according to the modified Curie-Weiss law  $\chi = M(T)/H = \chi_0 + C/(T+\theta)$ , where  $\chi_0$  represents weak non-paramagnetic susceptibility,  $C = N\mu^2/3k$  is the curie constant which represents the paramagnetic ion concentration ( $N =$  number of magnetic ions per gram,  $\mu =$  magnetic moment of the ion and  $k =$  Boltzman constant),  $T$  is the temperature in K and  $\theta$  is the Curie-Weiss temperature which represents the magnetic exchange interactions between the localized spins. These fits yields  $\theta = 4.25, 3.8$  and  $-9.67$  K for 5%, 2% and 1% Gd-doped SnO<sub>2</sub> films,

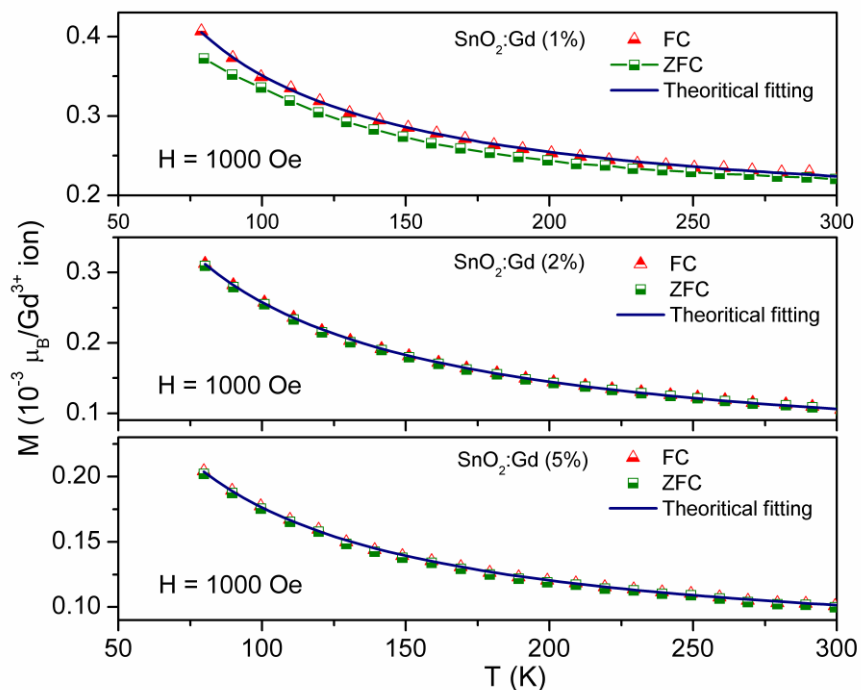


**Fig. 4.6.** ZFC-FC plots for all the Gd-doped SnO<sub>2</sub> thin films at a constant field of 1000 Oe along with the theoretical fitting of FC curves according to modified Curie-Weiss law.

respectively. It is noticeable that unlike other films 1% Gd-doped film showed negative Curie-Weiss temperature ( $\theta$ ) which demonstrates the existence of ferromagnetic exchange interaction in this film. The positive  $\theta$  value for 2 and 5% Gd-doped films signifies the existence of the antiferromagnetic exchange interaction between the Gd<sup>3+</sup> ions. Gd<sup>3+</sup>-O<sup>2-</sup>-Gd<sup>3+</sup> superexchange interaction might be the possible origin of the antiferromagnetism whereas the Gd<sup>3+</sup>-Gd<sup>3+</sup> direct interaction is paramagnetic in nature.

### 4.3.4 Photoluminescence properties

The study of the magnetic properties of the pure and Gd-doped SnO<sub>2</sub> thin films generates two questions: (i) whether magnetic ions (like Gd<sup>3+</sup>) play any role in inducing FM in such oxides and (ii) what made pure SnO<sub>2</sub> thin film ferromagnetic? To address those questions it is essential to study the intrinsic defects that might be present in SnO<sub>2</sub> thin films. Hence, we have performed RT PL measurements, shown in Fig. 4.7, to investigate the types of structural defects present in the pure and Gd-doped SnO<sub>2</sub> thin films. It is found that under an excitation of 330 nm light from the Xe source all the nanocrystalline thin films exhibit intense broad PL emission band centered at 390 nm (3.17 eV). Since this emission energy (3.17 eV) is much lower than the energy band gap of SnO<sub>2</sub> (3.6 eV), the visible emission cannot be assigned to the direct recombination of conduction electron to the holes in valance band, rather to the defect related emission. The strong blue emission from the thin films might be related to the inherent crystalline defects induced during their growth [26-28]. It is important to notice, that the broad nature of the PL emission band clearly indicates that the luminescence should have been originated from the multiple sources rather than a single source as the PL band can be well fitted with the multiple PL peaks. It is reported that the SnO<sub>2</sub> nanostructures can exhibit emission bands between 400 and 600 nm because of the presence of different crystalline defects [20-22]. The cation vacancies i.e. Sn vacancies ( $V_{\text{Sn}}$ ) and the oxygen vacancy defects are the main structural defects present in the SnO<sub>2</sub> nanostructures responsible to introduce the defect states in the mid band gap leading to luminescence in the visible region [23]. Although the formation energy of  $V_{\text{Sn}}$  being higher than that of the  $V_{\text{O}}$ , it is expected that the concentration of the  $V_{\text{Sn}}$  defects in the SnO<sub>2</sub> should be much lower than that of the oxygen vacancies [24]. It has been reported that the nanocrystalline SnO<sub>2</sub> thin

films exhibit intense photoemission at around 3.13 eV at different temperatures [25]. The blue luminescence from the SnO<sub>2</sub> thin films in the wave length range of 400-450 nm has also been reported by others [26, 27] still the origin of this PL emission band has not been understood properly. It is assumed that the PL peaks might be attributed to the defects in the nanocrystal grains [25, 26] or the oxygen vacancy defects [24-26] or even the tin interstitial defects [11]. However, the broad photoemission peak centered around 400 nm is believed to be originated because of the electron transition mediated by the oxygen vacancy related defects in the band gap [25-27].

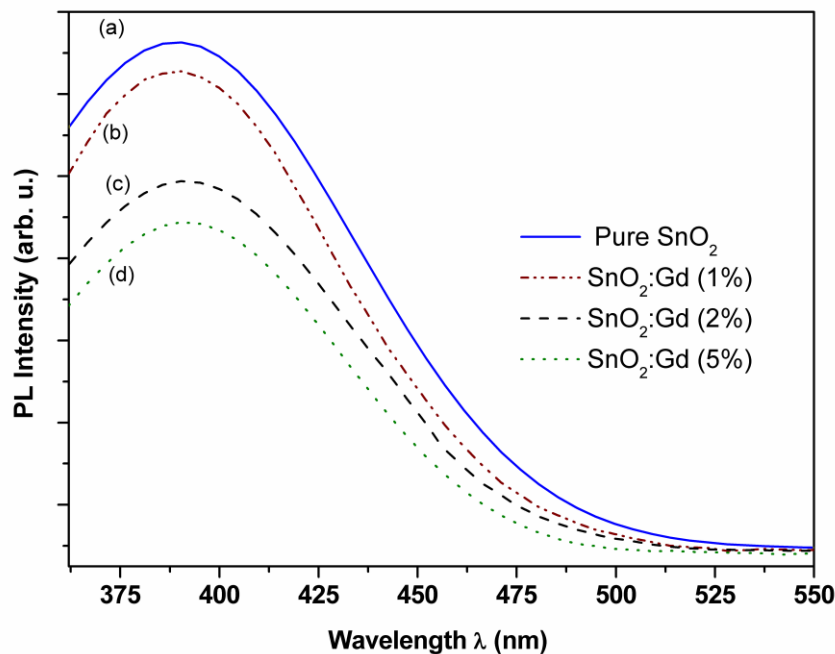


**Fig. 4.7:** PL spectrum of (a) pristine SnO<sub>2</sub> (b) 1 at.% (c) 2 at.% and (d) 5 at.% Gd-doped SnO<sub>2</sub> thin films.

The energy level of the oxygen vacancy defects being highly controversial, in this experiment the PL emission peak centered around 390 nm is attributed to the oxygen vacancy related defects, mainly singly ionized oxygen vacancy ( $F^+$  center or  $V_{O^+}$ ) defects, which are believed to be the recombination centre for the luminescence [8, 28]. In our experiment it is quite expected that the films should contain the oxygen vacancy defects as the films are deposited in an oxygen deficient atmosphere. Although here we cannot also discard the presence of the  $V_{Sn}$  defects in the pure and Gd-doped SnO<sub>2</sub> films as the cation vacancy defects are also quite

obvious in the lattice of the oxide semiconductors. Recently, the cation vacancy related defects are attributed to the visible emission as well as to the RTFM in the doped ZnO thin films and nanostructures [29-31]. It has been found that the doping of the suitable element can also help in the formation of the cation vacancies in the lattice [29]. It is evident from Fig 4.7 that the intensity of the PL emission centred at 390 nm is maximum for the pure SnO<sub>2</sub> thin film. Therefore, it is expected that the singly ionized oxygen vacancy ( $V_{O^+}$ ) defect concentration is maximum in the pristine SnO<sub>2</sub> nanocrystalline film compared to the Gd-doped films. However, the decrease of the intensity of the PL emission band with the increase of the Gd concentration in the Gd-doped SnO<sub>2</sub> films may be attributed to the considerable attenuation of the oxygen vacancies in the lattice, where the  $V_{Sn}$  defects could predominate and the PL emission bands becomes broader in nature with the increase of the Gd concentration in the matrix.

Here, it is important to mention that enough precaution is taken during the preparation of the films to avoid any kind of contamination. Non-magnetic tweezers having plastic tips are used to transfer the films during different measurements. In fact, no impurities have been detected from XRD and EDAX analysis considering their detection limit. Moreover, we also have tried to exclude any kind of instrumental error by conducting the magnetic measurements repeatedly. Therefore, to discuss about the origin of FM in pristine SnO<sub>2</sub> thin film, it is quite clear from the PL studies that intrinsic defects are playing the key role to induce FM in SnO<sub>2</sub>. The present PL analysis has shown that the structural defects like  $V_{O^+}$  defects are maximum in the pure SnO<sub>2</sub> thin film. Here, it is worth mentioning that a single  $V_{O^+}$  defect can generate a localised magnetic moment of  $\sim 1.0 \mu_B$  and when this type of defect ( $V_{O^+}$ ) concentration reaches above the percolation limit, a ferromagnetic exchange interaction can be stabilized [32-33], observed in the pure SnO<sub>2</sub> thin film. On the other hand,  $V_{O^+}$  defect concentration found to be decrease with the increase of Gd-doping in SnO<sub>2</sub> films. Although  $V_{O^+}$  defect concentration decreased in 1% Gd-doped film, still the amount might be sufficient to mediate ferromagnetic interaction in this film. Therefore, the 1% Gd-doped film exhibit weak FM signature compared to that of the pure SnO<sub>2</sub> film. But when Gd concentration exceeds 2 at.% the  $V_{O^+}$  defect concentration might have reached below the required percolation limit to sustain long-range ferromagnetic ordering between  $V_{O^+}$  defects and hence the destruction of FM. But the paramagnetic moments associated with the localised Gd<sup>3+</sup>

ions still exists and that is contributing to the total magnetic moments. Previously we have seen from the Curie-Weiss fittings that the exchange interaction exists between Gd<sup>3+</sup> ions are only antiferromagnetic type at very low temperatures but not ferromagnetic one. Therefore, we demonstrate that the FM arises only due to the intrinsic structural defects like V<sub>O</sub><sup>+</sup> defects of SnO<sub>2</sub> lattice and here the magnetic ions (like Gd<sup>3+</sup>) have no influence in inducing ferromagnetism in SnO<sub>2</sub> thin films. However, it is important to mention that the Sn vacancy (V<sub>Sn</sub>) defects are also reported to generate localised magnetic moments [34, 35]. The previous PL measurements indicate that there might have been some V<sub>Sn</sub> defects present in the thin films, may be low in concentration because of their high formation energy [24]. Hence, it is expected that the concentration of the V<sub>Sn</sub> defects present in the films should be much below the required percolation threshold to mediate long-range ferromagnetic ordering both in the SnO<sub>2</sub> thin films as it is not probable to have considerable amount of V<sub>Sn</sub> defects in SnO<sub>2</sub> without proper defect-engineering. The chance of the formation of V<sub>O</sub><sup>+</sup> defects is quite easier due to its low formation energy<sup>33</sup> and in this work the formation of V<sub>O</sub><sup>+</sup> defects in SnO<sub>2</sub> thin films are quite possible because all the thin films are deposited in an oxygen deficient atmosphere, where the oxygen to Ar ratio is 1:10.

### 4.3.5 Electrical properties

The study of the electrical conductivity and the type of the charge carriers present in the oxide semiconductor thin films can also provide information about the intrinsic nature of the films. In this regard, here, we have investigated the types of charge carriers and the carrier concentrations by Hall measurements and also the electrical conductivity of the pure and Gd-doped SnO<sub>2</sub> thin films. The variations of the resistivity ( $\rho$ ), carrier concentration ( $n$ ), Hall coefficient ( $R_H$ ) and mobility ( $\mu$ ) of the SnO<sub>2</sub> thin films with Gd-doping concentration are shown in Fig. 4.8 and their values are summarized in Table 2. The negative value of  $R_H$  in case of the pure SnO<sub>2</sub> and 1% Gd-doped thin film indicates n-type semiconducting nature, which is because of the presence of the oxygen vacancies [24, 36, 37]. On the other hand, 2 and 5% Gd-doped SnO<sub>2</sub> films show positive value of  $R_H$ , which indicates their p-type semiconducting behaviour. This n-type to p-type transformation of the pure SnO<sub>2</sub> thin film with Gd-doping can be understood due to the gradual substitution of

Gd<sup>3+</sup> ions at Sn<sup>4+</sup> sites that enhances hole concentration into the SnO<sub>2</sub> system. From Fig. 4.8, it is seen that as the Gd-doping increases in SnO<sub>2</sub> film, the electron concentration decreases gradually which means an increase of hole concentration. The previous PL study also indicates that with the increase of the Gd concentration in the SnO<sub>2</sub> film the V<sub>Sn</sub> defects could predominate as the concentration of the V<sub>O</sub> defects reduce significantly. The acceptor-type V<sub>Sn</sub> defects may also contribute to the p-type nature of the doped SnO<sub>2</sub> films. The n-type conductivity of the pure SnO<sub>2</sub> thin film signifies that the film is enriched with the oxygen vacancy defects, whereas the doping of Gd<sup>3+</sup> ion at Sn<sup>4+</sup> site can modify the multivalence of tin probably through the population of tin interstitial and thus the donor level inside the conduction band. As a result, the resistivity ( $\rho$ ) of the pure SnO<sub>2</sub> thin film increases with the increase of the Gd-doping concentration. The 5% Gd-doped SnO<sub>2</sub> thin film becomes the most resistive one ( $\rho = 8.3 \times 10^3$  ohm-cm). The carrier concentration ( $n$ ) is found to be of the order of  $1.1 \times 10^{20}$  cm<sup>-3</sup> in the pure SnO<sub>2</sub> thin film and it decreases monotonically with the increase of Gd concentration. The mobility ( $\mu$ ) of the charge carriers also decreases with Gd-doping and it is quite expected as the mobility of holes is less than that of electrons.

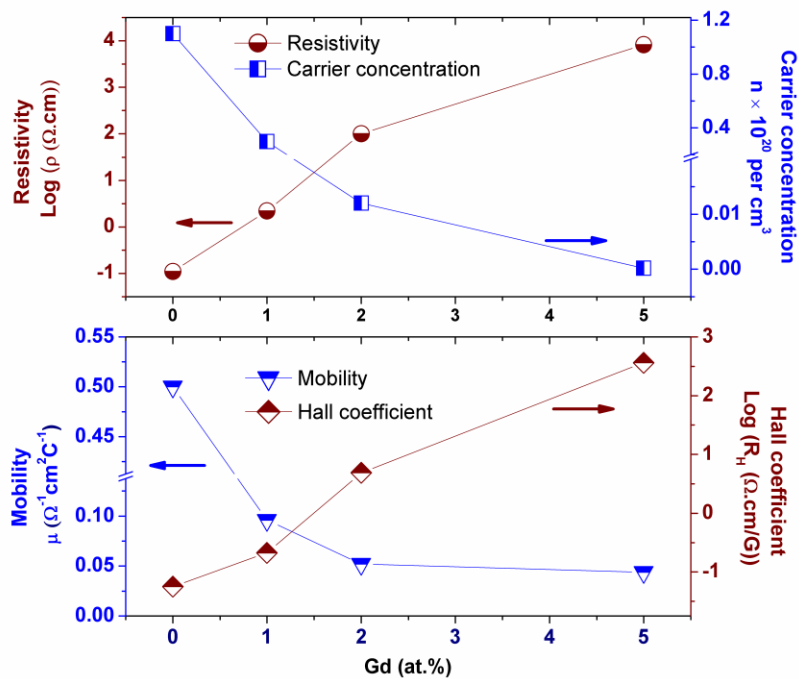


**Fig. 4.8:** Variation of resistivity ( $\rho$ ), carrier concentration ( $n$ ), hall coefficient ( $R_H$ ) and mobility ( $\mu$ ) of SnO<sub>2</sub> thin films with Gd concentration.

Table 2. Typical Estimated Values of Resistivity ( $\rho$ ), Hall Coefficient ( $R_H$ ), Carrier Concentration ( $n$ ), Mobility of Carriers ( $\mu$ ), and Types of Semiconductors for Pristine and Gd-Doped SnO<sub>2</sub> Thin Films

thin film	resistivity, $\rho$ ( $\Omega$ cm)	Hall coefficient, $R_H$ ( $\Omega$ cm/G)	carrier concentration, $n$ ( $\text{cm}^{-3}$ )	mobility, $\mu$ ( $\Omega^{-1}\text{cm}^2\text{C}^{-1}$ )	type of semiconductor
SnO <sub>2</sub>	$1.1 \times 10^{-1}$	$-5.6 \times 10^{-2}$	$1.1 \times 10^{20}$	0.50	n-type
SnO <sub>2</sub> :Gd (1%)	2.2	$-2.1 \times 10^{-1}$	$3.0 \times 10^{19}$	$9.6 \times 10^{-1}$	n-type
SnO <sub>2</sub> :Gd (2%)	$10^2$	+4.87	$1.2 \times 10^{18}$	$5.2 \times 10^{-1}$	p-type
SnO <sub>2</sub> :Gd (5%)	$8.3 \times 10^3$	$+3.6 \times 10^2$	$1.7 \times 10^{16}$	$4.4 \times 10^{-1}$	p-type

## 4.4 Conclusion

In summary, we have studied the role of structural defects in inducing FM in pristine SnO<sub>2</sub> thin film and the effects of Gd-doping on the magnetic, photoluminescence and electrical conduction of SnO<sub>2</sub> nanocrystalline thin films. Only the pristine SnO<sub>2</sub> thin film exhibits FM in both room and low temperature while the FM signature in pure SnO<sub>2</sub> film is found to be suppressed initially with low Gd-doping but is completely destroyed with higher dopant concentration. The MFM study indicates long range magnetic ordering in pure SnO<sub>2</sub> films at room-temperature. The PL spectra reveals the presence large numbers of  $V_{\text{O}}^+$  defects, which are found to be responsible for the observed FM in n-type pristine SnO<sub>2</sub> thin film. The studies indicate that the doping of Gd ions at Sn sites reduces the  $V_{\text{O}}^+$  defect concentration significantly and makes the films highly resistive and p-type while the pure SnO<sub>2</sub> film is highly conductive and n-type in nature. Although Gd ions introduce localised paramagnetic moments, still no long range ferromagnetic ordering is observed in the Gd-doped SnO<sub>2</sub> thin films. The result signifies that the magnetic ions like Gd have little influence in inducing FM in SnO<sub>2</sub> thin film. Our work will certainly help to overcome the controversy about the origin of ferromagnetism in such magnetic ions-doped wide band gap oxide semiconductors.

## References

- [1] S. Ghosh, D. De Munshi, K. Mandal, *J. Appl. Phys.* **107**, 123919 (2010).
- [2] S. Ghosh, M. Mandal, K. Mandal, *J. Magn. Magn. Mater.* **323**, 1083 (2011).
- [3] S. Ghosh, M. Mandal, K. Mandal, *J. Magn. Magn. Mater.* **323**, 1083 (2011).
- [4] S. Ghosh, G. G. Khan and K. Mandal, *ACS Appl. Mater. Interfaces*, **4**, 2048 (2012).
- [5] C. Kittel, *Introduction to Solid State Physics*, Wiley-INDIA seventh edition.
- [6] X. F. Liu and R. H. Yua, *J. Appl. Phys.* **102**, 083917 (2007).
- [7] M. Venkatesan, C. B. Fitzgerald, J. M. D. Coey, *Nature*, **430**, 630 (2004).
- [8] A. Sundaresan, R. Bhargavi, N. Rangarajan, U. Siddesh et al., *Phys. Rev. B* **74**, 161306 (2006).
- [9] A. Ney, K. Ollefs, S. Ye, T. Kammermeier, V. Ney, T. C. Kaspar et al., *Phys. Rev. Lett.* **100**, 157201 (2008).
- [10] Xu, Q.; Zhou, S.; Marko, D.; Potzger, K. et al., *J. Phys. D: Appl. Phys.* **42**, 085001 (2009).
- [11] Barla, A.; Schmerber, G.; Beaupaire, E.; Dinia, A. et al., *Phys. Rev. B* **76**, 125201 (2007).
- [12] Fernandes, V.; Schio, P.; de Oliveira, A. J. A.; Schreiner, W. H. et al., *J. Appl. Phys.* **110**, 113902 (2011).
- [13] Ghosh, S.; Mandal, K. *J. Magn. Magn. Mater.* **322**, 1979 (2010).
- [14] Dakhel A. A.; El-Hilo M.; *J. Appl. Phys.* **107**, 123905 (2010).
- [15] Sakamoto, N. *J. Phys. Soc. Jpn.* **17**, 99 (1962).
- [16] Kumagai, H.; Oka, Y.; Kawata, S.; Ohba, M. et al., *Polyhedron* **22**, 1917 (2003).
- [17] Heng, T. S.; Wong, M. F.; Qi, D. et al., *Adv. Mater.* **23**, 1635 (2011).
- [18] Philip J.; Punnoose, A.; Kim, B. I.; Reddy, K. M.; Layne, S.; Holmes, J. O.; Satpati, B.; Leclair, P. R.; Santos, T. S.; Moodera, J. S. *Nature Mater.* **5**, 298 (2006).
- [19] Jeon, H. C.; Jeong, Y. S.; Kang, T. W.; Kim, T. W.; Chung, K. J.; Chung, K. J.; Jhe, W.; Song, S. A. *Adv. Mater. (Weinheim, Ger.)* **14**, 1725 (2002).
- [20] He, H.; Wu, T.H.; Hsin, C.L.; Li, K.M.; Chen, L.J.; Chueh, Y.L.; Chou, L.J.; Wang, Z.L. *Small* **2**, 116 (2006).
- [21] Luo, S.; Fan, J.; Liu, W.; Zhang, M.; Song, Z.; Lin, C.; Wu, X.; Chu, P.K. *Nanotechnology* **17**, 1695 (2006).
- [22] Luo, S.; Chu, P.K.; Liu, W.; Zhang, M.; Lin, C. *Appl. Phys. Lett.* **88**, 183112 (2006).
- [23] Zhu, W. ; Wang, W. ; Xu, H. ; Shi, J. *Mater. Chem. Phys.* **99**, 127 (2006).
- [24] Kiliç, Ç.; Zunger, A. *Phys. Rev. Lett.* **88**, 095501 (2002).
- [25] Kim, T.W.; Lee, D.U.; Yoon, Y.S. *J. Appl. Phys.* **88**, 3759 (2000).
- [26] Jeong, J.; Choi, S. P.; Chang, C. I.; Shin, D. C.; Park, J. S.; Lee, B. -T.; Park, Y.-J.; Song H-J. *Solid State Communications* **127**, 595–597 (2003).

- [27] Gu, F.; Wang, S. F.; Lu, M. K.; Cheng, X. F.; Liu, S. W.; Zhou, G. J.; Xu, D.; Yuan, D. R. J. of Crystal Growth **262**, 182–185 (2004).
- [28] Xing, G. Z.; Yi, J. B.; Wang, D. D.; Liao, L.; Yu, T.; Shen, Z. X.; Huan, C. H. A.; Sum, T. C.; Ding, J.; Wu, T. Phys. Rev. B **79**, 174406 (2009).
- [29] Yi, J. B.; Lim, C. C.; Xing, G. Z.; Fan, H. M.; Van, L. H.; Huang, S. L.; Yang, K. S.; Huang, X. L.; Qin, X. B.; Wang, B.Y.; Wu, T.; Wang, L.; Zhang, H. T.; Gao, X.Y.; Liu, T.; Wee, A. T. S.; Feng Y. P.; Ding, J. Phys. Rev. Lett. **104**, 137201 (2010).
- [30] Li, Y.; Deng, R.; Yao, B.; Xing, G.; Wang, D.; Wu, T. Appl. Phys. Lett. **97**, 102506 (2010).
- [31] Zhang, B. Y.; Yao, B.; Li, Y. F.; Liu, A. M.; Zhang, Z. Z.; Li, B. H.; Xing, G. Z.; Wu, T.; Qin, X. B.; Zhao, D. X.; Shan, C. X.; Shen D. Z. Appl. Phys. Lett. **99**, 182503 (2011).
- [32] Wang, H.; Yan, Y.; Li, K.; Du, X.; Lan, Z.; Jin, H. Phys. Status Solidi B **247**, 444 (2010).
- [33] Xing, G.; Wang, D.; Yi, J.; Yang, L.; Gao, M.; He, M.; Yang, J.; Ding, J.; Chien Sum, T.; Wu, T. Appl. Phys. Lett. **96**, 112511 (2010).
- [34] Bouzerar, G.; Ziman, T. Phys. Rev. Lett. **96**, 207602 (2006).
- [35] Rahman, G.; Garcia-Suarez, V. M. ; Hong, S. C. Phys. Rev. B **78**, 184404 (2008).
- [36] Du, X.; Du Y.; George, S. M. J. Vac. Sci. Technol. A **23**, 581 (2005).
- [37] Yan, H.; Chen, G.H.; Man, W.K.; Wong S.P.; Kwok, R.W.M. Thin Solid Films **326**, 88 (1998).

# Chapter 5

## Defect-induced $d^0$ Ferromagnetism and Photoluminescence of Template embedded 1D Oxide Nanowires

### 5.1. Preface

So far, in all previous chapters, we have discussed the role of magnetic ion-doping such as TM or RE ions in inducing ferromagnetism in SnO<sub>2</sub> and ZnO in which the magnetic moment are mainly originate from the unpaired electrons in the d or f shell of respective magnetic ion. However, room temperature ferromagnetism (RTFM) was also observed in pure SnO<sub>2</sub> nanorods (discussed in chapter 3) and also in SnO<sub>2</sub> thin films (discussed in chapter 4) which do not have any unpaired d or f electrons. Therefore, one obvious question arises that where from the magnetic moment is originating? As we have seen earlier in chapter 3, the RTFM observed in as-prepared pure SnO<sub>2</sub> nanorods was found to vanish when the sample is annealed at high temperature in O<sub>2</sub>. Magnetization was found to depend largely on particle size and most interestingly, no ferromagnetism was observed in bulk SnO<sub>2</sub>. This

indicates that structural defects might have playing a role to induce magnetism in such low dimensional (1D/2D) SnO<sub>2</sub>. Such kind of defect-induced ferromagnetism is known as “ $d^0$  ferromagnetism” as discussed in Chapter 1. During growth of one dimension (1D) nanostructures or two dimensional (2D) thin films, various structural defects can stabilize within such wide band oxides. Therefore, to investigate the origin of such unexpected magnetism, it is important to identify the presence of various defects within the materials.

Therefore, the stabilization and proper control on the defect-induced ferromagnetism in such wide band oxides can solve the problem regarding TM-based DMS and also can provide desired opportunity for appropriate spin functionality. In the present chapter, we have investigated the origin of  $d^0$  ferromagnetism and related photoluminescence properties in pure SnO<sub>2</sub> and ZnO nanowires (NWs) with considering the role of various nonmagnetic substitutional defects. The chapter moves as following: First, we have discussed about the origin of  $d^0$  ferromagnetism in pristine SnO<sub>2</sub> NWs by correlating the photoluminescence (PL) spectroscopy and electron paramagnetic resonance (EPR) studies [1]. Then the origin of RTFM in pure ZnO NWs and nonmagnetic potassium (K)-doped ZnO NWs is investigated considering the role of K-substitution [2]. Then we have shown how such RTFM can be stabilized, enhanced and tuned in ZnO using proper dopant or dopant combinations [3]. Finally, we will also discuss the magnetic, luminescence and electrical properties of different group-1A alkali metal (Li, Na and K)-doped ZnO thin films prepared by pulsed laser deposition (PLD) technique. Effect of film thickness and oxygen partial pressure of PLD chamber on the ferromagnetic, optical and electrical properties will also be discussed.

## 5.2 Arrays of pristine SnO<sub>2</sub> nanowires

### 5.2.1 Fabrication of SnO<sub>2</sub> nanowires

The arrays of SnO<sub>2</sub> nanowires were synthesized by an easy template assisted route, where the nanoporous anodic aluminium oxide (AAO) template was first fabricated by the controlled two-stage electrochemical anodization of aluminium foil (as discussed in chapter 2). After fabrication the AAO template, SnO<sub>2</sub> nanowires

(NWs) were synthesized within the pores of the AAO by a wet chemical template based sol-gel method [1]. A solution was prepared by adding 1.2 M urea in a saturated 0.2 M solution of  $\text{SnCl}_4 \cdot 5\text{H}_2\text{O}$  prepared in ethanol. After the solution was transformed into a transparent sol at RT the AAO template was immersed in the sol and left for four days. The sol containing the template was ultrasonicated several times in order to help the sol to reach inside the pores of AAO. Taking out the template from the solution the sol was removed carefully from its surface and the template was dried under IR source. Finally  $\text{SnO}_2$  NWs were obtained by annealing the template at  $450^\circ\text{C}$  in air inside a furnace for 2 h.

Field emission scanning electron microscope (FESEM, FEI Helios Nanolab-600) was used to study the morphology of the as grown  $\text{SnO}_2$  NWs by partially removing the AAO template in 2 M NaOH solution. X-ray diffraction (XRD, X'Pert Pro, Panalytical) was used to obtain the crystallographic information of the template embedded  $\text{SnO}_2$  NWs. Chemical composition of the NWs was determined by energy dispersive x-ray (EDAX) attached with the FESEM. PL measurement of the template embedded NWs was carried out by using a spectrofluorometer (Horiba Jobin Yvon, Fluorolog-3) having Xe lamp source. The EPR (Jeol JES-FA100) studies were conducted on the released  $\text{SnO}_2$  NWs. Temperature dependent magnetic measurements of the aligned arrays of undoped  $\text{SnO}_2$  NWs were carried out by using a vibrating sample magnetometer (VSM, Lakeshore, model 7144) in the temperature range of 80 to 300 K.

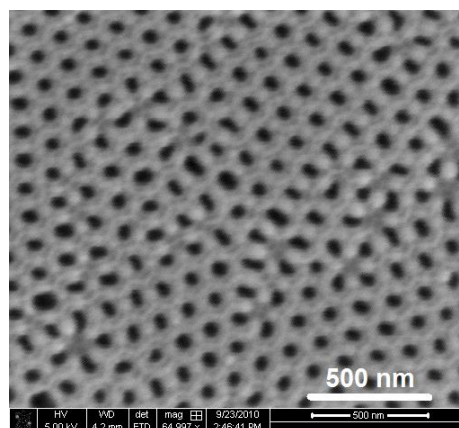


**Fig. 5.1:** FESEM image of Anodic aluminium oxide (AAO) template used to deposition for  $\text{SnO}_2$  NWs

## 5.2.2 Results and discussion

### 5.2.2.1 Study of morphology and crystallography

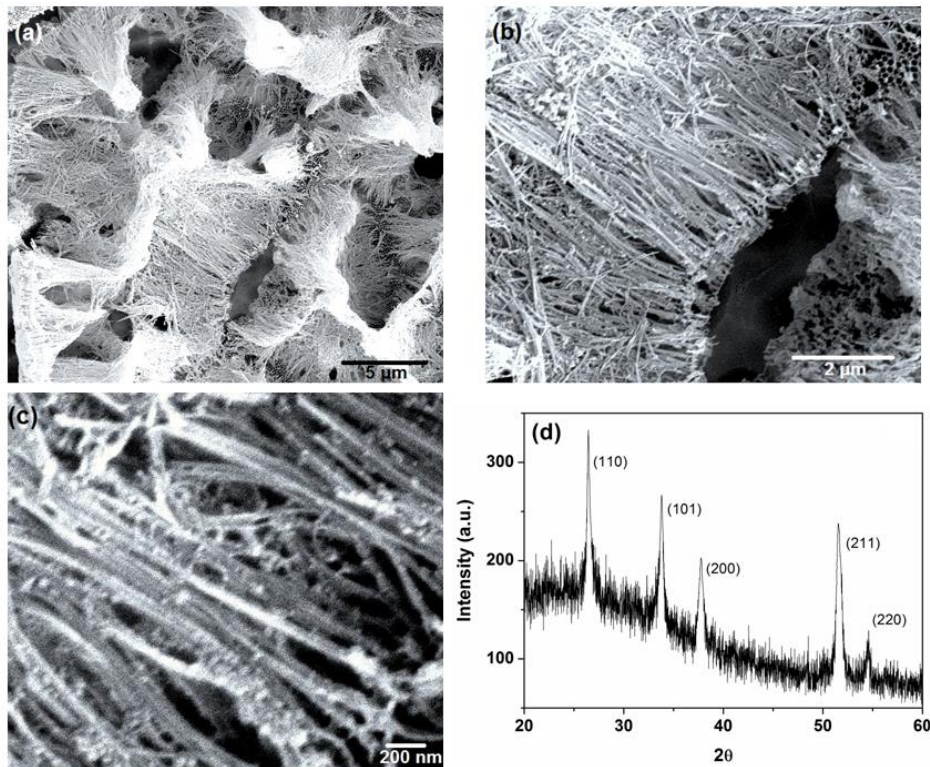


**Fig. 5.2 :** FESEM micrographs of the as prepared pure SnO<sub>2</sub> NWs released from the AAO template at different magnifications (a) to (c). (d) XRD pattern of the pure SnO<sub>2</sub> NWs.

The FESEM micrographs of the different magnification of the arrays of SnO<sub>2</sub> NWs released from the AAO template is shown in Fig. 5.2. The large aspect ratio NWs are prepared in this method. The as grown NWs of uniform diameter are evident from Fig. 5.2 (b) and (c). The diameter of the NWs is about 50 nm, which is found to be very close to the diameter of the pores of the prepared AAO template. The XRD pattern of the as grown pristine SnO<sub>2</sub> NWs is shown in Fig. 5.2 (d), which indicates pure rutile type crystal structure of the NWs (JCPDS card no. 41-1445) and the NWs are polycrystalline in nature. The EDAX analysis confirms the formation of SnO<sub>2</sub> NWs within AAO template.

### 5.2.2.2 Photoluminescence study

PL spectroscopy is an exciting tool to investigate the defect-related emissions from the semiconductors. The RT PL emission spectrum of the template embedded SnO<sub>2</sub> NWs is recorded under an excitation of 450 nm light from a Xe lamp is shown in Fig. 5.3. The AAO template provides a broad blue emission band centered at 430 nm because of the oxygen vacancy related defects [4]. It is found that the SnO<sub>2</sub> NWs provide luminescence in the green-yellow wavelength region centered around 510 nm. Generally, SnO<sub>2</sub> nanostructures exhibit emission bands between 450-600 nm because of the crystalline defects induced during the growth [5-7]. Sn vacancies ( $V_{Sn}$ ) and  $V_O$  defects are the main structural defects appeared in the SnO<sub>2</sub> nanostructures during their fabrication and it is believed that they generate trapping states in the band gap leading to luminescence in the visible wavelength region [5].

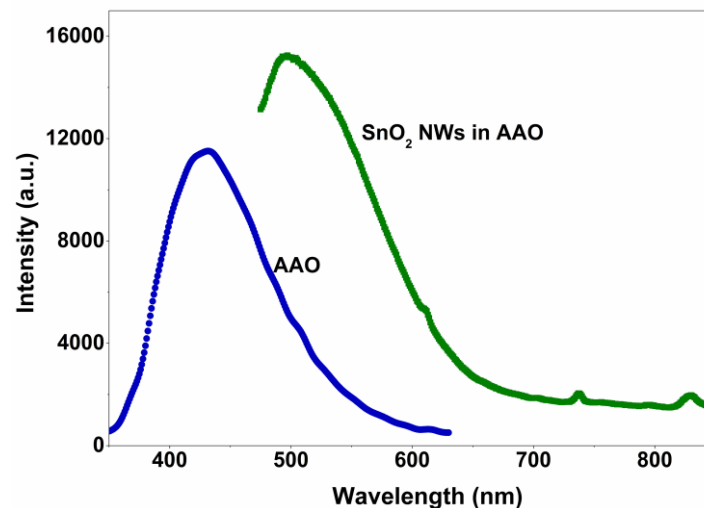


**Fig. 5.3:** Room temperature PL spectra of the AAO template and the pure SnO<sub>2</sub> NWs embedded in the AAO template.

However, because of the high formation energy of  $V_{Sn}$  it is expected that the concentration of the  $V_{Sn}$  defects in the pure SnO<sub>2</sub> should be much lower than that of the  $V_O$  defects [8]. In this regard the luminescence from SnO<sub>2</sub> nanostructures in the visible green-yellow wavelength region is ascribed to the  $V_O$  related defects [6, 7, 9-11]. These  $V_O$  can introduce defect levels situated in the band gap and make a contribution to the mid-gap luminescence activities. The green or green-yellow luminescence from the SnO<sub>2</sub> NWs in our experiment is believed to be originated

from the trapped state electronic transition related to the  $V_O$  defects [9, 10]. However, there are three kinds of  $V_O$  defects namely oxygen vacancies without trapped electron or neutral oxygen vacancies ( $V_O^0$ ), singly ionized oxygen vacancies ( $V_O^*$ ) and doubly ionized oxygen vacancies ( $V_O^{**}$ ). As the  $V_O^{**}$  defects introduce very shallow donor state [12] hence, it is expected that the yellow-green visible light emission occurs due to the  $V_O^*$  acceptor state. Very recently, Kar *et al.* [13] have elaborately demonstrated the possible luminescence mechanism of the  $\text{SnO}_2$  NWs and the studies indicate that the  $V_O^*$  defects introduces a deep level mid gap defect state [14] responsible for the yellow-orange luminescence from  $\text{SnO}_2$  NWs. Correlating our experimental result with these recent reports, we firmly believe that the characteristics visible green-yellow luminescence from the pristine  $\text{SnO}_2$  NWs found in our work is originated from the  $V_O^*$  defects, most probably situated in the band gap at nearly 2.4 eV above the valence band.

### 5.2.2.3 Electron paramagnetic resonance spectroscopy

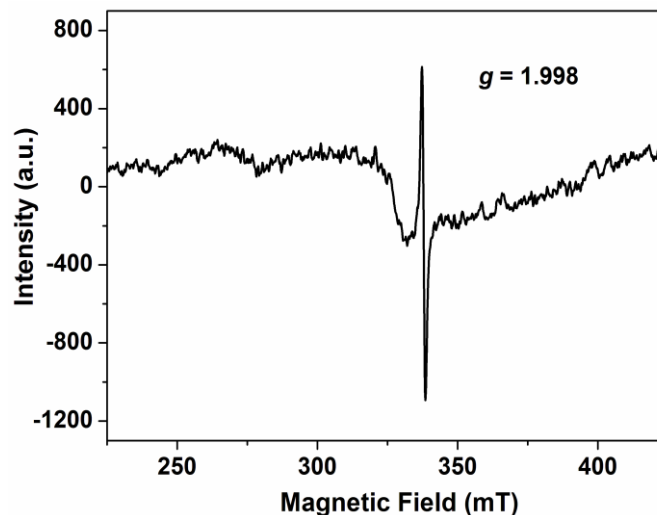


**Fig. 5.4:** The EPR spectrum of the as prepared pristine  $\text{SnO}_2$  NWs released from the AAO template.

The EPR spectroscopy is an efficient experimental technique to investigate the different kinds of structural defects like of  $V_O$  defects present in the materials. The as prepared pure  $\text{SnO}_2$  NWs were studied by EPR (see Fig. 5.4) and by calculating the  $g$

factor (EPR parameter) using Eq. 1, it is possible to get an account of the type of  $V_O$  defects.

$$g\mu_B H = h\nu \quad (5.1)$$

Where,  $H$  is the magnetic field (gauss),  $\nu$  is the frequency (Hz),  $\mu_B$  is the Bohr magneton equal to  $9.274 \times 10^{-21}$  erg/Gauss, and  $h$  is Planck's constant,  $6.626 \times 10^{-27}$  erg-s/cycle.

From the above calculation an EPR signal of  $g = 1.998$  appears from the pure  $\text{SnO}_2$  NWs. Recently, Özcan *et al.* [15], have shown that the  $\text{Sn}^{+4}$ ,  $\text{Sn}^{+2}$ ,  $V_O^0$  and  $V_O^{**}$  defect states have an even number of electrons and these are ESR-silent singlets. Furthermore, based on the DFT calculations they also have demonstrated that the  $g$  factor around 2.00 can appear because of the  $V_O^*$  defects in the  $\text{SnO}_2$  and this defect is only ESR active [15]. Popescu *et al.* [16] and Kar *et al.* [11] have also attributed the ESR signal with the  $g$  factor around 2.00 to  $V_O^*$  defects in undoped  $\text{SnO}_2$  nanostructures. Therefore, our EPR spectroscopy result with  $g$  factor close to 2 for the pristine  $\text{SnO}_2$  NWs suggests that this signal is originated from the  $V_O^*$  defects in the NWs, which are believed to be the recombination centres for the luminescence processes [11]. Considerably large concentration of the  $V_O^*$  luminescent centres present in the  $\text{SnO}_2$  NWs is attributed to the visible light emission (trap emission) in the green-yellow region. The EPR study indicates the presence of large concentration of  $V_O^*$  defects in the  $\text{SnO}_2$  NWs fabricated in our work.

#### 5.2.2.4 Magnetic properties of $\text{SnO}_2$ NWs

Figure 5.5 shows the hysteresis loops of the as prepared pure  $\text{SnO}_2$  NWs embedded AAO template at room temperature (300 K). A clear evidence for FM is observed in the as grown pristine  $\text{SnO}_2$  NWs with low saturation magnetic field ( $\sim 2000$  Oe). In the inset of Fig. 5.5 the  $M-H$  loops of the pure  $\text{SnO}_2$  NWs at 300 and 80 K are shown after subtracting the background diamagnetic signal arising from AAO template. The RTFM has been reported in the undoped wide band gap semiconductor thin films and nanoparticles like  $\text{ZnO}$ ,  $\text{TiO}_2$ ,  $\text{CeO}_2$ ,  $\text{SnO}_2$ ,  $\text{In}_2\text{O}_3$  and

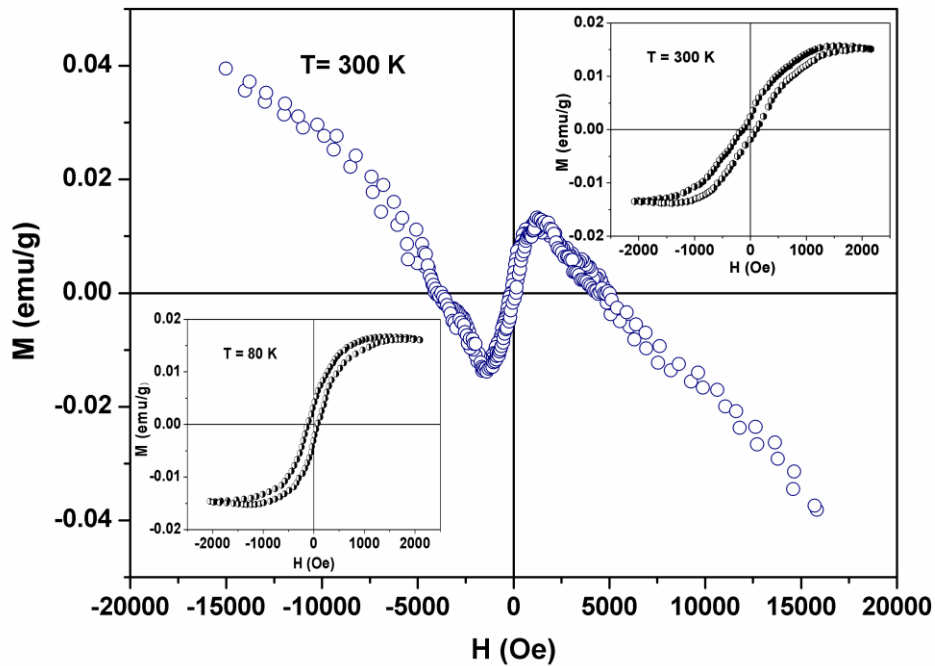


**Fig. 5.5:** Magnetic hysteresis loop of the as prepared pristine SnO<sub>2</sub> NWs measured at 300 K. The insets show the hysteresis loops of pure SnO<sub>2</sub> NWs at 300 and 80 K after subtracting the background diamagnetic signal.

Al<sub>2</sub>O<sub>3</sub>, where the origin of the FM is addressed based on the oxygen vacancy defects [9, 17, 18]. According to Sundaresan *et al* [9] the RTFM is a general feature for all the oxide semiconductor nanoparticles and they assumed that this is because of exchange interactions between localized electron spin moments of the oxygen vacancies at the surface of the nanoparticles. For ZnO thin films and nanostructures the Zn vacancies ( $V_{Zn}$ ) have also been suggested to have localised moment and the cation vacancy defects have been attributed to the ferromagnetic ordering [19]. However, studies show that among the oxygen vacancy defects, the  $V_{O}^{**}$  centres, which are the shallow donors, form a  $1s^2$  singlet state and can only establish weak antiferromagnetic ordering [14]. Coey *et al.* [14] has reported that the cation vacancies and the adjacent  $V_{O}^*$  centres ( $F^+$  centres) or  $V_{O}^*$  centre clusters form a triplet state and can initiate defect related hybridization causing charge transfer from a donor-derived impurity state to the unoccupied states at the Fermi energy level to establish a long-range ferromagnetic interaction. In our work, it is expected that the concentration of the cation vacancy defects (Sn vacancies,  $V_{Sn}$ ) should be low because of their high formation energy and hence the concentration should be much

below the required percolation threshold to mediate long-range ferromagnetic ordering in pristine  $\text{SnO}_2$  NWs [10]. Here, we have not traced the presence of significant amount of Sn vacancies, hence we believe that the  $V_{\text{O}}^*$  centre defect clusters are responsible for the FM ordering in pure  $\text{SnO}_2$  NWs. The presence of the high concentration of the  $V_{\text{O}}^*$  defects in the  $\text{SnO}_2$  NWs fabricated in this work has already been confirmed from the earlier PL and EPR spectroscopy studies. The high concentration of the  $V_{\text{O}}^*$  centre defects would possibly promote the formation of the  $V_{\text{O}}^*$  defect clusters (anion vacancy clusters), which can induce magnetization through the defect band related hybridization at Fermi level causing localized electron spin moments.

## 5.3 Nonmagnetic Potassium (K)-doped ZnO NWs

In present section, we will discuss about the role of nonmagnetic group-1 alkali metal-doping in stabilizing room-temperature (RT)  $d^0$  FM in one-dimensional (1D) ZnO such as nanowires (NWs). ZnO nanostructures or thin films are generally enriched with different types of intrinsic point defects or lattice imperfections. The most common lattice defects in ZnO are zinc vacancies, oxygen vacancies, zinc interstitials, zinc antisites, oxygen interstitials and oxygen antisites [20]. Generation of these defects depends upon the sample preparation conditions as well as on the type of the dopants used. Doping in ZnO can also lead to the formation of structural inhomogeneity. Some of the intrinsic defects or structural imperfection have significant role behind the magnetic origin of the ZnO nanostructures and thin films. Therefore, proper understanding of defect-induced  $d^0$  FM in ZnO is very important in order to fabricate ZnO based DMS. Here, we have synthesized pure ZnO, K-doped ZnO NWs by an easy wet chemical template assisted route using nanoporous anodic aluminium oxide (AAO) as template [2]. The magnetic properties are studied in details by correlating photoluminescence (PL) and x-ray photoelectron spectroscopy (XPS).

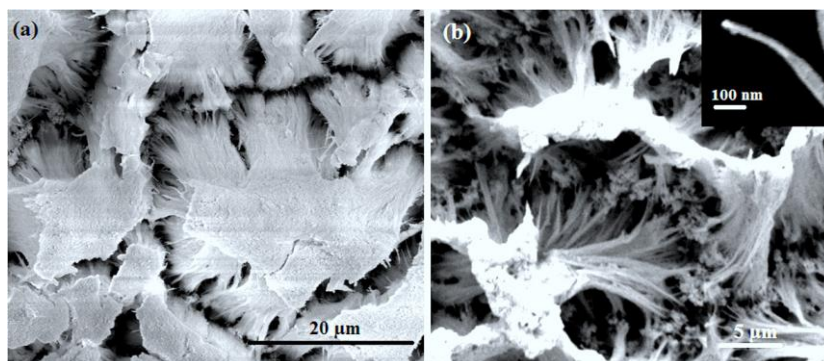
### 5.3.1 Fabrication of K-doped ZnO NWs

Arrays of un-doped and K-doped ZnO NWs were fabricated within the pores of the AAO template (see Fig. 5.1) by employing a simple wet chemical method. The

arrays of ZnO NWs were grown by dipping the template into a saturated 0.1 M solution of  $\text{Zn}(\text{CH}_3\text{COOH})_2 \cdot 2\text{H}_2\text{O}$  prepared in ethanol followed by drying and annealing of the template. For the fabrication of various (2, 4 and 8 at.%) K-doped ZnO NWs selective amount of potassium acetate was added in the zinc acetate solution in appropriate ratios. AAO templates were immersed in these mixed solution and left for five days so that the solution can reach inside the nanopores. Surface of the templates were washed very carefully in order to remove the mixed acetate solution from surface. All the templates dipped in the zinc acetate and the mixed acetate solution were dried in room temperature and annealed in air at  $450^\circ\text{C}$  for 2 h. During annealing the arrays of ZnO NWs and K-doped ZnO NWs were grown within the pores of AAO through the decomposition of the acetate salts.

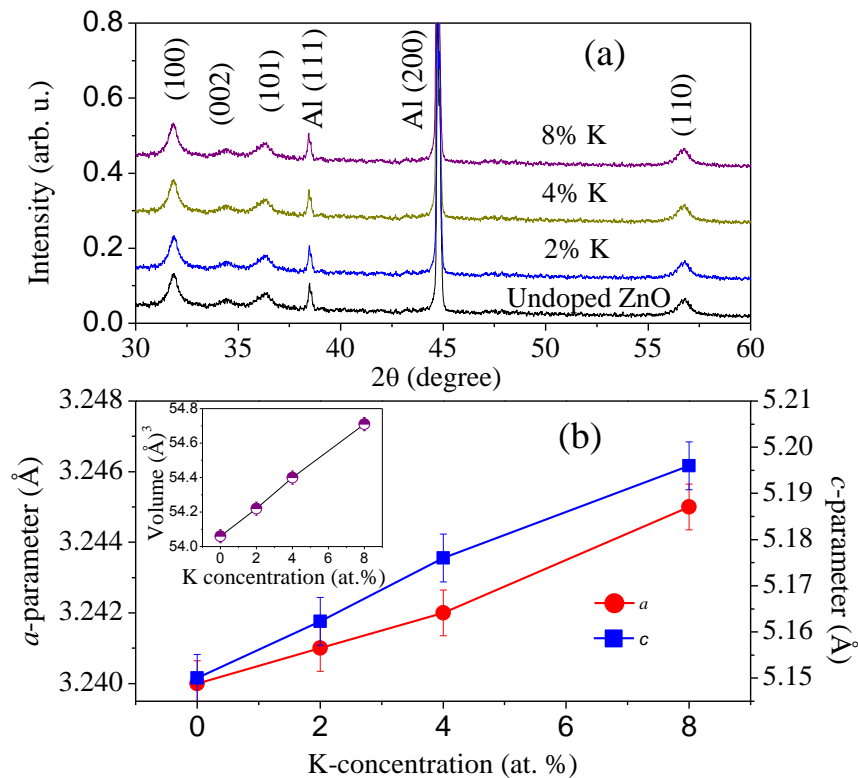
### 5.3.2 Morphology and crystal structure

Figure 5.6 (a) shows the representative low magnification FESEM image of the bunch of as prepared 4 at.% K-doped ZnO NWs released from AAO template. The high magnification FESEM image of the same is shown in Fig. 5.6 (b) and the inset of Fig. 5.6 (b) shows the FESEM image of a single broken NW. The diameter of NWs is about 50 nm, which is found to be very close to the diameter of the pores of the AAO. The elemental composition obtained from the EDAX analysis indicates the presence of 1.94, 3.89 and 7.09 at.% K in ZnO NWs host and it is less than the nominal percentage 2, 4 and 8, respectively.



**Fig. 5.6:** (a) Low and (b) high magnification FESEM images of 4% K-doped ZnO NWs partially released from AAO. The inset shows a broken single NW.

XRD patterns of un-doped and the K-doped ZnO NWs are shown in Fig. 5.7 (a), which indicates hexagonal wurzite crystal structure of ZnO. All the NWs are found to be polycrystalline in nature. The lattice parameters of the hexagonal unit cell for all the K-doped ZnO NWs are estimated using Bragg's diffraction law. The variation of lattice parameters ( $a$  and  $c$ -parameters) are plotted in Fig. 5.7 (b). Both the lattice parameters  $a$  and  $c$  are found to increase almost linearly with K concentration, which ascertains the substitution of K ions replacing Zn ions. However, a close inspection shows that the change in  $c$ -parameter is more rapid than  $a$ -parameter. The result indicates that the majority of K ions are substituted along  $c$ -axis of the unit cell resulting significant elongation of the  $c$ -parameter. Consequently, an expansion of lattice volume ( $a^2c$ ) is also observed in K-doped ZnO NWs (see inset of Fig. 5.7 (b)). The expansion of lattice volume is due to the substitution of large  $K^{1+}$  ions (151 pm) replacing the relatively small  $Zn^{2+}$  ions (74 pm). The strong diffraction peaks at  $2\theta$  values of 38.48 and 44.84 appear from the electropolished Al substrate underneath AAO template.



**Fig. 5.7:** (a) XRD patterns of un-doped and K-doped ZnO NWs. (b) Lattice parameters ( $a$  and  $c$ ) and lattice volume (inset) of K-doped ZnO NWs as a function of K doping concentration.

### 5.3.3 Photoluminescence properties

PL spectroscopy has been employed extensively to study the optical properties of a variety of ZnO nanostructures. Generally, at room temperature ZnO nanostructures exhibit luminescence in the UV region as well as in the blue-green, green and yellow regions because of the crystalline defects and/or impurities [21-23]. The RT PL spectra of the as prepared pure and K-doped ZnO NWs embedded in AAO are shown in Fig. 5.8 (a). AAO template itself provides a broad blue emission band centered around 2.9 eV as shown in Fig. 5.8 (b) due to the presence of oxygen vacancy defects as reported previously [4, 24]. Both the un-doped and K-doped ZnO NWs provide a UV emission near 3.37 eV, which is attributed to the near band edge (NBE) electronic transition and/or the free exciton recombination through an exciton-exciton collision process [21, 25]. It is evident from Fig. 5.8 (a) that K-doping results in the enhancement of intensity of the NBE UV emission in doped NWs and the 4% K-doped ZnO NWs provide strongest UV luminescence.

An extra emission peak is found to appear at 3.21 eV with the introduction of K in ZnO. The emission peak near to the ZnO band edge is quite expectable because of the electronic transition from conduction band minimum (CBM) to the shallow  $K_{Zn}$  acceptor levels [26, 27]. The presence of the shallow  $K_{Zn}$  acceptor states can push the ZnO system from n-type to p-type direction [26]. Looking at the intensity of the peak it is clear that maximum amount of K ions are substituted at Zn site in case of 4 at.% K-doped NWs. For higher K-doping, the substitution process might get saturated and K ions can move to lattice interstitial ( $K_i$ ) position which acts as a donor [26, 27] and thereby can reduce the p-type nature of ZnO. Therefore, the hole concentration should maximum in the 4 at.% K-doped ZnO NWs compared to the others.

The un-doped and K-doped ZnO NWs exhibit a green deep level emission (DLE) peak centered at 2.43 eV. However, the reason behind the origin of this well known green emission of ZnO nanostructures is still highly controversial and it is believed that it may not be due to a single source of luminescence. Among the several hypotheses, the oxygen vacancy related defects are made responsible for the visible green emission [28], but the other in-depth investigations have revealed that the green luminescence of ZnO nanostructures is mainly related to the  $V_{Zn}$  rather than the  $V_O$  defects [20, 29, 30]. Generally, oxygen vacancy defect related

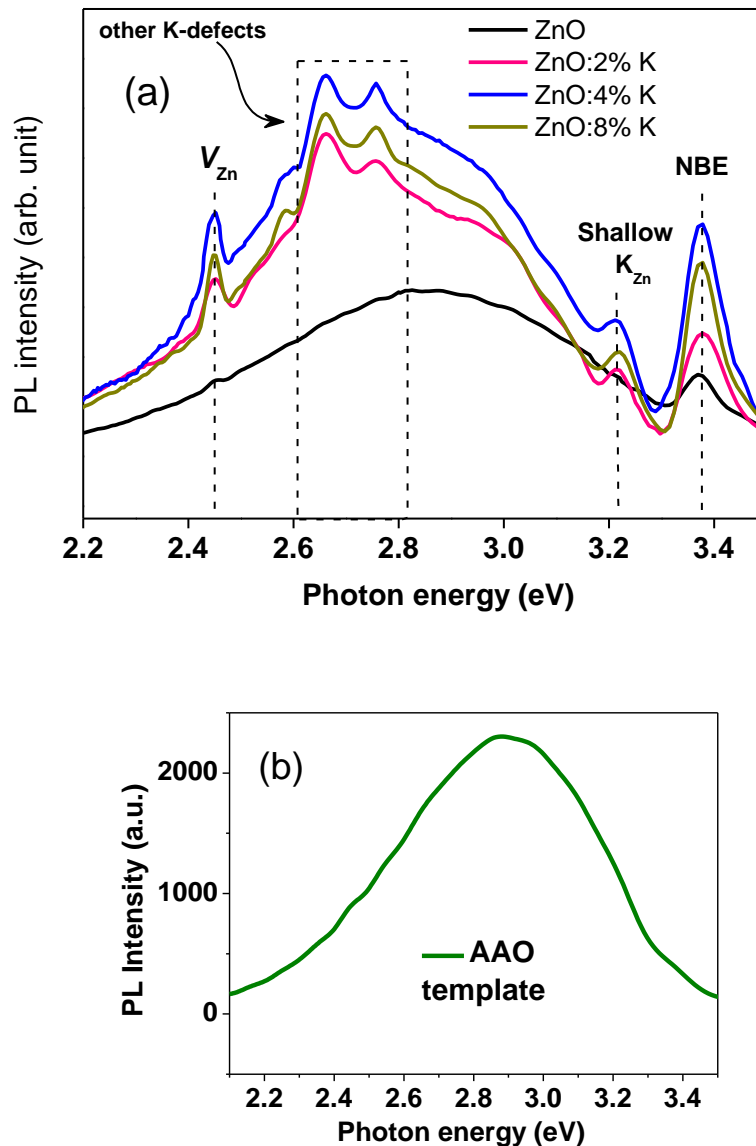


**Fig. 5.8:** (a) Room temperature PL spectra of the aligned un-doped ZnO and K-doped ZnO NWs embedded in the AAO template. (b) PL spectra of AAO template.

luminescence bands for ZnO nanostructures appear at higher wavelength region [31]. However, it is reported that the  $V_{Zn}$  have low formation energy under  $n$ -type conditions [20], which indicates that the annealing conducted in air in order to synthesize the ZnO NWs promotes the formation of  $V_{Zn}$  [32]. Therefore, the ZnO NWs grown in this work should contain large amount of  $V_{Zn}$  defect. Recently, Yi *et al.* [33] demonstrated that the formation energy of the  $V_{Zn}$  decreases because of Li doping in ZnO matrix and hence the  $V_{Zn}$  are stabilized [20]. However, it is

interesting to notice that in our experiment, the intensity of the green luminescence peak of the pure ZnO NWs is significantly low. Whereas, the green emission peak becomes sharper in case of the K-doped ZnO NWs and its intensity increases with the increase of the K concentration up to 4 % K-doping. These results indicate that the K-doping in ZnO NWs promotes the formation of more  $V_{Zn}$  and hence helps the NWs to exhibit enhanced luminescence in the green wavelength region. Therefore, correlating our experimental evidences with these reports, we believe that the green emission of the un-doped and K-doped ZnO NWs can be ascribed to the  $V_{Zn}$ .

K-doped ZnO NWs also exhibits few intense blue-green emission peaks at 2.6-2.8 eV, which are not present in the PL spectrum of the un-doped ZnO NWs. Therefore, the blue-green emissions of the K-doped ZnO NWs might have originated from different K-defects such as K substitutional ( $K_{Zn}$ ) and/or K interstitials ( $K_i$ ) [34]. The 4% K-doped NWs exhibit strongest blue-green luminescence characteristics among the all K-doped ZnO NWs samples. Therefore, K-doping in ZnO NWs leads to significant enhancement in the PL.

### 5.3.4 Magnetic properties of K-doped ZnO NWs

Figure 5.9 (a) and (b) show the hysteresis (M-H) loops of the un-doped and K-doped ZnO NWs at 300 and 80 K, respectively. The magnetic signal of the aligned ZnO NWs was obtained after subtracting the magnetic response of the AAO template. It is evident that the un-doped ZnO NWs exhibit FM at RT and at low temperature. Interestingly, ferromagnetic response is found to enhance after K-doping in ZnO NWs. The magnetic moment increases initially with the increase of K concentration upto 4 % K-doping and then decreases with further doping. The maximum saturation magnetization ( $M_s$ ) of 0.38 emu/g has been obtained for 4 % K-doped ZnO NWs at  $T = 300$  K. Figure 5.9 (c) shows the temperature dependence of magnetization of the un-doped and 4% K-doped ZnO NWs. The Curie temperature ( $T_c$ ) of un-doped and 4% K-doped ZnO NWs is 386 and 516 K, respectively. The variation of  $T_c$  with K concentration is shown in Fig. 5.9 (d). It is found that the  $T_c$  of the K-doped ZnO NWs also increases with the increase of K concentration in ZnO NWs up to 4% K-doping and then decreases with further doping, which follows the similar trend of the saturation magnetization. Therefore, an optimum K

concentration of 4% can be defined, where ferromagnetic properties of K-doped ZnO NWs became strongest.

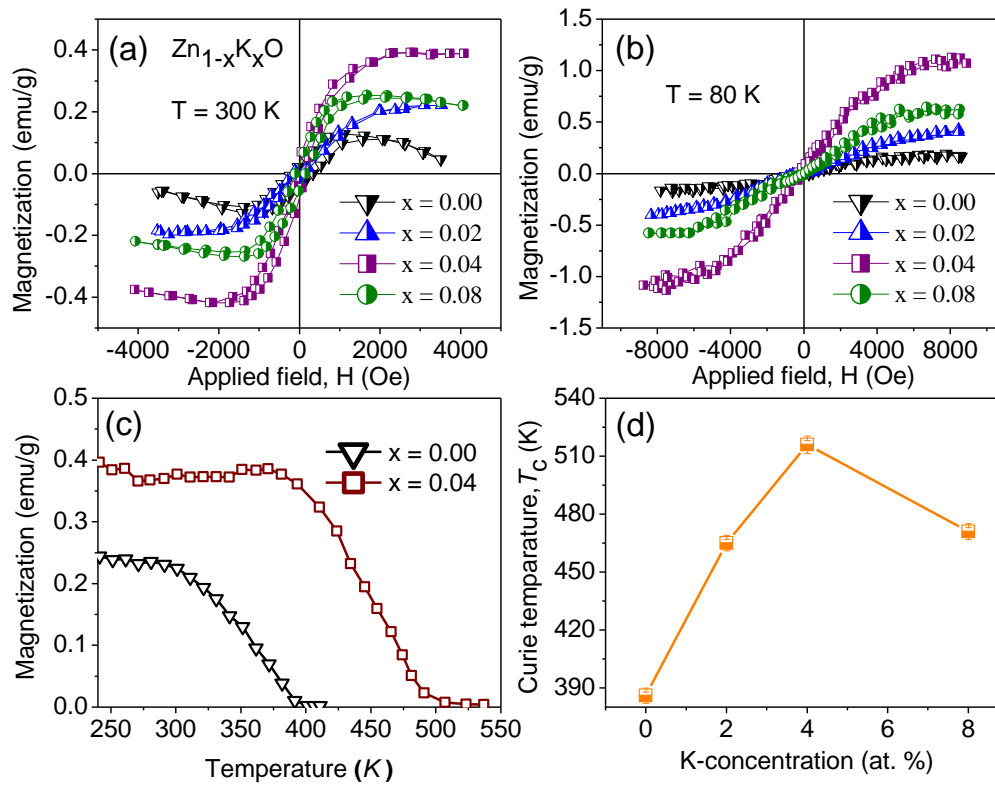


**Fig. 5.9:** Magnetic hysteresis (M-H) loops for un-doped and K-doped ZnO NWs measured at (a) 300 and (b) 80 K after subtracting the diamagnetic response of the AAO template (c) Temperature dependence of magnetization for un-doped ZnO and 4 % K-doped ZnO NWs and (d) Estimated Curie temperature ( $T_c$ ) as a function of K-concentration.

Here, we demonstrate that the origin of the FM in the pristine ZnO NWs is because of the  $V_{Zn}$  defect. This kind of cation vacancy defects can grow in the ZnO NWs during its fabrication through annealing at high temperature under oxygen rich condition and their signature is also confirmed from the PL measurements. However, in ZnO,  $V_O$  is also a common defect and the  $V_O$  clusters can also introduce moments in the system [35, 36]. Therefore, the influence of  $V_O$  clusters in the FM of ZnO NWs is also considerable. Although in our experiment the major contribution to the ferromagnetic response of the un-doped ZnO NWs is believed to be due to the presence of cation vacancies ( $V_{Zn}$ ). However, an interesting correlation between the

nature of  $M_s$  and the green emission intensity ( $I_G$ ) should be noticed for the K-doped ZnO NWs, where both of them increase with the increase of K concentration in ZnO up to 4% K-doping (see Fig. 5.10). Additionally, earlier PL measurements of K-doped ZnO NWs (see Fig. 5.8) indicate that significant amount of  $K_{Zn}$  and/or  $K_i$  defects are also present in the NWs. Therefore, formation of defect combination like  $K_{Zn}$  and/or  $K_i$  lowers the formation energy of each Zn vacancy and hence stabilizes  $V_{Zn}$ , similar to the case of Li-doped ZnO thin films [33]. With the increase of K-doping in ZnO NWs more  $K_{Zn}$  and/or  $K_i$  defects are likely to form and hence more  $V_{Zn}$  are grown (evident from PL spectra), which results into enhancement in the magnetization. The 4% K-doped ZnO NWs have largest amount of K related defects as well as  $V_{Zn}$  defects. Therefore, the 4% K-doped ZnO NWs exhibit the strongest FM signature because of the large concentration of  $V_{Zn}$  defects. However, the decrease of  $V_{Zn}$  concentration and consequently the magnetization beyond 4% K-doping suggests that the formation of  $V_{Zn}$  depend upon the relative abundance of  $K_{Zn}$  and/or  $K_i$  defects. The observed correlation between the  $V_{Zn}$  concentration and saturation magnetization fairly suggest that the origin of FM is related to  $V_{Zn}$ . Some important estimated values for the K-doped ZnO NWs are summarized in the Table I.

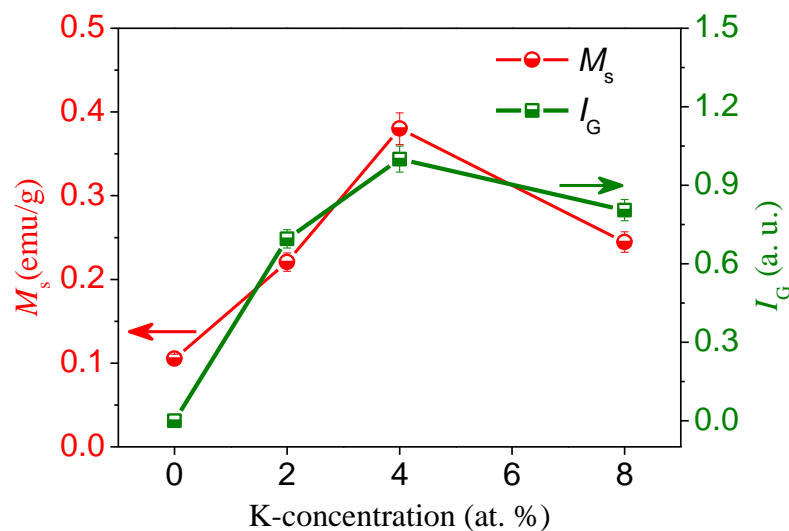


**Fig. 5.10:** Change in saturation magnetization ( $M_s$ ) and relative intensity of green emission peak ( $I_G$ ) of the NWs with K-concentration.

TABLE I. Typical estimated values of lattice volumes, relative intensity of green emission ( $I_G$ ) of PL spectra, saturation magnetization ( $M_s$ ), coercivity ( $H_c$ ), retentivity ( $M_r$ ), and Curie temperature ( $T_c$ ) for un-doped and K-doped ZnO NWs.

NWs	K % (nominal) (at. %)	Lattice volume ( $\text{\AA}$ ) <sup>3</sup>	Relative Intensity of green emission peak $I_G$ (a.u.)	Saturation magnetization $M_s$ (emu/g) at 300 K	Coercivity $H_c$ (Oe)	Retentivity (emu/g)	Curie temperature $T_c$ (K)
ZnO	0	54.06	0.05	0.10	256	0.03	386
ZnK2	2	54.22	0.69	0.22	93	0.02	465
ZnK4	4	54.40	1.00	0.38	99	0.05	516
ZnK8	8	54.71	0.81	0.24	124	0.04	471

For further confirmation about the magnetic origin in K-doped ZnO NWs, we have re-annealed the as grown NWs again at 500°C in O<sub>2</sub> atmosphere and measured the M-H loops. Figure 5.11 shows the RT M-H loops for the as grown and annealed 4 and 8% K-doped ZnO NWs. It is interesting to notice that the magnetization has enhanced slightly for both the samples after annealing in O<sub>2</sub> atmosphere. Moe Børseth *et al.* [30] have demonstrated that the high temperature annealing in O-rich condition decreases  $V_O$  concentration, whereas the  $V_{Zn}$  concentration may increase. If the origin of magnetic moment were associated with  $V_O$  defects, then the magnetization should have been decreased after annealing in O<sub>2</sub> atmosphere. But that was not happened in our experiment. Therefore, enhancement of magnetization in annealed NWs certainly confirms the  $V_{Zn}$  induced ferromagnetism in K-doped ZnO NWs.

It has been reported that the magnetic moment in the ZnO NWs is originated from unpaired  $2p$  electrons of O atom in the immediate vicinity of  $V_{Zn}$  [37]. The substitutional defects (like  $K_{Zn}$ ) originated due to the doping of group-I elements as well as the  $V_{Zn}$  introduce holes in the system and the ferromagnetic interaction can be mediated by these holes between the magnetic moments of  $V_{Zn}$  to have a long range interaction [33]. The model proposed by Bouzerrer and Ziman [38] have shown the dependency of vacancy-induced local magnetic moment and magnetic coupling required by long-range ordering described via a single correlated band of oxygen orbitals with additional random potentials. This type of potential arises due to the substitutional defects and density of vacancies present in the matrix. For small potential antiferromagnetic nearest neighbour coupling exists. As the potential increases, ferromagnetic coupling begins to dominate but with further increase of potential or substitutional defect concentration, coupling becomes antiferromagnetic again. They predicted that a well defined region of potential, defect concentration, as

well as carrier density exists where the ferromagnetism with high temperature is possible with few percentages of vacancies or substitutional defects like Li, Na, K etc. Beyond the optimum window of defect concentration, magnetic moment as well as  $T_c$  vanishes as the magnetic couplings are destroyed by Rudermann-Kittel-Kaysa-Yashida type oscillations or antiferromagnetic superexchange. Here in our study we also have observed that up to 4% K-doping the  $T_c$  increases and then decreases on further K-doping. With the increase of K-doping in ZnO the hole concentration should increase in the matrix and after an optimum hole concentration the ferromagnetic ordering is destroyed gradually resulting in decrease of magnetic moment as well as  $T_c$  beyond 4%-K doping in the ZnO NWs.

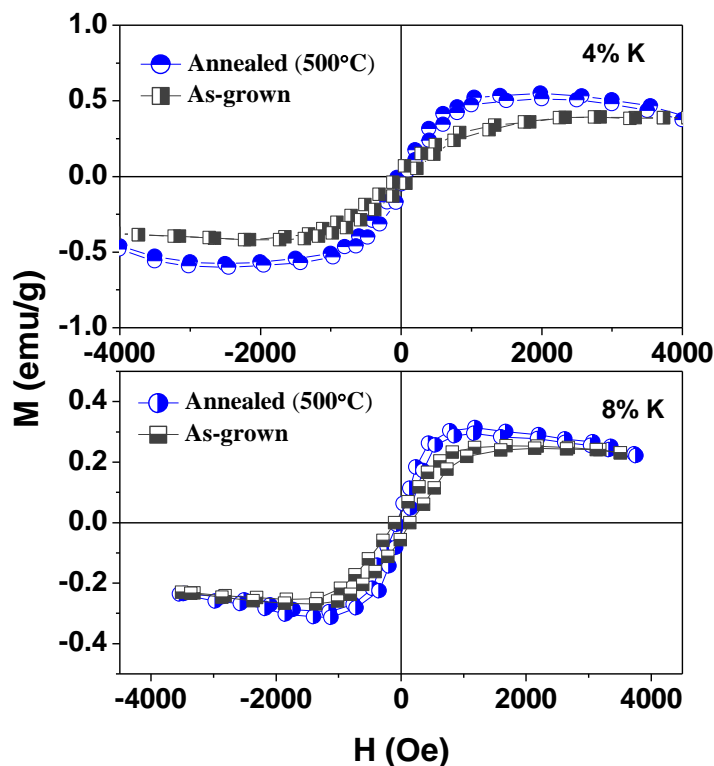


**Fig. 5.11:** RT M-H loop for the as-prepared and annealed (a) 4% and (b) 8% K-doped ZnO NWs in O-rich atmosphere.

## 5.4 Nitrogen (N)/Fluorine (F) and Lithium (Li) codoped ZnO NWs: Evidence of hole-mediated $d^0$ ferromagnetism

In previous section, Zn vacancy-induced  $d^0$  ferromagnetism in ZnO NWs is found to stabilize with the substitution of non-magnetic group-1A element K. Substitutional of K at Zn site introduces a hole which mediates the ferromagnetic exchange interaction between the two nearest  $V_{Zn}$  defects. Here, we have investigated the effect of n/p-type doping on ferromagnetic and luminescence properties of Li-doped ZnO NWs [3]. Nitrogen (N) is generally known to be p-type dopant of ZnO which donates hole to the valence band. However, it is found difficult to achieve p-type ZnO by N doping alone due to the huge compensation effects [39]. In this regard, co-doping of N along with Li can be very effective to achieve better p-type conduction in ZnO [40]. On the other hand, F is known as n-type dopant of ZnO which donates electron to the conduction band [41]. Therefore, the concentration of excess charge carriers (electron/hole) in Li-N/F-codoped ZnO NWs can be used as an important parameter to enhance and tune the RT  $d^0$  ferromagnetic and luminescence properties of doped ZnO.

### 5.4.1 Fabrication of Li-N/F codoped ZnO NWs

Similar to K-doped ZnO NWs, Li doped, Li-N and Li-F co-doped ZnO NWs are fabricated by wet-chemical template assisted route using AAO as template. The arrays of pure ZnO NWs have been grown by dipping the AAO template into a saturated 0.1 M solution of Zn acetate prepared in ethanol. Estimated amount of high purity (99.999%) lithium acetate ( $CH_3COOLi$ ), ammonium acetate ( $CH_3COONH_4$ ) and ammonium fluoride ( $NH_4F$ ) salt are used to prepare the precursor solution for the preparation of 6 at.% Li, Li-N and Li-F co-doped ZnO NWs. The AAO templates (5×5 mm) are immersed in these mixed solutions and left for five days so that the solution can reach inside the nanopores of the template. Afterwards, taking the templates out of the solutions the surface of the templates has been washed very carefully in order to remove the solution from surface and then dried in oven at 80°C and also annealed in air at 450°C for 2 h. During annealing the arrays of undoped, Li-doped, Li-N and Li-F co-doped ZnO NWs are grown within the pores of AAO through the thermal decomposition of the acetate salts. The N

dopant concentrations are varied from 2 to 15 at.% and F concentration is changed from 2 to 10 at.% while the Li concentration is kept fixed at 6 at.% in all the Li-N/F co-doped ZnO NWs. The 6 at.% N and F doped ZnO NWs (with no Li-doping) are also fabricated for the better understanding of the results. For easy description in this text, we have termed all the ZnO NWs with corresponding identification (Id) numbers. For example, pristine ZnO is named as ZnO, 6% Li, N and F doped ZnO NWs as ZL6, ZN6 and ZF6, respectively. In case of Li-N co-doped ZnO NWs, the sample identification as follows ZLN2, ZLN4, ZLN6, ZLN8, ZLN10, ZLN12, ZLN15 for 2-15 at.% N and 6% Li co-doped ZnO NWs. Similarly, ZLF2, ZLF4, ZLF6, ZLF8, ZLF10 represents 2-10 at.% F and 6% Li co-doped ZnO NWs.

To study the morphology of the NWs by field emission scanning electron microscope (FESEM, FEI Helios Nanolab-600), the AAO template was partially dissolved in 2 M NaOH solution to release the NWs. X-ray diffraction (XRD, X'Pert Pro, Panalytical) was used to obtain the crystallographic phase of the pure and doped ZnO NWs embedded in AAO template. The chemical composition of the NWs was determined by energy dispersive x-ray (EDAX) analysis attached with the FESEM system. X-ray photoelectron spectroscopy (XPS) measurements were performed using a VG ESCA system to investigate the chemical compositions of the NWs as well as to know the valence state of the dopants incorporated into the ZnO lattice. Room temperature photoluminescence (PL) spectroscopic measurements of the template embedded NWs were conducted by using a spectrofluorometer (Horiba Jobin Yvon, Fluorolog-3) having Xe lamp source with an excitation wavelength of 330 nm. Magnetic measurements of the vertically aligned template embedded pure and doped ZnO NWs were carried out by using a vibrating sample magnetometer (VSM, Lakeshore, model 7144) in the temperature range of 80 to 700 K.

## 5.4.2 Crystal structure and morphology

The crystallographic phases of the pure and doped ZnO NWs are identified from XRD analysis. Some of the typical XRD patterns for ZL6, ZLN10 and ZLF10 NWs are shown in Fig. 5.12. All the peaks are identified which correspond to hexagonal wurtzite crystal structure of ZnO. Extra peaks at  $2\theta$  values of 38.48 and 44.84 belong to the pure electro-polished Al substrate underneath the AAO template [2]. It is worth noticing that all the samples are in single phase and no impurity peaks are identified within the detection limit

of X-ray diffractometer. The inset of Fig. 5.12 shows the enlarged region around the (100) peak which show a significant shift towards lower and higher angle side for ZLN10 and ZLF10 respectively compared to that of ZL6 NWs. This observation signifies the insertion of N as well as F ion replacing oxygen (O) inside the ZnO host matrix [42]. From Fig. 5.12 (a), it is observed that the lattice parameters ( $a$  and  $c$ ), consequently the lattice volume ( $V$ ) of ZnO unit cell, shown in Fig. 5.12 (c) increases initially with N doping up to 10 at.% and then remains almost unchanged. This type of lattice expansion, inset of Fig. 5.12 (a), can be understood due to insertion of larger  $N^{3-}$  ion (0.132 nm) in ZnO lattice replacing the smaller  $O^{2-}$  ion (0.126 nm) [42]. The saturation like behaviour above the 10 at.% N concentration indicates that the substitution of N at O site ( $N_O$ ) might get complete and the excess N might be inserting into the lattice interstitial ( $N_i$ ), hence no further increase in unit cell volume is observed. On the other hand, Fig. 5.12 (b) shows a decrease of lattice parameters with the increase of F concentration that signifies substitution of smaller  $F^{-1}$  ions (0.119 nm) replacing  $O^{2-}$  ions. Fig. 5.13 shows the representative FESEM images of ZLN10 NWs released from AAO template which indicates the formation of well-developed NWs within the nanopores of template. The average diameter of the nanowires is found to be 45-50 nm which is very consistent with pore diameters ( $\sim 50$  nm) of AAO template and the length is of the order of few micro meters.

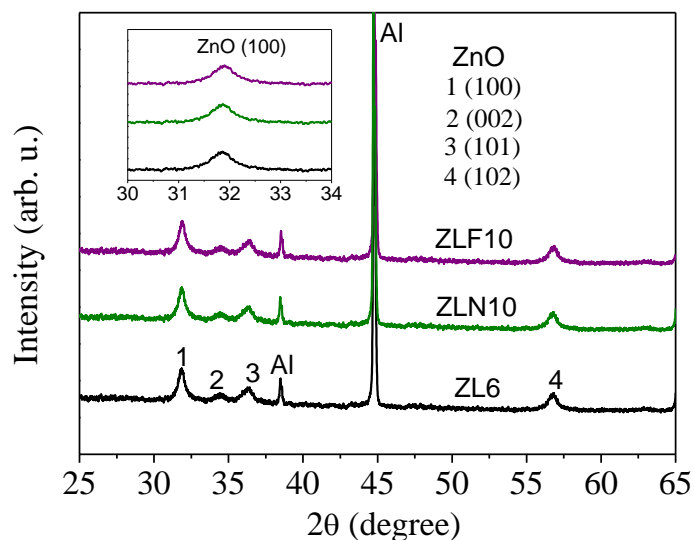


**Fig. 5.12:** Representative XRD pattern of ZL6, ZLN10, and ZLF10 NWs show hexagonal wurtzite crystal structure of doped ZnO. Inset: Relative shift of (100) peak with respect to ZL6 NWs signifies N/F is doped in ZnO lattice.

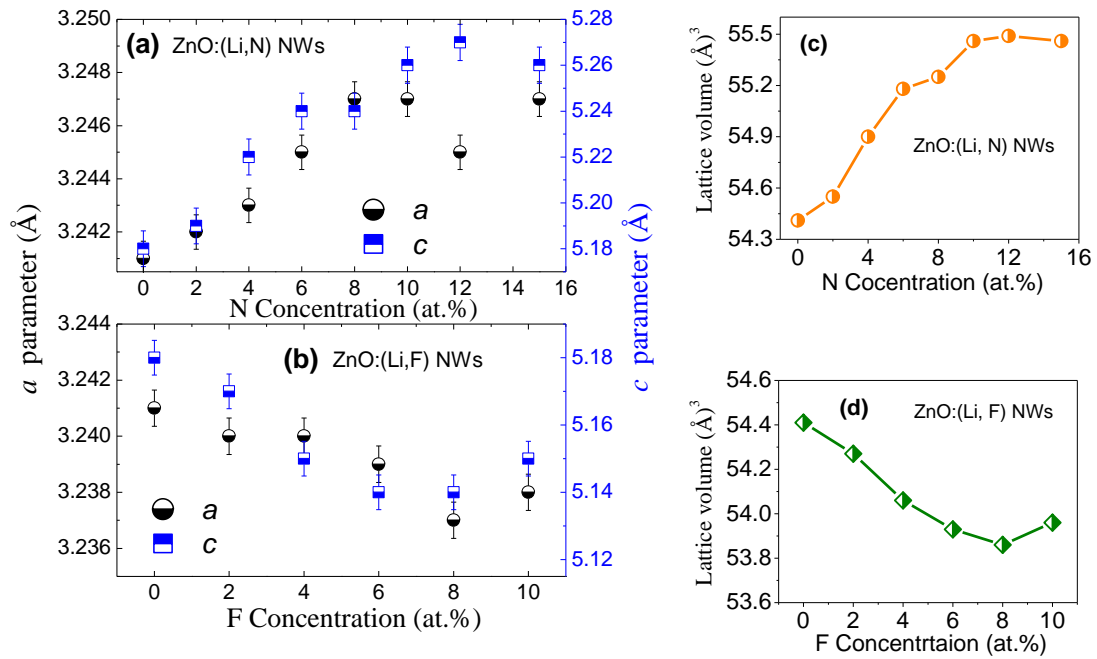


**Fig. 5.12:** Variation of lattice parameters of Li-N/F co-doped ZnO unit cell with (a) N and (b) F concentration, Inset: Corresponding change in lattice volume ( $V$ ) for (c) Li-N and (d) Li-F co-doped ZnO.

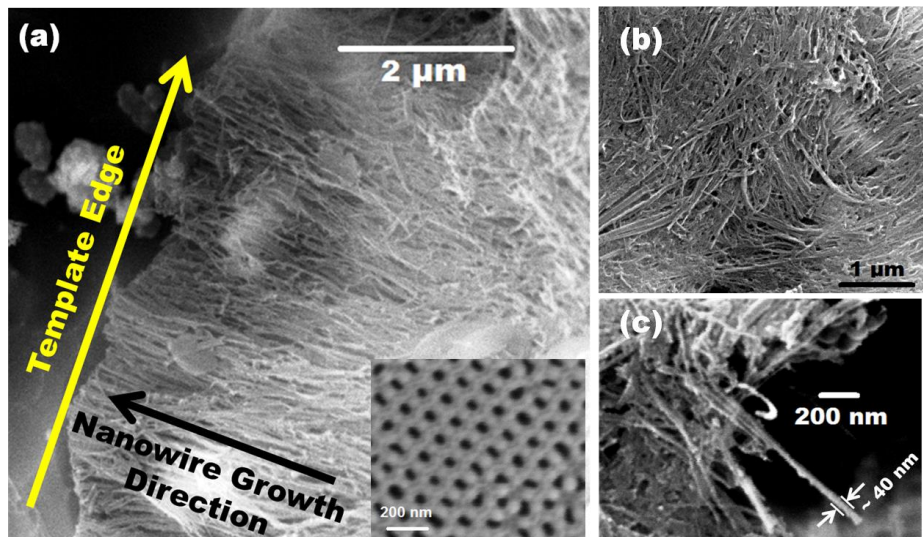


**Fig. 5.13:** FESEM images of ZLN10 NWs with (a) partially released (b) fully released from the AAO template, and (c) show an isolated single nanowire showing average diameter  $\sim 40$  nm. Inset of (a) show the FESEM image of AAO template with average pore diameter  $\sim 50$  nm.

### 5.4.3 X-ray photoelectron spectroscopy (XPS)

The representative high-resolution XPS spectrum of the Zn 2p core level for ZLN10 NWs, shown in Fig. 5.14 (a), displays a doublet located at 1022.6 and 1045.75 eV respectively, corresponding to the core lines of Zn 2p<sub>3/2</sub> and 2p<sub>1/2</sub> states. The binding energy difference (23.15 eV) between the two peaks is in good argument with the standard reference value of ZnO [43]. Herein, the spectrum contains no peak at 1021.50 eV caused by the pure metallic Zn. Therefore, it is confirmed that all the Zn present in the doped ZnO NWs exists only in the oxidized state [44]. The estimated values of the binding energies and the binding energy difference of the Zn 2p spectrum clearly indicate that the Zn is in the +2 oxidation state [45]. Similar results are also obtained for the Li-F co-doped ZnO NWs. The representative O 1s peak of the doped NWs, as shown in Fig. 5.14 (b), can be fitted with two Gaussian components situated at 530.8 and 532.3 eV. The low energy peak (530.8 eV) can be attributed to the formation of O-Zn bond, because of the O<sup>2-</sup> ions on the wurtzite crystal structure of the hexagonal Zn<sup>2+</sup> ion array [46, 47]. On the other hand, the 532.3 eV peak can be correlated to the oxygen deficient region in the ZnO [48] or the Zn-OH bond due to the formation of the Zn(OH)<sub>2</sub> phase in the ZnO matrix by the absorption of moisture from atmosphere [47, 49, 50]. For a better understanding of the chemical bonding of Li ions in the doped ZnO NWs, the high-resolution Li 1s spectrum of the doped ZnO NWs is shown in Fig. 5.14 (c). The peak position of the Li 1s line for all the doped NWs appears at the same energy (centred at 55 eV) indicates the Li incorporation in the ZnO lattice. Here, the broad Li 1s peak can be fitted into two different peaks situated at 53.6 and 55.3 eV. The high energy peak located at 55.3 eV is attributed to the formation of the Li-O bonds through the substitution of the Zn ions by the Li ions ( $Li_{Zn}$ ) in the ZnO matrix [51, 52]. The low energy peak at 53.6 eV can be related to the Li interstitial ( $Li_i$ ) defects corresponding to the valence state of incomplete oxidation [52]. Therefore, it is important to notice that both the substitutional Li ( $Li_{Zn}$ ) and Li interstitial ( $Li_i$ ) defects are present in the lattice.

The nitrogen incorporation in the ZnO NWs has been confirmed by conducting the XPS for the N doped and Li/N co-doped NWs. Fig. 5.14 (d) shows the N 1s narrow scan spectra of the ZLN10 NW sample. Generally, N doping in the ZnO matrix generates much complex chemical states [53, 54]. Here, the N 1s line

located at 396.7 eV can be related to the N-Zn bond formed by substituting a single N ion at O site ( $N_O$ ), corresponds to the p-type doping in ZnO [47, 55, 56]. Furthermore, the high energy peak around 405.7 eV can be assigned to the  $(N_2)_O$ -Zn bonds because of the substitution of  $N_2$  on the O atom site ( $(N_2)_O$ ) in the ZnO lattice [47]. The high-resolution XPS peak of F 1s, shown in Fig. 5.14 (e) confirms the presence of the F in the F-doped ZnO NWs. The F 1s peak centred at 684.4 eV in the F co-doped ZnO NWs indicates the incorporation of the  $F^{1-}$  ions in the ZnO matrix replacing O ions which corresponds to n-type doping [57]. The dopant concentrations in Li-N/F co-doped ZnO NWs, estimated using XPS, are found to be close to individual nominal concentration respectively. For example, the estimated concentration of N and Li are found to be 9.44 and 5.64 at.% respectively for the ZLN10 NWs, whereas the ZLF10 NWs contain 9.57 and 5.62 at.% F and Li respectively.

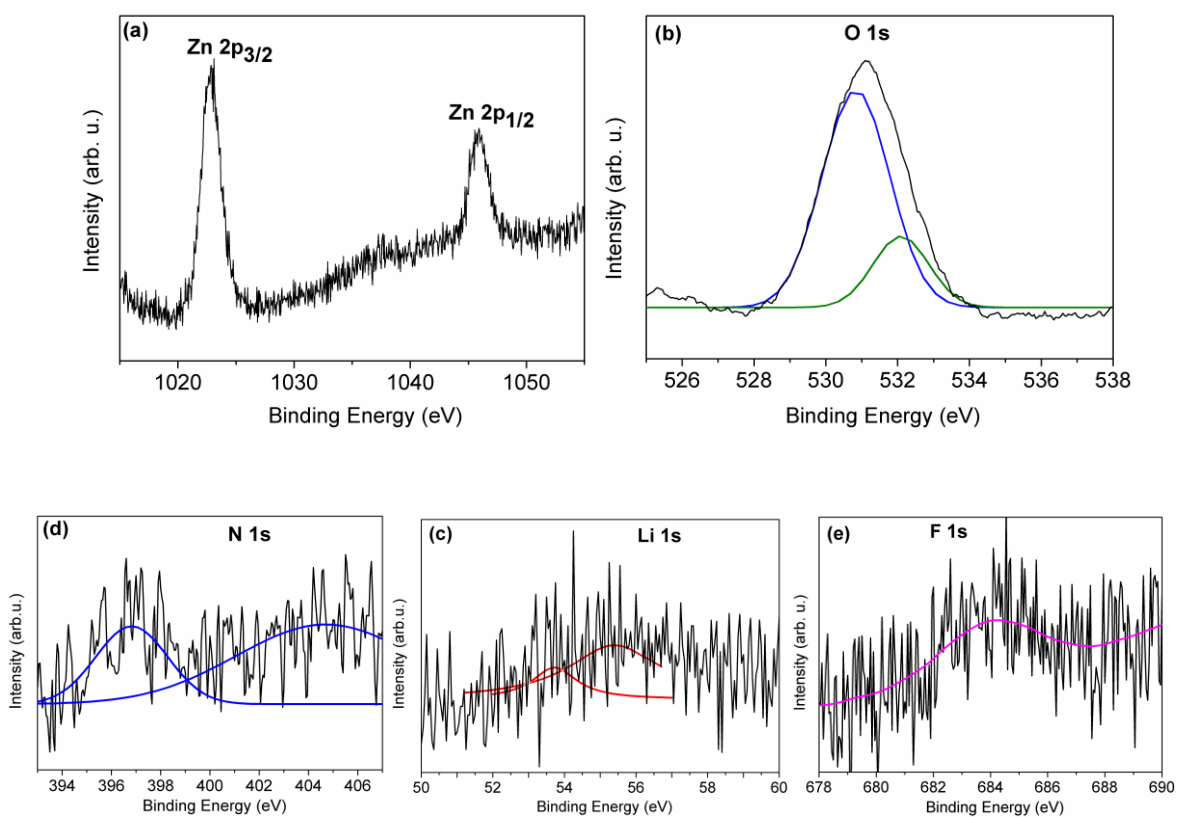


**Fig. 5.14:** XPS spectra for (a) Zn 2p (b) O 1s (c) Li 1s (d) N 1s and (e) F 1s core level in Li-N/F co-doped ZnO representing chemical state of dopant ions as well as host ions.

#### 5.4.4 Defect analysis using photoluminescence spectroscopy

The room-temperature normalized PL spectra of the template embedded Li-N and Li-F co-doped ZnO NWs are shown in Fig. 5.15 (a) and (b), respectively, with reference to the pure ZnO NWs. The increase of N doping concentration in the Li-N co-doped ZnO NWs results in an overall increase of PL intensity up to a certain limit whereas significant reduction in PL intensity is observed with the increase of F concentration in Li-F co-doped ZnO NWs. In the F-doped ZnO NWs, where no Li is present as dopant, the PL emission becomes much more insignificant. The concentration of Li in all the NWs being almost similar ( $\sim 6$  at.%), whatever effects on PL spectra are observed can be associated due to N/F co-doping. However, the broad emission band of the doped ZnO NWs clearly indicates that the emission band could be well divided into several peaks. Both the near band-edge (NBE) and defect related emissions are observed in the N-doped ZnO:Li NWs. Here, for a better understanding the broad PL emission band can be well resolved into seven different peaks along the entire emission range, as shown in Fig. 5.15 (c) for ZLN8 NWs. The emission peak E1 is related to the NBE emission situated at the 3.28 eV corresponds to the free exciton (FX) recombination through an exciton–exciton collision process.<sup>41</sup> The emission peak E2 located at 3.14 eV with an energy difference of 140 meV from the peak E1 is ascribed to the second longitudinal optical (LO) phonon replicas of FX as the difference between two corresponding replicas of LO-phonon energy of ZnO is 72 meV [59].

Interestingly, it is found that the intensity of the PL spectrum of the pure ZnO NWs in Fig. 5.15 (a) decreases gradually below the energy value of 3.13 eV whereas, in case of the Li-N co-doped NWs the intensity of the PL emission band increases below the same energy. Hence, it is expected that in case of the Li-N co-doped NWs there should be another PL emission peak located in between 3.1 to 3 eV, which is not present in the pristine ZnO NWs. In fact, it is found that in all the Li-N co-doped NWs there appears another emission peak E3 at 3.02 eV, which is not present in case of the pure ZnO NWs. Furthermore, the intensity of peak E3, as shown in Fig. 5.15(d), is also gradually increasing with the increase of N concentration in ZnO:Li system. Therefore, it is believed that peak E3 is originated because of the N dopant in the ZnO lattice and it could be ascribed to the defect transition from conduction band to the  $N_O$  acceptor level [60, 61]. Here, it is seen that  $N_O$ -defect concentration

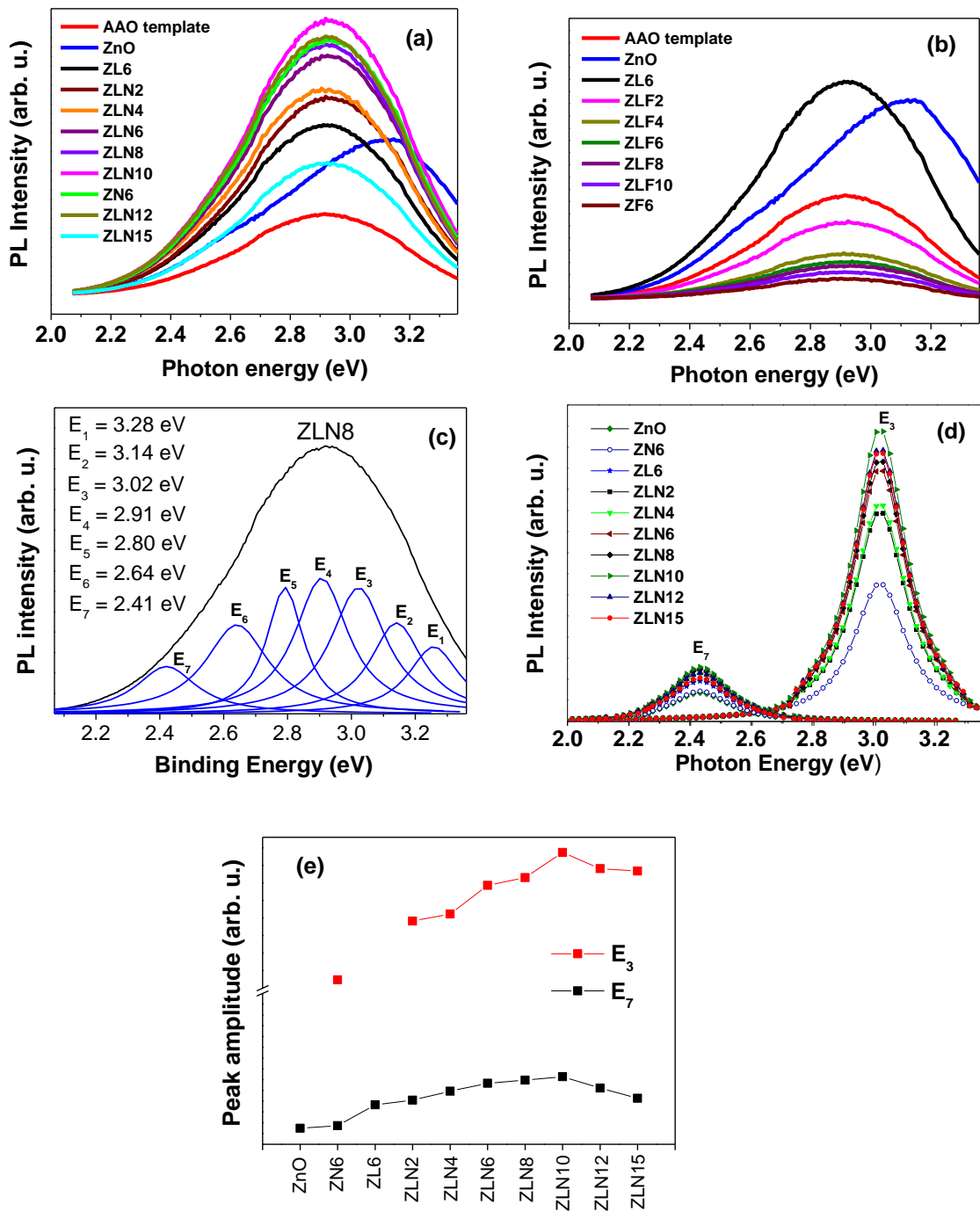


**Fig. 5.15:** Normalised room-temperature PL spectra of (a) Li-N and (b) Li-F co-doped ZnO NWs with respect to pristine ZnO NWs. (c) Representative multiple peak fitting for ZLN8 NWs and (d) the variation of NBE ( $E_3$ ) and green emission ( $E_7$ ) band and (e) variation of Peak amplitude of  $E_3$  and  $E_7$  of Li-N co-doped ZnO NWs with N doping concentration.

increases gradually in Li-N co-doped NWs with the increase of N-doping upto 10 at.%. But, no further enhancement of  $E_3$  peak is observed for 12 and 15 at.% N co-

doping which signifies that  $N_O$  defects might become almost constant for higher doping and the excess N might enter into the interstitial site ( $N_i$ ) in ZnO lattice or substitution of  $N_2$  molecule at O site ( $(N_2)_O$ ) can also be possible. Similar indication is also obtained from XRD analysis where we have seen that the unit cell volume ( $V$ ) become almost same for higher N co-doping because no more N ions are substituting at O site. However, the peak E4 appears at energy of 2.91 eV (427 nm) is originated from the AAO template [2, 4]. The peak E5 around 2.80 eV may be attributed to Zn interstitial defects in the ZnO [60] or even the nitrogen impurity related defects like nitrogen interstitial ( $N_i$ ) incorporated in the ZnO lattice [47]. Similarly, peak E6 situated at 2.64 eV may be correlated to the defects due to the implantation of N into the ZnO lattice or even this blue-green luminescence might have contribution from the different Li-defects such as Li substitutional ( $Li_{Zn}$ ) and/or Li interstitials ( $Li_i$ ) defects in the lattice because of the incorporated Li ions. We also have observed such blue-green emission which was attributed K substitutional ( $K_{Zn}$ )/interstitial ( $K_i$ ) defects in K-doped ZnO NWs [2].

Finally, the green emission peak (E7) appears at 2.41 eV in the Li-N co-doped ZnO NWs is attributed to the zinc vacancy ( $V_{Zn}$ ) related defects present in the ZnO lattice [2, 33, 62, 63]. It is evident from Fig. 5.15 (a) that the intensity of the green emission peak for the pristine ZnO and the only N-doped ZnO (where Li is absent) NWs are same as both the spectrum overlaps at the low energy region and this indicates that only N doping might have a little influence in green emission of ZnO NWs. But a significant increase in the intensity of the green emission (E7) is observed when 6 at.% Li is doped in ZnO as it is shown in Fig. 5.15 (d). This indicates that only the Li doping in ZnO helps in the formation of the more  $V_{Zn}$  defects in the matrix. This result is consistent with the previous report, which shows that the incorporation of Li in ZnO thin film helps in reducing the formation energy of the  $V_{Zn}$  and hence more  $V_{Zn}$  defects are generated in the matrix. We also observed similar phenomena in the K-doped ZnO NWs in our previous work [2]. It is also interesting to note that (Fig. 5.15 (e)) with the increase of the N-doping concentration in Li-N co-doped ZnO NWs, the green emission peak increases very slowly which indicates a little increase in  $V_{Zn}$  concentration with Li-N co-doping. This slow increase in  $V_{Zn}$  concentration is quite understandable because the  $Li_i$  donor which generally acts as recombination centre for  $V_{Zn}$ , will be killed by the gradual enhancement in  $N_O$

acceptor through the formation of  $N_{\text{O}}\text{-Li}_i$  defect complex [70, 71]. On the other hand, it is obvious from Fig. 5.15 (b) that the F co-doping in the ZnO:Li NWs has some negative influence on their luminescence property as the intensity of the emission decreases significantly with the increase of the F-doping. This result is consistent with the report on the F-doped ZnO nanoparticles and thin films [64, 65]. Therefore, the intensities of all the NBE, blue, blue-green and green emissions (related to the  $V_{\text{Zn}}$  defects) are falling consistently with the increase of the F concentration in the ZnO:Li lattice.

### 5.4.5 Magnetic properties of Li-N/F codoped ZnO NWs

Fig. 5.16 (a) and (b) show the field dependent magnetization  $M$  (H) curves for pristine ZnO, Li and Li-N co-doped and Li-F co-doped ZnO NWs at 300 K respectively, presented after subtracting the template diamagnetic contribution. The pristine as well as all the doped ZnO NWs shows distinct ferromagnetic behaviour with significant saturation magnetization and coercivity. The pristine ZnO NWs show a saturation magnetization ( $M_s$ ) of  $\sim 0.11$  emu/g and coercivity ( $H_c$ )  $\sim 41$  Oe. The  $M_s$  increases to 0.63 emu/g when 6 at.% Li is doped in ZnO. In our previous work, we also have observed significant enhancement in magnetization by substituting potassium (K) in ZnO NWs, which shows a maximum  $M_s$  of  $\sim 0.40$  emu/g for 4 at.% K doping [2]. Here in our present experiment, further enhancement in  $M_s$  is observed in case of Li-N co-doped ZnO NWs, having maximum  $M_s \sim 2.52$  emu/g for ZLN10 NWs in which 10 at.% N is co-doped along with 6 at.% Li. Interestingly, the  $M_s$  is found to decrease when the N concentration reaches above 10 at.%. Unlike the reports about  $d^0$  ferromagnetism in N-doped ZnO thin films [66, 67], here, we have not observed any significant improvement in the RTFM of ZnO NWs with 6 at.% N doping only, which demonstrates that the doping of N alone may not have significant influence on the ferromagnetism in ZnO NWs. On the other hand, the co-doping of F with Li is found to exhibit a contrasting magnetic behaviour as in case of Li-F co-doped ZnO NWs, shown in Fig. 5.16 (b). As the F substitution ( $F_{\text{O}}$ ) starts to increase with the increase of F doping concentration in Li-F co-doped ZnO NWs, the  $M_s$  starts to diminish gradually. In fact,  $M_s$  has found to fall down even lower than the undoped ZnO NWs when the F concentration has reached at 4 at.% and higher. Unlike the only N doped ZnO NWs, the 6 at.% F doped ZnO NWs (with

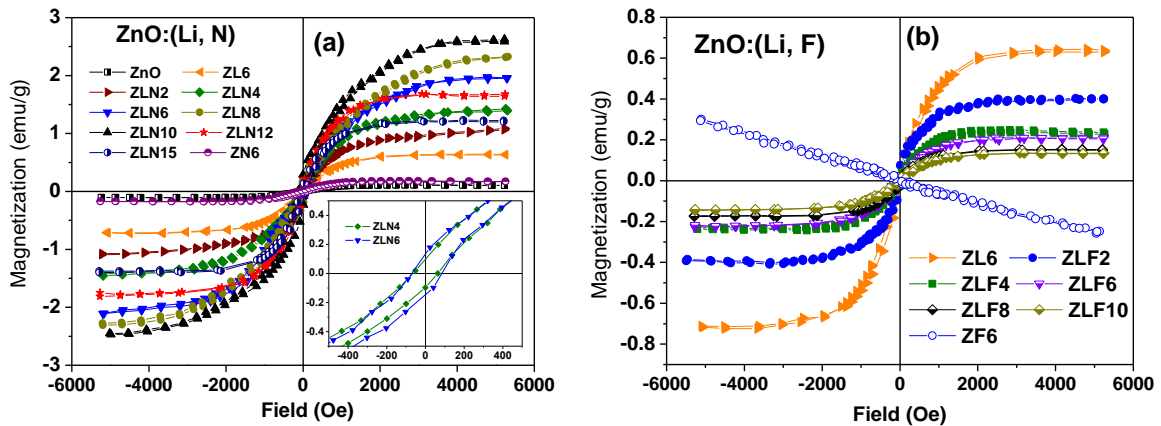


**Fig. 5.16:** Room-temperature Field dependent Magnetization  $M$  (H) loop of (a) pristine, Li doped, Li-N co-doped ZnO NWs and (b) Li-F co-doped ZnO NWs.

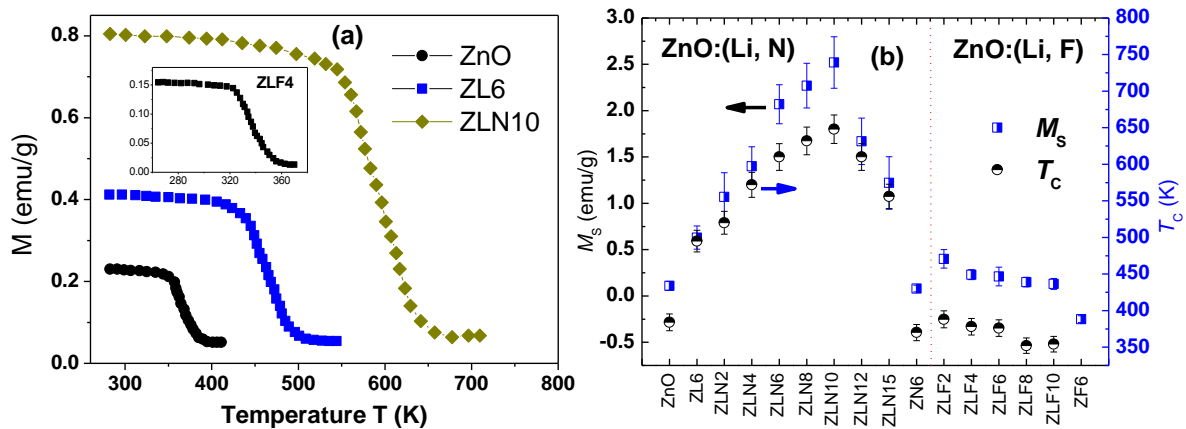


**Fig. 5.17:** High temperature  $M$  (T) measurements for (a) pristine ZnO, ZLN6, ZLN10 and ZLF4 NWs (inset). (b) Change in Curie temperature ( $T_C$ ) and corresponding saturation magnetization ( $M_S$ ) with N/F concentration for all the NWs. The side right to the dotted line (red) is for Li-N co-doped ZnO whereas the left for F-Li co-doped ZnO NWs.

no Li content) exhibit a diamagnetic behaviour as shown in Fig. 5.16 (b). Therefore, the substitution of F at O sites ( $F_O$ ) is playing a negative role on the ferromagnetic interaction in Li-F co-doped and pristine ZnO NWs. Thermal dependence of magnetization  $M$  (T) is measured for all the doped ZnO NWs at a constant applied magnetic field  $H = 500$  Oe. Fig. 5.17 (a) shows the representative high-temperature  $M$  (T) curves of undoped ZnO, ZL6 and ZLN10 NWs whereas the inset is for ZLF4 NWs. The Curie temperature estimated from the  $M$  (T) data for all the NWs is

plotted in Fig. 5.17 (b) along with the corresponding values of saturation magnetization ( $M_s$ ). It is evident from Fig. 5.17 (b) that the Li-N co-doped NWs show higher  $T_C$  as well as higher  $M_s$  values compare to the Li-F co-doped ZnO NWs. The Curie temperature ( $T_C$ ) has found to be 495 K for 6% Li-doped ZnO NWs. The maximum  $T_C \sim 648$  K is observed for ZLN10 NWs. Therefore, the overall FM in ZnO NWs has enhanced due to Li-N co-doping whereas Li-F combination putting a negative impact to the ferromagnetic properties of ZnO NWs.

To discuss the origin of intrinsic magnetism in our pristine and doped ZnO NWs, we should look back the previous PL study along with the discussion on XPS analysis. Considering the present situation, it is quite evident that the intrinsic structural modifications (i.e. defects) in crystal itself, due to different substitutional dopants like Li, N, F are playing a key role to induce, stabilize and tune the ferromagnetic properties of ZnO NWs. In the PL spectral analysis, we have seen the significant increase of the green luminescence intensity (2.41 eV) when 6 at.% Li is doped in ZnO which indicate the presence of considerable amount of  $V_{Zn}$  defects in ZL6 NWs. Zinc vacancy ( $V_{Zn}$ ) is found to carry a localised magnetic moment which originates from the unpaired 2p electrons of O atom in the immediate vicinity of  $V_{Zn}$  defect [33, 68]. Wang et al. [68] showed that generally  $V_{Zn}$  have high formation energy within the bulk of ZnO matrix, but comparatively have lower formation energy at the surface of the matrix. Therefore, it is quite possible to obtain the significant amount of  $V_{Zn}$  at the surface of ZnO nanostructures like NWs having large surface to volume ratio compared with bulk ZnO. Additionally, it has been reported that Li-doping can significantly reduce the formation energy of  $V_{Zn}$  in ZnO matrix and thus helps to stabilize more  $V_{Zn}$  defects [33]. In our previous work, we also have observed the stabilization of large amount of  $V_{Zn}$  defects in ZnO lattice by doping with potassium (K) and ferromagnetism is also found to enhance in K doped ZnO NWs [2]. Here, in case of Li doped ZnO NWs, amount of  $V_{Zn}$  defects (evident from PL spectra) may reach above the required percolation limit and the ferromagnetic interaction between  $V_{Zn}$  defects can be mediated by the holes due to  $Li_{Zn}$  and  $V_{Zn}$  [69]. Although it is expected that some amount of  $V_{Zn}$  as well as  $Li_{Zn}$  [70, 71] acceptors will be compensated by  $Li_i$  donor which is still less in number (Fig. 4 (e)) compare to that of acceptors leads to a overall p-type conduction. Thus the presence of  $Li_i$  donor may reduce the effective amount of  $V_{Zn}$  which is expected to be

stabilized due to the introduction of  $Li_{Zn}$  only [70]. Therefore, the effect of  $Li_i$  donors is desired to be neutralised with introducing some suitable co-dopant to enhance the population of  $V_{Zn}$  and  $Li_{Zn}$  to obtain stronger ferromagnetism response of the Li-doped ZnO NWs. In fact, this is exactly what we have done by introducing N co-dopant in ZnO:Li system which will be discussed in the next paragraph. In case of pristine ZnO NWs, it is expected that the presence of  $V_{Zn}$ , which can grow during the growth of the NWs in O-rich atmosphere [66], as well as the singly ionized oxygen vacancies ( $V_{O^+}$ ) [9, 18] contributes in the observed RTFM.

The p-type conductivity of the ZnO thin films is found to increase with the increase of the Li concentration in the matrix [33]. Recent studies also show that the co-doping of N with Li becomes much effective to stabilize p-type conductivity in ZnO thin films with higher hole concentration [71] and enhanced RTFM [70]. Here in case of Li-N co-doped ZnO NWs, earlier we have observed that the amount of  $N_O$  acceptors increases with the increase of N concentration. Therefore, the  $Li_i$  donor will combine with  $N_O$  acceptor through the formation of  $Li_i-N_O$  defect complex and this can actually help in stabilizing more  $V_{Zn}$  as well as  $Li_{Zn}$  in Li-N co-doped ZnO which pushes the system towards better p-type conduction i.e. higher hole concentration. The slow increase of  $V_{Zn}$  defect population with the increase of N is also evident from PL spectrum of Li-N co-doped ZnO NWs. Therefore, one of the probable explanations of the observed enhancement in  $M_S$  with increase of N dopant in our Li-N co-doped ZnO might be due to the increase of effective  $V_{Zn}$  as well as the hole concentration in the system. As N concentration increases, more numbers of  $Li_i-N_O$  become stable and thus  $V_{Zn}$  concentration increases resulting into the consequent enhancement of the ferromagnetism. But when the N concentration reaches above 10 at.%, the other N donor defects such as  $(N_2)_O$  or  $N_i$  becomes stabilized to compensate the effect of  $N_O$  acceptor, thereby reduces the amount of  $Li_i-N_O$  which results a decrease in both  $V_{Zn}$  and hole concentration. Therefore, the magnetization is found to diminished for Li-N co-doped NWs with higher N concentration (>10 at.%). Furthermore, recently, the  $Li_i+N_O+V_{Zn}$  defect complex is found to have magnetic moment and the increase of  $Li_i+N_O+V_{Zn}$  concentration with the increase of Li doping is found to be responsible for enhanced ferromagnetism in Li-N dual doped ZnO thin films [70]. Although our case is quite different from their consideration<sup>14</sup> because in our Li-N co-doped ZnO NWs, the Li doping concentration remains fixed

while the N concentration is changed. In our experiment, the increase of  $N_O$  acceptor as well as  $V_{Zn}$  with the increase of N doping can lead to the enhancement of  $Li_i+N_O+V_{Zn}$  defect formation leading to the significant increase in the  $M_S$  in the Li-N co-doped ZnO NWs. The magnetic moment of  $Li_i+N_O+V_{Zn}$  defect complex is mainly arises from the magnetic moment of  $V_{Zn}$  [70]. For higher N doping concentration (>10 at.%), the population of  $Li_i+N_O+V_{Zn}$  can diminish due to decrease of  $N_O$  as well as  $V_{Zn}$  resulting the decrease of  $M_S$ . Therefore, we attribute both the isolated  $V_{Zn}$  defects as well as the  $Li_i+N_O+V_{Zn}$  complex defects to the origin of RTFM in the Li-N co-doped ZnO NWs. On the other hand, the substitutional F ( $F_O$ ) serves as the donor in ZnO nanocrystalline thin film and the n-type conductivity of the F-doped ZnO is found to increase with F concentration [71]. Here, in case of Li-F co-doped ZnO NWs the  $F_O$  donor will certainly compensate the  $Li_{Zn}$  and  $V_{Zn}$  acceptors reducing the p-type nature as well as the  $V_{Zn}$  defect concentration in the matrix. From PL analysis we also have observed the evidence of significant decrease of  $V_{Zn}$  concentration in Li-F co-doped ZnO NWs which results into week ferromagnetism in the system. With the increase of F doping concentration in the Li-F co-doped NWs, the compensation effect becomes more pronounced as the Li concentration in the ZnO is constant, leading to a gradual decrease of both  $V_{Zn}$  and holes and effectively the corresponding  $M_S$ . Furthermore, the absence of ferromagnetism as well as the insignificant luminescence in 6 at.% F doped ZnO NWs (with no Li dopant) certainly signifies that the stabilization of  $V_{Zn}$  defects might not be favoured in presence of  $F_O$  donor states.

## 5.5 Conclusions

In summary, the experimental evidence of defect-induced FM at RT is observed in case of various oxide nanowires prepared within nanopores of AAO template. For pure  $SnO_2$  NWs, singly ionized oxygen vacancies are found to induce RTFM. On the other hand, cation vacancies ( $V_{Zn}$ ) are found to playing an important role in stabilizing FM in ZnO NWs and the FM signature is found to enhance with the substitution of alkali element K at Zn site. The concentrations Zn vacancies as well as the p-type conductivity of the ZnO NWs are found to increase significantly with K-doping and the FM signature increases consequently. For higher K-doping concentration, the stabilization donor like K-interstitial defects compensates the

effects of K-substitutional and Zn vacancy acceptors and thereby reducing the degree of p-type nature which diminishes the related FM consequently. In another work, considerable enhancement of the ferromagnetic signature in Li-doped ZnO NWs is observed by additional nitrogen (N) co-doping at oxygen site. On the other hand, fluorine (F)-codoping results in poor ferromagnetic response in the Li-F co-doped ZnO NWs. The saturation magnetization ( $M_s$ ) as well as the Curie temperature ( $T_C$ ) in Li-N co-doped ZnO NWs is found to increase initially up to a certain N concentration and then decreases for higher N doping. Li-doping is found to assist in stabilizing zinc vacancies ( $V_{Zn}$ ) in ZnO NWs, which acts as the dominant magnetic origin and also introduces holes in the system at the same time giving rise to ferromagnetic interaction between the  $V_{Zn}$ . The compensation effect due to Li interstitial ( $Li_i$ ) donor is reduced in the presence of  $N_O$  acceptor defects in Li-N co-doped ZnO NWs, which leads to enhancement of effective  $V_{Zn}$  concentration and consequently the saturation magnetization. For higher N doping concentration, the formation of donor type defects like  $(N_2)_O$  or  $N_i$  begins to compensate different acceptors like  $N_O$ ,  $Li_{Zn}$  which leads to a decrease of  $V_{Zn}$  concentration and consequently the  $M_s$ . We also found that the formation of  $Li_i + N_O + V_{Zn}$  defect complex can be another possible reason for enhanced ferromagnetic response in Li-N co-doped ZnO NWs. On the other hand, the substitutional F at O site which acts as donor is found to be unfavourable to stabilize  $V_{Zn}$  defects and hence it results in a decrease of  $M_s$  for the Li-F co-doped ZnO NWs. Therefore, the stabilization of defect-induced FM in such oxides can be an exciting approach to prepare new class of magnetic semiconductors for spintronics and opto-spintronics applications. We also demonstrate that the Li-N co-doping can be an effective parameter to stabilize, enhance the amount of Zn vacancy as well as to introduce sufficient holes to mediate long-range ferromagnetic interaction between the Zn vacancies.

## References

- [1] Khan, G. G.; Ghosh, S.; Mandal, K. *J. Solid State Chem.* **2012**, 186, 278.
- [2] Ghosh, S.; Khan, G. G.; Das, B.; Mandal, K. *J. Appl. Phys.* **2011**, 109, 123927.
- [3] Ghosh, S.; Khan, G. G.; Varma, S.; Mandal, K. *J. Appl. Phys.* **2012**, 112, 043910.
- [4] G.G. Khan, N. Mukherjee, A. Mondal et al., *Mats. Chem. Phys.* 122 (2010) 60.
- [5] H. He, T.H. Wu, C.L. Hsin, K.M. Li et al., *Small* 2 (2006) 116.
- [6] S. Luo, J. Fan, W. Liu, et al., *Nanotechnology* 17 (2006) 1695.
- [7] S. Luo, P. K. Chu, W. Liu, et al., *Appl. Phys. Lett.* 88 (2006) 183112
- [8] C. Kilic, A. Zunger, *Phys. Rev. Lett.* 88 (2002) 095501.
- [9] A. Sundaresan, R. Bhargavi, N. Rangarajan et al., *Phys. Rev. B* 74 (2006) 161306(R).
- [10] X. Liu, J. Iqbal, Z. Wu, B. He, R. Yu, *J. Phys. Chem. C* 4790 (2010) 114.
- [11] A. Kar, S. Kundu, A. Patra, *J. Phys. Chem. C* 118 (2011) 115.
- [12] K. Vanheusden, W.L. Warren, C.H. Seager et al., *J. Appl. Phys.* 10 (1996) 7983.
- [13] A. Kar, M.A Stroschio, M. Dutta et al., *Semicond. Sci. Technol.* 25 (2010) 024012.
- [14] J.M.D. Coey, M. Venkatesan, C. B. Fitzgerald, *Nature Mats*, 4 (2005) 173.
- [15] N. Özcan, T. Kortelainen, V. Golovanov et al., *Phys. Rev. B* 81 (2010) 235202.
- [16] D. A. Popescu, J. M. Herrmann et al., *Phys. Chem. Chem. Phys.* 3 (2001) 2522.
- [17] X. Wei, R. Skomski, B. Balamurugan et al., *J. Appl. Phys.* 105 (2009) 07C517.
- [18] R. Podila, W. Queen, A. Nath et al., *Nano Lett.* 10 (2010) 1383.
- [19] Q. Wang, Q. Sun, G. Chen, Y. Kawazoe, P. Jena, *Phys Rev. B* 77 (2008) 205411.
- [20] A. Janotti and C. G. Van de Walle, *Rep. Prog. Phys.* 72, 126501 (2009).
- [21] Y.C. Kong, D.P. Yu, B. Zhang, W. Fang, S.Q. Feng, *Appl. Phys. Lett.* 78, 407 (2001).
- [22] A. B. Djurišić, W. C. H. Choy, V. A. L. Roy et al., *Adv. Funct. Mater.* 14, 856 (2004).
- [23] A. B. Djurišić, Y. H. Leung, *Small* 2, 944 (2006).
- [24] Y.B. Li, M.J. Zhenga, L. Ma, *Appl. Phys. Lett.* 91 (2007) 073109.
- [25] K. Vanheusden, W. L. Warren, C. H. Seager et al., *J. Appl. Phys.* 79, 7983 (1996).
- [26] C. H. Park, S. B. Zhang, and S. H. Wei, *Phys. Rev. B* 66, 073202 (2002).
- [27] E. C. Lee and K. J. Chang, *Phys. Rev. B* 70, 115210 (2004).
- [28] Y. Li, G.W. Meng, L.D. Zhang, *Appl. Phys. Lett.* 76 (2000) 2011.
- [29] A.F. Kohan, G. Ceder, D. Morgan et al., *Phys. Rev. B* 61 15019 (2000).
- [30] T. Moe Børseth, B. G. Svensson et al., *Appl. Phys. Lett.* 89, 262112, (2006).
- [31] L. Ke, S. C. Lai, J. D. Ye, V. L. Kaixin, and S. J. Chua, *J. Appl. Phys.* 108, 084502, (2010).
- [32] F. Oba, S. R. Nishitani, S. Isotani, H. Adachi, and I. Tanaka, *J. Appl. Phys.* 90, 824, (2001).
- [33] J. B. Yi, C. C. Lim, G. Z. Xing et al., *Phys. Rev. Lett.* 104, 137201 (2010).
- [34] L. Xu, X. Li and J. Yuan, *Superlattices and Microstructures* 44, 276 (2008).
- [35] R. Podila, W. Queen, A. Nath et al., *Nano Lett.* 10, 1383 (2010)

- [36] S. Banerjee, M. Mandal, N. Gayathri and M. Sardar, Appl. Phys. Lett 91, 182501 (2007).
- [37] Q. Wang, Q. Sun, G. Chen, Y. Kawazoe and P. Jena, Phys Rev. B 77, 205411 (2008).
- [38] G. Bouzerar and T. Ziman, Phys. Rev. Lett. 96, 207602 (2006)
- [39] Eun-Cheol Lee, Y.-S. Kim, Y.-G. Jin, and K. J. Chang Phys. Rev. B, 64, 085120 (2001).
- [40] B. Y. Zhang, B. Yao, Y. F. Li et al., Appl. Phys. Lett. 97, 222101 (2010).
- [41] A. Janotti and C. G. Van de Walle, Phys. Rev. B 76,165202 (2007).
- [42] Y. Cao, L. Miao, S. Tanemura et al., Appl. Phys. Lett. 88, 251116 (2006).
- [43] C. D. Wagner, W. M. Riggs, L.E. Davis et al., in: Handbook of X-ray Photoelectron Spectroscopy, Perkin Elmer, Eden Prairie, 1979.
- [44] M. N. Islam, T. B. Gosh, K. L. Chopra et al., Thin Solid Films 280 20 (1996).
- [45] D. K. Mishra, P. Kumar , M. K. Sharma et al., Physica B 405, 2659 (2010).
- [46] Z. B. Gu, M. H. Lu, J. Wang et al., Appl. Phys. Lett. 88, 082111 (2006).
- [47] B. Yang, P. Feng, A. Kumar et al., J. Phys. D: Appl. Phys. 42, 195402 (2009).
- [48] J. C. C. Fan, J. B. Goodenough, J. Appl. Phys. 48, 3524 (1977).
- [49] T. Ghoshal, S. Biswas, S. Kar et al., Nanotechnology 19, 065606 (2008).
- [50] O. Lupan, G. A. Emelchenko, V. V. Ursaki et al., Mater. Res. Bull. 45, 1026 (2010).
- [51] J. C. Dupin, O. Gonbeau, P. Vinatier et al., Phys. Chem. Chem. Phys. 2, 1319 (2000).
- [52] J. G. Lu, Y. Z. Zhang, Z. Z. Ye et al., Appl. Phys. Lett. 89, 112113 (2006).
- [53] J. P. Zhang, L. D. Zhang, L. Q. Zhu et al., Appl. Phys. 102, 114903 (2007).
- [54] S. Jiao, Y. Lu, Z. Zhang et al., J. Appl. Phys. 102, 113509 (2007).
- [55] C. L. Perkins, S-H Lee, X. Li et al., J. Appl. Phys. 97, 034907 (2005).
- [56] E. C. Lee, Y. S. Kim, Y. G. Jin and K. J. Chang, Phys. B: Condens. Matter 308 912 (2001).
- [57] H. Y. Xu, Y. C. Liu, R. Mu et al., Appl. Phys. Lett. 86, 123107 (2005).
- [58] Y. C. Kong, D. P. Yu, B. Zhang, W. Fang, and S.Q. Feng, Appl. Phys. Lett. 78, 407 (2001).
- [59] X. Meng, Z. Shi, X. Chen, X. Zeng, and Z. Fu, J. Appl. Phys. 107, 023501, (2010).
- [60] K. Y. Wu, Q. Q. Fang, W.N. Wang et al., J. Appl. Phys. 108, 063530 (2010).
- [61] A. Zeuner, H. Alves, D. M. Hofmann et al., Phys. Status Solidi B 234, R7 (2002).
- [62] A. F. Kohan, G. Ceder, D. Morgan et al., Phys. Rev. B 61, 15019 (2000).
- [63] T. M. Børseth, B. G. Svensson et al., Appl. Phys. Lett. 89, 262112 (2006).

- 
- [64] R. Gonzalez-Hernandez, Arturo I. Martinez et al., *Materials Letters* 64,1493 (2010).
- [65] A. El Hichou, A. Bougrine, J. L. Bubendorff et al., *Semicond. Sci. Technol.* 17, 607 (2002).
- [66] C. F. Yu, T. J. Lin, S. J. Sun and H. Chou, *J. Phys. D: Appl. Phys.* 40, 6497 (2007).
- [67] Hu Xu, A. L. Rosa, Th. Frauenheim et al., *Phys. Status Solidi B* 247, 2195 (2010).
- [68] Q. Wang, Q. Sun, G. Chen, Y. Kawazoe, and P. Jena, *Phys Rev. B* 77, 205411 (2008).
- [69] Y. Li, R. Deng, B. Yao, G. Xing, D. Wang and T. Wu, *Appl. Phys. Lett.* 97, 102506 (2010).
- [70] B. Y. Zhang, B. Yao, Y. F. Li et al., *Appl. Phys. Lett.* 99, 182503 (2011).
- [71] B. Y. Zhang, B. Yao, Y. F. Li et al., *Appl. Phys. Lett.* 97, 222101 (2010).

# Chapter 6

## Defect-driven Magnetic, Luminescence and Electrical properties of Alkali-Metal doped ZnO Thin Films prepared by Pulsed Laser Deposition

### 6.1. Preface

One-dimension (1D) ZnO nanostructures are generally found to be enriched with large concentration of defects or crystal imperfections, especially surface defects, due to their very high surface to volume ratio. In previous sections (sec. 5.3-5.4), we have seen the stabilization, enhancement and also tuning of cation (Zn) defect-induced  $d^0$  ferromagnetism and photoluminescence in case of 1D pristine and non-magnetic doped ZnO nanowires. Now question arises what will happen if we increase the size or dimension of the host semiconducting system i.e. switching from 1D nanostructure to two-dimension (2D) thin film? In the thin films, which are basically two-dimensional (2D) system, the thickness of film can vary from a few nm

to few hundred nm. Therefore, it is quite interesting to investigate whether such defect-induced ferromagnetism can also be stabilized in case of thin film structures. The high- $T_C$  ferromagnetic oxide thin film layers are also quite desirable for the modern spintronic or optospintronic application. Therefore, in current section, we have investigated defect-induced magnetic, luminescence and electrical properties in pure and alkali-metal-doped ZnO thin films prepared by pulsed laser deposition (PLD) technique. The effect of various group-1A alkali metal (Li, Na and K) substitutional defects, film-thickness and oxygen partial pressure of the PLD chamber in determining magnetic, luminescence and electrical properties of doped ZnO thin films are investigated in details.

## 6.2 Alkali-doped ZnO thin films: A comparative study on effects of Li, Na and K substitutional defects

### 6.2.1 Fabrication of Li, Na and K-doped ZnO thin films

All the pristine and doped ZnO thin films are deposited by pulse laser deposition (PLD) technique on c-axis-sapphire ( $Al_2O_3$ ) substrate using a KrF excimer laser of laser power density of  $2.14 \text{ J/cm}^2$  and pulse repetition rate of 5 Hz. The targets were prepared from the mixture of high purity (99.99%) ZnO and Li-acetate, Na-acetate and K-acetate powders for the deposition of pure ZnO and 6 at.% Li, Na and K-doped ZnO thin films respectively. The base pressure and oxygen pressure ( $PO_2$ ) of the deposition chamber was maintained at  $5 \times 10^{-5}$  and  $1 \times 10^{-2}$  torr respectively, keeping substrate temperature fixed at  $500^\circ \text{ C}$ . All the films are intentionally prepared under high oxygen pressure ( $10^{-2}$  torr) to reduce the formation of oxygen vacancy within the films. Each film was deposited with a total of 12,000 laser shot.

### 6.2.2 Characterization of alkali-doped ZnO thin films

The thicknesses of the films are measured by ellipsometry technique and found to be consistent within the range of 180-210 nm. All the films are characterized by Grazing Incidence X-ray Diffraction (GIXRD, X'Pert Pro, Panalytical), Atomic Force Microscope (AFM). X-ray Photoelectron Spectroscopy (XPS) measurements

were performed using a VG ESCA system to investigate the chemical compositions of the films as well as to know the valence state of the alkali dopants. Magnetic measurements are performed by superconducting quantum interference devices (SQUID) at room-temperature. Photoluminescence (PL) spectroscopic measurements are conducted to observe the defect-levels transitions between the energy band-gap of ZnO by using a spectrofluorometer (Horiba Jobin Yvon, Fluorolog-3) having Xe lamp source with an excitation wavelength of 330 nm. Hall measurement is carried out to investigate the types (n-type /p-type) of the semiconductors and to estimate the carrier concentrations. The resistivity of films is measured with standard four-probe method with two current and voltage leads. It is important to mention that all the measurements were performed several times to avoid any types of unexpected experimental errors in the data due to system's temporal instability or any other facts. The handling of the samples was done with extreme care (using nonmagnetic tweezers) to avoid any sort of magnetic contamination in the films.

## 6.2.3 Results and discussions

### 6.2.3.1 X-ray diffraction and crystal structure

Crystal phase of the pure and alkali metal (Li, Na, K)-doped ZnO thin films are identified from X-ray diffraction (XRD) as shown in Fig. 6.1 (a). All the films are found to have hexagonal wurtzite ZnO crystal structure grown on c-axis (006) Al<sub>2</sub>O<sub>3</sub> substrate. The appearance of only ZnO (002) and ZnO (004) diffraction peaks indicates that the pure ZnO and alkali (Li, Na)-doped ZnO films are preferentially grown along c-axis (002) direction except the K-doped ZnO film. For Li-doped ZnO, the position of ZnO peaks is found to be shifted towards the higher angle (2 $\theta$ ) side while for Na and K-doped films, the diffraction peaks are shifted in the opposite direction. The values of lattice parameters (*a* and *c*-parameter) as well as the lattice volumes (*V*) of the hexagonal ZnO unit cell are estimated and shown in Fig. 6.1(b). It is found that the variation of *c*-parameter is quite significant for all the doped samples whereas the *a*-parameter remains almost unchanged for all the samples except the K-doped ZnO film. The substitution of smaller Li<sup>1+</sup> ion (0.73 Å) replacing Zn<sup>2+</sup> ions (0.74 Å) leads to a contraction of ZnO lattice volume (*V*) in Li-doped ZnO whereas the substitution of comparably larger Na (0.97 Å) and K (1.33 Å) ions lead

an expansion of ZnO lattice volume as shown in inset of Fig. 1(b). This significant change of lattice parameters provides an indication of successful substitution of alkali ions at Zn site within the ZnO lattice [1, 2].

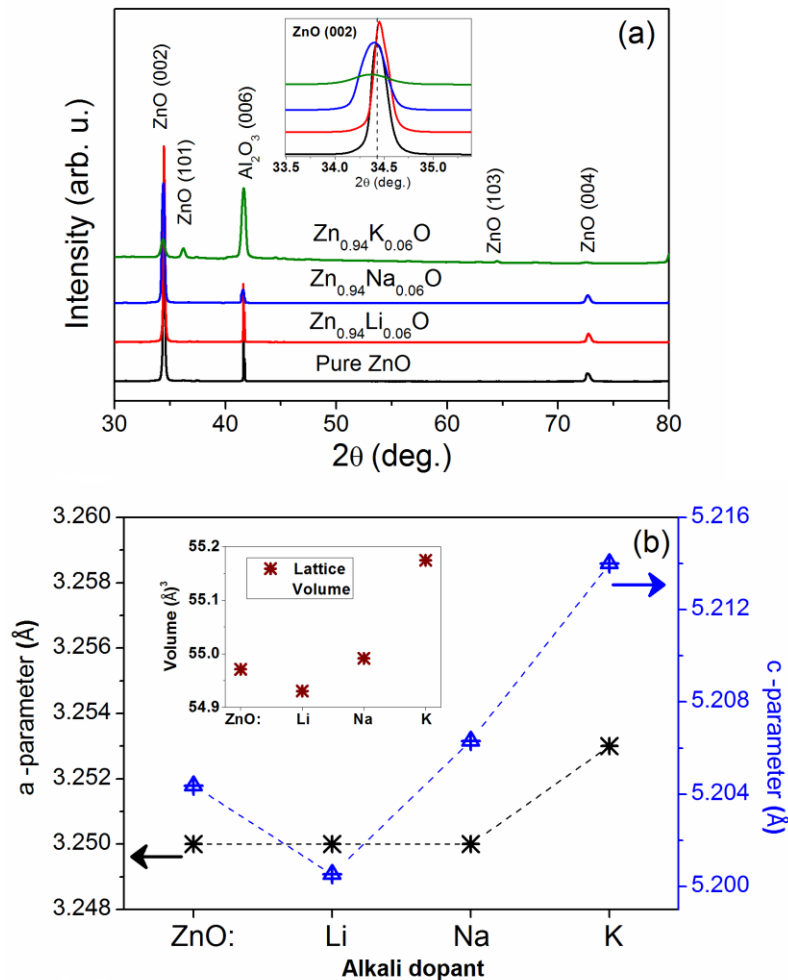


**Fig. 6.1:** (a) X-ray diffraction patterns for pure and alkali-doped ZnO films indicating single phase hexagonal wurtzite ZnO with preferential growth along c-axis (002). Inset: Indicating the shifting of diffraction peak due to alkali-doping. (b) Variation of lattice parameters ( $a$  and  $c$ -parameter) of ZnO unit cell due to doping of different alkali atoms.

### 6.2.3.2 Magnetic properties

Figure 6.2 (a) show the field-dependent magnetization,  $M$  (H) curves for undoped and alkali-doped ZnO thin films. The  $M$ - $H$  data are presented after subtracting the substrate diamagnetic contribution. The pure ZnO thin film exhibits a linear  $M$ - $H$  with negative slope which signifies a diamagnetic behaviour. However, the alkali-doped ZnO films are found to exhibit significant RT ferromagnetism.

Among the three different alkali-doped films, the Li-doped ZnO film is found to exhibit strongest RTFM with saturation magnetization ( $M_S$ ) of  $\sim 2.28$  emu/cm<sup>3</sup>

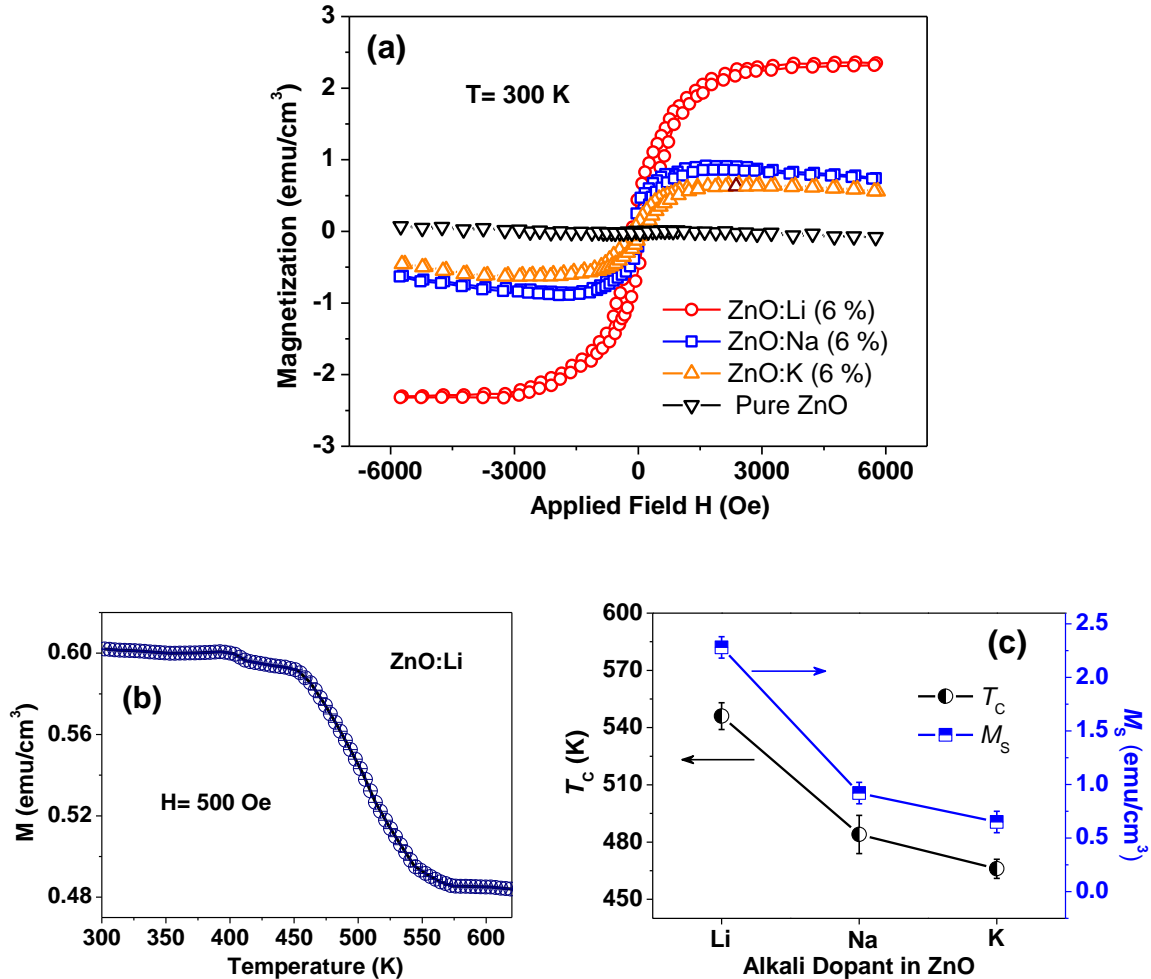


**Fig. 6.2:** (a) RT field-dependent magnetization,  $M$  ( $H$ ) curves of pure and alkali-doped ZnO films after subtracting the substrate diamagnetic contribution. Inset: (i) Temperature-dependent magnetization  $M$  ( $T$ ) curve for Zn<sub>0.94</sub>Li<sub>0.06</sub>O film. (ii) Variation of  $M_S$  and  $T_C$  in different alkali-doped ZnO films.

whereas the Na and K-doped film show comparably weaker FM. The values of  $M_S$  in Na and K-doped ZnO films are found to be  $\sim 0.80$  and  $0.64$  emu/cm<sup>3</sup>, respectively. The temperature dependent  $M$  ( $T$ ) measurements are performed at high temperature, ranging 300-650 K for all the films and Fig. 6.2 (b) shows a representative  $M$  ( $T$ ) behaviour for Li-doped ZnO film. Using the  $M$  ( $T$ ) data, the values of Curie temperature ( $T_C$ ) for the alkali-doped ZnO films have been estimated and the variations of  $T_C$  and  $M_S$  for the different alkali-doped ZnO films are plotted

in Fig. 6.2 (c). The highest value of  $T_C \sim 546$  K is observed for Li-doped ZnO film whereas comparatively lower  $T_C \sim 484$  K and 466 K are observed for Na- and K-doped ZnO films respectively. Therefore, the experimental observation indicates that the non-magnetic group-1 alkali-metal-doping must have significant role to stabilize RTFM in ZnO films. It can be expected that the modification of various defects or defect complexes within the ZnO lattice due to different alkali-metal doping may be holding the key to stabilize RTFM.

### 6.2.3.3 Magnetic force microscopy studies

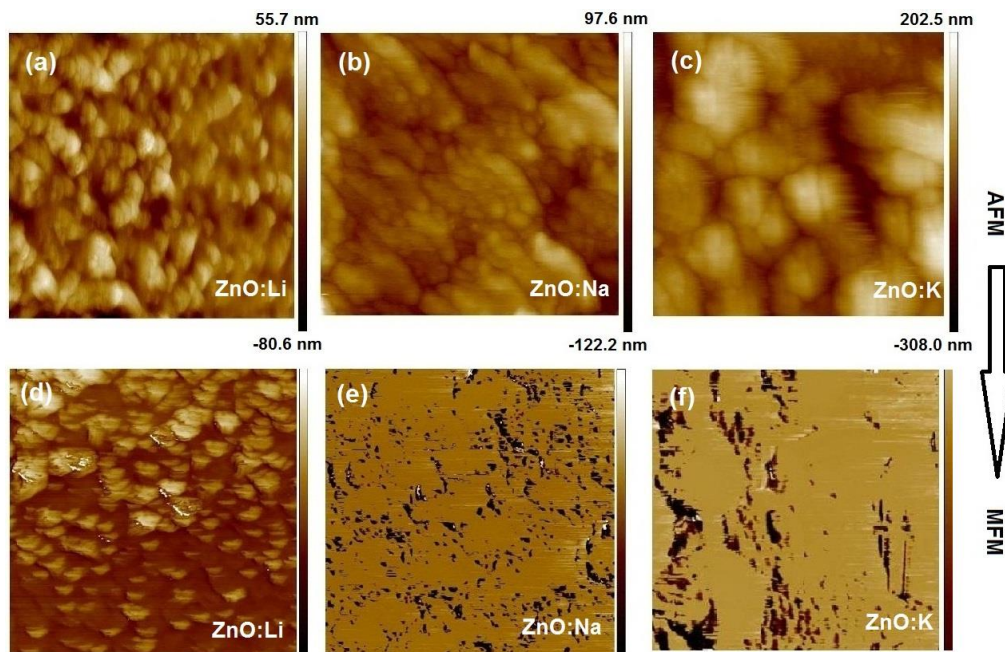


Fig. 6.3: AFM micrographs ( $2.5 \mu\text{m} \times 2.5 \mu\text{m}$ ) of alkali-doped ZnO films in (a)-(c), and the corresponding MFM images showing the respective domain configurations within the film in (d)-(f).

In order to visualize the domain structures and domain configuration inside the films, atomic force microscope (AFM) and magnetic force microscope (MFM) are used with a lift height of  $\sim 300$  nm over a scan size of  $2.5 \times 2.5 \mu\text{m}$ . Figure 6.3 (a)-(c) show the AFM micrographs of Li-, Na- and K-doped ZnO films which show the variation of film surfaces due to different alkali-metal-doping. The corresponding MFM images, taken on the same region are shown in Fig. 6.3 (e)-(f), in which bright and dark contrasts of the domains correspond to high concentrations of positive and

negative poles, respectively. It is noticeable that the magnetic domains are most prominent and quite regularly distributed in the Li-doped ZnO film compared to the other films, indicating the existing of strong FM. In K-doped ZnO film, the grains are very much defused, irregular and also widely apart. For Na-doped ZnO film although the large number of grains are present, corresponding magnetic domains are found to be very small in size, results in lowering of  $M_s$  compared to Li-doped ZnO film.

### 6.2.3.4 X-ray photoelectron spectroscopy studies

The account of chemical composition, valence state and the introduction of defects due to alkali-doping within the ZnO matrix are examined by XPS measurements using the Mg  $K_{\alpha}$  source. Figure 6.4 (a) shows the typical XPS survey scan for Li-doped ZnO thin film which indicates the presence of Zn, O, C and Li as the preliminary elements. The high-resolution XPS spectrum of the Zn 2p core level, shown in inset (i) of Fig. 6.4 (a), displays a doublet located at 1022.79 and 1045.89 eV respectively that corresponds to the core lines of Zn 2p<sub>3/2</sub> and 2p<sub>1/2</sub> states. The binding energy difference (23.1 eV) between the two peaks is in good agreement with the standard reference value of ZnO [3]. The estimated values of the binding energies and the binding energy difference of the Zn 2p spectrum indicate that the Zn is in the +2 oxidation state [4]. The core level Li 1s spectrum is shown in the inset (ii) of Fig. 6.4 (a). The observation of peak at an energy value of 55.4 eV indicates the presence of Li-O bond within Li-doped ZnO film which signifies the successful substitution of Li<sup>1+</sup> ions at Zn site [5, 6]. For K-doped ZnO film, two major peaks at 293.5 eV and 296 eV, observed in the core level K 2p spectra in Fig. 6.4 (b), corresponding to K 2p<sub>3/2</sub> and 2p<sub>1/2</sub> line is associated with the substitutional K<sup>1+</sup> ion at Zn site ( $K_{Zn}$ ). However, the appearance of weak peak around 292.9 eV can be associated with K-interstitial ( $K_i$ ) defects within ZnO matrix [7-9]. The core-level O 1s peak for Li-doped ZnO, as shown in inset of Fig. 6.4 (b), can be fitted with two Gaussian components centred at 531.07 and 532.33 eV. The low binding energy peak (531.07 eV) can be attributed to O-Zn bond, which is related to O<sup>2-</sup> ions on the wurtzite structure of the hexagonal Zn<sup>2+</sup> ion array [10]. On the other hand, the higher energy peak (532.33 eV) is usually due to the presence of Zn(OH)<sub>2</sub> phase which may form by absorbing the atmospheric moisture [10]. Hence, from the XPS study, it can be confirmed that that the alkali atoms (Li, Na, K) substitutes at Zn site

within the ZnO and are in +1 oxidation state. It is necessary to mention that the substitution of monovalent alkali ions replacing divalent Zn ion can introduce a hole into the ZnO system and presence of sufficient amount of such substitutional defects ( $M_{Zn}$ ) can sometimes leads to p-type conductivity for the alkali-doped ZnO films [11-15]. The concentration of Li, Na and K within doped ZnO films, as estimated from XPS analysis (Table 1), are found to be 5.37, 5.13 and 4.97 at.% of Li, Na and K against the 6 at.% nominal concentration for each dopants.

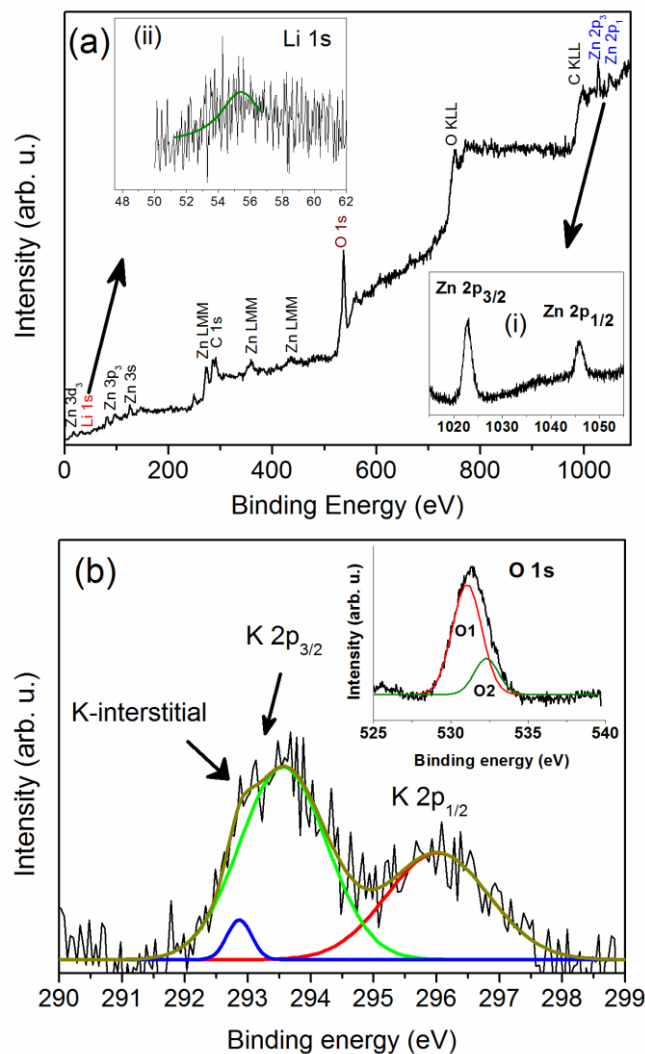


**Fig. 6.4:** (a) Typical XPS survey scan for  $Zn_{0.94}Li_{0.06}O$  thin film using Mg  $K_{\alpha}$  source. Inset (i) and (ii) show the high resolution XPS spectrum for Zn 2p and Li 1s core level, (b) K 2p, and O 1s (in inset) core level XPS spectrum within the  $Zn_{0.94}K_{0.06}O$  film (solid lines indicates the fitted peaks).

### 6.2.3.5 Photoluminescence spectroscopy studies

In order to investigate the modification of different defect-related states within the ZnO energy band-gap, photoluminescence (PL) spectroscopic measurement performed for all the films. Figure 6.5 (a) shows the normalised PL spectra observed at room temperature for undoped and alkali-doped ZnO films while the individual PL emission are analysed in details, as shown in Fig. 6.5 (b)-(e). Undoped ZnO film is found to exhibit intense UV-emission at  $\sim 3.1$  eV along with comparatively weaker defect-related green emission band at 2.38 eV. The UV emission corresponds to the free exciton (FX) recombination near the band edge (NBE) through an exciton-exciton collision process [16]. On the other hand, the broad green emission band centred at 2.38 eV must be related to the intrinsic defects in ZnO. After doping with alkali elements the UV emission is found to be suppressed significantly while the mid-band defect emission bands ranging from 2.1-2.6 eV became very strong. In addition, the UV emission for Li and Na-doped ZnO is also found to be red-shifted. This redshift of UV emission can be understood due to the incorporation of defect-related energy states near to valence/conduction band edge within the ZnO energy-gap due to alkali-doping. In fact, the alkali substitutional defects are known to create a shallow acceptor state above the valence band maximum (VBM) [11-13]. Hence, the emission band centred at 2.90 eV, shown in Fig. 6.5 (c) for Li-doped ZnO film can be attributed due to electronic transition from conduction band minimum (CBM) to the shallow acceptor states of Li substitutional ( $Li_{Zn}$ ) defects [14, 15]. Similarly, for the Na-doped film, the existence of shallow acceptor states of Na substitutional ( $Na_{Zn}$ ) within 2.85-3.0 eV can also be visualised by comparing the PL emission near the UV zone (2.85-3.10 eV) of undoped and Na-doped ZnO films. The extended broad nature of emission band in UV region for Na-doped ZnO might be possibly due to the convergence of both band to band (CBM to VBM) electronic transition and as well as the transition related to CBM to substitutional Na ( $Na_{Zn}$ ) acceptor states. However for the K-doped film, no such emissions in UV region are observed.

Besides the near band edge emission (NBE), each alkali-doped ZnO film is found to exhibit strong emission band at green (2.38 eV) and yellow-orange region (2.1-2.2 eV), as can be seen from the Fig. 6.5 (c)-(d). The origin of green luminescence in ZnO PL spectra became quite controversial. Sekiguchi *et al.* [17] and Raynolds *et*

*al.* [18, 19] have suggested that Zn vacancy can produce significant green luminescence in ZnO. Several groups also reported that oxygen vacancy is the source of green luminescence in ZnO [20, 21]. Green luminescence is also observed for Cu-doped ZnO in which the presence of Cu impurities has been suggested as source of green luminescence, however even for the samples not contained any Cu impurity also exhibited green luminescence [22]. In a recent review, Janotti *et al.* [23] addressed the controversy and have presented strong arguments in favour of Zn vacancies ( $V_{Zn}$ ), instead of oxygen vacancies ( $V_O$ ), for the origin of green

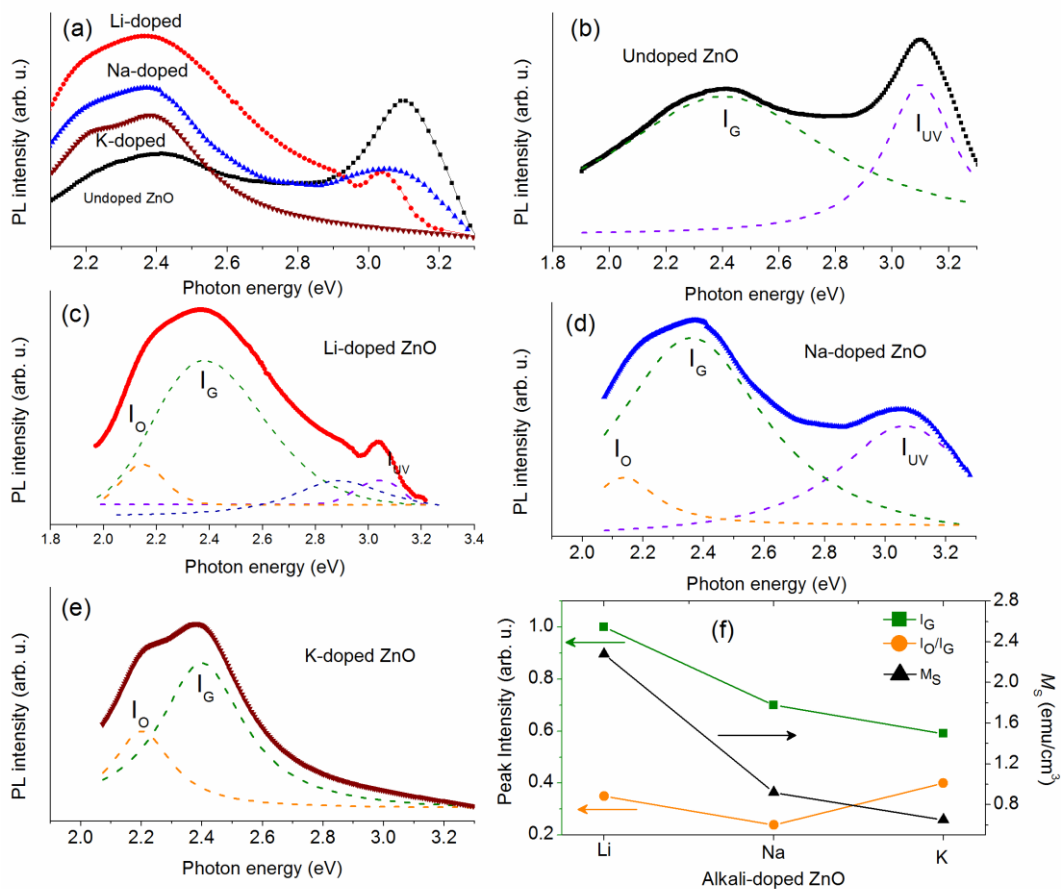


**Fig. 6.5:** (a) Room-temperature PL spectrum of pure and alkali-doped ZnO films. Individual PL emissions with multiple peak fitting (dashed lines) in (b) undoped ZnO, (c) Li-doped, (d) Na-doped (e) K-doped ZnO films (f) the variations of  $I_G$ ,  $I_O/I_G$  and  $M_s$  with alkali-dopants which reveals a correlation between  $M_s$  and  $I_G$  for different alkali-doped ZnO films.

luminescence. Earlier, for K- doped ZnO nanowires [24], we have also observed significant change in green emission due to K-doping in ZnO, which is attributed to

$V_{Zn}$  defects. Here, for the alkali-doped ZnO films, the probability of considerable amount  $V_O$  formation should be very low due to the following reasons: (i) Firstly, all the films are prepared under high oxygen pressure ( $\sim 10^{-2}$  mbar) which reduce the possibility of formation of significant oxygen vacancies in the films, whereas  $V_{Zn}$  may stabilize under oxygen-rich condition [24-25]. Secondly, all the films after deposition are annealed in  $O_2$  atmosphere at high temperature which will again reduce the possibility of  $V_O$  formation. Recently, it has been suggested that the incorporation of alkali-dopants can reduce the formation energy of  $V_{Zn}$  in ZnO and thereby can also stabilize considerable amount of  $V_{Zn}$  [24, 26, 27]. Hence, we attribute the intense green luminescence band centred at 2.38 eV to the electronic transition between conduction band minimum (CBM) and the Zn vacancy ( $V_{Zn}$ ) acceptor state [17, 18, 23, 24, 29]. Therefore, from Fig. 6.5 (a) it is quite obvious that the Li-doped ZnO film contains the maximum amount of  $V_{Zn}$  compared to the Na/K-doped ZnO films. On the other hand, the yellow-orange emission band observed in each alkali-doped ZnO films can be attributed due to electronic transition from CBM to the deep acceptor-type alkali-substitutional ( $M_{Zn}$ ) defects [29, 30]. Besides shallow acceptor states, the group-I alkali elements are also found to create a deep acceptor defect with binding energy of 600-800 meV, which can provide yellow luminescence around 2.2 eV in the PL spectra [14, 29, 30].

### 6.2.3.6 Electrical behaviour

The nature of conductivity of the films is measured by standard hall measurement set-up using four probe method. Figure 6.6 (a) and (b) shows the variation of different electrical transport parameters such as resistivity ( $\rho$ ), hall coefficient ( $R_H$ ), carrier (electron/hole) concentration ( $\eta$ ) and carrier mobility ( $\mu$ ). The negative value of Hall coefficient ( $R_H$ ) for pure ZnO film indicates n-type conduction while the values of  $R_H$  are found to be positive for alkali-doped ZnO films, signifies their p-type behaviour. The carrier (electron) concentration for undoped ZnO is found to be  $\sim 8.7 \times 10^{17}/\text{cm}^3$ . On the other hand, the carrier (hole) concentration ( $\eta$ ) as well as carrier mobility ( $\mu$ ) in alkali-doped ZnO film, are found to decrease gradually as we change the alkali dopant element from Li to Na and then to K. As a result the resistivity ( $\rho$ ) of the film found to increase. The p-type conductivity mainly arises due to the doping of alkali-metals in ZnO. The substitution of monovalent

alkali ions ( $M^+$ ) at  $Zn^{2+}$  ions site, as evident from XRD and XPS measurements, can introduce hole into the system [11, 14]. In addition, we have seen that the alkali-doped films do not contain significant amount of  $V_O$  which act as a donor within ZnO. On the other hand, the alkali-doped films contains large amount of acceptor-type  $V_{Zn}$  defects which can also play an important role to achieve p-type conductivity [23, 28].

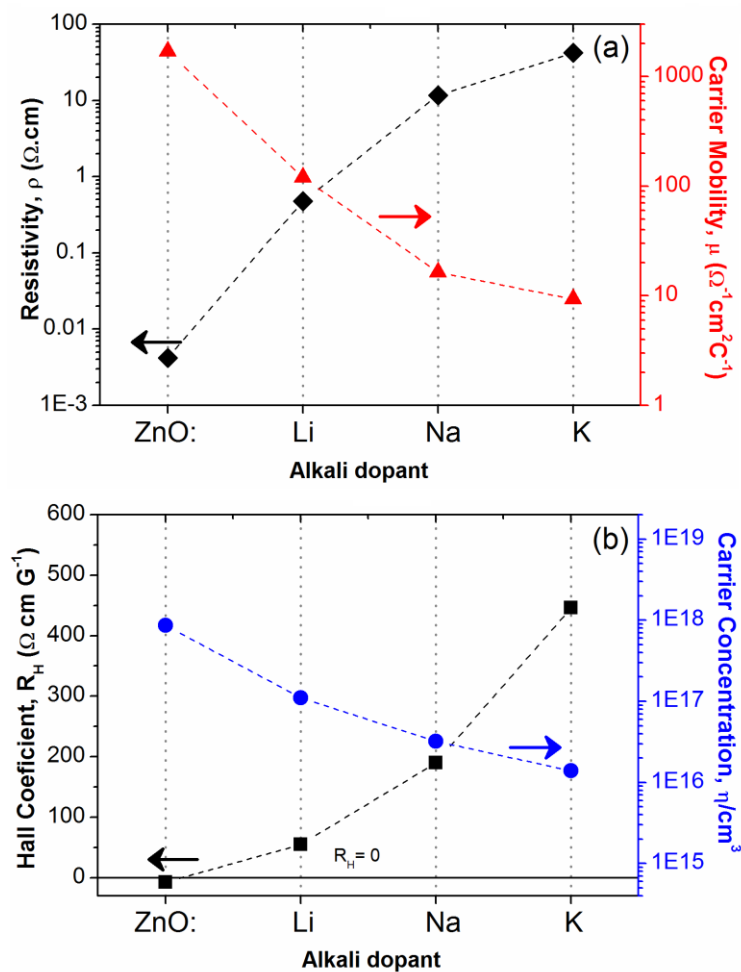


**Fig. 6.6:** Estimated values of (a) film resistivity ( $\rho$ ) and carrier mobility ( $\mu$ ); (b) Hall coefficient ( $R_H$ ) and carrier concentration ( $n$ ) of pure and alkali-doped ZnO films.

We attribute the origin of RTFM in the alkali-doped ZnO films mainly to  $V_{Zn}$  defects. Wang *et al.*[31] have shown that the presence of  $V_{Zn}$  leads to the spin polarization of O 2p orbital which is source of localised magnetic moment. Besides  $V_{Zn}$ , the substitutional alkali defects such as  $Li_{Zn}$ ,  $Na_{Zn}$ ,  $K_{Zn}$  etc. can also induce localised magnetic moment which can contribute to the overall magnetic moment

[27, 32]. The concentration of  $V_{Zn}$  increases due to the doping of such alkali metals and when the concentration exceeds the percolation threshold, long-range ferromagnetic exchange interaction between the localised moments can be mediated by the hole due to  $M_{Zn}$  acceptors. The strength of ferromagnetic interaction not only depends on the defect concentration but also on the effective hole concentration exists in the system. In a proposed model, Bouzerar and Ziman [27] have shown that for a fixed defect ( $V_{Zn}$ ) concentration, there exists an definite window of hole concentration within which the ferromagnetic exchange interaction becomes most stable. Here, from the Fig. 6.5 (f) it is seen that the ratio of the intensities of green and yellow-orange emission, i.e.  $I_O/I_G$  does not changed significantly with the variation of alkali dopants. This implies that the yellow-orange emission does not have a direct control over the magnetic properties of the alkali-doped ZnO films. However, a direct correlation is observed between the green luminescence ( $I_G$ ) and corresponding saturation magnetization ( $M_S$ ) of the respective alkali-doped film which indicates that intensity of green emission i.e.  $V_{Zn}$  defects are playing a key role to stabilize and enhance RTFM in the alkali-doped ZnO films. The  $V_{Zn}$  as well the hole concentration is found to be maximum in Li-doped ZnO and consequently it exhibits large  $M_S$  and also highest  $T_C$ . Moving vertically down through the group-1A column in the periodic, for example from Li to Na, then to K and so on, the ionic size difference between the  $Zn^{2+}$  and respective alkali ions ( $M^{1+}$ ) increases gradually and as a result, the possibility of partial substitution of the alkali atom may increase. This means a few percentage of alkali atoms may occupy the lattice interstitial site as observed in K2p core level XPS spectra of K-doped ZnO film. As the size of the alkali-dopants increase more and more, the percentage of interstitial donor defects in ZnO lattice can also increase which should reduce the effective hole concentration through the donor-acceptor recombination process. Consequently, the strength of the ferromagnetic interaction in Na/K-doped ZnO should also decrease due to the gradual decrease of effective hole concentration, as evident from the Hall measurements. It is also important to discuss that although the undoped ZnO film also contain some amount  $V_{Zn}$  defects, no RTFM is observed. The low intensity of green emission ( $I_G$ ) indicates the  $V_{Zn}$  concentration in undoped ZnO film should be quite low, may be below the require threshold vacancy concentration [18] to sustain long-range ferromagnetic ordering.

## 6.3 Luminescent *p*-type Na-Doped ZnO Thin Films: Influence of Film-thickness and Oxygen Pressure

### 6.3.1 Fabrication of *p*-type Na-doped ZnO thin films

Pure and Na-doped ZnO thin films are deposited by pulse laser deposition (PLD) technique on the *c*-axis-sapphire ( $\text{Al}_2\text{O}_3$ ) substrate using a KrF excimer laser of power density of  $2.14 \text{ J/cm}^2$  and pulse repetition rate of 5 Hz. High purity ZnO and Na-acetate (99.99%) powders are mixed in appropriate ratio have been palletized and then sintered at  $800^\circ \text{C}$  to prepare of targets for 6 at.% Na-doped ZnO films. The base pressure of the deposition chamber and the substrate temperature was maintained at  $5 \times 10^{-5}$  torr and  $500^\circ \text{C}$ , respectively. Keeping the  $PO_2$  of the PLD chamber fixed at a particular level, the thickness of the  $\text{Zn}_{0.94}\text{Na}_{0.06}\text{O}$  films is varied from 69 to 216 nm by changing the total numbers of laser shots. Another sets of  $\text{Zn}_{0.94}\text{Na}_{0.06}\text{O}$  films with constant thickness are prepared by changing the level of  $PO_2$  from  $10^{-4}$  to  $10^{-2}$  torr.

### 6.3.2 Results and discussions

#### 6.3.2.1 Structural and electrical properties

The crystallographic phases of pure ZnO and  $\text{Zn}_{0.94}\text{Na}_{0.06}\text{O}$  films are indentified using grazing incidence XRD (GI-XRD), shown in Figure 6.7. The observation of only ZnO (002) and (004) diffraction peak indicates that the ZnO film have hexagonal wurtzite crystal structure and highly oriented along the *c*-axis [001] direction. The preferential growth of ZnO thin films along the [001] direction are due to the fact that the ZnO films are deposited on (001) sapphire (*c*-plane  $\text{Al}_2\text{O}_3$ ) substrates. As both ZnO and  $\text{Al}_2\text{O}_3$  substrate has hexagonal crystal structure with definite *c/a* ratio, the ZnO film prefers to grow along the existing growth direction of the  $\text{Al}_2\text{O}_3$  substrate which is [001] here. However, it is also noticeable that the intensity of the (006) diffraction peak of the thick *c*- $\text{Al}_2\text{O}_3$  substrate ( $\sim 1 \text{ mm}$ ) is very weak compared with the diffraction peaks for very thin ZnO films (only 64-194 nm). It happens because here we have conducted the GI-XRD measurements. The GI-XRD technique uses small incident angle ( $\sim 1^\circ$  with the film surface) for the incoming x-ray beam, so that diffraction can be made only surface sensitive and thus it is quite

able to avoid the strong diffraction peaks arising from the thicker substrate. In addition, the ZnO (002) peak for Na-doped ZnO film is found to be shifted towards lower  $2\theta$  direction (inset of Figure 6.7) which confirms the successful substitution of large  $\text{Na}^+$  ions (radius  $\sim 0.097$  nm) replacing smaller  $\text{Zn}^{2+}$  ions (radius  $\sim 0.074$  nm) [33]. The increase of the peak width of ZnO with Na-doping signifies a reduction of the crystallite size for Na-doped ZnO films. Hall measurement was performed to estimate the carrier concentrations and the types (n-type/p-type) of the semiconducting films. All the Na-doped ZnO films are found to be p-type while the pure ZnO film is found to be n-type. The substitution of monovalent Na at divalent Zn site can introduce holes into the system and therefore, the transformation from n-type to p-type ZnO due to Na-doping is possible. Figure 6.8 shows the variation of carrier (hole) concentrations ( $\eta$ ), film resistivity ( $\rho$ ) and carrier mobility ( $\mu$ ) in case of the Na-doped ZnO films with similar thickness ( $\sim 114$  nm) grown at different oxygen partial pressures ( $P_{\text{O}_2} = 10^{-3}$ ,  $10^{-4}$  and  $10^{-2}$  torr). The hole concentration is found to increase gradually with increase of  $P_{\text{O}_2}$  while the values of film resistivity and carrier mobility are found to decrease with  $P_{\text{O}_2}$ .

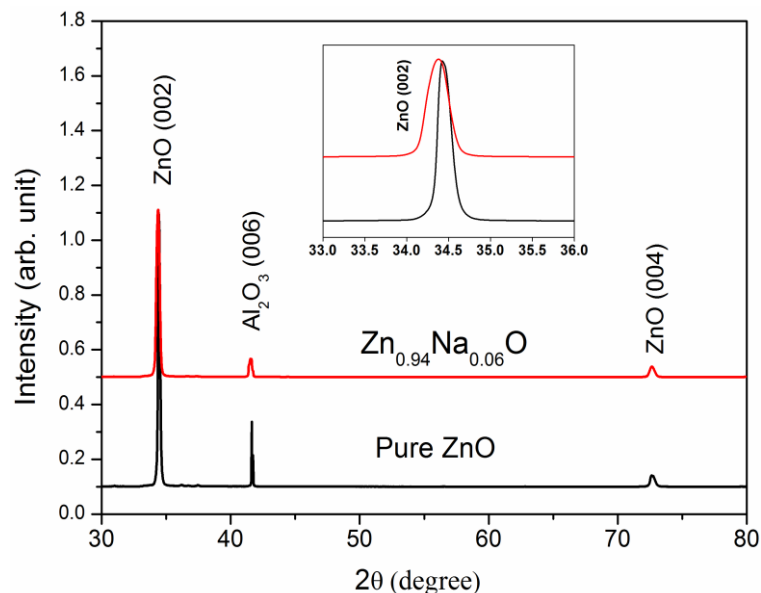


**Fig. 6.7:** XRD pattern of pure ZnO and  $\text{Zn}_{0.94}\text{Na}_{0.06}\text{O}$  thin films. Inset: High magnification view of ZnO (002) diffraction peak which indicating the shifting of (002) diffraction peak towards lower  $2\theta$  direction for Na-doped ZnO film.

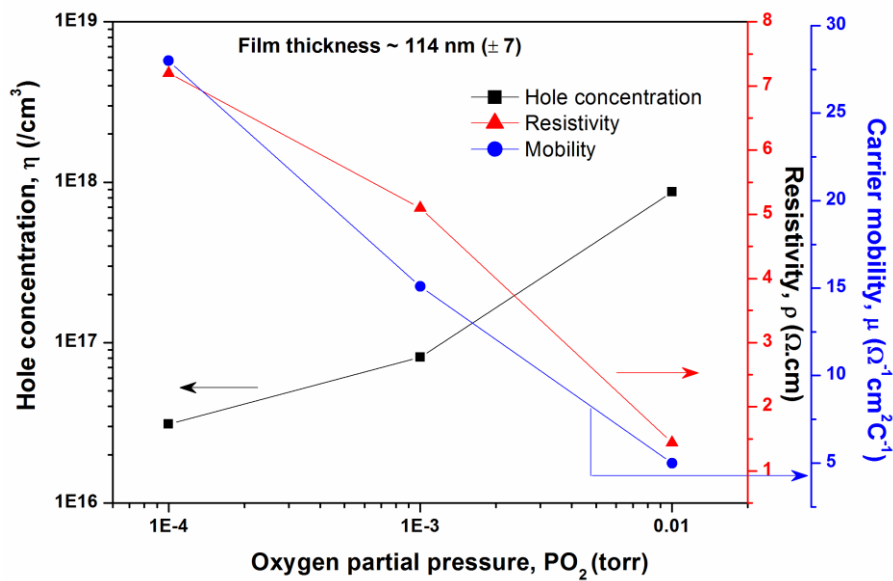


**Fig. 6.8:** Variation of carrier (hole) concentration ( $\eta$ ), film resistivity ( $\rho$ ) and carrier mobility ( $\mu$ ) in case of the Na-doped ZnO films with similar thickness ( $\sim 114$  nm) grown at different oxygen partial pressures ( $PO_2 = 10^{-3}$ ,  $10^{-4}$  and  $10^{-2}$  torr).

### 6.3.2.2 Thickness dependent magnetic behavior

Figure 6.9 (a) shows the RT field-dependent magnetization (M-H) measurements for  $Zn_{0.94}Na_{0.06}O$  films of different thicknesses prepared under  $PO_2 \sim 10^{-2}$  torr. All the  $Zn_{0.94}Na_{0.06}O$  films with various thicknesses are found to exhibit significant FM at RT. It is important to notice that the  $Zn_{0.94}Na_{0.06}O$  film with lowest thickness ( $\sim 64$  nm) exhibits largest saturation magnetization ( $M_S$ )  $\sim 2.02$  emu/cm<sup>3</sup> and the value of  $M_S$  decreases gradually with increase of film-thickness. Figure 6.9 (b) shows a representative temperature-dependent magnetization, M (T) data for  $Zn_{0.94}Na_{0.06}O$  film of 114 nm thick. The values of Curie temperatures ( $T_C$ ) estimated from the high temperature M (T) measurements are found to be well above the RT (300 K). However, like  $M_S$ , the values of  $T_C$  are also found to decrease consistently with increasing of the film-thickness. The highest value of  $T_C$  ( $\sim 526$  K) obtained for 64 nm thick  $Zn_{0.94}Na_{0.06}O$  film. RT ferromagnetic behaviour is also observed even in case of undoped ZnO film of  $\sim 69$  nm thick, but the value of  $M_S$  is found to be one order less in magnitude compared to the  $Zn_{0.94}Na_{0.06}O$  film with similar thickness ( $\sim 64$  nm) prepared under same level of  $PO_2$  ( $\sim 10^{-2}$ ) torr. However, the pure ZnO film with larger thickness ( $\sim 196$  nm) no RTFM is observed (not shown here), instead showed a diamagnetic behaviour. Therefore, the observation the RTFM in low

thickness films indicates that significant change of structural defects which might be playing crucial role to stabilize magnetic interaction.

In order to visualize the domain structures and domain configuration inside the ferromagnetic films, magnetic force microscope (MFM) have been used. Figures 6.9 (c) and (d) show the comparison of the MFM micrographs of pure ZnO (~ 69 nm thick) and Zn<sub>0.94</sub>Na<sub>0.06</sub>O films (~ 64 nm thick) respectively. The existence of strong ferromagnetic ordering in Zn<sub>0.94</sub>Na<sub>0.06</sub>O film can be visualize through the regular distribution of magnetic domains where the bright and dark contrasts correspond to high concentrations of positive and negative poles, respectively. On the other hand, the MFM micrograph of pure ZnO film with a few irregular, defused grains signifies its relatively weak ferromagnetic ordering.

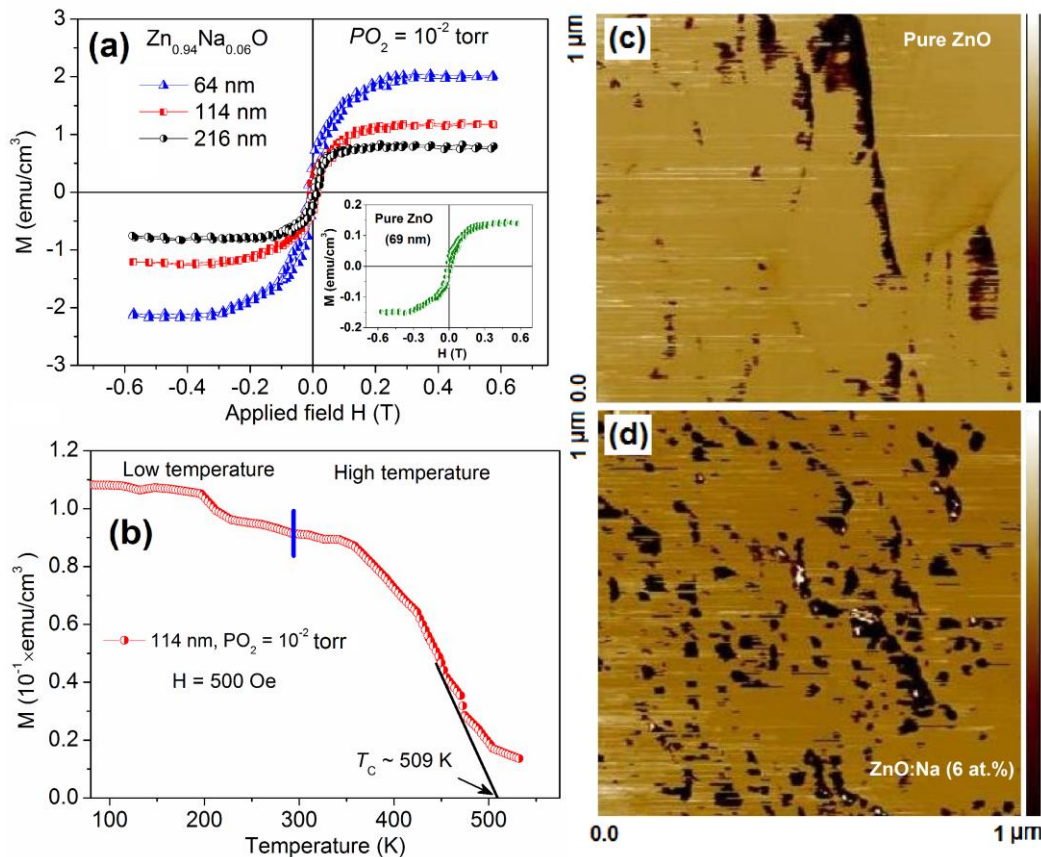


**Fig. 6.9:** (a) Room-temperature M-H measurements for Zn<sub>0.94</sub>Na<sub>0.06</sub>O films with various thicknesses prepared under  $PO_2 \sim 10^{-2}$  torr. Inset: M-H behaviour of pure ZnO film at 300 K. (b) Temperature dependent magnetization,  $M$  (T) curves for 114 nm thick Zn<sub>0.94</sub>Na<sub>0.06</sub>O film. MFM micrographs of (c) pure ZnO and (d) Zn<sub>0.94</sub>Na<sub>0.06</sub>O film revealing the individual domain configurations within the films.

### 6.3.2.3 Magnetic properties of Na-doped ZnO thin film: Influence of oxygen pressure

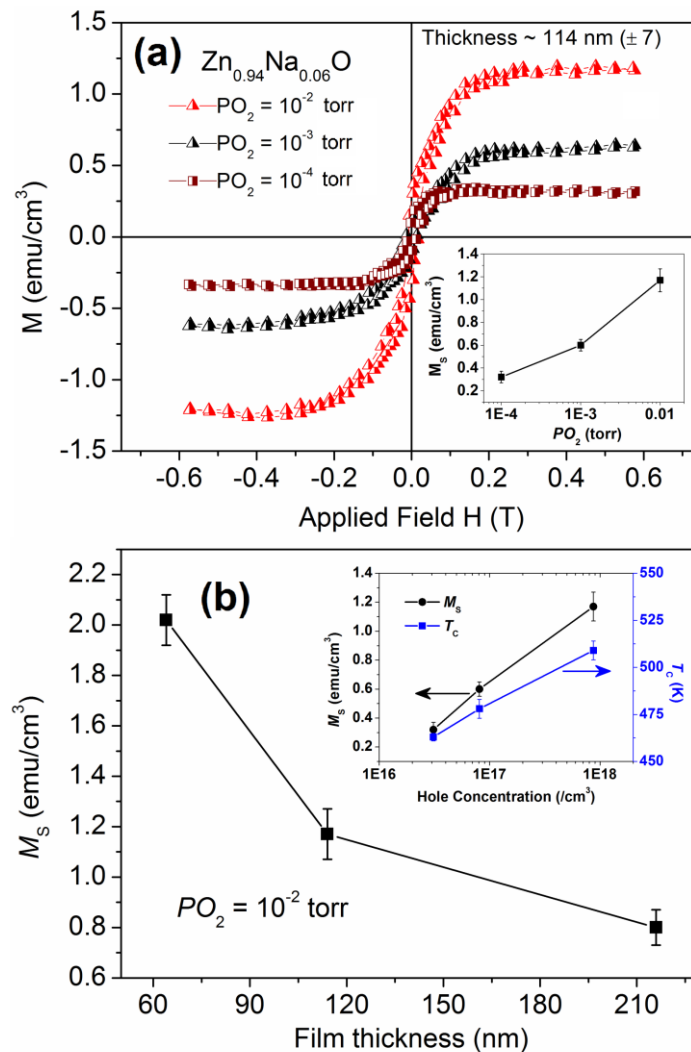


**Fig. 6.10:** (a) Room-temperature M-H measurements for similar thick ( $\sim 114$  nm)  $Zn_{0.94}Na_{0.06}O$  films prepared under different level of  $PO_2$ . Inset: Change in  $M_S$  with the level of  $PO_2$ . (b) Variation of  $M_S$  of  $Zn_{0.94}Na_{0.06}O$  films with the film-thickness, Inset: The change of  $M_S$  and  $T_C$  with the hole concentration ( $n$ ) in the 114 nm thick  $Zn_{0.94}Na_{0.06}O$  films grown at different oxygen partial pressure ( $PO_2 = 10^{-2}, 10^{-3}$  and  $10^{-4}$  torr).

The dependency of ferromagnetic signature in  $Zn_{0.94}Na_{0.06}O$  film on the oxygen partial pressure ( $PO_2$ ) under which the films were deposited, have also been examined and the corresponding M-H measurements are shown in Figure 6.10 (a). The film grown under highest level of ' $PO_2$ ' ( $\sim 10^{-2}$  torr) is found to exhibit largest  $M_S \sim 1.17$  emu/cm<sup>3</sup> and the values of  $M_S$  is found to decrease consistently with the decrease of  $PO_2$  (inset of Figure 4a). This is quite interesting observation because the

film prepared under low level of  $PO_2$  should have contain more oxygen vacancy ( $V_O$ ) defects [34]. Hence, if the magnetic moments were associated with the  $V_O$  defects then the film fabricated under low  $PO_2$  should exhibit larger magnetic moment. On the contrary, the gradual decrease of  $M_S$  with lowering of  $PO_2$  clearly indicates the magnetic moment in Na-doped ZnO films is not associated with  $V_O$  defects and must be originated from any other defects. The values of  $M_S$  and  $T_C$  of Na-doped ZnO films with similar thickness ( $\sim 114$  nm) are plotted against the corresponding hole concentration, as shown in the inset of Figure 6.10 (b). It is noticeable that both  $M_S$  and  $T_C$  in the  $Zn_{0.94}Na_{0.06}O$  films ( $\sim 114$  nm) increase with the increase of hole concentration. This observation gives the indication of hole-mediated ferromagnetic interaction in Na-doped ZnO films. On the contrary, the FM observed in case of pure ZnO film seems to be electron-mediated as the undoped material is found to be n-type.

#### 6.3.2.4 X-ray photoelectron spectroscopy studies

Figure 6.11 shows the XPS survey scan for  $Zn_{0.94}Na_{0.06}O$  film using Mg  $K_{\alpha}$  source and the high resolution XPS spectra of Zn 2p core level. From the XPS scan, as shown in Fig. 6.11 (a), no impurity elements except carbon (C) are detected in within the detection limit of XPS. The C 1s (284.6 eV) peak is usually used as an internal reference in the spectrum [35]. The C 1s peak may also be because of the carbon tape used during the measurements. The core level Zn 2p spectrum, shown in Figure 6.11 (b) displays a doublet located at 1022.10 and 1045.24 eV respectively corresponds to the core lines of Zn  $2p_{3/2}$  and  $2p_{1/2}$ . The binding energy difference (23.14 eV) between the two peaks of the Zn 2p spectrum clearly indicates that the Zn is in the +2 oxidation state [35, 36]. The core level of O 1s peak at 530.64 eV, shown in Figure 6.11 (c) indicates the Zn-O bond in the hexagonal wurtzite ZnO crystal structure [37] whereas, the observation Na 1s core level peak at 1071.40 eV as shown in Fig. 6.11 (d) confirms the presence of Na-O bond due to substitution of  $Na^{1+}$  at  $Zn^{2+}$  Site ( $Na_{Zn}$ ) within ZnO lattice [35, 38-40]. No evidence of metallic Na is observed in Na-doped ZnO films. Although it is also possible that some fraction (a little amount) of Na atoms may occupy the lattice interstitial site which can give rise to small shoulder peak at low binding energy than the substituted  $Na^{1+}$ . However, here, in

the Na 1s spectra we have not observed such evidence. In addition, the evidence of substituted  $\text{Na}^{1+}$  at Zn site has been observed during analysis of X-ray diffraction

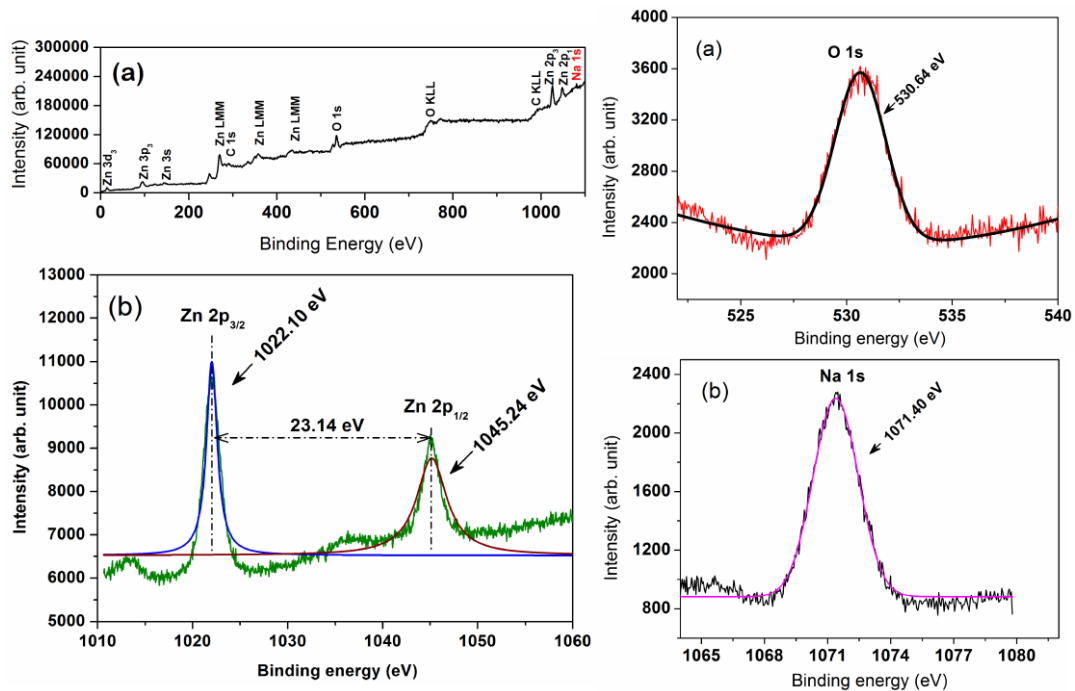


**Fig. 6.11:** (a) Typical XPS survey scan of  $\text{Zn}_{0.94}\text{Na}_{0.06}\text{O}$  film using  $\text{Mg K}\alpha$  source and (b) high resolution XPS spectra of (b) Zn 2p, (c) O 1s and (d) Na 1s core level in  $\text{Zn}_{0.94}\text{Na}_{0.06}\text{O}$  film.

patterns also. Therefore, we believe that the majority of Na atoms are substituted at Zn site ( $\text{Na}_{\text{Zn}}$ ) within the ZnO lattice. The  $\text{Na}_{\text{Zn}}$  defect is known to create a shallow acceptor states which can be responsible for the p-type conductivity of the Na-doped ZnO films [41, 42] as observed from the Hall measurements. The Na-doping concentration within the ZnO is also estimated from XPS analysis and found to be consistent within the range of 5.66 to 5.84 at.% which is less than the nominal concentration of 6 at. %.

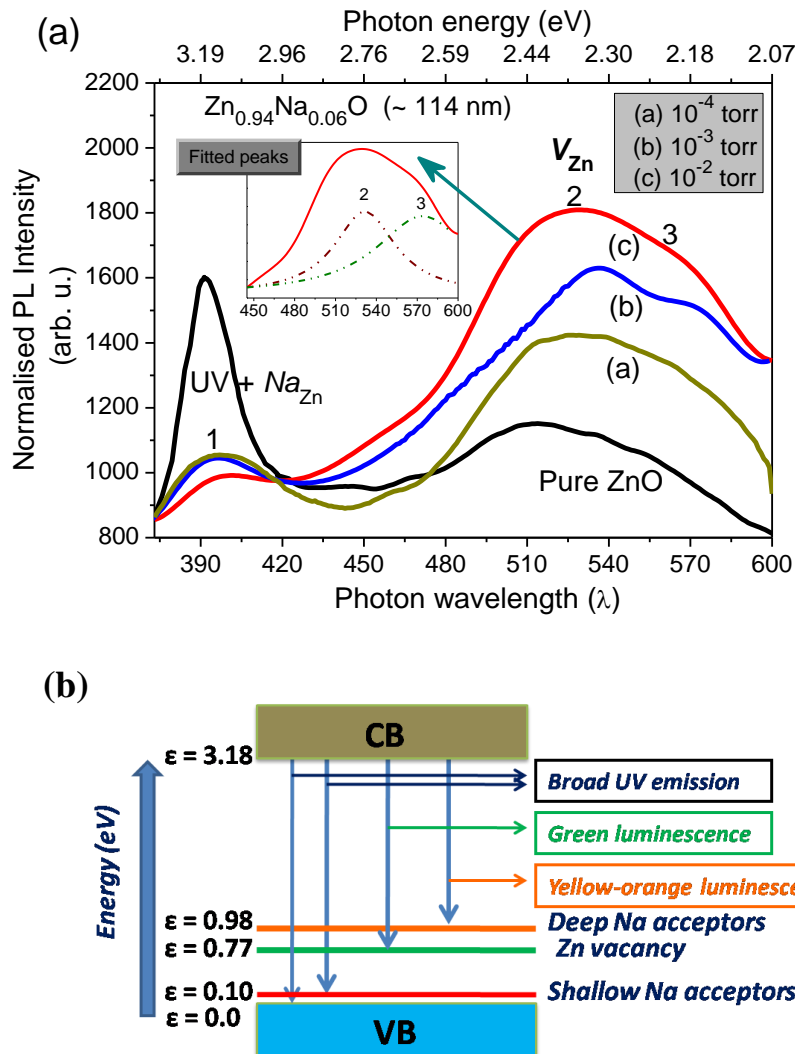
### 6.3.2.5. Room-temperature photoluminescence properties

Figure 6.12 (a) shows the room-temperature PL spectra of the pure ZnO and  $\text{Zn}_{0.94}\text{Na}_{0.06}\text{O}$  films of almost similar thickness prepared under various level of  $\text{PO}_2$  under an excitation wavelength ( $\lambda_{\text{ex}}$ ) of 330 nm. The PL spectrum of the pure and the Na-doped ZnO thin films is found to be exhibit both the defect-related and ultraviolet-visible (UV) emissions. With the incorporation of Na in ZnO, the UV

(peak 1) emission is found to suppress considerably due to the dominance of defect-related emissions like green (peak 2,  $\sim 2.38$  eV) and yellow-orange emission (peak 3,  $\sim 2.20$  eV). It is found that both the UV and the defect related bands becomes broad and red shifted in the Na-doped ZnO films compared with that of the pure ZnO film. The UV emission (peak 1) at 3.18 eV in the pure ZnO film is associated to the near band edge (NBE) emission due to the free exciton (FX) recombination through an exciton-exciton collision process [43]. The substitutional Na ( $Na_{Zn}$ ) defect is usually found to create shallow acceptor states above the valence band maximum (VBM) and the electronic transition between the conduction band minimum (CBM) and  $Na_{Zn}$  acceptors can generate emission peak around 3 to 3.1 eV in the PL spectrum of the Na-doped ZnO thin films [41, 42]. Therefore, the UV emission of the  $Zn_{0.94}Na_{0.06}O$  films becomes broad and red shifted due to the convergence of the electronic transitions from CBM to both shallow  $Na_{Zn}$  acceptor states and to the valence band (band to band transition). Besides shallow acceptor states, the group-I alkali elements are also found to create a deep acceptor state with binding energy of  $\sim 600$ - $800$  meV, which can provide yellow-orange luminescence around 2.2 eV (peak 3) in the PL spectra [44, 45]. Therefore, here, in case of  $Zn_{0.94}Na_{0.06}O$  films, the observed emission (peak 3) at yellow-orange zone (2.18 eV) can be assigned to the electronic transition from CBM to the deep  $Na_{Zn}$  acceptor levels [44, 45]. Due to appearance of yellow-orange emission in the Na-doped ZnO films the defect related band becomes broad and seems to be red-shifted compared with that of the pure ZnO film. Again with the increase of  $PO_2$  from  $10^{-4}$  to  $10^{-3}$  torr, the defect-emission band of Na-doped ZnO initially red-shifted due to relative increase of yellow-orange emission intensity. However, for further increase of  $PO_2$  ( $10^{-3}$  to  $10^{-2}$  torr), the defect-emission band becomes blue-shifted due to dominance of green emission. The entire PL emission processes are described in Figure 6.12 (b) with a schematic energy band diagram with different defect-levels within the ZnO band gap.

It is interesting to notice that all the  $Zn_{0.94}Na_{0.06}O$  films are found to exhibit significant green emission centred around 2.38 eV (peak 2) which is found to be enhanced due to Na-doping (Fig. 6.12 (a)). However, the origin of the green emission in ZnO thin films and nanostructures remains quite controversial [46]. Previously, it was suggested that that stabilization of  $V_O$  is responsible for green emission in ZnO but, recent studies have shown that it is Zn vacancy also or rather than  $V_O$ , which is

responsible for green luminescence in ZnO thin films and nanostructures [24, 34, 46-48]. The  $V_{Zn}$  defect is found to create deep acceptor level at  $\sim 0.9$  eV above the VBM



**Fig. 6.12:** (a) Room-temperature PL spectra of similar thick ( $\sim 114$  nm)  $Zn_{0.94}Na_{0.06}O$  films prepared under various level of  $PO_2$ . (b) Schematic energy band diagram exposing the position of different defect-states within the ZnO energy band gap and their electronic transitions occurring during PL emission.

and the electronic transition from the CBM to  $V_{Zn}$  acceptor levels often leads to the emission of visible green luminescence at 2.35-2.45 eV [46-48]. Here, the  $Zn_{0.94}Na_{0.06}O$  film prepared under  $PO_2 \sim 10^{-2}$  torr exhibits highest green-emission and the intensity of green-emission is found to fall gradually with decrease of  $PO_2$ . The  $V_O$  concentration is generally known to be inversely proportional to the oxygen partial

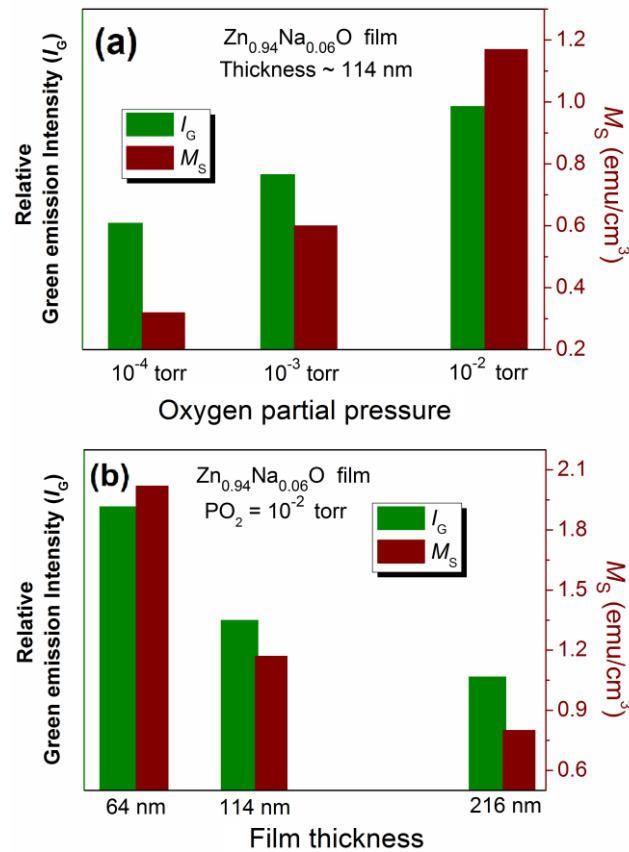


**Fig. 6.13:** Correlation between the magnitude of  $M_S$  and green luminescence intensity ( $I_G$ ), obtained from PL spectra, in  $Zn_{0.94}Na_{0.06}O$  films with various (a) film-thickness and (b)  $PO_2$ .

pressure ( $PO_2$ ) [34]. Therefore, in case of Na-doped ZnO films, the decrease of green emission intensity ( $I_G$ ) with the decrease of  $PO_2$  clearly excludes the possibility of  $V_O$  as the origin of green emission. On the other hand, the formation of Zn vacancy ( $V_{Zn}$ ) in ZnO is found to be energetically favourable under high level of  $PO_2$  [34]. Recently, Yi *et al.*[26] have suggested that the formation energy of  $V_{Zn}$  in ZnO can be reduced significantly in presence of the substitutional Li ( $Li_{Zn}$ ) and interstitial Li ( $Li_i$ ) defects through the formation of defect complexes such as  $V_{Zn}+Li_{Zn}+Li_i$  and  $V_{Zn}+Li_i$ . Hence, it is quite possible to stabilize considerable amount of  $V_{Zn}$  defects through the cationic substitution of alkali metal such as Li, K in ZnO [26, 24]. Therefore, similar to the Li and K, in present study, the Na-doping also might favour to stabilize  $V_{Zn}$  defects along with the Na substitutional ( $Na_{Zn}$ ) defects in  $Zn_{0.94}Na_{0.06}O$  films, where with the increase of  $PO_2$ , the concentration of  $V_{Zn}$  increases (evident from PL spectra). The intensity of the green luminescence is also found to decrease gradually

with the increase of film-thickness, which indicates that the stabilization of  $V_{Zn}$  defects in  $Zn_{0.94}Na_{0.06}O$  film might be favoured by decreasing the film-thickness. This may be due to the reason that  $V_{Zn}$  always prefer to reside at the surface due to low formation energy [31] and therefore, the probability of formation of  $V_{Zn}$  defects in a low thickness ZnO film may be high compared to a thicker film.

Therefore, the origin of magnetic moment in Na-doped ZnO films can be attributed mainly to  $V_{Zn}$  defects [26, 49, 50]. Figures 6.13 (a) and (b) provide the direct correlation between the  $M_S$  and green emission intensity ( $I_G$ ) with the corresponding film-thickness and  $PO_2$  respectively. The largest  $M_S$  in 64 nm thick  $Zn_{0.94}Na_{0.06}O$  film is due to the presence of highest amount of  $V_{Zn}$  defects. The variation of  $M_S$  is found to follow a similar trend with variation of  $V_{Zn}$  concentration. Hence, the observed RTFM in  $Zn_{0.94}Na_{0.06}O$  film might be arises due to  $V_{Zn}$  defects which stabilize because of Na-doping. Besides  $V_{Zn}$  defects, the substitution of Na at Zn site ( $Na_{Zn}$ ) can also create one hole per alkali atom in the neighbouring oxygen atom [25, 26]. The increase of  $M_S$  and  $T_C$  with the increase of hole concentration as shown in the inset of Figure 6.10 (b) indicates the ferromagnetic interaction between the magnetic moments is mediated by the holes originated due to both  $Na_{Zn}$  and  $V_{Zn}$  acceptors. The increase of magnetic moment in thinner films can be explained by considering that the  $V_{Zn}$  lies on or near to the surface possess larger magnetic moment compared to the  $V_{Zn}$  lies deep inside the bulk [31]. The majority of  $V_{Zn}$  defects in the thinner  $Zn_{0.94}Na_{0.06}O$  films should lie on the surface or near to the surface layer to show large magnetic moment, whereas for thick films most of the  $V_{Zn}$  defects lie deep inside, far from the surface and therefore, the overall magnetic moment get reduced. Besides  $V_{Zn}$  defect, the  $Na_{Zn}$  defects at divalent Zn site can also induce local magnetic moment ( $\sim 1\mu_B$ ) in ZnO [27, 51]. Although, the magnetic moment arises due to substitutional Na ( $Na_{Zn}$ ) defect is comparatively less in magnitude than the  $V_{Zn}$  ( $\sim 2\mu_B$ ) defect, but still would contribute to the overall ferromagnetic moment. Hence, the magnetic moments of both  $V_{Zn}$  and  $Na_{Zn}$  defects or even their various defect complexes of  $V_{Zn}$  and  $Na_{Zn}$  defects could be mediated by holes due to Na-doping to stabilize long-range ferromagnetic ordering in p-type Na-doped ZnO films. Pure ZnO film with 69 nm thick showed weak FM due to presence of small amount of  $V_{Zn}$  defects. However, similar to case of Na-doped ZnO films, the concentration of  $V_{Zn}$  in pure ZnO films also decreases as the thickness of the film increases. As a result the thicker pure ZnO film ( $\sim 196$  nm) does not exhibit RTFM

possibly due to lack of enough  $V_{Zn}$  concentration (may be below the required threshold  $V_{Zn}$  concentration) to sustain long range ferromagnetic ordering.

## 6.4 Conclusion

Evidence of Zinc vacancy-induced room-temperature  $d^0$  ferromagnetism is observed in series of ZnO thin films by doping with different group-1 alkali metals such as Li, Na and K. XPS measurements show the alkali metals are mainly substitute at Zn site and are in +1 oxidation state. PL analysis showed the evidence of stabilization of large amount  $V_{Zn}$  in the alkali-doped ZnO films. Among the different alkali-doped ZnO films, Li-doped ZnO film is found to exhibit the strongest RTFM with highest  $M_S$  and  $T_C$  whereas K-doped ZnO film shows the weakest RTFM. PL and Hall measurements show that both  $V_{Zn}$  and hole concentration in alkali-doped ZnO films decreases gradually when the alkali-dopant element is varied from Li to Na, then to K, and resulting a decrease of  $M_S$  and  $T_C$ . The ionic size difference between  $Zn^{2+}$  and the respective alkali ions such as  $Li^{1+}$ ,  $Na^{1+}$  and  $K^{1+}$  is likely to have crucial role in the formation of  $V_{Zn}$  and also to establish the p-type conductivity to stabilize long-range ferromagnetic interaction. The influence of film-thickness and the oxygen pressure ( $PO_2$ ) on the RT ferromagnetic behaviour of p-type  $Zn_{0.94}Na_{0.06}O$  films fabricated by PLD technique are also investigated. At a fixed  $PO_2$ , the  $Zn_{0.94}Na_{0.06}O$  film with lowest thickness ( $\sim 64$  nm) exhibits largest  $M_S$  and also highest  $T_C$ . On the other hand, the  $M_S$  of almost similar thick  $Zn_{0.94}Na_{0.06}O$  films is found to decrease consistently with decrease of  $PO_2$ . The suppression of FM in  $Zn_{0.94}Na_{0.06}O$  film with the decrease of  $PO_2$  excludes the possibility of oxygen vacancy defects as the origin of RTFM. The  $V_{Zn}$  concentration is also found to vary significantly with the film-thickness and  $PO_2$  and so the ferromagnetic response of  $Zn_{0.94}Na_{0.06}O$  films. Therefore, this study demonstrates that group-1 alkali-elements can be the prime candidates to stabilize high- $T_C$  ferromagnetism in ZnO which can find potential application in the field of modern spintronic and opto-spintronics applications.

## References

- [1] C.W. Zou, H. J. Wang, M. L. Yi et al., *Appl. Surface Science* **256** 2453, (2010).
- [2] H. Gu, Y. Jiang, Y. Xu, M. Yan, *Appl. Phys. Lett.* **98**, 012502, (2011).
- [3] C. D. Wagner, W. M. Riggs, L.E. Davis, J. F. Moulder, G. E. Muilenberg, in: *Handbook of X-ray Photoelectron Spectroscopy*, Perkin Elmer, Eden Prairie, 1979.
- [4] D. K. Mishra, P. Kumar, M. K. Sharma et al., *Physica B* **405**, 2659, (2010).
- [5] J. C. Dupin, O. Gonbeau, P. Vinatier et al., *Phys. Chem. Chem. Phys.* **2**, 1319, (2000).
- [6] J. G. Lu, Y. Z. Zhang, Z. Z. Ye et al., *Applied Physics Letters* **89**, 112113 (2006).
- [7] S. Lee, R. Matsuno, K. Ishihara and M. Takai, *Applied Physics Express* **4**, 025803 (2011).
- [8] K. Y. Chun, C. J. Lee, *Journal of Physical Chemistry C* **112**, 4492 (2008).
- [9] J. Chastain (1992) *Handbook of X-ray photoelectron spectroscopy*. Perkin, Eden Prairie, MN, USA
- [10] B. Yang, P. Feng et al., *Journal of Physics D: Applied Physics* **42**, 195402 (2009).
- [11] C. H. Park, S. B. Zhang, S. H. Wei, *Physical Review B* **66**, 073202 (2002).
- [12] E. C. Lee and K. J. Chang, *Physical Review B* **70**, 115210 (2004).
- [13] K. Kobayashi, Y. Tomita, Y. Maeda et al., *Physical Status Solidi (c)* **5**, 3122 (2008).
- [14] C. Rauch, W. Gehlhoff, M. R. Wagner et al., *J. Appl. Phys.* **107**, 024311 (2010).
- [15] S. Polarz, A. Orlov, A. Hoffmann et al., *Chem. Mater.* **21**, 3889 (2009).
- [16] Y. C. Kong, D. P. Yu, B. Zhang et al., *Applied Physics Letters* **78**, 407 (2001).
- [17] T. Sekiguchi, N. Ohashi, Y. Terada, *Japanese Journal of Applied Physics* **36**, L289 (1997).
- [18] D. C. Reynolds, D. C. Look, B. Jogai et al., *Solid State Communication* **101**, 643 (1997).
- [19] D. C. Reynolds, D. C. Look, B. Jogai et al., *Solid State Communication* **106**, 701 (1998).
- [20] S.A. Studenikin, N. Golego, M. Cocivera, *Journal of Applied Physics* **84**, 2287 (1998).
- [21] K. Vanheusden, W.L. Warren, C. H. Seager et al., *J. Appl. Phys.* **79**, 7983 (1996).
- [22] K C Mishra, P C Schmidt, K H Johnson et al., *Physical Review B* **42**, 1423 (1990).
- [23] A. Janotti and C. G. Van de Walle, *Reports on Progress in Physics* **72**, 126501 (2009).
- [24] S. Ghosh, G. G. Khan, B. Das, K. Mandal, *J. Appl. Phys.*, **109**, 123927 (2011).
- [25] S. Ghosh, G. G.Khan, S. Varma, K. Mandal, *J. Appl. Phys.* **112**, 043910 (2012).
- [26] J.B. Yi, C.C. Lim, G.Z. Xing et al., *Physical Review Letters* **104**, 137201 (2010).
- [27] G. Bouzerar, T. Ziman, *Phys. Rev. Lett.* **96**, 207602 (2006).
- [28] A. Janotti and C. G. Van de Walle, *Physical Review B* **76**, 165202 (2007).
- [29] T. M. Børseth, B. G. Svensson et al., *Appl. Phys. Lett.* **89**, 262112 (2006).
- [30] B. K. Meyer, J. Stehr, A. Hofstaetter et al., *Applied Physics A* **88**, 119 (2007).
- [31] Q. Wang, Q. Sun, G. Chen et al., *Physical Review B* **77**, 205411 (2008).
- [32] P. Dev, P. Zhang, *Physical Review B* **81**, 085207 (2010).
- [33] H. Gu, Y. Jiang, Y. Xu, M. Yan, *Appl. Phys. Lett.* **98**, 012502 (2011).

- [34] T. M. Børseth, B. G. Svensson et al., *Appl. Phys. Lett.* 89, 262112 (2006).
- [35] Wagner, C. D.; Riggs, W. M.; Davis, L. E.; Moulder, J. F.; Muilenberg, G. E. 1979 in: *Handbook of X-ray Photoelectron Spectroscopy*, Perkin Elmer, Eden Prairie.
- [36] D. K. Mishra, P. Kumar, M. K. Sharma et al., *Physica B* 405, 2659 (2010).
- [37] Z. B. Gu, M. H. Lu, J. Wang et al., *Appl. Phys. Lett.* 88, 082111 (2006).
- [38] A. G. Joshi, S. Sahai, N. Gandhi et al., *Appl. Phys. Lett.* 96, 123102 (2010).
- [39] J. Lv, K. Huang, X. Chen et al., *Optics Communications*, 284 2905, (2011).
- [40] S. S. Lin, H. P. He, Y. F. Lu, Z. Z. Yeb, *J. Appl. Phys.* 106, 093508 (2009).
- [41] C. H. Park, S. B. Zhang, S. H. Wei, *Phys. Rev. B* 66, 073202 (2002).
- [42] E. C. Lee, K. Chang, *J. Phys. Rev. B* 70, 115210 (2004).
- [43] Y. C. Kong, D. P. Yu, B. Zhang, W. Fang, S. Q. Feng, *Appl. Phys. Lett.* 78, 407 (2001).
- [44] C. Rauch, W. Gehlhoff, M. R. Wagner et al., *J. Appl. Phys.* 107, 024311 (2010).
- [45] B. K. Meyer, J. Stehr, A. Hofstaetter et al., *Appl. Phys. A* 88, 119 (2007).
- [46] A. Janotti, C. G. Van de Walle, *Phys. Rev. B* 76, 165202 (2007).
- [47] D. C. Reynolds, D. C. Look, B. Jogai et al., *Solid State Commun.* 101, 643 (1997).
- [48] D. C. Reynolds, D. C. Look, B. Jogai et al., *Solid State Commun.* 106, 701 (1998).
- [49] Y. Li, R. Deng, B. Yao, G. Xing, D. Wang, T. Wu, *Appl. Phys. Lett.* 97, 102506 (2010).
- [50] X. G. Xu, H. L. Yang, Y. Wu et al., *Appl. Phys. Lett.* 97, 232502 (2010).
- [51] P. Dev, P. Zhang, *Phys. Rev. B* 81, 085207 (2010).

# Chapter 7

## Positron Annihilation Spectroscopy study of Li-doped ZnO Nanoparticles

### 7.1 Preface

In last two chapters, we have seen that the evidence of stabilization of RT ferromagnetism in case of low dimensional ZnO (nanostructures or thin films) by doping with nonmagnetic monovalent alkali atoms (Li, Na, and K). There we have used X-ray photoelectron spectroscopy to investigate or confirm the substitution of alkali ions at Zn site and photoluminescence spectroscopy measurements showed the evidence of Zn vacancy which were found to be the main defect species for the origin of RTFM in ZnO. Positron annihilation spectroscopy (PAS) is known to be extremely sensitive instrument which can provide useful information about the intrinsic or extrinsic vacancy-type defects mainly cation vacancy or vacancy clusters [1]. Therefore, the idea to include the present chapter on PAS study of Li-doped ZnO is to show the direct evidence of stabilization of Zn vacancy in ZnO due to alkali-metal (for example, Li here) doping and thereby the stabilization of RTFM which can

be an very exciting way to prepare ZnO-based high- $T_C$  magnetic semiconductor for spintronic applications.

## 7.2 Introduction to positron annihilation spectroscopy

Positron ( $e^+$ ) is known as antiparticle of electron ( $e^-$ ). Because of electromagnetic interaction between electron and positron pair, they annihilate into quanta of electromagnetic field and produces  $\gamma$ -photon. Conventional source of positron are artificial radioisotopes emitting  $\beta^+$  radiation. The energy spectra of positron emitted by such radioisotopes are of continuous distribution ranging from zero to an end-point energy which is typically of the order of 0.1-1 MeV [1-5]. Principal channel of this reaction is the two-photon annihilation,

$$e^+ + e^- = \gamma_1 + \gamma_2$$

In prior to annihilation, positron penetrate through matter where they undergo various processes like electronic excitation, ionization, electron hole pair creation, phonon interaction etc. in which they losses their energy. At highest positron energies, the main mechanism of energy loss is ionization, i.e., the positron excites the core electron of the host atoms in collisions. The lower energies electron hole pair creation takes place. When the positron energy has reduced to a fraction of eV, the scattering of phonons dominates. Eventually, positrons reach in thermal equilibrium with the medium, maintained due to phonon emissions and absorption. During the process of thermalization, the initial kinetic energy of the positrons drops below 0.1 eV. Thermalized positrons are characterized of with thermal wavelength [184], which implies that such a positron moves through the medium as quantum mechanical waves. After reaching at thermal equilibrium with the host, the positron state develops as a diffusion process. In metals at room temperature, the positron mean free path  $l_+$  is typically of the order of 10 nm whereas the total diffusion length  $L_+$  is of the order of 100 nm [4]. During the diffusion, the positron interacts with its surroundings and eventually annihilates with an environmental electron. In homogeneous defect-free medium, all positrons annihilates with the same rate  $\lambda_b$  which is a characteristics of the given material.

Due to Coulomb repulsion by the positron ion cores, positrons in a condensed medium prefer to reside in the inter-atomic spacing. Because of reduced Coulomb repulsion, the potential sensed by the positrons at the open volume defects like monovacancies, larger vacancy clusters, dislocations etc. is lowered. As a result a localized positron state at the defect can have a lower energy compared with delocalized or free positron state. The transition from the delocalized state to the localized one is called positron trapping. Positron binding energy  $E_b$  to defects like monovacancies, are typically of a few eV. Thermal detrapping is impossible from such deep traps and positron remains trapped until annihilation. If a positron trap is shallow enough ( $E_b \leq 0.1$  eV), phonon-assisted detrapping occurs. As the local electron density at the defect site is lowered compared to that of the unperturbed regions, the lifetime  $\tau_t$  of the trapped positrons is longer than  $\tau_b = 1/\lambda_b$ . Positron trapping is characterized by the trapping rate  $\kappa_d$ , which is proportional to the defect concentration  $c_t$  in the sample,  $\kappa_d = \nu c_t$ . The trapping coefficients  $\nu$ , together with annihilation rate  $\lambda_t = 1/\tau_t$ , are specific for the given kind of defect. Additional exponential components occur in the measured positron lifetime spectra. Their appearance can be explained by the trapping models which give the rate of equitation for the positrons annihilating from the delocalized state and from the localized states. There are different trapping models among them we will discuss two-state trapping model. In many insulators, positron can form hydrogen like bound state with an environmental electron, called positronium (Ps) [3, 4]. The binding energy of the Ps atom is 6.1 eV and its radius is 0.106 nm. Ps atom can exist either in the singlet (parapositronium, pPs) or the triplet (orthopositronium, oPs) state. While the two-photon self-annihilation of pPs is the allowed process, the two-photon annihilation of oPs can proceed only via pick-off reaction with an electron of the host. Due to exchange interaction of the electron with environmental electrons, Ps atom is repelled to an unoccupied space in the material. oPs also undergo 3-gamma self-annihilation process.

Positron annihilation spectroscopy (PAS) is a nondestructive nuclear physics method, which by means of annihilation process of positron with electron allows the study of micro and nanostructures of condensed matter [3-5]. PAS can be used to study the various types of defects in solid materials. Positron lifetime within the matter depends on the local electron density at the annihilation site. Because of reduced density at the vacancy site, positron lifetime is found to be increased than in

the defect free bulk part of the material. Additional information can be gathered from the momentum density of annihilating electron-positron pairs. It reflects the spatial and momentum (i.e. energy) distribution of electrons within the materials. In case of positron trapping, the momentum density is found to be very much sensitive to the type of defects as well as on its chemical environment. This property enables the PAS method to identify the defects. As soon as the positron gets generated, they start to diffuse through the material (diffusion length is  $\sim 50$ - $100$  nm in solids) [6]. Hence, if the grain sizes are less than this limit, positrons will diffuse out to the grain surfaces before annihilation. This makes them useful for exploring the diffused vacancy-type defects on nanocrystalline grain surfaces. The characteristics positron lifetimes and the annihilation gamma ray spectral line shape parameters can quantitatively represent the electronic structures and properties as well as changes in them during process like phase transformation and growth as well as compensation and annealing of defects [3-5].

### 7.3 Two-state trapping model

In an imperfect solid, the simple form of positron trapping can be in two ways. Positron can annihilate either in bulk region of the solid with a lifetime  $\tau_b$  ( $1/\lambda_b$ , where  $\lambda_b$  is the annihilation rate in the bulk) or after getting trapped into the defect. In the defect the positron will have a lifetime  $\tau_d$  ( $1/\lambda_d$ , where  $\lambda_d$  is the annihilation rate in the defect). At any instant of time  $t$ , let  $n_b$  be the number of positrons in bulk and  $n_d$  be the number of positrons in the defects. Then the positron annihilation process in the solid are governed by the following two rate equations [7]

$$\frac{dn_b}{dt} = -\lambda_b n_b - \kappa_d n_b \quad (7.1)$$

$$\frac{dn_d}{dt} = -\lambda_d n_d + \kappa_d n_b \quad (7.2)$$

Where  $\kappa_d$  is the rate of trapping of positrons from the bulk into the defects, Integrating Eq. 7.1, we get

$$n_b = N_0 e^{-\lambda_1 t} \quad (7.3)$$

where,  $\lambda_1 = (\lambda_b + \kappa_d)$ . Here we have used the boundary condition that at  $t = 0$ , all the positrons are in bulk, i.e.  $n_b(t = 0) = N_0$ . Putting the values of  $n_b$  in Eq. 7.2,

$$\frac{dn_d}{dt} = -\lambda_d n_d + \kappa_d N_0 e^{-\lambda_1 t} \quad (7.4)$$

$$\frac{dn_d}{dt} + \lambda_d n_d = \kappa_d N_0 e^{-\lambda_1 t} \quad (7.5)$$

Multiplying Eq. 7.5 by  $e^{\lambda_d t}$  and then integrating, we get

$$n_d e^{\lambda_d t} = -\frac{\kappa_d N_0}{(\lambda_1 - \lambda_d)} e^{-(\lambda_1 - \lambda_d)t} + C$$

Again, as per the boundary condition assumed above, at  $t=0$ , all the positrons are in the bulk and  $n_d(t=0) = 0$ . Therefore, we get the integration constant  $C = \frac{\kappa_d N_0}{(\lambda_1 - \lambda_d)}$ .

Then, we get

$$n_d = -\frac{\kappa_d N_0}{(\lambda_1 - \lambda_d)} e^{-\lambda_1 t} + \frac{\kappa_d N_0}{(\lambda_1 - \lambda_d)} e^{-\lambda_d t} \quad (7.6)$$

The total number of positrons at any time  $t$ ,

$$N(t) = n_b + n_d = N_0 e^{-\lambda_1 t} \left[1 - \frac{\kappa_d}{(\lambda_1 - \lambda_d)}\right] + N_0 \frac{\kappa_d}{(\lambda_1 - \lambda_d)} e^{-\lambda_d t}$$

$$N(t) = N_0 \frac{\lambda_1 - \lambda_d - \kappa_d}{(\lambda_1 - \lambda_d)} e^{-\lambda_1 t} + N_0 \frac{\kappa_d}{(\lambda_1 - \lambda_d)} e^{-\lambda_d t}$$

$$N(t) = I_1 e^{-\lambda_1 t} + I_2 e^{-\lambda_d t}$$

$$N(t) = I_1 e^{-t/\tau_1} + I_2 e^{-t/\tau_2} \quad (7.7)$$

And this can be compared with the nature of positron lifetime spectrum, given by

$$N(t) = \sum_{i=1}^n I_i e^{-t/\tau_i} \quad (7.8)$$

Where  $n$  is the number of positron lifetime in the spectrum. In real positron lifetime experiments, we use sources of strength  $\sim \mu\text{Ci}$  and hence, at any given time, the number of positrons in the sample  $N_0 = 1$ , Eq.s 7.7 and 7.8 can be compared to get

$$I_1 = \frac{\lambda_1 - \lambda_d - \kappa_d}{\lambda_1 - \lambda_d} \quad (7.9)$$

$$I_2 = \frac{\kappa_d}{\lambda_1 - \lambda_d} \quad (7.10)$$

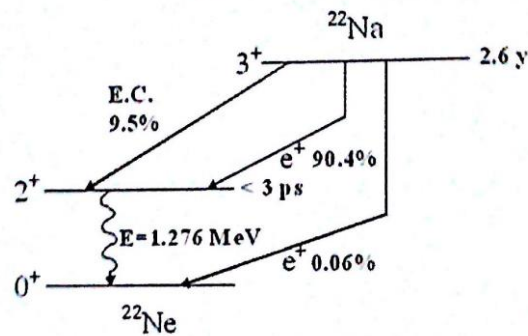
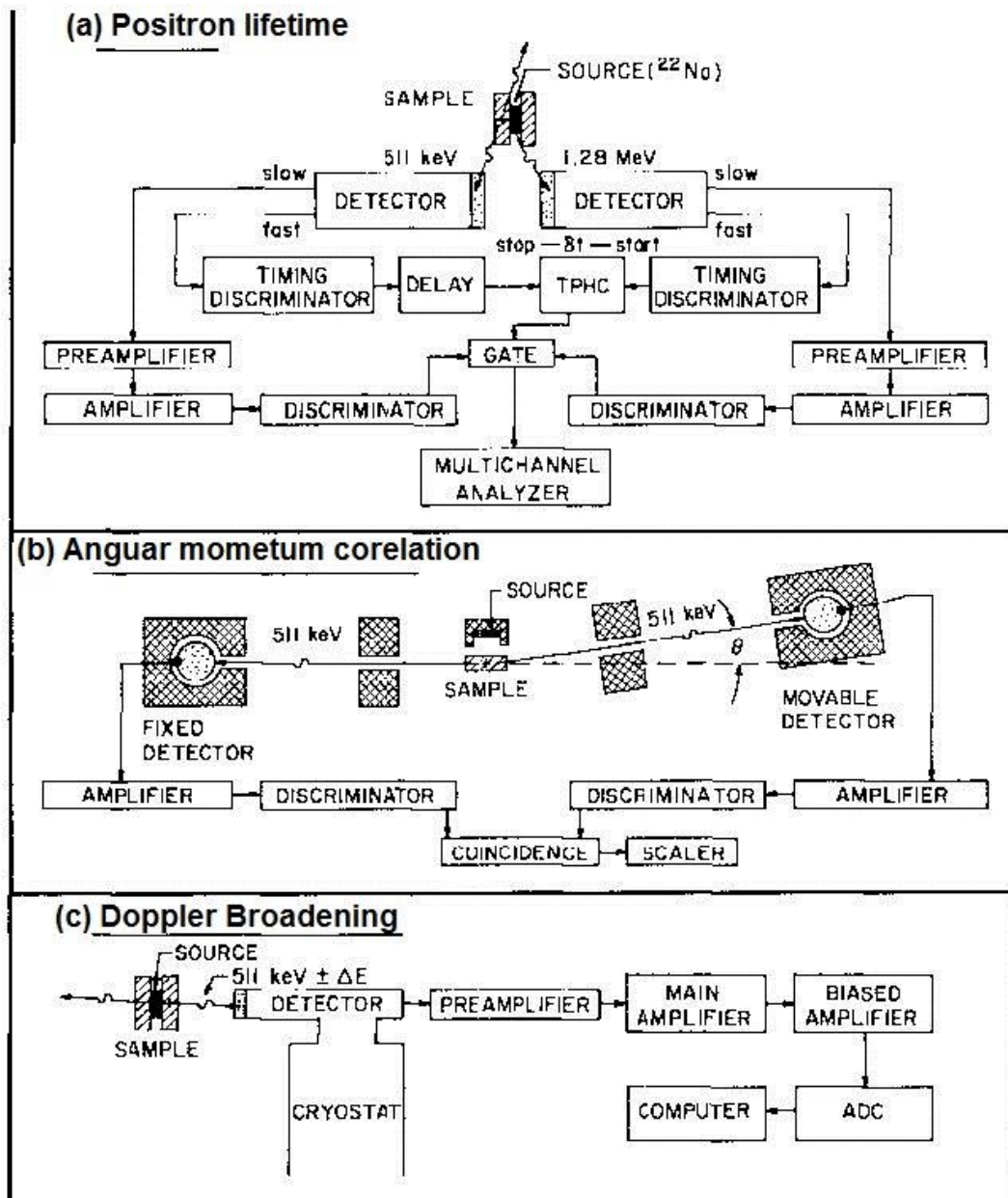


Fig. 7.1 Decay scheme of  $^{22}\text{Na}$ .

## 7.4 Positron lifetime spectroscopy

Positron lifetime spectroscopy is one of the most basic measurement techniques among the different measurement techniques of PAS. Principal measurements are carried out with  $^{22}\text{Na}$  radioisotopes as the positron source. Its decay scheme is shown in Fig. 7.1. The end point energy of positrons emitted from  $^{22}\text{Na}$  is at 545 keV. An important feature of  $^{22}\text{Na}$  decay is the simultaneous emission (within a few ps) of  $\beta^+$  radiation and  $\gamma$ -radiation with energy  $E_\gamma = 1276 \text{ keV}$ . Although there exists two fundamental modes of decay, viz. electron capture (E.C.) and positron ( $e^+$ ) emission. The latter is the dominant mode (90.4%) and helps in the positron lifetime measurements. The first excited state ( $2^+$ ) of the daughter nucleus, i.e.  $^{22}\text{Ne}$ , is very much short-lived ( $< 3 \text{ ps}$ ) and the nucleus instantaneously deexcites to the ground



**Fig. 7.2:** Schematic diagrams of typical PAS apparatus for the measurement of (a) lifetime, (b) angular correlation, and (c) Doppler broadening. TPHC = time-to-pulse-height converter; ADC = analogue-to-digital converter; cross-hatched forms are lead collimators or shields.

state, ( $0^+$ ) releasing the excess energy as the gamma ray ( $E \sim 1.276$  MeV). This energy is recorded as the "birth signal" of one of the annihilation gamma rays serve as the 'death signal'. The probability of direct decay to the ground state (0.06%) is ignored. The positron is implanted into the sample almost simultaneously with the birth  $\gamma$ -

rays of the energy 1276 keV. Hence the lifetime of the individual positrons can be measured as time differences between the emission of  $\gamma$ -quantum and one of the annihilation photon [8]. Positron annihilation lifetime spectroscopic measurements then consist of measuring of spectrum of delayed coincidences of  $\gamma$ -1176 -  $\gamma$ -511 keV. Fig 7.2 (a) shows the simplest configuration of a positron lifetime spectrometer.

## 7.5 Doppler broadening spectroscopy

During the annihilation of positron with electron, the energy and linear momentum remains conserved. In the centre of mass frame of the  $e^+ - e^-$  pair, the energies of both the annihilation photon are equal to the rest mass energy of the electron (positron),  $E_0 = m_0c^2$ , and the two photon are emitted in exactly opposite directions. However, in reality, positrons are very rapidly thermalized in a material medium and their linear momentum can be neglected as compared to those electrons. Thus in the laboratory frame, in which positron is considered to be at rest, the energies of the two annihilation photons are shifted with respect to  $E_0$  by  $\Delta E \approx \pm cp_x/2$  and the angle between the emission directions of the two photons differs from  $180^\circ$  by  $\Delta\theta \approx p_x/m_0c$ . In these expressions, non-relativistic approximation is used and symbol  $p_x$  is the momentum component along the propagation direction of the  $\gamma$ -rays and  $p_z$  denotes the transverse component of the electron momentum, respectively. The momentum of the center of mass of the annihilating pair with respect to the laboratory frame of reference gives rise not only to the deviation angle of the photons from  $180^\circ$  but also to the Doppler broadening of the annihilating line (0.511 eV).

Because of the conservation of momentum during the annihilation process, the emitted radiation contains information on the electron momentum distribution at the annihilation site. Hence this can be used for the study of electronic structure in solids and for the investigation of defects. There are two basic techniques for studying the momentum distribution; (i) Doppler broadening spectroscopy and (ii) angular momentum correlation of annihilation radiation method. We have used Doppler broadening spectroscopic method for characterization of the defects in our samples, Li-doped ZnO nanoparticles [9]. The experimental set up for Doppler broadening spectroscopy is shown in Fig. 7.2 (b).

## 7.6 Experimental procedure of positron lifetime spectroscopy

A special sandwich arrangement of foil source and the samples, guarantees that all positrons emitted from the source are getting annihilated within the sample material. The activity of the source must be sufficiently low ( $\sim\mu\text{Ci}$ ) in order to ensure that on average only one positron is present in the sample at a time. This avoids the overlap the start and stop quanta originating from different annihilation events. Two BaF2 scintillators with XP2020Q photomultiplier tubes (PMTs) act as the gamma ray detectors in positron lifetime measurements. These detectors convert the  $\gamma$ -rays into analog electrical pulses. The anode pulses are fed to constant fraction discriminators (CFDs). The CFDs are used to convert the pulses of varying amplitudes from the PMTs into signals of a fixed cross-over point to trigger the next processing stage, thereby minimizing the inherent spread in measured time intervals of supposedly equal magnitudes. The CFD output pulses are fed to the START and STOP inputs of the time-to-pulse-height converter (TPHC). The amplitude of the output pulse is proportional to the time difference between the birth and the annihilation  $\gamma$ -quanta and, thus, represents a measure of the positron lifetime. TPHC positive output is recorded in the multi-channel analyzer (MCA). The single annihilation event is stored after analog-digital conversion in a multi-channel analyzer. The channel numbers represents the time scale. In order to obtain a satisfactory good lifetime spectrum, about more than  $10^6$  annihilation events must be recorded. A nanosecond delay is introduced in the STOP channel for the storage of pulse height distribution in a convenient range in the MCA. The introduction of the delay in the STOP channel will shift the spectrum without affecting the timing information. This can be shown as follows. Let  $y$  be the output pulse height from the TPHC. Then

$$y \propto (t_{stop} - t_{start}) = k(t_{stop} - t_{start}) \quad (7.11)$$

Let us assume that a delay, 'd' is introduced in the STOP channel. Then

$$y' = k(t_{stop} + d - t_{start}) = kd + k(t_{stop} - t_{start}) = kd + y \quad (7.12)$$

which is only a linear shift of the full spectrum. The delay can be chosen in between 1 to 63 nanoseconds, depending upon the requirement. The dynode signals are derived through t pre-amplifiers and are fed to amplifiers. After propyl shaping the

pulses (peaking time = 1  $\mu$ s), they are fed to single channel analyser (SCAs). The SCA helps in selecting the pulses corresponding to the photopeaks (full energy absorption events) of the pulse height distribution and their outputs are fed to a fast coincidence (FC) unit. FC unit produces gate or strobe signal for the TPHC provided that the coincidence event of the photons with proper energies occurred. This will enable the TPHC to send the event generated by it from the STRAT and STOP signals for recording into the MCA. Thus only correlated events are recorded [9].

## 7.7 Experimental procedure of Doppler broadening spectroscopy

Doppler broadening of the annihilation line can be measured with a standard  $\gamma$ -ray spectrometer equipped with the HPGe detector. The energy resolution of such devices is  $\delta E_{\gamma} \sim 1.2$  keV at 511 keV. The basic requirement in this experiment is the accurate and precise measurements of the changes due to Doppler shift in the energies of the positron annihilation  $\gamma$ -rays. HPGe detectors have the best energy resolution among the different detectors currently in use and they can be used for a long-time data acquisition due to very good stability and reliability of their performances. Under the applied high voltage of several kV, the annihilation photons cause a charge separation that is converted by a preamplifier into an electrical pulse. Its amplitude is the measure of the photon energy and can be recorded after amplification using an amplifier. 2  $\mu$ s shaping time was used for processing the signals. A resolution (FWHM) of 1.29 keV at 511 keV was obtained for subsequent measurements. A digital peak stabilizing system as a part of the MCA allows the long-term collection of several million of counts. The time of measurement is comparatively less than to the collection time of a positron lifetime spectrum. Both the techniques can easily be performed at the same time because the Ge detector would be separated sufficiently from the sample in order to avoid pile-up effects in the detector system. Line shapes are usually characterized with shape parameters S and W. S parameter is determined as the relative area of the central part of the line shape while W parameter expresses the relative contribution of the peak tails to the local peak area. Thus the S-parameter is higher if the relative contribution of lower-momentum electrons to positron annihilation is higher while the W parameter becomes greater if contribution of the core electrons with higher

momenta is enhanced. For example, relative increase in the fraction of positrons trapped at the open-volume defects can be markedly reflected by increased value of the S-parameter [9].

## 7.8 Positron annihilation study of Li-doped ZnO nanoparticles

### 7.8.1 Preparation of Li-doped ZnO nanoparticles

Pure and Li-doped ZnO nanoparticles (NPs) are prepared by chemical co-precipitation method. High purity (99.999%) chemical reagents such as Zn-acetate ( $\text{Zn}(\text{O}_2\text{CCH}_3)_2 \cdot 2\text{H}_2\text{O}$ ) and Li-acetate ( $\text{CH}_3\text{COOLi}$ ) and sodium hydroxide ( $\text{NaOH}$ ) are used for the synthesis of Li-doped ZnO NPs. Two precursor solutions; (i)  $\text{Zn}(\text{O}_2\text{CCH}_3)_2 \cdot 2\text{H}_2\text{O}$  and  $\text{CH}_3\text{COOLi}$  salts with appropriate Zn:Li ratio, in mixture of 200 ml water and Triton X-100 (0.5 M) (Precursor A) and (ii) 0.05 M  $\text{NaOH}$  in 50 ml water (Precursor B). Precursor A was then heated at  $80^\circ\text{C}$  under constant stirring and precursor B was added slowly drop by drop in boiled Precursor A using sophisticated pressure equalizer. Then the resultant solution was heated constantly for 1h at  $80^\circ\text{C}$  until a precipitate was formed which was washed repeatedly with water and ethanol and dried at  $80^\circ\text{C}$  for 24 h. The as-prepared samples were annealed at  $500^\circ\text{C}$  in a tube furnace under a continuous flow of oxygen ( $\text{O}_2$ ). The crystal phases and morphology of the samples are identified using x-ray diffraction (XRD) with  $\text{Cu K}_\alpha$  radiation ( $\lambda = 1.540598\text{\AA}$ ) and transmission electron microscopy (TEM), High resolution TEM (HRTEM). UV-Visible absorption spectroscopic measurements are conducted to estimate the effect of Li-doping on the energy band-gap of ZnO. Magnetic measurements are performed using a vibrating sample magnetometer (VSM) (Lake Shore Cryotronics) at room-temperature. Photoluminescence (Horiba Jobin Yvon, Fluorolog-3) a spectroscopy is carried out to identify various defect states within the ZnO band-gap due to Li-doping. The direct evidence of vacancy-type defects are also identified using positron annihilation spectroscopy (PAS) which were performed by embedding a  $^{22}\text{Na}$  source emitting positrons in the powdered sample taken in a glass tube.

## 7.8.2. Results and discussion

### 7.8.2.1. Particle size and lattice effects

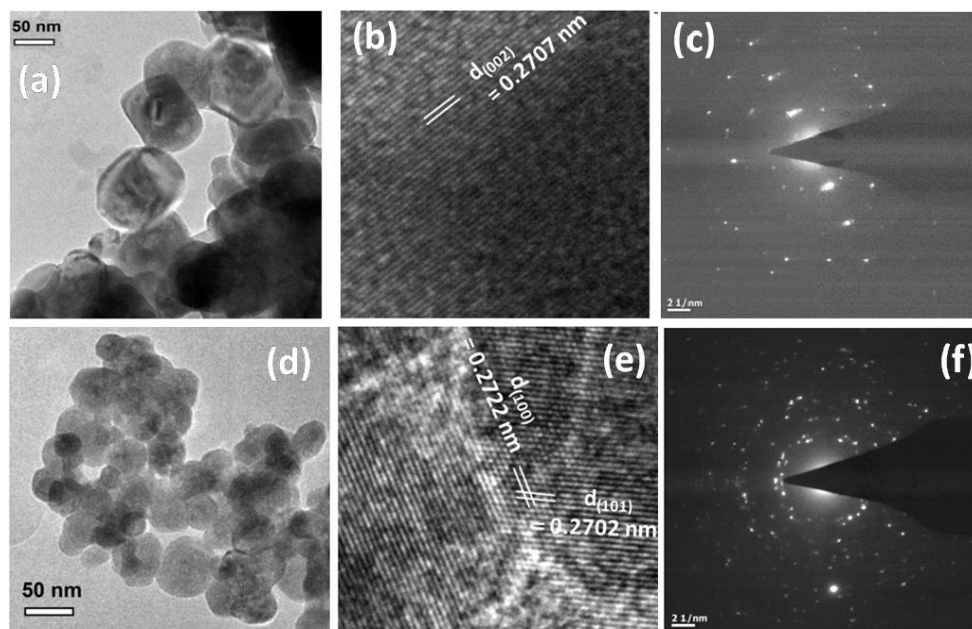


**Fig. 7.3:** (a) TEM micrographs (b) high resolution TEM (HRTEM) and selected area electron diffraction (SAED) pattern for undoped ZnO while the similar images for 3.5 at.% Li-doped ZnO are shown in (d), (e) and (f) respectively.

In order to estimate particle shape, size and nature of crystalline, TEM analysis are conducted for pure and Li-doped ZnO samples. Figure 7.3 shows the representative (a) TEM micrographs (b) high resolution TEM (HRTEM) and selected area electron diffraction (SAED) pattern for undoped ZnO while the similar images for 7.0 at.% Li-doped ZnO are shown in (d), (e) and (f) respectively. From Fig. 1(a) can be seen that the particles of pure ZnO are found to be ~80 -100 nm in size with hexagonal shape. The particle size for 7.0 % Li-doped ZnO (Fig. 1(c)) is found to be ~40-50 nm which is less compared to that of undoped ZnO. In fact, with the increase of Li%, the particle size is found to reduce initially up to 7.0 % Li-doping and then increase on further increase of Li doping concentration (see Table 7.1). High resolution TEM (HRTEM) images of the particle are shown in Fig. 1 (b) for pure ZnO and (e) for 7.0 at.% Li-doped ZnO. SAED patterns of the samples are indicating that both undoped ZnO and Li-doped ZnO NPs are polycrystalline in nature.

The samples had been initially tested for their phase purity and composition through x-ray diffraction and the patterns of a few samples are given in Figure 7.4. The diffraction patterns agreed well with the standard literatures which indicate that undoped and all Li-doped ZnO have hexagonal wurtzite crystal structure. Although the crystal structure of ZnO remained unchanged after significant Li-doping, significant shifting of the individual peak position is observed. The inset image of Fig. 7.4 shows the direction of shifting of ZnO (100) diffraction peak due to gradual Li-doping. The peak is initially shifts towards higher  $2\theta$  -direction up to 7 at.% Li-doping and then shifts in reverse direction which signifies the contraction and expansion of lattice due to Li-doping. Using XRD, the values of lattice parameters of hexagonal ZnO unit cell are estimated and their variations with Li-doping concentration are shown in Fig. 7.5 (a). Both the lattice parameters,  $a$  and  $c$  are found to decrease initially up to Li concentration of 7 at.% and then started to increase on further Li-doping. The decrease of lattice parameter is due to substitution of comparatively smaller size  $\text{Li}^{1+}$  ion ( $0.73\text{Å}$ ) replacing the  $\text{Zn}^{2+}$  ( $0.74\text{Å}$ ) ion within ZnO [10]. However, when the Li concentration exceeds over 7 at.%, then the Li ions begins to occupy the lattice interstitial sites which may result in expansion of ZnO unit cell. The XRD patterns also served to estimate the average crystallite sizes in the samples via peak-width analysis using the standard Scherrer equation<sup>7</sup>

$$d_c = \frac{K\lambda}{\beta \cos \theta} \quad (7.13)$$

where  $K = 0.89$  is a constant,  $\lambda = 1.54\text{Å}$  is the wavelength of the Cu  $K_\alpha$  radiation used and  $\beta$  is the full width at half maximum of the peak. A significant observation, as illustrated in Fig. 7.5(b), is that similar to the lattice parameters, the particle sizes also decreased initially with Li-doping up to  $x = 7\%$  and it rose rather monotonously with additional doping. (In the figure and those given later, the solid lines are drawn to guide the eyes only.) The range of particle sizes we obtained in the present samples ( $d_c = 30 - 40\text{ nm}$ ) is a medium one, i.e., too large to observe quantum confinement effects and too small to prevent positrons diffusing out to the surfaces and getting annihilated there. The latter aspect is discussed again afterwards.

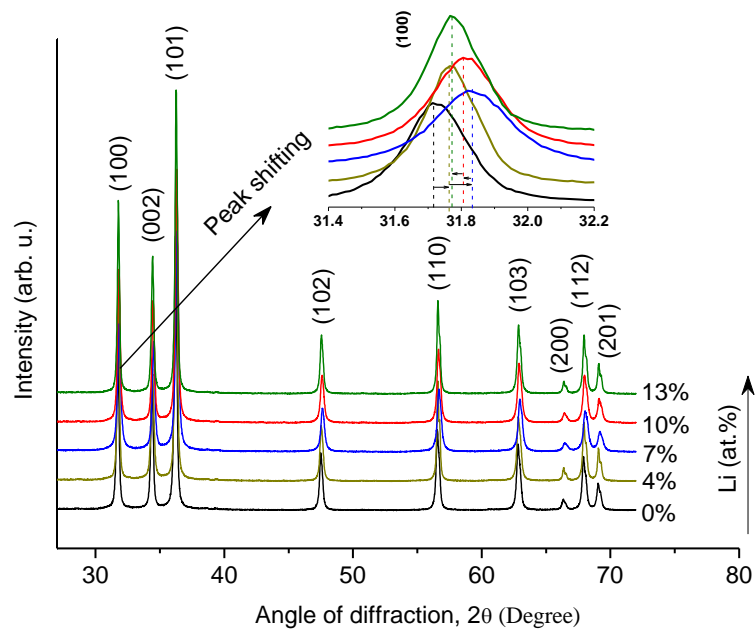


**Fig. 7.4:** XRD pattern of Li-doped ZnO nanoparticles; Inset shows the shifting of ZnO (100) diffraction peak due to increase of Li doping.

**Table 7.1:** Typical estimated values of some important parameters of Li-doped ZnO samples

No. of samples	Li (at.%) in ZnO	Lattice parameters		Unit cell volume ( $\text{\AA}^3$ )	Crystallite Size, (nm) from XRD	Particle size (nm) from TEM	Energy band gap, $E_g$ (eV)
		a ( $\text{\AA}$ )	c ( $\text{\AA}$ )				
1	0.0	3.25794	5.21699	55.374	35.8	80	3.24
2	4	3.25269	5.21312	55.154	34.8	65	3.27
3	7	3.24747	5.19967	54.836	30.7	45	3.26
4	10	3.24877	5.20928	54.920	33.5	52	3.27
5	13	3.25269	5.20928	55.114	39.2	63	3.30
6	16	3.2537	5.21001	55.156	40.1	69	3.32

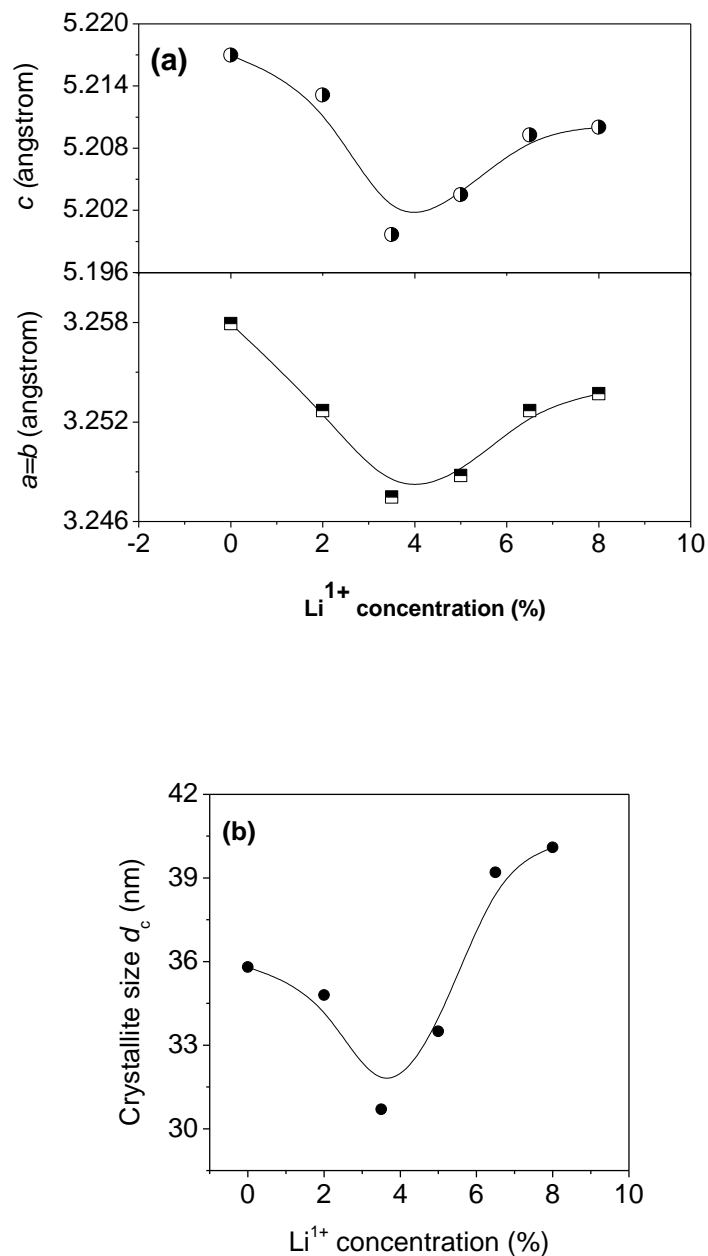
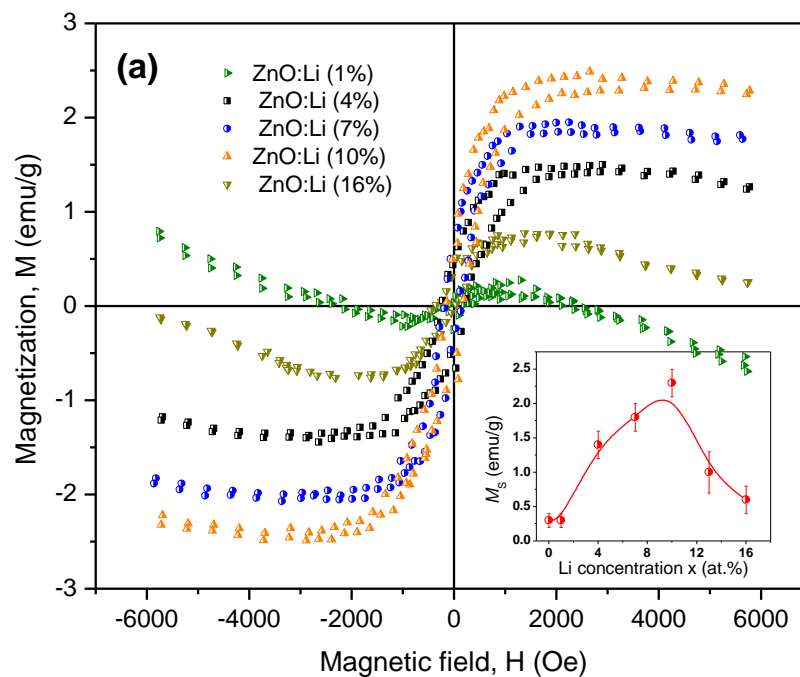


**Fig. 7.5:** The variation of (a) the lattice parameters,  $a$  and  $c$ -parameters, of hexagonal ZnO unit cell and (b) the average crystallite sizes estimated from XRD with the increasing Li concentration ( $x$ ).

### 7.8.2.2. High-temperature ferromagnetism

Magnetic properties of all pure and Li-doped ZnO nanoparticles are measured with extreme care using VSM, (Lakeshore model) at room temperature (RT) and above. Figure 7.6 show the (a) field and (b) temperature-dependent magnetization plots of Li-doped ZnO samples and in inset the values of saturation moment ( $M_S$ ) and Curie temperature ( $T_C$ ) are plotted as a function Li-doping

concentration  $x$  (at.%). Similar to that of Li-doped ZnO nanowires and thin films (as discussed in Chapter 5 and 6), here also Li-doped ZnO NPs exhibit significant ferromagnetism having  $T_C$  well above the room temperature (300K). Both saturation magnetization ( $M_S$ ) (inset of 7.5a) and also  $T_C$  (inset of 7.5b) are found to enhance gradually from 1 to 10 at.% Li-doping and then falls on further doping. In case of potassium (K)-doped ZnO nanowires (as discussed in Chapter 5), similar variation of  $M_S$  and  $T_C$  with K-doping concentration are observed i.e. both the parameters were increased upto 4 at.% K-doping and then decreased for higher doping concentration. There we have conducted photoluminescence spectroscopy to identify the presence of various defects and found the evidence of Zn vacancy induced ferromagnetism in ZnO. However, here we have employed positron annihilation spectroscopy study to investigate the defect modification with ZnO host due to Li doping and investigate the origin of ferromagnetism.



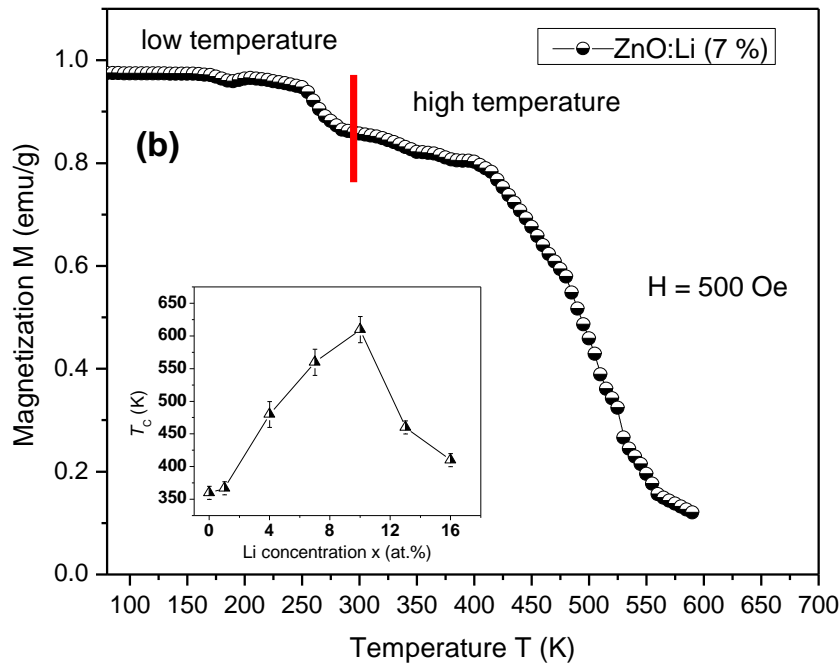


**Fig. 7.6:** (a) Room temperature M-H plots of Li-doped ZnO nanoparticles; Inset: Typical variation of  $M_s$  with Li-doping concentration and (b) representative M-T curve for 7 at.% Li-doped ZnO, Inset: Plot of  $T_c$  as a function of Li-doping concentration  $x$ .

### 7.8.2.3. Photoluminescence spectroscopy study

Figure 7.7 shows the room-temperature photoluminescence (PL) spectra of Li-doped ZnO nanoparticles under an excitation wavelength ( $\lambda_{ex}$ ) of 330 nm. The PL spectra of pure ZnO is found to exhibit strong ultraviolet-visible (UV) emission (peak 1) at 383 along with very weak defect band centred around 540 nm. With the incorporation of Li in ZnO, the UV emission is found to suppress significantly due to dominance of defect-related band. The UV emission (peak 1) in the pure ZnO film can be assigned as the near band edge (NBE) emission due to the free exciton (FX) recombination through an exciton-exciton collision process [11]. However, the broad defect band can be decomposed into two most significant emissions such as green emission (peak 2) at 540 nm and yellow-orange emission (peak 3) around 590 nm. The origin of yellow-orange luminescence is due to the stabilization of various Li-related defects such as deep Li acceptors, Li-interstitial etc [12, 13]. The gradual enhancement of yellow-orange emission intensity with the increase of Li concentration indicates the successful doping of Li atom in ZnO host. Besides the

strong yellow-orange emission, Li-doped ZnO nanoparticles are also found to exhibit significant green emission (peak 2) centered around 540 nm (i.e. at 2.3 eV) which is found to be enhanced gradually due to increase of Li-doping (Figure 7a). However, the origin of the green luminescence in ZnO thin films and nanostructures remained quite controversial. Earlier, it was suggested that that oxygen vacancy ( $V_O$ ) is responsible for such green emission in ZnO but, several recent studies have shown that it is Zn vacancy ( $V_{Zn}$ ) rather than  $V_O$ , which is responsible for green luminescence observed in case of ZnO thin films and nanostructures [14-18].  $V_{Zn}$  defects are found to create deep acceptor band around 0.9 eV above the valence band maximum (VBM) and the electronic transition from the conduction band minimum (CBM) to  $V_{Zn}$  acceptor levels often leads to the emission of visible green luminescence at 2.30– 2.40 eV [16-18]. Therefore, the enhancement of green luminescence after gradual Li doping indicates the stabilization of more and more  $V_{Zn}$  defects within the Li-doped ZnO nanoparticles. The increase of  $V_{Zn}$  concentration with increase of Li doping in ZnO is also confirmed from the positron annihilation spectroscopic measurements which is discussed in the next section.

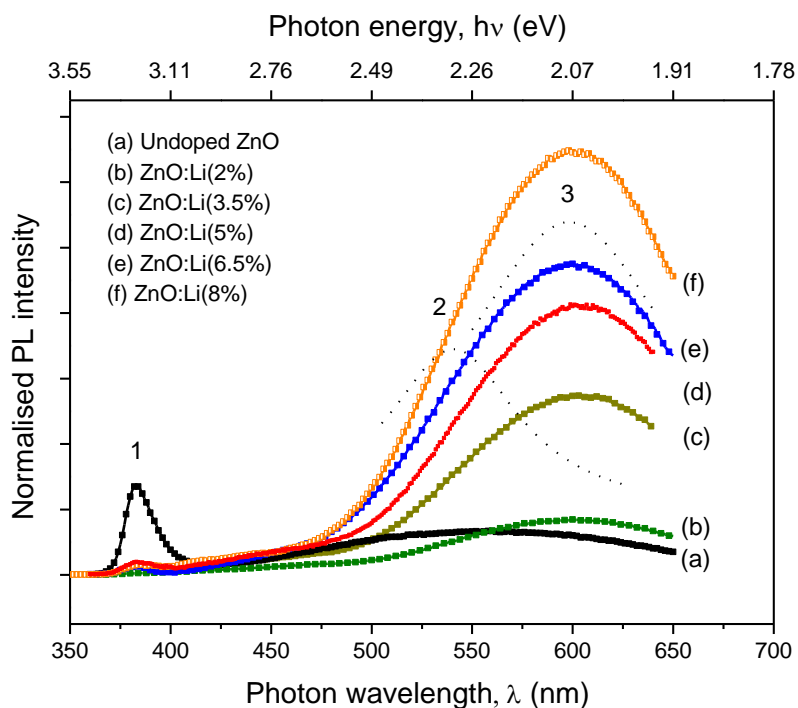


**Fig. 7.7:** Room-temperature PL spectra of Li-doped ZnO nanoparticles.

## 7.8.2.4 Positron annihilation spectroscopy studies

### 7.8.2.4.1 Results of positron lifetime measurements

Peak-normalized positron lifetime spectra of two samples, i.e., the undoped ZnO and after doping with  $\text{Li}^{1+}$  to a concentration 16%, are shown in Fig. 7.8. The nature of the spectra indicates an enhancement in the positron lifetime in the doped sample, suggesting the generation of more vacancies in the sample as a result of the continued reduction of the positive ions. From the positron lifetime spectra, we had resolved three lifetime components and their respective relative intensities using the program PALSfit [19]. The reason for choosing three lifetimes has not been arbitrary but based on a judicial judgment on the different types of positron annihilation sites that are probable in such nanocrystalline systems. Indeed a satisfactory variance of fit  $\nu = \chi^2/f$  within the limits of acceptability ( $1.00 \pm 0.19$ ) also justified such a choice. ( $f$  is the degree of freedom [19].) A short lifetime less than the reported bulk lifetime in ZnO due to free annihilation of positrons can occur and the average of such lifetimes will be the shortest lifetime component in the analysis. It is termed as  $\tau_1$ . The longer components  $\tau_2$  and  $\tau_3$  can arise from positron annihilation within the vacancy-type defects in the crystallites and the formation and annihilation of orthopositronium atoms in the regions between the crystallites [20]. The latter are spin triplet bound states of positrons with electrons and their lifetimes, i.e., the longest component  $\tau_3$  ( $\sim 1-4$  ns), is a result of the very low electron density pervading in the intercrystallite region. Its intensity  $I_3$  however is very small, for example, less than 0.6% in the present case. Ignoring the presence of this component, however, resulted in poor variance of fit ( $\nu > 2-3$ ) and hence not accepted as an alternative route. Further discussion is no more made about this component.

Positron lifetime in pure ZnO ( $\tau_b$ ) has been reported as any value from 151 ps to 177 ps by several authors [21]. The value we obtained in a previous experiment was 179 ps.<sup>25</sup> Normally, in the presence of just one type of defects,  $\tau_1$  will be less than  $\tau_b$ . This follows from the two-state trapping model [22-23]. When the positrons get trapped in defects, they will have a further lifetime of  $\tau_2$ . The survival time in the pre-trapped state is called the Bloch state residence time because the positron during this time interval will be diffusing through the interstitial position under the influence of the periodic potential (called Bloch potential). The maximum delocalized (free) positron lifetime is  $\tau_b$ , i.e., if the positron is not trapped in the

defect during this time, it will be annihilated from the bulk with the lifetime  $\tau_b$ . Hence the average of the Bloch state residence time and  $\tau_b$  will be always less than  $\tau_b$ . The situation can change if there are two or more types of defects in the sample, in which case  $\tau_1$  can be greater than  $\tau_b$ . This is not the present case. It is found that  $\tau_1$  is less than  $\tau_b$  for all the samples. This means there is only one predominant type of positron trapping sites and the surfaces of nanocrystallites are the likely attributions. Since the nanocrystallites of all the samples used here are of sizes less than the thermal diffusion length of positrons ( $\sim 52$  nm for ZnO [24, 25]), they can thermally diffuse on to the grain surfaces and get annihilated there. The large magnitudes of  $\tau_2$  are proof to this.

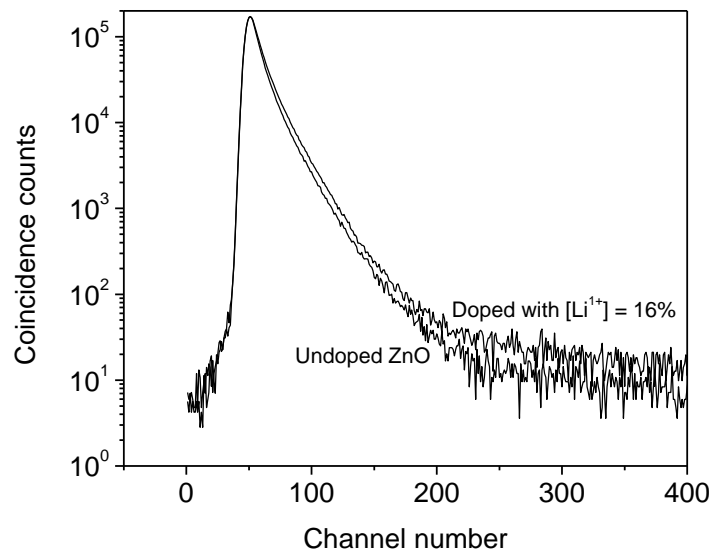


**Fig.7.8:** Peak-normalized positron lifetime spectra of the undoped and the highest doped ( $[Li^{1+}]=16\%$ ) samples.

However, the positron lifetime on the grain surfaces should have been a saturation lifetime and should not have shown any variation with the doping by  $Li^{1+}$  ions. As illustrated in Fig. 7.9, all the positron annihilation parameters exhibit two opposite trends. Up to  $x = 7\%$ , all the positron lifetimes decrease and then at higher values of  $x$ , they increase. This means,  $\tau_2$  also contains a contribution from the electron density within the particles. Vacancy clusters are possible within the particles and they arise from the non-stoichiometry of the semiconductor material. Hence  $\tau_2$  is treated here as an average of the positron lifetimes within the vacancy clusters and the crystallite surfaces, whose numerical values are close to one another.

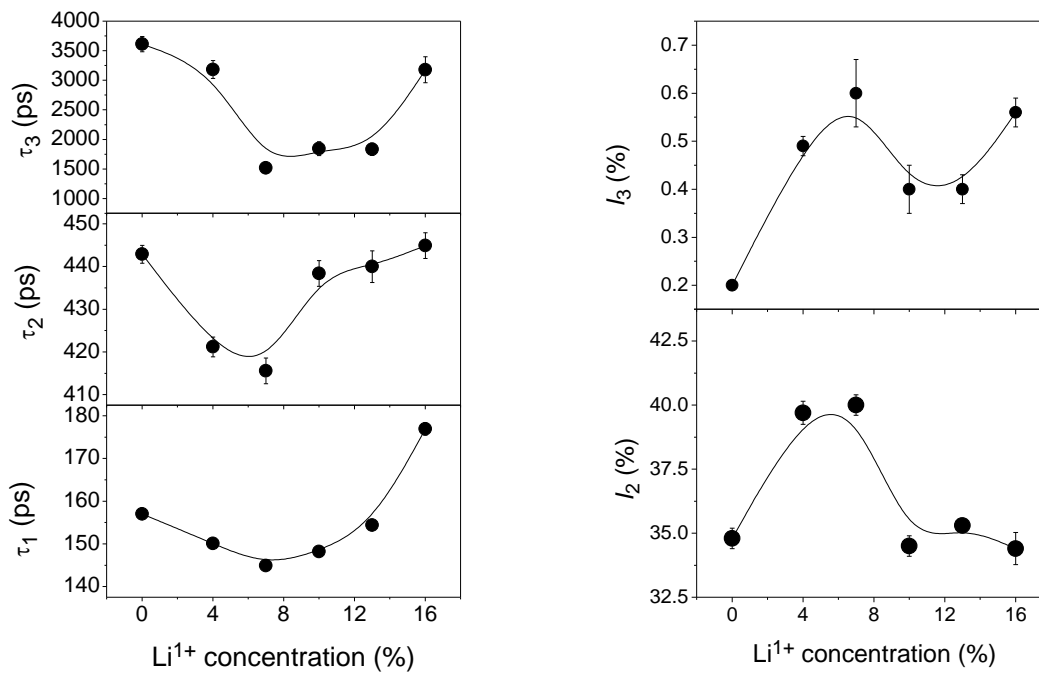


**Fig. 7.9:** The positron lifetimes and the relative intensities of the two longer lifetimes versus the concentration of  $\text{Li}^{1+}$  doping in the ZnO nanocrystalline samples.

The variations of the positron lifetimes and intensities with increasing concentration of  $\text{Li}^{1+}$  ions can result from two opposite effects (Fig. 7.9). In the initial stages of doping, vacancy clusters of the type  $V_{\text{Zn}+\text{O}+\text{Zn}}$  are partially filled by  $\text{Li}^{1+}$  ions, reducing them to lithium-vacancy complexes and this will cause the positron lifetime  $\tau_2$  to fall as the effective size of the vacancy cluster is decreased. At the same time, there are also substitution effects in which  $\text{Zn}^{2+}$  ions will be replaced by  $\text{Li}^{1+}$  ions. The reduction will introduce fresh oxygen vacancies in the samples. Since oxygen vacancies are positively charged, positrons cannot get trapped into them directly but their agglomeration with the existing monovacancies of  $\text{Zn}^{2+}$  will result into neutral divacancies of the form  $V_{\text{Zn}+\text{O}}$ . Positrons get trapped in them and the effect is reflected as a sharp increase in the intensity  $I_2$ . Above  $x = 7\%$ , however, the doped  $\text{Li}^{1+}$  ions with a unit positive charge start occupying the interstitial sites and this abruptly block the free diffusion of the positrons. Positron trapping in defects is therefore immensely reduced as indicated by a drastic fall in  $I_2$  and the principal contribution to the lifetime  $\tau_2$  at this stage comes from those getting annihilated at the crystallite surfaces. Although the longest lifetime component  $\tau_3$  and its intensity  $I_3$  also show systematic variations with the doping concentrations, as already stated

before, much significance is not attributed as the concerned intensity  $I_3$  is really small ( $< 0.6\%$ ).

#### 7.8.2.4.2 Coincidence Doppler broadening spectroscopic (CDBS) measurements

The CDBS measurements are carried out first by recording the spectra of energies of annihilation gamma rays going in the opposite directions using high pure germanium detectors and then generating a two-parameter spectrum with the sum and difference of the energies in the x- and y-axes and the time correlated events in the z-axis [26, 27]. The distribution of events parallel to the y-axis in the sum interval  $1022 \pm 2.4$  keV is a Doppler broadened positron annihilation gamma ray spectrum free of the detector resolution function and nuclear background effects.

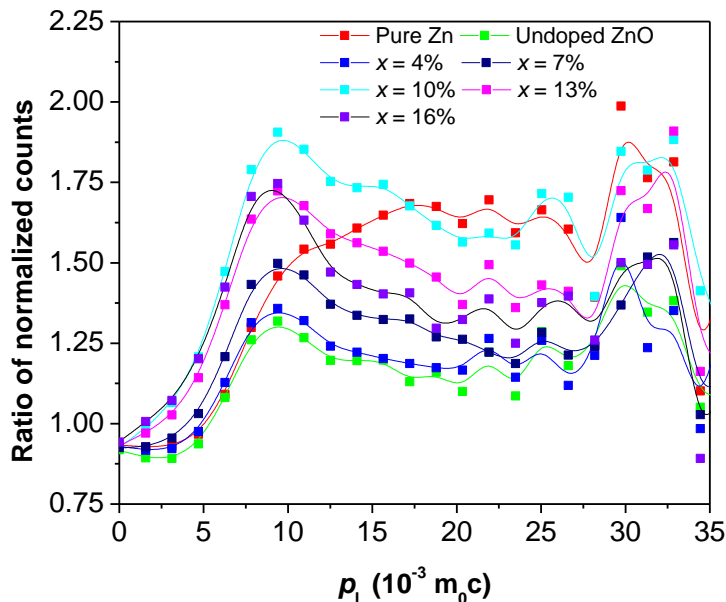


**Fig. 7.10:** The quotient spectra obtained from the CDBS data of the different samples with respect to single crystalline Al reference samples.

It is therefore a true reflection of the electron momentum distribution in the material under study. The changes in electron momentum distribution are however too small to differentiate. Hence, in order to magnify the very small differences, the spectra so obtained are generally divided by an identical spectrum obtained for a pure defect-free reference sample. In this case, we had used single crystalline Al sample as the reference. It had purity better than 99.999% and was annealed at  $600^\circ\text{C}$  for 2 hours in vacuum before the measurements. It gave a single-component positron

lifetime spectrum with a value 165 ps, close to 162 ps reported for Al in literature. The spectra so obtained are called quotient spectra or ratio curves. These are shown in Fig. 7.10. All the curves exhibit two distinct peaks, the one at the longitudinal electron momentum  $p_L = 9.39 \times 10^{-3} m_0c$  is due to elemental oxygen environment surrounding the cationic vacancies where positrons get strongly trapped. A less prominent peak at  $p_L = 29-33 \times 10^{-3} m_0c$  needs special mention as it shows a certain consistency with the increasing annihilation of positrons with the electrons of  $Li^{1+}$ .

To examine the spectra better, the value of  $p_L$  and the peak amplitude for the different samples are illustrated in Fig. 7.11 (a) and (b). With the increase of  $Li^{1+}$  ion concentration, the peak gets shifted towards higher electron momenta and the amplitudes of the peaks too increase. The latter is understandable as due to increasing number of  $Li^{1+}$  ions whereas a definite shift of the peak towards higher electron momenta points towards excess  $Li^{1+}$  ions segregating over defects and surfaces and positrons getting increasing proximity to interact and get annihilated with the electrons. An interesting observation is the smooth variation of the two quantities (Fig. 7.12) thereby emphasizing the increasing substitution of  $Zn^{2+}$  ions by the  $Li^{1+}$  ions. It suggests that Li is a very appropriate cation to modify the properties of ZnO nanocrystals to an appreciable extent.

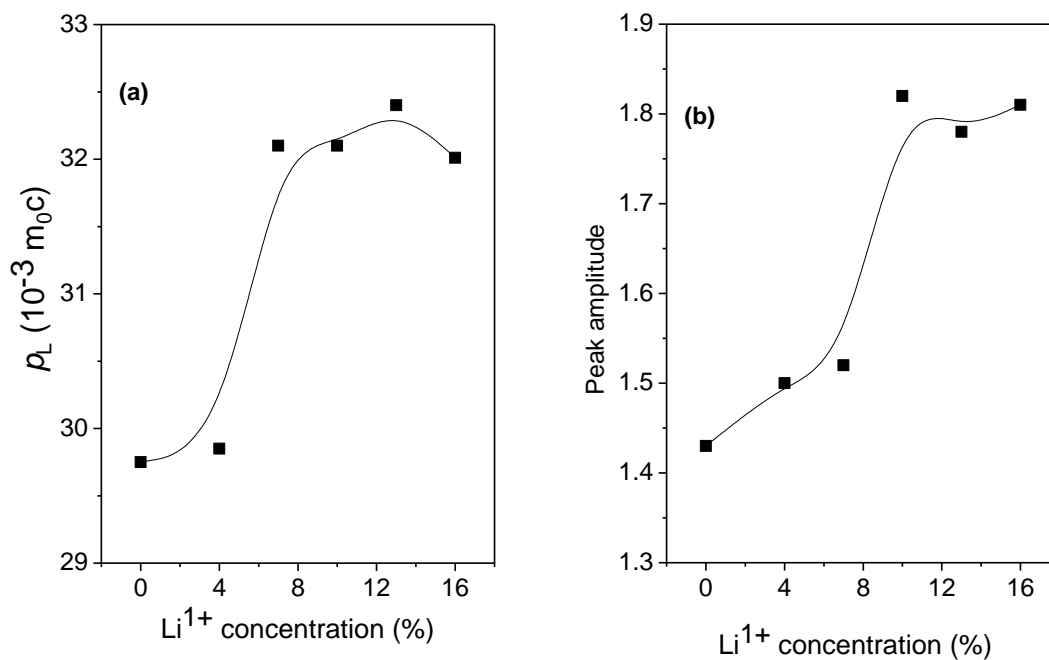


**Fig.7.11:** (a) The longitudinal electron momentum  $p_L$  corresponding to the secondary peak and (b) the peak amplitude in the CDB spectra of the  $Li^{1+}$ -doped ZnO nanocrystalline samples.

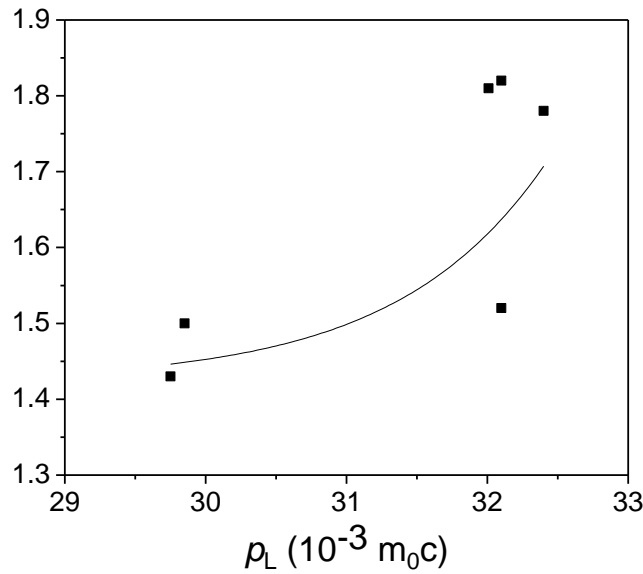


**Fig. 7.12:** A plot depicting the smooth variation of the amplitude of the secondary peak of the CDB spectra with the corresponding longitudinal electron momentum  $p_L$ .

Before concluding, a look at the variation of the two lineshape parameters  $S$  and  $W$  helps to understand the evolution of defects during the doping process. These parameters have been derived from the projected one-dimensional spectra described above, according to the relations

$$S = \frac{\sum_{i=-2}^2 N_i(\Delta E)}{\sum_{i=-50}^{50} N_i(\Delta E)} \quad 1(a)$$

and

$$W = \frac{\sum_{i=-12}^{-4} N_i(\Delta E) + \sum_{i=4}^{12} N_i(\Delta E)}{\sum_{i=-50}^{50} N_i(\Delta E)} \quad 2(b)$$

Here in these equations,  $i = 0$  corresponds to  $E_1 - E_2 = 2\Delta E = 0$  and each channel was calibrated for 400 eV. The calculated  $S$  and  $W$  parameters are plotted against the  $\text{Li}^{1+}$  doping concentration and shown in Fig. 7.13. The figure depicts a continuously rising  $S$  parameter with increasing doping concentration while the  $W$  parameter shows a continuous decrease. Consequently the  $S$ - $W$  plot which is used to illustrate the defect evolution process is a falling straight line (Fig. 7.14.).

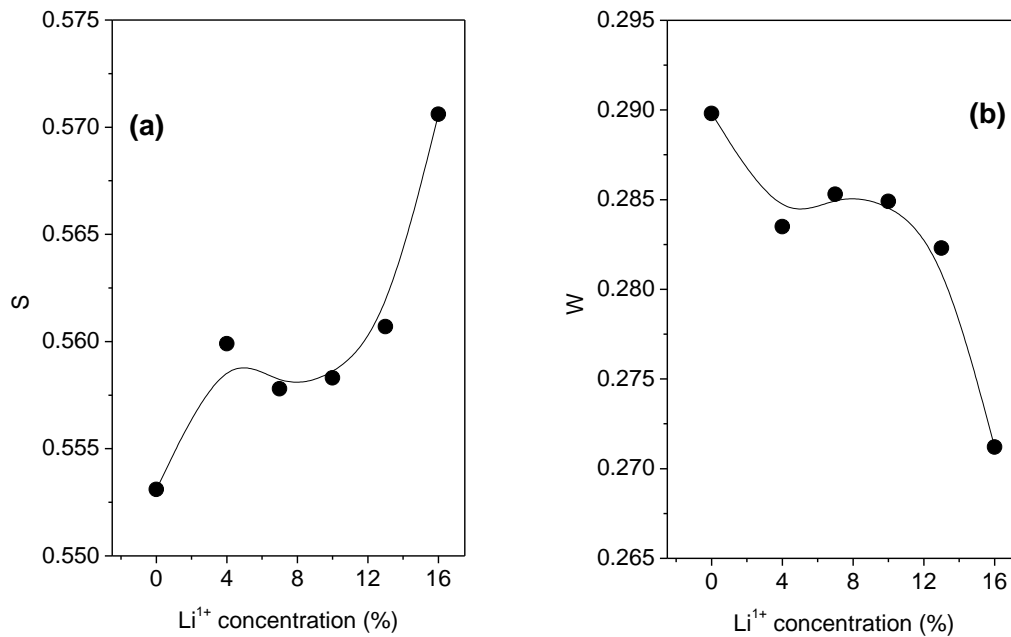


**Fig. 7.13:** The lineshape parameters (a) *S* and (b) *W* versus the concentration of Li<sup>1+</sup> doping in the ZnO nanocrystalline samples.

The *S* and *W* parameters basically represent the fractions of low and high momentum electrons annihilated by the positrons. The relative values of these fractions are characteristics of the defects and their change can throw some light on the major defect evolution process. The straight line behavior of the parameters, as shown in Fig. 7.14, confirms the existence of vacancy clusters that have still not undergone any structural changes or annealing during the range of doping used and can still play a significant role in deciding the related properties of the material, as discussed elsewhere [28]. One difference is, however, very much visible. In the positron lifetime results, there was a clear reversal of variation across  $x = 7\%$ . In CDBS, such a demarcation is not to be seen and the variation is continuous. This is to be understood from additional investigations using complementary experimental techniques that can support the findings from positron annihilation measurements.

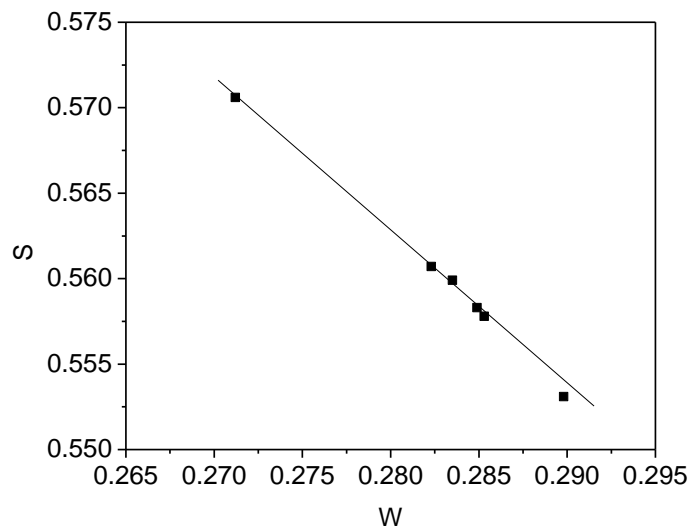


Fig. 7.14: The S-W plot.

The S-parameters represent the positron annihilation with the low momentum electrons i.e. in vacancy sites or voids within the sample. Here, in Li-doped ZnO, the gradual increase of S-parameter indicates the increase of Zn vacancy ( $V_{Zn}$ ) or vacancy cluster concentration due to Li-doping. Earlier, PL spectra also showed the evidence of enhancement of  $V_{Zn}$  concentration due to Li doping. Wang *et al.*[30] have shown that the presence of  $V_{Zn}$  leads to the spin polarization of O 2p orbital which is source of localised magnetic moment. Besides  $V_{Zn}$ , the Li substitutional ( $Li_{Zn}$ ) can also induce localised magnetic moment which can contribute to the overall magnetic moment [29, 31]. The concentration of  $V_{Zn}$  increases due to the Li-doping in ZnO nanoparticles and when the concentration exceeds the percolation threshold, long-range ferromagnetic exchange interaction between the localised moments can be mediated by the hole due to  $Li_{Zn}$  acceptors. The strength of ferromagnetic interaction not only depends on the defect concentration but also on the effective hole concentration exists in the system. In a proposed model, Bouzerar and Ziman [29] have shown that for a fixed defect ( $V_{Zn}$ ) concentration, there exists a definite window of hole concentration within which the ferromagnetic exchange interaction becomes most stable. Earlier from XRD analysis we have seen that initially Li ions substitute at Zn site up to 7 at.% Li-doping and then it starts to occupy the lattice interstitial site. On contrary to  $Li_{Zn}$ , Li interstitial ( $Li_i$ ) is a donor defect which may kill the hole arising due to  $Li_{Zn}$ .

Therefore, in dilute doping level it is expected that the hole concentration in should increase gradually with increase of Li-doping and then after a certain doping level when Li interstitial ( $\text{Li}_i$ ) defects starts to appear, the hole concentration will fall down. As the ferromagnetic interaction between  $V_{\text{Zn}}$  defects are mediated by the hole, the decrease hole concentration results in decrease of  $M_s$  (see the inset of Fig. 7.6 (a)) when Li doping concentration exceeds beyond 10 at. %.

Therefore, the positron annihilation study here, confirms that the stabilization of  $V_{\text{Zn}}$  defects or defect clusters due to alkali-metal Li-doping and which are the main reason behind the observed RTFM in ZnO. Not only the Li-doped ZnO, but also the other alkali metals such as Na, K-doped ZnO nanowires or thin films (as seen in earlier Chapters, i.e. Chapter 5 and 6) also showed RTFM due to  $V_{\text{Zn}}$  defects [32, 33]. Besides inducing considerable magnetic moment, the substitution of such monovalent alkali ions in ZnO also makes Curie temperature ( $T_C$ ) quite high which satisfies the primary goal needed for spintronic application. Hence proper control and manipulation of such defects in ZnO can produce huge opportunity to modify the materials properties and make them suitable for various multifunctional applications. Therefore, defect-induced ferromagnetic oxide semiconductors can be used as alternatives of transitional metal-doped magnetic semiconductors as spintronic material.

### 7.8.3. Conclusions

The main aim of this chapter was to investigate the defect evolution due to Li-doping in ZnO using positron annihilation spectroscopy and to find a correlation positron annihilation results to the magnetic origin within Li-doped ZnO. Here, the element Li represents the alkali metals i.e. the group 1A elements. We found, at lower concentrations ( $x < 7\%$ ),  $\text{Li}^{1+}$  is found as an effective substituent at Zn site and results in reduction in both particle sizes and lattice constants. However, at  $x > 7\%$ ,  $\text{Li}^{1+}$  ions are found to prefer the interstitial positions and, as a result, there is lattice expansion and increase of particle sizes. All the Li-doped ZnO nanoparticles exhibited high temperature ferromagnetism and the both  $M_s$  and  $T_C$  are found to increase up to 10 at.% Li-doping and then decreases on further Li-doping. PL spectroscopic measurement showed the indication of presence of considerable amount Zn vacancies which was also confirmed by positron annihilation

measurements. We found that the enhancement of Zn vacancy concentration due to Li-doping and is responsible to induce high- $T_c$  ferromagnetism in Li-doped ZnO. Hence proper control and manipulation of such defects in ZnO can produce huge opportunity to modify the materials properties and make them suitable for various multifunctional applications. Therefore, it is quite interesting to conclude that these defect-induced ferromagnetic oxide semiconductors can be used as alternatives of transitional metal-doped magnetic semiconductors as spintronic material.

## References

- [1] R.W. Siegel, Positron annihilation Spectroscopy, *Annu. Rev. Mater. Sci.* 10, 393–425 (1980).
- [2] I Prochazka, *Materials Structures* 8, 55-60 (2001).
- [3] Positrons Solid-state Physics, Proc. Internat. School of Physics <<Enrico Fermi>>, Course LXXXIII, Varenna 1981, W. Brandt and A. Dupasquier, eds., (IOS Press, North-Holland, Amsterdam, 1983).
- [4] Positron Spectroscopy of Solids, Proc. Internat. School of Physics <<Enrico Fermi>>, Course LXXXIII, Varenna 1993, A. Dupasquier and A. P. M. Jr., eds., (IOS Press, North-Holland, Amsterdam, 1995).
- [5] R.W. Siegel, *Annu. Rev. Mater. Sci.* 10, 393–425 (1980).
- [6] M. J. Puska and R. M. Nieminen, *Rev. Mod. Phys.* 66 841 (1994).
- [7] D. C. Connors and R. N. West, *Phys. Lett. A* 30, 24 (1969).
- [8] Positron lifetime Spectroscopy, <http://www.positronannihilation.net/techniques/Momentum%20Distribution%20Techniques.pdf> (Accessed April 15, 2006).
- [9] Momentum Distribution Techniques, <http://www.positronannihilation.net/techniques/Positron%20Lifetime%20Spectroscopy.pdf> (Accessed April 15, 2006).
- [10] C.W. Zou, H. J. Wanga, M. L. Yi et al., *Appl. Surface Science* 256 2453, (2010).
- [11] Kong, Y. C.; Yu, D. P.; Zhang, B.; Fang, W.; Feng, S. Q. *Appl. Phys. Lett.* 78, 407 (2001).
- [12] Rauch, C.; Gehlhoff, W.; Wagner et al., *J. Appl. Phys.* 107, 024311 (2010).
- [13] Meyer, B. K.; Stehr, J.; Hofstaetter, A. et al., *J. Appl. Phys. A* 88, 119 (2007).
- [14] Ghosh, S.; Khan, G. G.; Das, B.; Mandal, K. J. *Appl. Phys.*, 109 123 927 (2011).
- [15] Børseth, T. M.; Svensson, B. G.; Kuznetsov et al., *Appl. Phys. Lett.* 89, 262112 (2006).
- [16] Janotti, A.; Van de Walle, C. G. *Phys. Rev. B* 76, 165202 (2007).
- [17] Reynolds, D. C.; Look, D. C.; Jogai, B.; Morkoc, H. *Solid State Commun.*, 101, 643 (1997).
- [18] Reynolds, D. C.; Look, D. C.; Jogai et al., *J. Solid State Commun.* 106, 701 (1998).

- [19] J.V. Olsen, P. Kirkegaard, N. J. Pedersen et al., *Phys. Stat. Sol. (c)* 4 (2007) 4004-4006.
- [20] R. Krause-Rehberg, and H.S. Leipner, (Eds.) *Positron Annihilation in Semiconductors - Defect Studies* (Springer: Berlin, 1999) pp. 1-126.
- [21] Tandra Ghoshal, Soumitra Kar et al., *J. Phys. Chem. C* 113 (9) 3419-3425 (2009).
- [22] B. Bergersen, and M.J. Stott, *Solid State Communication*. 7(17) (1969) 1203-1205.
- [23] P. Hautojärvi, and C. Corbel, *Positron spectroscopy of defects in metals and semiconductors*, In: A. Dupasquier and A.P. Mills, Jr., eds., *Positron Spectroscopy of Solids. Proceedings of the 125<sup>th</sup> International School of Physics "Enrico Fermi"*, July 6-16, 1993, Lake Como, Villa Monastero, Italy (Amsterdam: IOS Press 1995) 491-532.
- [24] T. Koida, S. F. Chichibu, A. Uedono et al., *Appl. Phys. Lett.* 82(4) 532-534 (2003).
- [25] A. Zubiaga, F. Tuomisto, F. Plazaola et al., *Appl. Phys. Lett.* 86 042103 (2005).
- [26] P. Asoka-Kumar, M. Alatalo, V.J. Ghosh et al., *Phys. Rev. Lett.* 77 (10) 2097-2100 (1996).
- [27] S. Szpala, P. Asoka-Kumar, B. Nielsen et al., *Phys. Rev. B* 54 (7) 4722-4731 (1996).
- [28] M. Clement, J.M.M. de Nijs, P. Balk et al., *J. Appl. Phys.* 79 (12) 9029-9036 (1996).
- [29] G. Bouzerar, T. Ziman, *Phys. Rev. Lett.* 96, 207602 (2006).
- [30] Q. Wang, Q. Sun, G. Chen et al., *Physical Review B* 77, 205411 (2008).
- [31] P. Dev, P. Zhang, *Physical Review B* 81, 085207 (2010).
- [32] S. Ghosh, G. G. Khan, B. Das, K. Mandal, *J. Appl. Phys.*, 109, 123927 (2011).
- [33] S. Ghosh, G. G.Khan, S. Varma, K. Mandal, *J. Appl. Phys.* 112, 043910 (2012).

# Chapter 8

## Conclusion and Scope for Future Study

In this thesis, we have investigated the role of different magnetic ions such as transitional metal (TM) or rare-earth (RE) impurities and vacancy-type defects such as cation (Zn, Sn) or anion (O) vacancy in stabilizing room-temperature (RT) ferromagnetism (FM) in wide-band oxide semiconductors with the correlation of their optical as well as electrical properties. We found absence of intrinsic FM in TM Co-doped ZnO and SnO<sub>2</sub> bulk powders prepared by mechanical milling process. Although the divalent Co ions substitute at Zn or Sn site within ZnO or SnO<sub>2</sub> lattice, no evidence of intrinsic FM is detected, instead a paramagnetic behavior is observed. However, with the reduction of particle size to nanoscale regime (< 50 nm), room-temperature ferromagnetism (RTFM) is found to be stabilize in Co-doped SnO<sub>2</sub> which decreases or even vanishes when the samples are annealed in oxygen atmosphere. This indicates that FM associated with the nanostructures arises due to structural defects, not due to the substituted Co ions. In Fe-doped SnO<sub>2</sub> bulk materials, an evidence of antiferromagnetic (AFM) interaction between the Fe<sup>2+</sup> ions are confirmed though Zero field-cooled (ZFC) and field-cooled (FC) magnetization studies whereas with the incorporation of additional nitrogen (N) at O site, ferromagnetic interaction between Fe<sup>2+</sup> ions mediate through the holes arising due to

N co-doping. Therefore, sufficient carrier concentration might be essential criteria to turn on the FM interaction between the TM ions substituted within the host lattice. Similar to pure SnO<sub>2</sub> nanorods, pure SnO<sub>2</sub> thin films prepared by radio-frequency (RF) magnetron sputtering technique also exhibited RTFM which interestingly, decreased gradually with RE ion Gd-doping. Photoluminescence (PL) and electron paramagnetic resonance (EPR) spectroscopic analysis showed that structural defects such as oxygen vacancy ( $V_O$ ) are the dominant source for the origin of magnetic moment in pure SnO<sub>2</sub> nanostructures. Defect-driven  $d^0$  RTFM are also observed in case of pure ZnO nanowires (NWs) fabricated within the nanopores of anodic aluminium oxides (AAO) template. This FM signature in ZnO NWs has enhanced significantly with doping of non-magnetic group-1 element potassium (K) up to a certain concentration limit. PL spectroscopy showed the evidence of large concentration of Zn vacancy ( $V_{Zn}$ ) which stabilized due K-substitution at Zn site. K-doping also introduces a hole at O site which mediate the FM interaction between the  $V_{Zn}$  defects. Substitution of Lithium (Li) at Zn site also found to stabilize high  $T_C$  FM in ZnO NWs. It is observed that saturation moment as well as the Curie temperature in Li-N co-doped ZnO NWs can be enhanced by increasing N concentration [9]. This indicates the role of holes to mediate FM interaction between the Zn vacancies in ZnO:Li matrix. On the other hand, F co-doping which donates electron into the system acts to oppose the FM interaction in Li-F codoped ZnO. A comparative study regarding the degree of efficiency of different alkali metals like Li, Na, K etc. to induce FM in ZnO thin films, prepared by pulsed laser deposition (PLD) is also performed and it is found that Li is the most effective alkali element compared its other co-group candidates. Effects of oxygen partial pressure ( $PO_2$ ) and film thickness on the magnetic, optical and electrical properties in sodium (Na)-ZnO thin films are also investigated. At last, positron annihilation spectroscopy (PAS) is employed to investigate the presence of different defects and their evolution depending on annealing temperature and atmosphere TiO<sub>2</sub> and also due to Li-substitution in ZnO nanoparticles. It is found that Li-substitution indeed enhances the  $V_{Zn}$  defect concentration which is mainly responsible to stabilize  $d^0$  FM in Li-doped ZnO. Therefore, our study shows that substitution of nonmagnetic group-1 alkali-metal in ZnO can be a promising direction to stabilize, enhance and tune high  $T_C$  FM and this can be an exciting approach to prepare new class of ZnO based DMS for spintronic and opto-spintronic applications.

### Scope for future study:

In this thesis, so far we have studied defect-originated ferromagnetic properties in group II-VI oxide compounds like ZnO in which the substitution of monovalent alkali metal like Li or Na or K introduces one charge deficiency i.e. creates one hole in O site. However, the substitution of such monovalent alkali ion in case of group IV-VI oxide semiconductor hosts such as SnO<sub>2</sub>, TiO<sub>2</sub> will induce three formal charge deficiency i.e. will create three holes at O site. We have seen in case of ZnO, the magnetic moment originates both from Zn vacancy as well as from the alkali substitutional defects. However, the magnetic moment in case of ZnO is found to be quite low in magnitude. On the other hand, from recent theoretical studies, it has been found that the magnetic moment of Sn vacancy in SnO<sub>2</sub> or Ti vacancy in TiO<sub>2</sub> are larger compared to that of Zn vacancy in ZnO. Hence, if it is possible to stabilize Sn vacancy or Ti vacancy in SnO<sub>2</sub> or TiO<sub>2</sub>, one can expect that alkali (Li, Na, K)-doped SnO<sub>2</sub> or TiO<sub>2</sub> should exhibit higher magnetic moment as high level of hole concentration which are more favourable to stabilize ferromagnetism with large magnetic moment. Therefore, our work in this thesis can be extended in case of SnO<sub>2</sub> or TiO<sub>2</sub> host systems which will increase the choice of magnetic semiconducting materials.

Except the nonmagnetic substitution at host cation site, several nonmagnetic doping at oxygen site such as carbon (C), nitrogen (N) are also being investigated to stabilize ferromagnetism in such oxides semiconductors. Still the origin of ferromagnetism in such system is not quite clear. Therefore, the study of such systems should also be studied in details.

Besides that, so far we have concentrated on methods of spin injection either using magnetic impurity doping or by introducing certain-type of defects in nonmagnetic wide band oxide semiconductors. After spin injection, spintronic application needs other two basic functionalities and they are spin transport and spin detection. To check the efficiency of spin transport one can study multi-layered sandwiched systems. One can prepare a ferromagnetic semiconducting layer (suppose Li-doped ZnO) on a substrate, then deposit a nonmagnetic semiconducting layer (TiO<sub>2</sub> or Si, C) on it and then again deposit another ferromagnetic layer above it and study the composite multi-layered system.